

1-th INTERNATIONAL CONFERENCE
NANOMATERIALS: APPLICATIONS & PROPERTIES
Alushta, Crimea, 27 - 30 s\September 2011



Nan**o**materials: **A**pplications & **P**roperties

1st NAP
Proceedings
Vol. 2, Part II

Edited by
Alexander Pogrebnjak
and Taras Lyutyy,
Sergey Protsenko



MINISTRY OF EDUCATION, SCIENCE,
YOUTH AND SPORTS OF UKRAINE
Sumy State University
V.N. Karazin Kharkiv National University
NATIONAL ACADEMY OF SCIENCE OF UKRAINE
Lublin University of Technology
Kaunas University of Technology

1-st INTERNATIONAL CONFERENCE

**NANOMATERIALS:
APPLICATIONS &
PROPERTIES**

NAP-2011

PROCEEDINGS

Vol. 2, Part II

Alushta, Crimea, Ukraine
Sept. 27-30, 2011

Sumy, Sumy State University
2011

The Proceedings NAP-2011 are in
commemoration of Academician
NAS of Ukraine
Shpak Anatolii Petrovich

Contents

Consolidated nanomaterials.....246

Advances in equipment and technologies286

Radiation effects in solids354

Organizing Committee

Chair

A. Shpak (Ukraine) chair A. Vasylyev (Ukraine), co-chair A. Pogrebnjak (Ukraine) co-chair

International Scientific Committee

A. Grigonis (Lithuania)	G. Abrasonis, (Germany)	P. Zukowski (Poland)
A. Cavaleiro (Portugal)	R. Andrievskii (Russia)	E. Levashov (Russia)
A. Korotaev (Russia)	P. Panjan (Slovenia)	E. Majkova (Slovakia)
N. Azarenkov (Ukraine)	V. Uglov (Belarus)	F. Komarov (Belarus)
N. Ali (UK)	V. Anishchik (Belarus)	J. Musil (Czech Republic)
F. Cui (China)	V. Beresnev (Ukraine)	I. Protsenko (Ukraine)
G. Abadias (France)	J.P. Riviere (France)	J. Han (Korea)
G. Bräuer (Germany)	D. Cameron (Finland)	A. Leson (Germany)
	R. Boxman (Israel)	

Organizing Committee

V. Uvarov (Ukraine), chair of Organazing Committee
T. Lyutyy (Ukraine) V. Kosyak (Ukraine) V. Partyka (Poland)
O. Ivanov (Russia) S. Protsenko (Ukraine)

Local Organizing Committee

Address: NAP-2011 Conference, Sumy State University
2, Rimsky-Korsakov Street, Sumy, 40007, Ukraine

Web: www.nap.sumdu.edu.ua

E-mail: nap@sumdu.edu.ua

Fax: + 380 542 33 40 58

Contact persons:

Salutation	Prof.	Ass. Prof.	Ass. Prof.
Name	Alexander	Taras	Serhiy
Family Name	Pogrebnjak	Lyutyy	Protsenko
Tel:	+ 380 68 6529647	+ 380 66 9379149	+380 50 6358863
E-mail:	alex@ekt.sumdu.edu.ua	lyutyy@oeph.sumdu.edu.ua	serhiy.protsenko@elit.sumdu.edu.ua

Consolidated nanomaterials

STRUCTURAL CHANGES IN FRICTION-STIR WELDED Al-Li-Cu-Sc-Zr (1460) ALLOY

Alla L. Berezina¹, Nataliya N. Budarina¹, Andriy V. Kotko¹,
Oleg A. Molebny^{1,2}, Alla A. Chayka², Alexander Ya. Ischenko²

- 1 G.V.Kurdiymov Institute for Metal Physics, National Academy of Sciences of Ukraine, Vernadsky Blvd. 36,03142, Kyiv, Ukraine
- 2 E.O.Paton Electric Welding Institute, National Academy of Sciences of Ukraine, Bozhenko Str. 11, 03680, Kyiv, Ukraine

ABSTRACT

Structure and properties of Al-2.3%Li-3%Cu-0.1%Sc-0.1%Zr (1460) were studied after FSW on thin cold-rolled sheets with the thickness of 2mm. Sheets were aged in the T8mode. During FSW, severe plastic deformation and material flow occurs at the temperature lower than melting temperature. Welding was performed at the tool rotation speed 2880 rps. The tool was moved along the weld joint at the constant speed 16m/h.

Key words: friction stir welding, Al-Li-Cu-Sc-Zr alloys, plastic deformation, recrystallization, structural evolution

INTRODUCTION

Friction stir welding (FSW) is a relatively new solid-state joining process. FSW and friction stir processing (FSP) are emerging as very effective solid-state joining/processing techniques. FSW was invented at the Welding Institute of UK in 1991 as a solid-state joining technique, and it was initially applied to aluminium alloys [1] (Thomas et al., 1991). During FSW the metal transforms to the special plasticized state (an analogue of non-Newtonian liquid) due to high-speed intense plastic deformation at high temperatures. FSW involves complex interactions among a variety of simultaneous thermo-mechanical processes. The interactions affect the heating and cooling rates, plastic deformation and flow, dynamic and post-dynamic recrystallization phenomena, as well as the mechanical integrity of the joint [2].

A unique feature of the friction-stir welding process is that the transport of heat is aided by the plastic flow of the substrate close to the rotating tool. The heat and mass transfer depends on material properties as well as welding variables including the rotational and welding speeds of the tool and its geometry. In FSW, the joining is produced by extrusion and forging of the metal at high strain rates. The effect of welding on microstructural evolutions and resulting joint properties have been investigated. Durometric, resistometric, X-ray and

* e-mail: moleb@imp.kiev.ua, tel: (+38)0444243210

electron-microscopy studies were performed on different weld zones: the stirred zone; the thermo-mechanically affected zone; the heat-affected zone; the base metal. The density and nature of dislocations, and average grain sizes in different weld zones were determined using X-ray diffraction peak profile analysis. Particular attention was given to the effect of post-weld ageing on the strength of the weld. Structural and durometric studies were performed after repeated aging.

METHODS OF SPECIMEN MANUFACTURING AND ANALYSIS

Structure and properties of Al-2.3%Li-3%Cu-0.1%Sc-0.1%Zr (commercial 1460 alloy) were studied after FSW on thin cold-rolled sheets 2mm thick. Sheets were aged in the T8 mode. During FSW, severe plastic deformation and material flow occurs at temperature lower than melting temperature. Welding was performed at the tool rotation speed of 2880rps. The tool was moved along the weld joint at the constant speed of 16m/h.

The cross-section of the FSW plate was cut in the middle along the plate length for the microstructural characterization.

Metallographic studies were carried out on polished and etched cross-section surface. Etching was done using Keller's reagent at room temperature. Four different etching zones were observed: A – stirred zone (SZ); B&C – thermo-mechanically affected zone (TMAZ); D – heat affected zone (HAZ) & base metal (BM). Location of HAZ can be estimated by hardness curve behavior.

The half-plate where the direction of tool rotation is the same as the direction of half-plate motion is called the *retreating* side (marked as C), with the other side designated as being the *advancing* side (marked as B). Extrusion phenomena were observed on the retreating side. This in itself proves that material flows from advancing to retreating side during FSW.

The phase structure as well as dislocations and grain sizes were observed in the base material and FSW sample using transmission electronic microscopy (TEM). Disc specimens (3mm in diameter) were prepared by mechanical grinding to 250 μ m thickness and electropolishing using a 30% nitric acid solution in methanol with 60V \times 1A at -20° C. Material for these specimens was taken from different weld zones at four different sites along the midthickness of the cross-section in FSW sample as marked with rectangles in *Fig. 1*.

Resistance measurements were carried out using an experimental arrangement based on the classical four-probe d.c. method. Measurements were performed at the heating rate of 3° C/min in the temperature range from room temperature to 600° C.

The X-ray diffraction profiles for the base material and FSW sample were measured by a HZG-1 diffractometer.

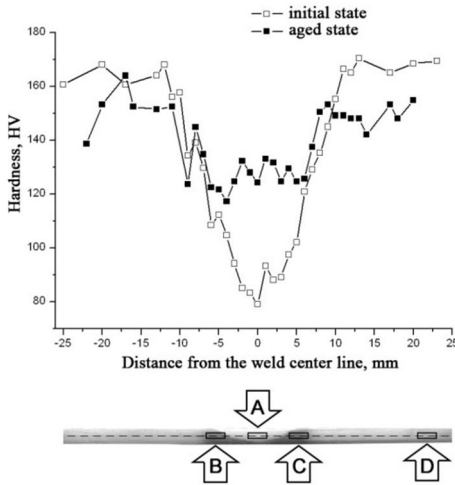


Fig. 1— Vicker's hardness plot scaled to the weld macrostructure picture

RESULTS AND DISCUSSION

The Vicker's hardness was measured on polished surfaces across the weld 1mm below the surface from the advancing to the retreating side from base metal to base metal (Fig. 1). Hardness data were obtained with a hardness meter, with the test load of 5kg and the load time of 20 s. Durometric study showed a 50% weakening in SZ after FSW and suggested a plausible hardening up to 75% of base metal hardness after aging in the T8 mode.

The following results were obtained by OM and TEM: texture and partial recrystallization were observed in the base metal zone. Nano-dispersed T_1 -phase and nano-composite δ'/θ' , $\delta'/Al_3(Sc,Zr)$ particles [3] were present in the matrix. This resulted in alloy hardening. Complete recrystallization occurred in the stirred zone after FSW, the texture disappeared, grains became equiaxial, were of 1-3 μm size, without substructure. θ' and T_1 phases dissolved. There were only δ' and $\delta'/Al_3(Sc,Zr)$ phases present in the stirred zone. The δ' and $\delta'/Al_3(Sc,Zr)$ phases were only present in the stirred zone; hardness decreased.

Grain sizes in the thermo-mechanically affected zone remained constant. But the volume part of T_1 phase increased significantly and T_2 phase appeared on the T_1 phase – matrix interface. Anomalous grain growth up to 30 – 100 μm occurred in the heat-affected zone.

TEM results (Fig. 2) are in good agreement with metallographic and resistometric ones.

The radiation was CuK_{α} at operating parameters of 20 mA and 35 kV, and Al_2O_3 single crystal (standard) was used to separate the instrument broadening effects. The pseudo-Voigt analytical function plus the linear background were fitted to the overlapping peaks. Physical broadening was obtained by the Halder-Wagner relation

$$\beta_{phys} = \sqrt{\beta_{exp}^2 - \beta_{exp}\beta_{etalon}}$$

where β is integral peak profile of experimental and standard peak profiles.

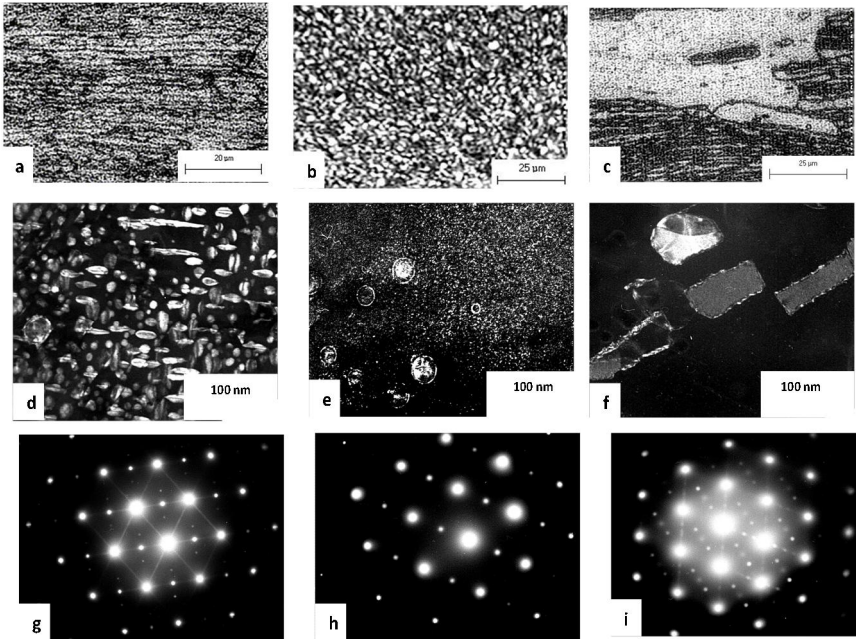


Fig. 2 – Metallographic and TEM studies: base metal: *a* – grain structure, *d* – phase structure, *g* – selected area diffraction pattern; stirred zone: *b* – grain structure, *e* – phase structure, *h* – selected area diffraction pattern; thermo-mechanically affected zone: *f* – phase structure, *i* – selected area diffraction pattern; heat-affected zone: *c* – grain structure

As one can see from the curves of changes in temperature coefficient of electrical resistivity (*Fig. 3*), two main temperature areas can be marked out on

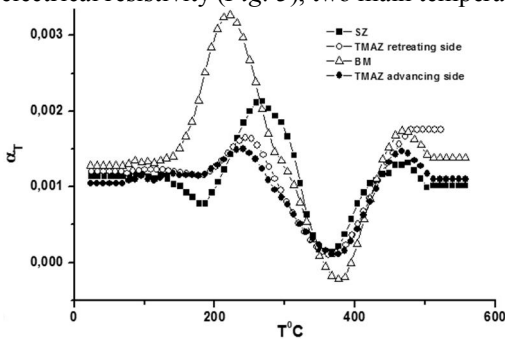


Fig. 3 – Changes in temperature coefficient of electrical resistivity α_T at continuous heating at the speed of $3^\circ\text{C}/\text{min}$ during 20-600°C temperature range

all curves: the positive peak at low temperatures caused by δ' phase dissolution and the negative peak at high temperatures, which can be accounted for by T_1 phase formation. Small negative peak before δ' phase dissolution peak on SZ sample curve proves that the material in SZ changed to solid solution state because of intensive

plastic deformation during FSW.

X-ray diffraction analysis is known to be a useful technique for evaluating the microstructural characteristics such as dislocation density and size of the coherent scattering domains [4]. The presence of dislocations and small size of crystallites lead to X-ray diffraction peak profile broadening, which is used in methods of microstructural parameters estimation.

The Williamson-Hall plots [5] show the qualitative behavior of diffraction peak broadening with full width at half maximum (or integral breadths) as a function of K , where $K=2\sin\theta/\lambda$, θ and λ are the diffraction angle and the wavelength of X-ray radiation, respectively. Strain anisotropy in the conventional Williamson-Hall plot was rationalized by substituting $KC^{1/2}$ for K [6], which is now known as the Williamson-Hall-Ungar method.

Where anisotropy microdistortion resulted in anisotropic diffraction line broadening [7], Ungar added the dislocation contrast factor \bar{C} , which can be determined by elastic anisotropy and dislocation type of the material [8], to the known relation:

$$\Delta K \cong \frac{0.9}{D} + \left(\frac{\pi M^2 b^2}{2} \right)^{1/2} \rho^{1/2} K \sqrt{\bar{C}} + O(K^2 \bar{C}) \Delta K \cong \frac{0.9}{D} + \left(\frac{\pi M^2 b^2}{2} \right)^{1/2} \rho^{1/2} K \sqrt{\bar{C}} + O(K^2 \bar{C}) \Delta K \cong \frac{0.9}{D} + \left(\frac{\pi M^2 b^2}{2} \right)^{1/2} \rho^{1/2} K \sqrt{\bar{C}} + O(K^2 \bar{C})$$

Where $K = 2 \sin \theta / \lambda$, $K = 2 \sin \theta / \lambda$, θ – diffraction angle, λ – X-ray wavelength, $\Delta K = \cos \theta [\Delta(2\theta)] / \lambda$, $\Delta K = \cos \theta [\Delta(2\theta)] / \lambda$, here $\Delta(2\theta)$ is the integral weight of diffraction peak, D – the average size of crystallites, M – the constant of effective outer cut-off radius of dislocation, ρ – the average dislocation density, b – Burgers module.

The average value of dislocation contrast factor is determined using elastic constants for Al, and constructed as a function of elastic constants for possible dislocations in face-centred cubic (f.c.c.) lattice.

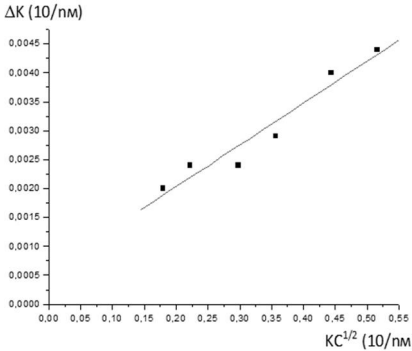


Fig. 4 – The Williamson-Hall-Ungar plot for base metal

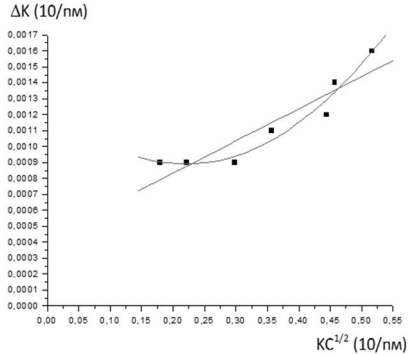


Fig. 5 – The Williamson-Hall-Ungar plot for stirred-nugget zone.

The Williamson-Hall-Ungar relations are shown in *Fig.4-6* for different states of materials. The Willimson-Hall-Ungar plot provides two important microstructural features in the material under investigation. First, the slope of the linear regression is proportional to the microstrain.

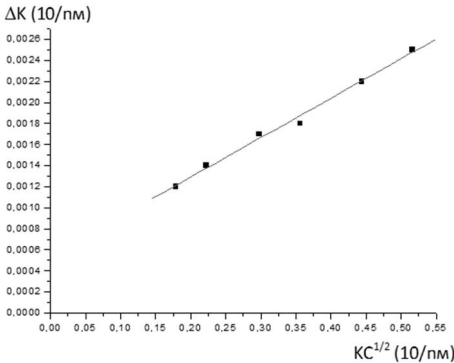


Fig. 6 – The Williamson-Hall-Ungar plot for TMAZ/HAZ

Second, the intercept of the linear regression with the data points at $K = 0$ is a rough size-estimation of the coherent scattering domains indicating by the similar average crystallite size.

Such type of dislocation structure was proved to persist in all specimens. This is evidenced by the fact that the best linear regressions were achieved with elastic constant $c_{12}/c_{44} = 2$. It is to be noted that the Williamson-Hall-Ungar plot

is parabolic for the stirred zone (*Fig. 5*). The average coherent domain size is 70.86 nm, which agrees with electronic microscopy data. It can be seen from *Table 1* that the largest distortions are present in the base material, and the smallest ones – in the stirred zone.

Calculation results of microstructural parameters are shown in *Table1* (R-factor is accuracy of regression):

Table 1

State	D, nm	ϵ	R-factor
-------	-------	------------	----------

Base metal	118.9	0.0077	0.96
Stirred zone	193.18 (linear regression)	0.0019	0.90
	70.86(parabolic regression)		0.96
NMAZ/HAZ	159.84	0.0037	0.99

CONCLUSIONS

It is possible to conclude relying on the data obtained that:

- the base alloy is non-recrystallized, textured, with banded grain structure, there are highest internal strains (Table 1) observed, work-hardening takes place due to composite phases δ'/θ' , $\delta'/Al_3(SC,Zr)$ and triple T_1 phase;
- there is complete recrystallization with dissolution of $\delta'/Al_3(SC,Zr)$ phases and T_1 phase observed in the stirred zone, complete relaxation of strains with the formation of equiaxial grains of 2-3 μm size. There are both composite $\delta'/Al_3(SC,Zr)$ phase particles and fine-dispersed homogeneous δ' phase particles present in the matrix;
- there are internal strains in the thermo-mechanically affected zone, grains are equiaxial of 2-3 μm size, there is mainly rough T_1 phase present in the matrix and T_2 phase emerged on the T_1 phase – matrix interface;
- the areas of anomalous grains growth appear in the heat-affected zone.

REFERENCES

- [1] Thomas, W.M., Nicholas, E.D., Needham, J.C., Murch, M.G., Temple-smith, P., Dawes, C.J., 1991. G.B. Patent Application 9125978.8.
- [2] R. Nandan, T. DebRoy and H. K. D. H. Bhadeshia. Progress in Materials Science 53 (2008) 980-1023
- [3] I.N.Fridlander, K.V.Chuistov, A.L.Berezina, N.N.Kolobnev. Aluminium-lithium alloys. Structure and properties. Naukova dumka. Kyiv. 1992
- [4] M.A.Krivoglaz. Theory of X-ray and Thermal Neutron Scattering by Real Crystals. Plenum Press. New York. 1996
- [5] G.K.Williamson, W.H.Hall, ActaMetall. 1 (1953) 22
- [6] T.Ungar, A.Borbely. Appl.Phys.Lett 69 (1996) 3173
- [7] G.Caglioti, A.Paoletti, F.P.Ricci, Nucl. Instrum. 3 (1958) 223
- [8] T.Ungar, I. Dragomir, A.Revesz, A.Borbely, J.Appl. Cryst. (1999) 32, 992

IMPROVING THERMO-MECHANICAL PROPERTIES OF TABULAR ALUMINA CASTABLES VIA USING NANO STRUCTURED COLLOIDAL SILICA

Alireza Souri*, Fatemeh Kashani Nia, Hossein Sarpoolaky

Iran University of Science and Technology, Tehran, Iran

ABSTRACT

Great attempts were made to reduce the amount of calcium aluminate cement (CAC) content in refractory castables to improve their hot strength. Using more than 2-3 wt% CAC may cause low melting phases formation in the refractory matrix leading to weak thermo-mechanical properties of the castables. Colloidal Silica can affect the structure of refractory castables to achieve superior thermo mechanical properties. Replacing calcium aluminate cement (CAC) by colloidal silica as a water base binder, speeds up drying, reduces the amount of liquid phase at high temperatures and may lead to mullite formation, which will increase the hot strength of the refractory castables. In this research, the influence of colloidal silica addition on bulk density, apparent porosity and HMOR of a tabular alumina based refractory castable containing have been studied. The results showed that samples containing colloidal silica have higher hot strength compared to those containing only CAC as binder due to the better compaction, less liquid phase formation at high temperature.

Keywords: Nano Silica, Alumina Castable, Cement, HMOR

INTRODUCTION

After more than 20 years of development and testing, low and ultra low-cement castables have proven their suitability for many applications in different industries particularly in iron and steel production. The main difference between the traditional and the castables with reduced cement content can be stated as fraction of fine (a few microns) and ultrafine (sub-micron) material addition.

These particles aid packing and increase thereby the compactness of the castables. Consequently, the cement and so the water needed for casting is lowered.[1] Using less water leads to less porosity when heated, so the castable loses less strength upon firing and will be less prone to gas and slag attack (*Fig. 1*). [2, 3]

Moreover, lowering cement content reduces CaO in alumina castables, decreases the amount of low melting phases at around 1200°C[2] which in turn improves the corrosion resistance and creep strength in service.[4]

* arsouri@gmail.com

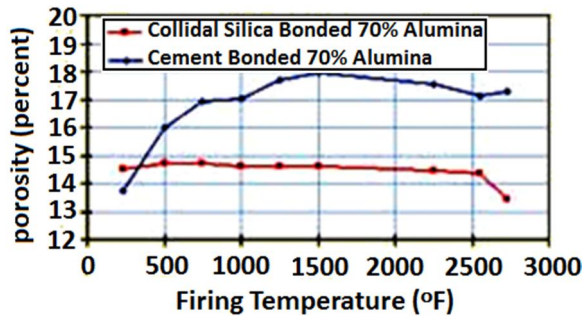


Fig. 1 – A comparison of porosity for cement bonded and colloidal silica bonded (a sub-micron agent) refractories[3].

Colloidal Silica is a sole with ultra fine particles of silica (*Fig. 2*) which can affect the structure of refractory castables due to its superior thermo mechanical properties. Replacing calcium aluminate cement (CAC) by colloidal silica as a binder, provides all the advantages of the low and ultra low cement castables, while eliminating most of their disadvantages. [5]. Although the colloidal silica bonded products show a lower initial strength than cement bonded ones due to decreased hydraulic bond, they show a good progression in strength development similar to the cement bonded products at moderate temperatures. At elevated temperatures, the strength differences become more dramatic.

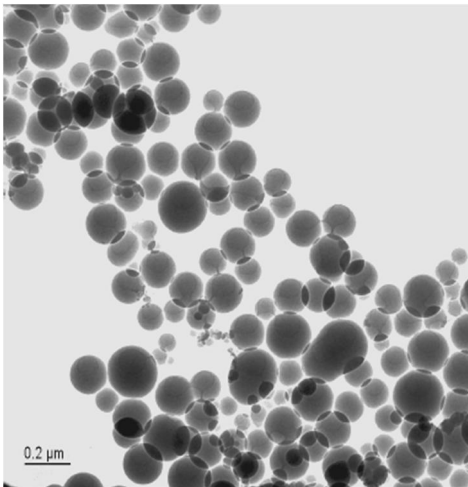


Fig. 2 – Colloidal Silica under TEM [6]

Low-melting-temperature $\text{CaO-Al}_2\text{O}_3\text{-SiO}_2$ phases associated with CAC castables are responsible for liquid phase formation which resulting lower hot strengths. Because the colloidal silica bonded materials are CaO-free, they do not generate these low melting phases and typically exhibit higher hot strengths which results in better in-service erosion resistance for these materials. [3] Also Silica fumes with extremely small particle size (average size is 0.15 μm) replace water by

attaching themselves to cement particles because of their opposite charge; so, lower water requirement reduces the porosity while increases the density and

strength. Moreover, since the cement is partially hydrated, there is no loss of strength for the colloidal silica containing castable at intermediate temperatures.[7] Another factor which increases the strength of colloidal silica bonded castables at high temperatures is the mullite bond formation. Mullite formation in refractory castables has been found dependant on several factors[8] such as using nano-sized silica which promotes it and causes mullite formation at lower temperatures. [9,10] Mullite is a very much desirable phase in castables developing improved hot strength, creep resistance, good thermal stability as well as slag penetration resistance.[11] In the present study, apparent porosity, bulk density, hot modulus of rupture and phase analysis of a cement-free colloidal silica containing castable have been compared to those of the normal LCC one.

EXPERIMENTAL

1. Raw Materials

The chemical analyses of the raw materials used in this study are listed in *Table 1*.

Table 1- Chemical analyses of the raw materials

	<i>Tabular Alumina,</i> <i>(wt%)</i>	<i>Reactive</i> <i>Alumina, (wt%)</i>	<i>Calcium Aluminate</i> <i>Cement(wt%)</i>	<i>Colloidal Silica,</i> <i>(wt%)</i>
Al ₂ O ₃	99.4	99.5	69.8-72.2	0
CaO	0.03	0.03	26.8-29.2	0
SiO ₂	0.03	0.04	0.2-0.6	40.2
Fe ₂ O ₃	0.02	0.02	0.1-0.3	0
Na ₂ O	0.35	0.04	< 0.5	0
K ₂ O	0	0		0

The recipes of the studied castables (sample C, which is a low cement castable, LCC, containing 5 wt% cement and sample N, a no-cement castable containing colloidal silica) are provided in *Table 2*.

Table 2 – Composition of castables

<i>Castable Composition (wt%)</i>	<i>C</i>	<i>N</i>
Tabular Alumina	85	87
Reactive Alumina	10	10
Cement	5	0
Colloidal silica	0	7.5
Dispersant	0.1	0.1
water	5	4.5

2. Castables Preparation

For each sample, a 3kg batch mixture using the formulation in *Table 2* was prepared by dry mixing for 4 minutes at slow speed, using a Hobart mixer with 5 liter capacity mixing bowl. Then wet mixing was carried out by addition

of water with further 4 minutes mixing at medium speed. Test samples were prepared by casting the mixture into the stainless steel molds for 1 minute, with the dimensions of 150*25*25 mm by vibrating at 50HZ, The castables were cured at 20°C and a relative humidity of 95% for 24 hours in the mold. After curing time, the samples were allowed to be dried at the temperature of 110°C, and then fired at 1400°C for 5 hours (by the rate of 300°C per hour).

3. Testing

Bulk density and apparent porosity were determined by ASTM standard methods. The given values of these properties in result section are the average of three samples for each formulation. Hot modulus of rupture, HMOR, was carried out according to DIN 51048 using the Netzsch 442D/3 model. These values are also the average of three measures.

RESULT AND DISCUSSION

1. Bulk density and apparent porosity

Bulk density and apparent porosity of the samples are given in Fig 3 and

Fig 4.

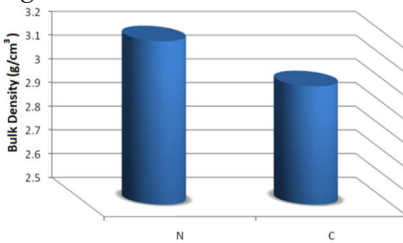


Fig. 3 – Bulk density of the samples fired at 1400°C for 5 hrs

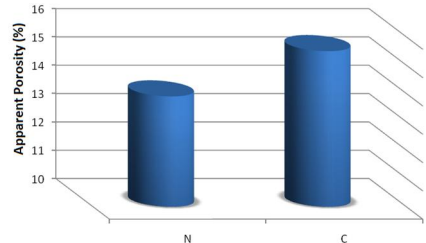


Fig.4 – Apparent porosity of the samples fired at 1400°C for 5 hrs

In LCC castables (Sample C), the cement content requires water for placement. This leads to high porosity when heated, the castable loses strength and becomes vulnerable to infiltration e.g. by slags. Besides, due to dehydration of the hydrate phases before the ceramic bond is formed, the castables also show a strength lowering at intermediate temperatures.[2] Colloidal silica particles, due to their nano sizes (~15 nm), could behave as a liquid[12] and so less water was needed in preparation of the sample N, which led to less amount of apparent porosity upon drying and firing.

Colloidal silica, due to its high specific area, anticipates sintering and so the sample N shows higher bulk density than sample C.

2. HMOR

The HMOR amounts of the samples are shown in Fig. 5. Using fine and reactive powders such as reactive alumina and colloidal silica in the bond phase of sample N can precipitate mullite needles from 1300°C in which the mullite needle-like particles grow out of a the matrix promote a good reinforcement

according to Schumacherr's report. [2] In *Fig. 5*, It can be seen that the sample containing colloidal silica (Sample N) shows higher amount of HMOR, better compaction, lower apparent porosity and higher bulk density due to presence of colloidal silica and consequently, formation and growth of long, needle-shaped mullite crystals.

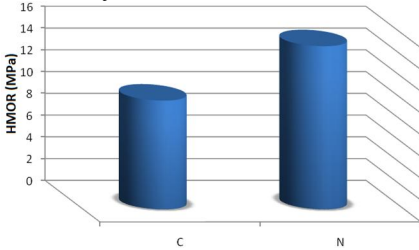


Fig.5 – Hot Modulus of Rupture (HMOR) of the samples fired at 1400°C for 5 hrs

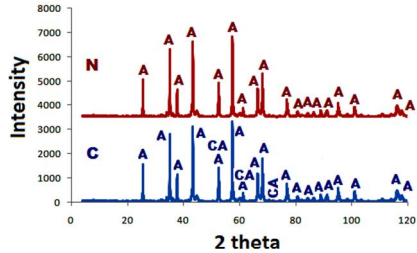


Fig. 6 – XRD patterns of the samples fired at 1400°C for 5 hrs. A represents alumina and CA represents calcium-hexaluminate($6\text{Al}_2\text{O}_3 \cdot \text{CaO}$)

3. Phase Analysis

The XRD patterns of the samples can be seen in *Fig. 6*.

In the XRD pattern of sample C, calcium aluminium oxide can be detected besides alumina, which is a cement phase and has a lower melting point than alumina and acts as a flux, so can lower the HMOR of the sample.

Phase analysis of the sample N reveals mullite ($3\text{Al}_2\text{O}_3 \cdot 2\text{SiO}_2$) peaks, although they are weak due to low amount in the total phase constituents of the castable, so mullite was assumed as a trace phase.

CONCLUSIONS

Colloidal silica sol could behave as a liquid and so the castables containing colloidal silica need less water to be prepared, which leads to lower their apparent porosity than that of LCC ones. Colloidal silica, due to its high specific area, anticipates sintering and so leads to better compaction. Comparing the traditional low calcium aluminate cement castables, colloidal silica containing refractory castables attains better mechanical strength at high temperatures.

REFERENCE

- [1] Bjorn Myhre, "Hot Strength and Bond-Phase Reactions in Low and Ultra-Low Cement Castables", Elkem a/s Refractories, P.O. Box 126, N-4602 Kristiansand, Norway.
- [2] Bjorn Myhre, "Tabular Alumina Based Refractory Castables", Elkem a/s Refractories, P.O. Box 126, N-4602 Kristiansand, Norway.

-
- [3] Michael Anderson, "Better Refractories through Nanotechnology", Metrel, Inc., Addison, Ill. October 1, 2005
- [4] S. Ghosh, R. Majumdar, B.K. Sinhamahapatra et al., *Ceramics International* 29 (2003),P. 671–677.
- [5] Ali Reza Souri, Behzad Mirhadi and Fatemeh Kashani Nia, "The Effect of Nano-Structured Collidal Silica on the Properties of Tabular Alumina Castables", XVI. International Conference on Refractories, Prague, The Czech Republic, 2008.
- [6] Florence Sanchez, Konstantin Sobolev, "Nanotechnology in concrete- A review", Elsevier 2010.
- [7] Subrata Banerjee, *Am. Ceram. Soc. Bull.*, 77 [10] (1998), ACerS Data Depository File No. 295.
- [8] C. Odegård, H. Fjeldborg and B. Myhre; "Mullite Formation In Refractory Castables", XIII. International Conference on Refractories, Prague, The Czech Republic, 2000.
- [9] M. R. Ismael, R.D. dos Anjos, R. Salomão and V.C. Pandolfelli, *Refractories Applications and News*, Vol. 11, N. 4, July/August 2006.
- [10] S. Hosein Badiie, Sasan Otraj, *Ceramics – Silikáty* 53 (4) 2009, P. 297-302
- [11] S. Mukhopadhyay, S. Ghosh, M. K. Mahapatra et al., *Ceramics International*, Volume 28, Issue 7, 2002, P. 719-729
- [12] M. R. Ismael, R.D. dos Anjos, R. Salomão and V.C. Pandolfelli, "Colloidal Silica as a nano-structured binder for refractory castables", *Refractories Applications and News*, Volume 11, Number 4, July/August 2006.

ULTRAFINE GRAIN REFINEMENT OF IRON INDUCED BY SEVERE PLASTIC DEFORMATION IN ASSISTANCE OF MULTI-DIRECTIONAL DEFORMATION MODE

Alexandra I. Yurkova^{1*}, Alexandra V. Byakova², Marina Gricenko¹

1 National Technical University of Ukraine “Kiev Polytechnic Institute”, Prospect Peremohy 37, 03056, Kiev, Ukraine

2 Institute for Problems of Material Science, National Academy of Sciences of Ukraine, Krzhyzhanivsky St. 3, 03142, Kiev, Ukraine

ABSTRACT

This study is primarily addressed to the problem of grain refinement of ferrite subjected to severe plastic deformation (SPD). In particular, ultra fine refining the original coarse grain of α -Fe was shown to be realistic using severe plastic deformation with friction (SPDF). Several structural sections of different scale regimes consisted of the grains from several nanometres at the top surface to several micrometres in the region adjacent to the strain-free matrix are formed in assistance of multi-directional deformation mode indicative of SPDF process. Structural revolution induced by SPD and governed by simultaneous high level of strain rate and temperature control was adequately described using Zener-Hollomon parameter, Z . Ultra grain refinement of ferrite down to submicrometer–nanometer scale regimes was found to be available when parameter Z exceeds the critical value roughly about 10^{16} s^{-1} . High efficiency of processes assisted by multi-directional deformation for ultra fine grain refining caused through continuous dynamic recrystallisation has been justified compared to those ensured by unidirectional deformation mode and supported by conventional dynamic recrystallisation. At the multi-directional deformation the variation of grain size d with Z parameter has a tendency to follow the equation $d = 6 \cdot 10^7 Z_0^{-0.47}$ while unidirectional deformation by shear or compression gives the equation $d = 3 \cdot 10^2 Z_0^{-0.16}$.

Key words: severe plastic deformation (SPD), iron, grain refinement, dynamic recrystallisation, Zener-Hollomon parameter

INTRODUCTION

In the recent years much attention has been paid to ultrafine grained (UFG) materials with grain sizes ranged from submicrometer- to nanometre-scale. UFG materials have been found to exhibit interesting combination of physical and mechanical properties, making them of growing interest to researches employed both in scientific and engineering applications [1-6]. However, structure and, hence, performance metrics of UFG materials are strongly

* e-mail: yurkova@list.ru ; tel: (+38)044 280 1780 tel: (+38)044 4068379

dependent on the particular route employed for their production. Compared to others routes severe plastic deformation (SPD) technique offers the essential advantages for ultra grain refining the structure of metallic materials, making them completely dense without risk of contamination. Generally, grain refinement induced by plastic deformation has been known for long time. During the last decade the efforts intent to microstructure refinement of metallic materials have been continued and tremendous progress has been achieved in material grain refining down to submicrometre- and nanometre-scale by using different techniques of severe plastic deformation (SPD) [1–6].

The formation of nanocrystalline structure with high-angle boundaries (HABs) is limited to those processes like ball milling [5, 6], surface mechanical attrition treatment (SMAT) called often by shot peening [5, 7], high speed drilling [5], hard turning [5], and sliding friction [4, 5, 8] or high-pressure torsion (HPT) [9]. Among these processes HPT is the mostly effective to produce bulk nanocrystalline materials whereas other processes are capable to give only nanocrystalline surface layers. As shown in previous papers [4, 8] high-energy friction process can result in SPD of metal, leading to generation of deformation-induced grain refinement of the surface layer and improvement properties of material work piece itself.

The present study describes characteristic features of grain refined structure created by severe plastic deformation of α -Fe pieces being subjected to friction (SPDF). Mechanism of grain refinement is discussed and clarified on the base of characteristic features of structural sections within deformation region induced by SPDF. Special attention is paid to finding the processing parameters and deformation mode responsible for ultra fine grain refinement and especially to those quite enough for creation of nanocrystalline structure.

METHODS OF SAMPLE MANUFACTURING AND ANALYSIS

Cylindrical-shaped samples of iron (purity 99.9 wt. %) with mean grain size of 80 μm with 8 mm in diameter and 50 mm in height were subjected to SPDF in argon gas using the set up described elsewhere [4, 8].

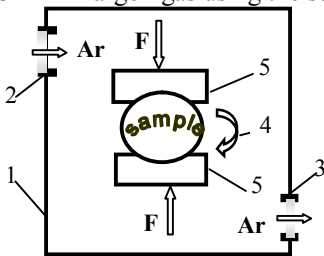


Fig. 1 – Schematic presentation of severe plastic deformation with friction (SPDF)

Fig. 1 shows schematically the set-up used for SPDF treatment. Meaningful parts of the set-up are as follow: (1) hermetically closed chamber filled by argon gas; (2), (3) system for argon gas inputting/outputting and pressure control; (4) sample rotation system; (5) two blocks of hard alloy (WC-8 % Co) being forced to the sample surface.

Sample sited between the forced blocks of hard alloy (5) was rotated with velocity about 6×10^3 rpm. Friction process

under forced blocks ensures its heating the rotated sample up to the constant temperature of 773 K. Rotation was stopped after the time about 60 min and the sample was free cooled down to the room temperature.

Structural characterisation of as-treated samples was performed on diffractometer (20 kV; 10 mA) with Fe K_{α} radiation. Stepwise X-ray diffraction (XRD) study including XRD line profile analysis was employed for estimation of the average size of coherent domains and mean dislocation density from the broadening the $(110)_{\alpha}$ and $(220)_{\alpha}$ peaks. Cross-sectional microstructure of as-treated samples was studied by using optical microscope Neophot-21. Morphology (size and shape) of refined grains and subgrains evolved by SPDF of iron samples was studied by transmission electron microscopy (TEM) images (bright and dark fields) and selected area electron diffraction (SAED) patterns performed using microscope JEM-CX (operating at a voltage of 125 kV).

RESULTS AND DISCUSSION

Fig. 2 shows cross-sectional microstructure of as-treated Fe sample observed by optical microscopy. Gradient deformation region with the overall thickness 60 μm and consisted of grains different to those of untreated α -Fe matrix is revealed in the surface layer.

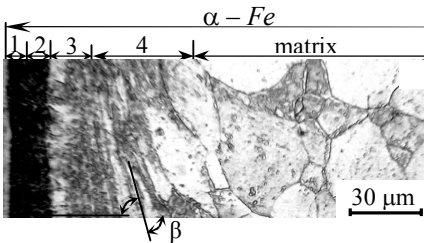


Fig. 2 – Typical cross-sectional optical observation of the as-treated Fe showing structural sections of different scale regimes

section (2) were expected to be refined down to nano- and/or submicrometre scale regimes. Section 2 is followed by section 3 consisted of fine and nearly equiaxed grains with the size ranging from 1 μm to 5 μm whereas the last section 4 adjacent to the strain-free matrix exhibits banded structure consisted of micrometre-sized (10 μm in the width) and elongated grains inclined to the sample cylindrical surface. In addition, interlayers of ultrafine and nearly equiaxed grains are sited between neighbouring pancake-shaped grains.

The results of XRD analysis show substantial broadening of Bragg diffraction peaks along the depth of deformation region compared to that for the strain-free matrix. XRD peak broadening is usually ascribed to grain refinement down to ultra fine domains as well as to increased dislocation density. According to the results of XRD line profile analysis listed in Table 1 the smallest size

Four meaningful structural sections of different grain morphology (size and shape) are well visible within deformation region, as indicated in Fig. 2. Section 1 at the top surface and adjacent to it dipper section 2 demonstrate very fine grain structure for which optical microscopy was inadequate to recognise grain size. If so, the structure of section (1) and that of

section (2) were expected to be refined down to nano- and/or submicrometre scale regimes. Section 2 is followed by section 3 consisted of fine and nearly equiaxed grains with the size ranging from 1 μm to 5 μm whereas the last section 4 adjacent to the strain-free matrix exhibits banded structure consisted of micrometre-sized (10 μm in the width) and elongated grains inclined to the sample cylindrical surface. In addition, interlayers of ultrafine and nearly equiaxed grains are sited between neighbouring pancake-shaped grains.

The results of XRD analysis show substantial broadening of Bragg diffraction peaks along the depth of deformation region compared to that for the strain-free matrix. XRD peak broadening is usually ascribed to grain refinement down to ultra fine domains as well as to increased dislocation density. According to the results of XRD line profile analysis listed in Table 1 the smallest size

of coherent domains about 13 nm is revealed in section 1. Moreover, this section is characterised by the highest dislocation density ranging from 10^{16} m/m³ to 10^{15} m/m³. As could be seen in *Table 1* the average coherent domain size increases gradually up to 150 nm in the direction from the top surface to strain-free matrix while dislocation density decreases steadily.

Table 1– Variation of structural characteristics along deformation region of as-treated α -Fe subjected to SPDF

Structural sections	Distance to surface (μm)	XRD analysis		Microscopy results
		Size of coherent domain (nm)	Dislocation density ρ (m/m ³)	Mean grain size d (nm)
1	0	13	$8.9 \cdot 10^{15}$	20*
1	3	18	$7.8 \cdot 10^{15}$	70*
2	10	23	$7.2 \cdot 10^{15}$	150*
2	20	37	$6.5 \cdot 10^{15}$	400*
3	30	70	$4.5 \cdot 10^{15}$	1000**
3	40	112	$2.5 \cdot 10^{15}$	2000**
4	50	146	$8.5 \cdot 10^{14}$	3000**
4	60	–	$5 \cdot 10^{14}$	7000**
strain free matrix		–	10^{11}	80000**

* data obtained by observation of TEM images and ** optical micrographs

Fig. 3 shows detailed cross-sectional TEM observations of the structure and corresponding SAED patterns attributed to the each of four sections created in the deformation region of as-treated Fe sample. Diffraction rings/spots in the SAED patterns attributed to all of the sections correspond to α -Fe, and no other phases were detected. In the sections numbered by 1, 2, and 3, the ringed SAED patterns with a great number of point reflections indicate the presence of ultrafine equiaxed grains with random crystallographic orientations.

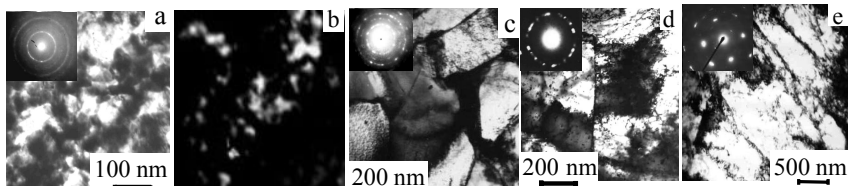


Fig. 3 – TEM images and SAED patterns of different structural sections of as-treated α -Fe: (a, b) –section 1 (of 1 μm deep to the top surface) (a) – bright-field image; (b) – dark-field image in $(110)_{\text{Fe}}$ reflection; (c) – section 2 (of 10 μm deep to the top surface); (d) – section 3 (of 30 μm deep to the top surface); (e) – section 4 (of 40 μm deep to the top surface)

Within the section 1 the number of point reflections located on the Debye rings is the greatest while their size is the smallest, indicating the presence of mostly fine grains at the top surface. Grain size measured using duck-field TEM images was believed to be about 20 nm at the top surface of section 1, as depicted in *Fig. 3b*. Correlation of TEM observation to XRD results determined for section 1 seems to be good, indicating for this case that the average size of coherently diffracting regions reflects actual grain size d , as could be seen in Table 1. If so, refined grains of actual crystal structure are formed in section 1.

As shown in *Fig. 3*, number of the point reflections presented on the debye rings of SAED patterns decreases along the depth of the sections 2 and 3 while their size increases step by step, demonstrating the increasing of grain size toward the free-strain matrix. It is noticeable that SAED pattern for section 4 consists of individual spots indicative of coarse grained Fe.

Generally, the results of plastic deformation are defined by dislocation activities in metals and depend strongly on crystal structure and stacking fault energy (SFE). For example, in materials with low SFEs, plastic deformation may only originate transformation from dislocation slipping to mechanical twinning while in materials with high SFEs and, in particular, in iron, where dislocation mobility is much higher, dislocation walls (DW) and cells will be formed, finally resulting in formation of sub-boundaries within the original grain. The refinement process of coarse grains upon plastic deformation, in principle, depends on many extrinsic factors such as intensity of strains and strain rates, deformation temperature, and so on. Apart from, dominating mechanisms and clear sceneries for ultra fine refining the coarse grains into the nanometer sized crystals are yet far from understanding.

Generally, three different mechanisms for deformation-induced grain refinement of ferrite under elevated temperatures are presently discussed in literature: (i) dynamic recovery (DRC) [10-13], (ii) conventional dynamic recrystallisation (DRX) [10-15], (iii) continuous dynamic recrystallisation (CDRX) or, equivalently, recrystallisation in situ [6, 12, 16-20]. The levels of strain and strain rate are commonly considered as basic regulative factors to initiate the ultra grain refinement by one or another mechanism.

As applied to subject matter SPDF process provides for unique opportunity to investigate the grain refinement mechanism owing to gradient variation of the strain and strain rates along the depth of deformation region. This means that microstructure features (including grain size and grain boundary misorientations) at the different sections of deformation region could be attributed to different levels of strains and strain rates. Therefore, one or another underlying mechanism for deformation-induced grain refinement in different scale regimes ranged from nanometre to micrometre levels can be recognised and specified.

The stored true strain, ϵ , along the structural sections involved in deformation region induced by SPDF process was estimated from dislocation densi-

ty, ρ , using the relation originally proposed in [6]: $\rho = 1,87 \cdot 10^{15} e^{0.6}$. In addition, following [21] stored true strain e operating the structural section 4 was derived from the shear strain, γ , being determined using the angle of grains slope, β , as shown in Fig. 2. It is noticeable that the values of true strain estimated in section 4 by two different ways were in good agreement. The results of calculations show that both extremely high stored strain about $13.5 \dots 10$ and strain rates about $10^4 - 10^3 \text{ s}^{-1}$ arise at the top surface of the sample and dropped steeply along the deformation region toward the strain free matrix.

The results show that structural sections 1, 2, and 3 consist of equiaxed grains with HABs, suggesting their formation through CDRX. The important point concerns the fact that the grain refinement in the sections above occurs under hot-to-warm working. Indeed, processing temperature about 773K was very close to the regular recrystallisation temperature, T_r . Moreover, T_r tends to decrease as the level of stored strain e increases.

Flattened shape of original grains with deformation-induced LABs formed in section 4 indicates the fact that dynamic recovery under warm working dominates structural evolution under considerable decreasing the stored strain and strain rate, as shown in Fig. 2, 3e. Development of CDRX micrometre-sized grains within interlayers between original grains is additional notable characteristic of banded structure in section 4. The former phenomenon is attributed to the large strain gradients evolved near initial grain boundaries and around triple junctions, as was pointed out in [20]. Strain incompatibilities between joint grains lead to formation of strain-induced LABs [20, 22, 23] followed by their fast transformation into HABs [24, 25]. Thus, it can be resumed that the level of stored strain and strain rate is not enough to refine completely grain structure of section 4 through CDRX.

Several aspects could be mentioned here. First of all the important point is that the transformation of cellular structure to granular one is achieved when dislocation density reached the critical density that was believed to be not less than about 10^{14} m/m^3 while the limit of dislocation density being achieved by SPD processes does not usually exceed 10^{16} m/m^3 [6]. Therefore, grain refinement continues to advance until dislocation multiplication superior to dislocation annihilation. Stabilized grain size is formed when refinement process gets the steady state at the balance between dislocation multiplication and annihilation. As pointed out in literature [7, 18] stabilised grain size is probably limited to about 10 nm since deformation takes place mainly by grain boundary sliding and/or grain rotation.

The next aspect concerns the fact that different levels of stabilized grain sizes are available by using different technical approaches. It seems that deformation mode contributes directly in final results of microstructural revolution induced by SPD. In fact, SPD techniques [4-8, 18] assisted by multi-directional

deformation are commonly considered to be mostly effective in term of their application for ultrafine grain refinement of α -Fe down to nanometre-scale level. Unlike to this grain refinement below submicrometre scale is probably difficult to achieve in processes assisted by unidirectional deformation. As evidenced from the data published in literature, application of multi-directional deformation involving compressive and shear modes is greatly beneficial in fast strain storage and generation of dislocations as compared to unidirectional deformation by shear. Nevertheless, assessment of techniques in term of their effect on grain refinement efficiency and finally stabilised grain size is rather complicated because of the differences in combination of strain rate and achievable stored strain, resulted from differences in deformation mode and temperature conditions.

The theory advanced in the latest publications [11, 14, 26] for grain refinement by repeated deformation could be viewed as that adequately describing grain formation in the regime governed by simultaneous high level of strain rate and temperature control. As applied to subject matter deformation-refined grain size has generally been reported with variation of Zener-Hollomon parameter, Z , presently considered as valuable criterion to govern a competitive effect of dislocation accumulation under high strain rate and dislocation annihilation caused by temperature. Following expression is commonly [14, 26] used for calculation of Z parameter with allowance for the effect above:

$$Z = \dot{\epsilon} \exp(Q/RT) \quad (1)$$

where $\dot{\epsilon}$ is strain rate in s^{-1} , Q is activation energy of deformation that is closed to the activation energy of volume diffusion of metallic atom (254 kJ/mol for ferrite iron); T is deformation temperature in K; $R = 8.31$ J/mol·K is universal gas constant.

According to [14, 15, 26] empirical relationship between finally stabilised grain size and Z parameter was given in convenient form:

$$d = kZ^{-m} \quad (2)$$

where d is grain size in μm ; k is numerical constant.

Following the procedure at which dependence of stabilised grain size on parameter Z is determined in logarithmic co-ordinates, the applicability of Eq. (2) in predicting final results under the present conditions was verified, as shown in *Fig. 4*. Actually, the data obtained in the present study for different structural sections are fitted well to a straight line. Moreover, the data reported in literature [6, 7, 13, 18] for grain refinement of α -Fe produced via the other processes being assisted by multi-directional deformation line up well on the strait line together with those determined in the present study.

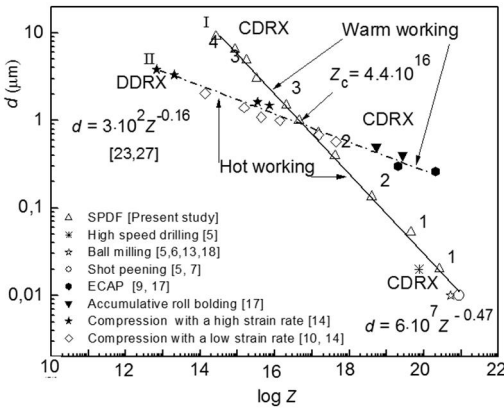


Fig. 4. Variation of grain size, d , of ferrite vs parameter Z for (I) multi-directional deformation mode, (II) unidirectional deformation mode either by shear or compression. Numbers at the strait (I) indicate structural sections in deformation region of as-treated α -Fe subjected to SPD

parameter could be expressed by the equation $d = 6 \cdot 10^7 Z^{-0.47}$ while it has a tendency to follow the expression $d = 3 \cdot 10^2 Z^{-0.16}$ under unidirectional deformation mode.

It is noticed that the value of constant and powder index at the Z parameter found under unidirectional deformation mode are numerically almost the same as those reported previously [10, 14, 26].

Several important conclusions could be derived from the data exhibited in First of all, it is clear that deformation-refined grain becomes smaller as parameter Z increases. Nevertheless, grain refinement of ferrite to submicrometer-, nanometer-scale level would be achieved when parameter Z exceeds the critical value Z_c roughly about 10^{16} . Apart from, as modified Zener-Hollomon parameter Z increases up to the value Z_c by using multi-directional deformation mode controlling effect on grain refinement is passed from CDRX under warm working to CDRX under hot working while at the unidirectional deformation mode DDRX under hot working was changed to CDRX under warm working. The next aspect concerns the fact that the value of Z parameter required for grain refinement down to nanometer-scale regime through CDRX mechanism is much smaller at the multi-directional deformation mode under hot working than that for processes supported by unidirectional deformation mode in assistance of CDRX under warm working. In particular, the value of Z parameter higher than 10^{19} is quite enough to ensure finally stabilised grains of nanometre-sized level under hot working performed by multi-directional deformation mode. Unlike the above it is easy to show that Z parameter has exceed the

However, the stabilised grain size of α -Fe achieved in processes being assisted by unidirectional deformation mode [14, 17], form different strait line with the slop that is smaller than that for the straight line joining the data determined by multi-directional deformation, as shown in Fig. 4. Thus, m power and numerical constant k in Eq. (4) are found to be variable and depend on the deformation mode. At the multi-directional deformation mode the variation of grain size d with Z para-

value about 10^{31} to achieve nanometre-sized grains of ferrite under warm working performed by unidirectional deformation mode. This means that in assistance of CDRX under warm working strain rates should be maintain at the level ranged on the order magnitude from 10^3 to 10^{13} s^{-1} that is hardly achieved by using presently developed SPD techniques performed by unidirectional deformation mode.

CONCLUSIONS

As a general conclusion it should be resumed that multi-directional deformation assisted by CDRX during straining under hot-to-warm working greatly facilitates grain refinement down to submicrometer-, nanometre-scale regimes although DDRX provided by unidirectional deformation mode during straining under hot working has a preference in grain refinement limited to the micrometre-scale regime.

The results of the present study hold the key for greater understanding the underlying mechanisms and kind of deformation mode operating ultrafine grain refinement of ferrite under severe plastic deformation and also could be promising for both the current basic research and application in engineering practice.

Acknowledgements

This work was funded by two projects: # 2211 of Ministry of Education and Science of Ukraine and NAS of Ukraine “Nano-Systems, Nano-Materials and Nano-Technologies”

REFERENCES

- [1] R. Valiev, Y. Estrin, Z. Horita, T.G. Langdon, M.J. Zehetbauer, Y.T. Zhu, The Journal of Materials 2006, Vol. 58, P. 33-39.
- [2] Nanomaterials by Severe Plastic Deformation (Eds M.J. Zehetbauer and R.Z. Valiev), Weinheim, Austria: Wiley-VCH, 2004.
- [3] Nanomaterials by Severe Plastic Deformation (Editor Z. Horita), Uetikon-Zurich, Switzerland: Trans Tech Publications, 2005.
- [4] A.I. Yurkova, A.V. Byakova, A.V. Belots'ky, Yu.V. Milman, Materials Science Forum, 2006, Vols. 503-504, P. 645-650.
- [5] M. Umemoto, Y. Todaka, J. Li and K. Tsuchiya, Materials Science Forum, 2006, Vols. 503-504, P. 11-18.
- [6] S. Takaki, Material Science Forum, 2003, Vols. 426-432, P. 215-222.
- [7] N.R. Tao, Z.N. Wang, W.P. Tong and et al., Acta Mater 2002, Vol. 50, P. 4603-4616.
- [8] Yurkova AI, Milman YuV, and Byakova AV. Russian Metallurgy (Metally), 2010, Vol. 2010, No. 4, P. 249-257.
- [9] R.Z. Valiev, Y.V. Ivanisenko, E.F. Rauch, and B. Baudelet, Acta Mater, 1996, Vol. 12, P. 4705-4712.
- [10] S.V.S. Narayana Murty, S. Torizuka, K. Nagai, and et al., Scripta Mater, 2005, Vol. 53, P. 763-768.
- [11] S.V.S. Narayana Murty, S. Torizuka, K. Nagai and et. al., Scripta Materialia, 2005,

- Vol. 52, P. 713-718.
- [12] A. A-Zadeh , B. Eghbali, *Mater Sci Eng A*, 2007, Vol. 457, P. 219-225.
 - [13] Z.G. Liu , H.J. Fecht, M. Umemoto, *Mater Sci Eng A*, 2004, Vols. 375–377, P. 839-843.
 - [14] J-H. Kang, S. Torizuka, *Scripta Mater*, 2007, Vol. 57, P. 1048–1051.
 - [15] S.V.S. Narayana Murty, S. Torizuka, K. Nagai, *Mater Sci Forum*, 2006, Vols. 503-504, P. 687-692.
 - [16] A. Belyakov, Y. Kimura, K. Tsuzaki, *Material Science and Engineering F*, 2005, Vol. 403, 249-259.
 - [17] B.Q. Han, S. Yue, *J. Materials Process Technol* 2003;136:100-104.
 - [18] Y. Xu, M. Umemoto, and K. Tsuchya, *Materials Transactions*, 2002, Vol. 43, P. 2205-2212.
 - [19] A. Belyakov, Y. Kimura, Y. Adachi, K. Tsuzaki, *Mater Trans*, 2004, Vol. 45, P. 2812-2820.
 - [20] N. Dudova , A. Belyakov , T. Sakai , R. Kaibyshev, *Acta Materialia*, 2010, Vol. 58, P. 3624-3632.
 - [21] Y. Ohno, Y. Kaneko, and S. Hashimoto, *Mater Sci Forum*, 2006, Vols. 503–504, P. 727-732.
 - [22] F.J. Humphreys, M. Hatherly. *Recrystallization and related annealing phenomena*. Oxford: Pergamon Press; 1996.
 - [23] A.Belyakov, T.Sakai, H.Miura, *Mater Trans JIM*, 2000, Vol.41, P.476-484.
 - [24] D. Kuhlmann-Wilsdorf, N. Hansen, *Scripta Metall Mater*, 1991, Vol. 25, P. 1557-1565.
 - [25] B. Bay, N. Hansen, D.A. Hughes, D. Kuhlmann-Wilsdorf, *Acta Metall Mater*, 1992, Vol. 40, P. 205-214.
 - [26] S. Torizuka, A. Ohmori, S.V.S. Narayana Murty, and K. Nagai, *Mater Sci Forum*, 2006, Vols. 503-504, P. 329-334.

COLD-SPRAY TECHNIQUE AS EFFICIENT ALTERNATIVE PROCESS FOR CONSOLIDATION OF POWDERED Al-Fe-Cr ALLOYS REINFORCED BY NANOQUASICRYSTALLINE PARTICLES

Alexandra V. Byakova^{1*,2}, Alexandra I. Yurkova^{2,1},
Vladyslav V. Cherednichenko^{2,1}, Alexander I. Sirko¹

1 Institute for Problems of Materials Science, National Academy of Sciences 3 Krzhyzhanivsky St., 03142, Kiev, Ukraine;

2 NTUU "Kiev Polytechnic Institute" 37 Prospect Peremohy, 03056 Kiev, Ukraine

ABSTRACT

A brief outline of the processing parameters involved in the search for technique offering efficient consolidation of high-temperature strength Al-based powdered alloys reinforced by metastable nanoquasicrystalline particles is presented. Feedstock powder of $Al_{94}Fe_3Cr_3$ alloy was employed in experiments. Superior advantages of the cold-spraying as alternative solid-state process for consolidation and structural performance of quasicrystalline alloys by plastic deformation is discussed in comparison with that resulted from currently employed hot extrusion put into practice at the 623 K. As opposed to extrusion assisted by unidirectional deformation, adiabatic shear instability is primary responsible for creating the mostly effective intimate metallic bonding between the adjacent Al-powder particles under cold spraying when the temperature was even well below melting point, i.e. 473 K. The main benefit of cold-spraying is that the composite quasicrystalline structure in the interior of heavily deformed particles was believed to be actually the same as that of feedstock powder while warm extrusion results in the decrease by 23% fraction volume of metastable quasicrystalline particles, shifting their decomposition to the lower temperatures. Advantage of cold-sprayed $Al_{94}Fe_3Cr_3$ alloy concerns excellent balance between high ductility (plasticity characteristic $\square_H \cong 0.9$) and high strength that superior roughly about 35% to that of as-extruded composite.

Key words: Cold spraying, Al-Fe-Cr alloy, nanoquasicrystalline particles, powder, consolidation, bonding, microstructure, mechanical properties

INTRODUCTION

High strength of Al-Fe-based nanoquasicrystalline alloys exhibited attractive mechanical properties are presently of great attention for researches employed in scientific and engineering applications [1-4]. Some of them show increased structural stability and, therefore, are much promising for application under elevated temperature. Quasicrystalline Al-Fe-based alloys belong to the

* e-mail: byakova@mail.ru, tel: (+38)0444238253

group of metal matrix nanoquasicomposite. Their microstructure typically consists of nanometer-sized icosahedral (i-phase) quasicrystalline particles embedded in an α -Al matrix [1]. Compared to commercial Al-based alloys recommended for service under elevated temperature, Al-based nanoquasicomposites show remarkable advantages in material mechanical performance because of excellent balance between high strength and sufficient ductility [2, 3]. Formation of quasicrystalline i-phase with long range orientation order and no translational symmetry in rapidly-cooled Al-alloys was originally discovered by Shehtman et al. in 1984 [5] and, then, promoted by additions of Mn, Fe, Cr, V, Ti, Zr, Nb and Ta [2-4, 6]. Since nanoquasicrystalline Al-based alloys are usually performed as semi-product in form of melt-spun ribbons/flakes, [6], and gas/water atomised powders [3, 4] their following consolidation is required for manufacturing the bulk-shaped material and, as consequence, further improvement of its microstructural stability is desirable to maximize elevated temperature. Superior advantages of cold-spraying as alternative solid-state process for consolidation and structural performance of nanoquasicrystalline Al-Fe-based alloys by plastic deformation is presented and discussed by comparison with currently employed warm powder extrusion under the temperature usually ranged from roughly about 673 to 723 K [3, 4].

METHODS OF SAMPLE MANUFACTURING AND ANALYSIS

Feedstock quasicrystalline powders of Al-alloy with nominal composition of $\text{Al}_{94}\text{Fe}_3\text{Cr}_3$ (oxygen content about 0.3%) was chosen for experimentations and fabricated by water-atomisation technique using inhibited high-pressure water with Ph 3.5 [8]. Fraction volume of quasicrystal particles contained by feedstock powder was not less than 35% [4]. After atomisation powder was sieved to less than 40 μm . Consolidation of powdered Al-based alloy was performed by two different techniques, i.e. by cold spraying and by powder extrusion process.

A commercial cold spray system (DYMET 403) was used in spraying experiments done under compressed air. Cold-sprayed principle and technical set-up for cold spraying are described elsewhere [9]. Velocity of air/particle jet was roughly about 700 m/s whenever its temperature was not higher than 473 K [10-12].

Consolidation of pre-compacted feedstock powder via extrusion was done in hermetic capsule at the temperature of 653 K [4, 10]. Prior extrusion degassing the capsule of 25mm in diameter filled by powdered compact was implemented at the temperature of 623 K during 1 hour. Press of 2000 kg in power equipped by extrusion die with inner diameter of 9.3 mm and length for working part of 2 mm was used in extrusion process. Extrusion was fulfilled in the single pass with reduction coefficient, k_e , of 7.2. Extrusion velocity was as great as $V_e = 15 \times 10^{-3}$ m/s.

Scanning electron (SEM) microscope Jeol Superprobe-733 (JEOL, Japan) equipped with X-ray detectors (EDX and EPMA) was used to recognise feedstock powder morphology (particle size and shape) and microstructure as well as to get basic information about particle/particle bonding achieved in cold-sprayed and extruded samples. Differential scanning calorimetry (DSC) together with X-ray diffraction (XRD) analysis using Cu K_{α} radiation and transmission electron microscopy (TEM) observation were employed to study thermal stability of the quasicrystalline phase under elevated temperatures. TEM images and selected area electron diffraction (SAED) patterns were performed using JEM 2100 F (JEOL, Japan) microscope.

Microhardness measurements were performed using conventional microhardness machine equipped by standardised Vickers pyramid and determined under indentation load as high as 1.0 N. Plasticity characteristic δ_H as dimensionless parameter that can vary in the range from 0 (for “pure” elastic contact) to 1 (for “pure” plastic contact) was derived by calculations through microhardness measurement results and Young’s modulus, E [14]. Microtester capable for load-displacement measurements and equipped by Berkovich pyramid was used to determine Young’s modulus, E , according to the test method procedure originally proposed by Oliver and Pharr [15]. In addition, plasticity characteristic δ_A , which is physically close to that denoted by δ_H was derived from loading and unloading data according to demands of International standard ISO 14577-1:2002 (E). Yield stress, σ_y , was extracted from ‘stress-strain’ curve constructed by a set of trihedral pyramids with different angles at the tip γ_1 (ranged from 45° to 85°) according to the test method procedure [16].

RESULTS AND DISCUSSION

Fig. 1 shows the XRD patterns recorded for the feedstock WA powder, as-extruded rod, and cold-sprayed alloy.

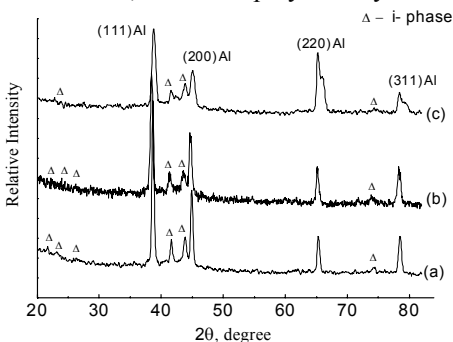


Fig. 1 – XRD patterns of (a) feedstock powder, (b) cold-sprayed material, and (c) extruded rod, all performed by $Al_{94}Fe_3Cr_3$ alloy

In all of the XRD patterns the presence of the X-ray peaks for α -Al is clearly seen together with those indexed as i-phase using Cahn’s indexing scheme [17].

Fig. 2 displays representative bright field TEM image showing the microstructure of the $Al_{94}Fe_3Cr_3$ alloy fabricated via different routes. All kinds of the $Al_{94}Fe_3Cr_3$ alloy show the

similar microstructure composed of quasicrystalline particles embedded in α -Al matrix, as shown in *Fig. 2a*. Quasicrystals have the clear and characteristic spherical shape with a diameter roughly about 200 nm and smaller. Selected area diffraction patterns (SAED) reveal five-fold reflection spots indicative of *i*-phase, as can be seen in *Fig. 2b*.

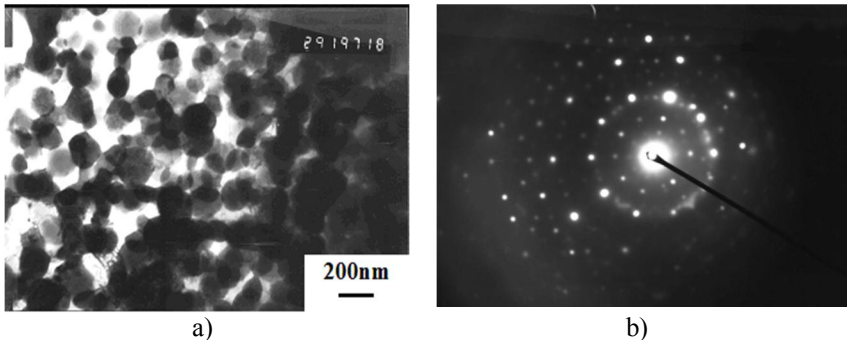


Fig.2 – (a) Bright field TEM image and (b) SAED pattern of the $\text{Al}_{94}\text{Fe}_3\text{Cr}_3$ alloy

However, intensity of diffraction peaks attributed to *i*-phase in the XRD pattern for as-extruded rod is much smaller, suggesting reduced fraction volume of metastable quasicrystalline particles. The proper are thought to be partially decomposed under combined effect of high pressure and enhanced temperature during extrusion process. This assumption is confirmed by the presence of the addition reflections for α -Al overlapping those typical for α -Al recorded in the feedstock powder and as-sprayed alloy. This is because of two α -Al solid solutions of different elementary composition were formed in the matrix after extrusion. As could be seen in Table 1, one of them has reduced lattice parameter a_o , indicating enrichment of α -Al by solute Fe and Cr. In addition, broadening of diffraction peaks for α -Al matrix, which could be resulted from combined effect of delaminating the α -Al solid solution and dislocation activity, are seen in the XRD pattern of as-extruded bar.

Table 1 – Lattice parameter a_o of elements and α -Al solid solutions in $\text{Al}_{94}\text{Fe}_3\text{Cr}_3$ alloy performed via different routes

Material	Al	Fe	Cr	Feedstock powder	Extruded rod	CS-alloy
a_o , nm	0.4049	0.2866	0.2885	0.4041	0.4045/0.4006	0.4045

Notice: CS – cold spray

The results of DSC analysis shown in *Fig. 3* are helpful to estimate the diminishing the fraction volume of quasicrystalline particles resulted from powder consolidation via extrusion process.

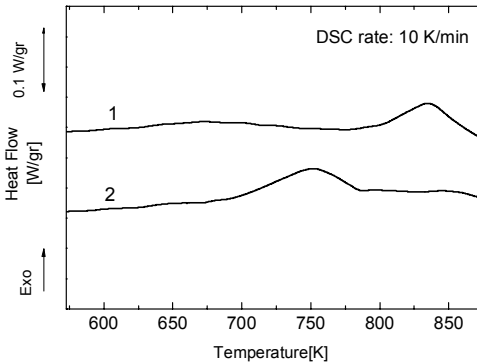


Fig. 3 – DSC traces reordered at the heating rate 10 K/min for (1) $\text{Al}_{94}\text{Fe}_3\text{Cr}_3$ feedstock powder and (2) as-extruded $\text{Al}_{94}\text{Fe}_3\text{Cr}_3$ alloy

position. Dislocation activity in α -Al matrix, which has been indicated by XRD analysis of as-extruded rod, can principally facilitates dissolution of alloying elements released from decomposed metastable quasicrystalline particles.

As opposed to extrusion process, cold spray technique allows one to retain entirely fraction volume of quasicrystalline phase created in powdered $\text{Al}_{94}\text{Fe}_3\text{Cr}_3$ alloy by rapid solidification. Processing temperature under cold spraying is much smaller than that for warm extrusion process. Despite of this cold spraying finds oneself capable to create effective intimate metallic bonding between the adjacent particles by breaking off the oxide films presented naturally on the feedstock Al-powder and promoting intimate contact between two clean surfaces the same as those in extrusion process. Actually, remnant agglomerations of broken oxide layer have been revealed by TEM observation at the particle/particle interfaces [12]. However, compared to extrusion process intimate bonding at the particle/particle interfaces under cold spraying is controlled by different mechanisms of deformation. Characteristic features observed in cross-sectional microstructures of cold-sprayed alloy and extruded rod are helpful to elucidate the matter at the issue above. With retaining the quasicrystalline particles of unchanged shape in deformation-induced structure, cold spraying causes powder particles to become flattened and heavily deformed in cross-sectional microstructure and get lens-like shape with aspect ratio $k_{fcs} \approx 4.7$ while extrusion process results in elongated powder particles of perfect fibred-like shape and aspect ratio $k_{fe} \approx 7.2$ that is the same as extrusion coefficient k_e , as shown in Fig. 4a and Fig. 4b.

It is easy to show that heat flow of exothermic reaction associated with decomposition of quasicrystalline phase in the as-extruded $\text{Al}_{94}\text{Fe}_3\text{Cr}_3$ alloy are smaller by roughly about 23% than that for quasicrystalline feedstock powder of the same composition. Moreover, a shift of the main exothermic peak toward lower temperature after extrusion indicates increased kinetic of quasicrystalline particles decom-

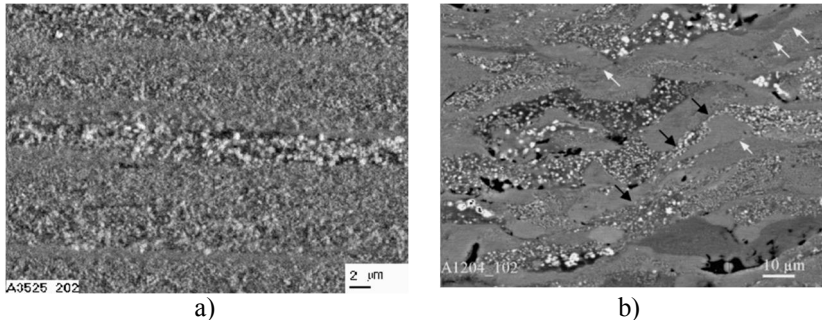


Fig. 4 – SEM images of cross-sectional microstructure for (a) extruded rod (b) cold-sprayed alloy, both performed by $\text{Al}_{94}\text{Fe}_3\text{Cr}_3$ -feedstock powder. Black arrows in (b) indicate the evidence of shear instabilities at the particle/particle boundaries whereas white arrows indicate the local metallurgical bonding between the powder particles due to impact fusion.

Homogeneous severe plastic deformation under extrusion results in elongation of powder particles that is assisted by two components of pressure such as longitudinal, P_l , and transversal one, P_t . By considering the accepted experimental conditions and following the calculation procedure reported previously in [10] components of pressure have been estimated as great as $P_l = 1.42$ GPa and $P_t = 3.30$ GPa. In contrast to extrusion process, two different kinds of deformation ensure intimate bonding at the particle/particle interfaces under cold spraying. Among them severe plastic deformation of powder particles results in their flattening and mechanical interlocking the splats by cold forging under forward pressure estimated in line with [10] as great as $p_f = 1.45$ GPa. Nevertheless, flow jet or adiabatic shear instability resulted from localised deformation at the particle boundaries is commonly believed to be primary responsible for creating the mostly effective intimate metallic bonding between the adjacent particles under extremely high strain rate as a result of high impact velocity. Adiabatic interaction between particle/particle is based on the fact that the thermal diffusion distance is very small (on the order of 10^{-6} m) during the very short operational time of impact, i.e. 10^{-7} to 10^{-5} s [18]. This is the reason of that why kinetic energy is mainly dissipated as heat, causing material softening and shear localisation and promoting intimate contact between two adjacent particles by mechanical interlocking and even by impact fusion, as evidenced from *Fig. 4b*.

Mechanical characteristics of feedstock powder, extruded rod and cold sprayed material, all performed by $\text{Al}_{94}\text{Fe}_3\text{Cr}_3$ -alloy, are listed in *Table 2*.

Several aspects resulting from mechanical performance of as-sprayed alloy could be mentioned here to clarify superior advantages of cold-spraying technique in comparison with extrusion process.

Table 2 – Mechanical characteristics of feedstock powder, extruded rod and cold sprayed material, all performed by $\text{Al}_{94}\text{Fe}_3\text{Cr}_3$ -alloy

Parameter Material	E, GPa	HV, GPa	Plasticity	Yield stress $\sigma_{0.2}$, MPa
			δ_H/δ_A	
Feedstock powder*	–	0.91±0.3	0.92/0.92	–
Extruded rod	87.5±2.3**	1.62±0.04	0.90/0.89	380
Cold sprayed alloy	90.0±2.5	2.19±0.02	0.86/0.87	515

Notice: * – adopted from [10]; ** – adopted from [4]

First of all it could be seen that the Vickers hardness, HV, of extruded rod and as-sprayed alloy is much higher than that of feedstock powder, suggesting material strain hardening upon consolidation. Compared to extrusion rod, Young's modulus is somewhat smaller whereas hardness number of the as-sprayed alloy is higher by roughly about 35%. The same is true for the value of yield stress of as-sprayed alloy that is by roughly 35% as high. The question is that what structural and processing parameters are responsible for enhanced strength properties of as-sprayed alloy. It is reasonable to think that retaining the entire number of quasicrystalline particles causes the strength of as-sprayed alloy to be greater than that for as-extruded material partly loosed quasicrystalline phase. The effect of quasicrystalline phase is intensified by extremely high values of strain rate (on the order of $10^5 \dots 10^7 \text{ s}^{-1}$) sustained by powder particle under impact. As was pointed out in [10] strain rate of powder particle under cold spraying exceeds by several orders magnitude to that for extrusion process. Following the calculation procedure [10] the latter could be estimated for the present study as great as 15.2 s^{-1} . Apart from reduced at the least by 180 K processing temperature of cold-spraying causes yield stress, σ_y , to rise up, suggesting the decrease of material deformation when applied pressure is of the same value. Taking into consideration nearly the same pressure conditions ($P_l \approx p_l$), essential increase of yield stress, σ_y could play crucial role in decrease of aspect ratio for powder particle in the as-sprayed alloy compared to that revealed in as-extruded material. As notable characteristic, it is easy to show that the ratio of true deformation for powder particles of as-extruded rod to that of as-sprayed alloy is nearly the same as the ratio of aspect ratio for powder particle in extruded rods to that revealed in as-sprayed material, i.e. $e_e/e_{cs} \approx 1.7$ and $k_{fe}/k_{fcs} \approx 1.6$. This result justifies the validity of suggestion attributed to that the difference in deformation conditions applied to extruded rods and a cold-sprayed alloy causes the difference in their structural features.

Another aspect concerns ductility of $\text{Al}_{94}\text{Fe}_3\text{Cr}_3$ -alloy fabricated via different techniques, i.e. water atomisation, extrusion, and cold-spraying. It is important that plasticity characteristics δ_H (δ_A) of feedstock powder are greater than critical value $\delta_H \geq 0.9$, indicating ductile behaviour of material in conventional tensile and bending tests [14] and, therefore, ensuring its good deformability

under consolidation. That is why no evidences of delaminating and cracking have been observed in microstructure of as-received extruded rod and cold-sprayed alloy, see Fig. 4. It is also essential that despite of increased hardness numbers for both kinds of $\text{Al}_{94}\text{Fe}_3\text{Cr}_3$ -alloy fabricated via extrusion process and cold-spraying keep the values of plasticity characteristics δ_H (δ_A) just about critical value, implying their workability under loading during exploitation. Thus, the essential advantage of both kinds of these metal matrix composites and especially that processed by cold spraying is their high hardness combined with rather high ductility valuable with respect to damage tolerance.

Among them composite performed by cold spraying gives mostly crucial benefit since its hardness number superior to that for hardest commercial Al alloys (Al-Cu-Mg-Fe-Ni) modified with 0.16 wt.% Sc and ascribed to series 7075-T6, which has been developed and successfully used for application under intermediate temperature ($\sim 230^\circ\text{C}$). As reported in [18] Vickers hardness of 2618 Al alloy is about 1.45 GPa whereas cold-sprayed $\text{Al}_{94}\text{Fe}_3\text{Cr}_3$ -alloy guarantees HV values by roughly 50 % as high. In addition, quasicrystalline Al-Fe-Cr -based alloys exhibit the thermal stability of mechanical properties at least up to 300°C [4], making them competitive with those of 2618 Al alloy for application in aircraft industry.

CONCLUSIONS

By using feedstock powder with nominal composition such as $\text{Al}_{94}\text{Fe}_3\text{Cr}_3$ the present study demonstrate significant advantages of cold-spraying in performance of composite Al-based coatings reinforced by metastable nano- and submicrometer-sized quasicrystalline particles as compared to currently employed warm extrusion process.

The main benefit of cold spraying is that the composite quasicrystalline structure of initial feedstock powder is entirely retained in as-sprayed material whereas extrusion process results in losing by roughly about 23% of quasicrystalline phase. The latter is presumably decomposed under combined effect of elevated temperature and high pressure used in extrusion process.

Overall, hardness number and yield stress of cold-sprayed $\text{Al}_{94}\text{Fe}_3\text{Cr}_3$ -alloy superiors nearly by 35 % to those of as-extruded material. Retaining the number of quasicrystalline particles at the most combined with extremely high values of strain rate sustained by powder particle under impact at the rather low processing temperature play crucial role in remarkable strain hardening of cold-sprayed alloy.

It was justified experimentally that essential advantage is combination of high hardness and rather high ductility valuable with respect to damage tolerance. Despite of strain hardening plasticity characteristics δ_H (δ_A) of cold-sprayed $\text{Al}_{94}\text{Fe}_3\text{Cr}_3$ -alloy was determined to be just about critical value $\delta_H \cong 0.9$ indicated in literature [14] as criterion for ductile behaviour of material under conven-

tional tensile and bending tests and, thus, quite enough for their workability under loading during exploitation.

Acknowledgements

Significant parts of the research were done in frame of projects: II-19-10 (H), 83/10 H (1) of the Ukrainian Academy of Science, and No 2210 of the Ministry for Education and Science of Ukraine. The authors are thankful to Dr. O. Neikov for performance of the quasicrystalline feedstock powder, Dr. N. Danylenko and Mr. A. Sameliuk for electron microscopy.

REFERENCES

- [1] A. Inoue, *Progress in Mater. Sci.*, 1998, Vol.43, P.365-520.
- [2] A. Inoue, H.M. Kimura, *J. Mater. Res.*, 2000, Vol. 15, No12, P. 2737-2744.
- [3] A. Inoue, H.M. Kimura, *Mat. Sci. Eng. A*, 2000, Vol. 286, P. 1 -////.
- [4] Yu.V. Milman, A.I. Sirko, M.O. Iefimov, and et al., *High temperature materials and processes*, 2006, Vol. 25, P. 19-29.
- [5] D. Shechtman, Blech., D. Gratias, J.V. Cahn, *Phys. Rev. Lett.*, 1984, Vol. 53, No20, P. 1951-1954.
- [6] M. Galano, F. Audebert, I.C. Stone, D. Cantor, *Acta Mater.*, 2009, Vol. 57, P. 5107-5119.
- [7] M. Galano, F. Audebert, A. Garcia Escorial, and et al., *Acta Mater.*, 2009, Vol. 57, P. 5120-5130.
- [8] O.D. Neikov, V.G. Kalinkin, and et al., *Patent Ru No 2078427*, *Information Bulletin*, 1977, No. 12.
- [9] A. Papyrin, V. Kosarev, S. Klinkov, A. Alkhimov, V. Fomin, *Cold Spray Technology*, Elsevier Science, 2006, 336 p.
- [10] M.V. Semenov, M.M. Kiz, M.O. Iefimov, A. I. Sirko, A.V. Byakova, Yu. V. Milman. *Nanosystem, Nanomaterials, and Nanotechnologies*, 2007, Vol. 4, No 4, P. 767-783.
- [11] M.M. Kiz, A.V. Byakova, A.I. Sirko, Yu. V. Milman, M. S. Yakovleva, *Ukr. J. Phys.*, 2009, Vol. 54, No 6, P. 594-599.
- [12] A.V. Byakova, M.M. Kiz, A.I. Sirko, M.S. Yakovleva, and Yu.V. Milman, *High Temperature Materials and Processes*, 2010, Vol. 29, No 5-6, P. 325-337.
- [13] A.V. Byakova, Yu.V. Milman, A.A. Vlasov, *Nanophysics, Nanosystems, and Nanomaterials*, 2004, Vol. 2, No 1, P. 215-225.
- [14] Yu.V. Milman, B.A. Galanov, S.I. Chugunova, *Acta. Metall. Mater.* 1993, Vol. 41, No 9, P. 2523-2532.
- [15] W.C. Oliver and G.M. Pharr J., *Mater. Res.*, 1992, Vol. 7, No 6, P. 1564-1583.
- [16] B.A. Galanov, Yu.V. Milman, S.I. Chugunova, I.V. Goncharova, *Superhard Materials*, 1999, Vol. 21, No 3, P. 23-35.
- [17] J.V. Cahn, D. Schehtman, D. Gratias, *J. Mater. Res.*, 1986, Vol. 1, P. 13-26.
- [18] Ajdelsztajn, A. Zuniga, B. Jodoin, E.J. Lavernia, *Surf. Coat. Technol.*, 2006, Vol. 201, No 12, P. 2109-2116.

HIGH PRESSURE TORSION OF NICKEL POWDERS OBTAINED BY ELECTRODEPOSITION

Lidija D. Rafailović^{1,2}, Christian Rentenberger², Aleksandra Gavrilović¹,
Christoph Kleber¹, Hans Peter Karthaler², Christoph Gammer²

1 CEST, Center of Electrochemical Surface Technology, Viktor-Kaplan- Straße 2, 2700 Wr. Neustadt, Austria

2 Faculty of Physics, Physics of Nanostructured Materials, Boltzmannngasse 5, 1090 Vienna, Austria

ABSTRACT

A new synthesis route for the production of bulk nanostructured materials is presented. Fine Ni powder was made by selected appropriate electrolysis conditions. A compact material with an average grain size below 40 nm was obtained by subsequent cold pressing. Then, using the high pressure torsion (HPT) deformation technique dense bulk nanocrystalline Ni was achieved. The detailed structural investigations of the as-prepared and HPT deformed Ni powder, including X-ray diffraction (XRD) and transmission electron microscopy (TEM), reveal in both cases the presence of a face centered cubic (FCC) phase without presence of any oxides. Coherently scattering domain size measurements by XRD show a value of 24 nm for the as-deposited powder and an even smaller value of 13.5 nm after HPT deformation. In addition, optical emission spectroscopy was employed to determine the impurity content of the obtained nanostructured material, showing a relatively low content of 0.9 % carbon and oxygen. The microhardness increased after deformation from (1.5 ± 0.08) GPa for the as-deposited Ni powder to (6.6 ± 0.2) GPa for the HPT deformed Ni powder.

Key words: electrodeposition, high pressure torsion, powder consolidation, hardness, bulk nanocrystalline Ni.

INTRODUCTION

Bulk nanocrystalline metals containing a large volume of grain boundaries receive increasing interest since they often show improved mechanical properties as high strength combined with high ductility [1]. Bulk metals are frequently made nanocrystalline using a top down approach (e.g. high pressure torsion [2-3]), but the final grain size that can be reached is limited. On the other hand bottom up approaches (e.g. electrodeposition [4]) allow the production of nanocrystalline metals with considerable smaller grain sizes, but the resulting material is present in the form of powders or thin films.

METHODS OF SAMPLE MANUFACTURING AND ANALYSIS

Ni powders were obtained galvanostatically at a selected high constant current density. As-deposited powders, compactified by cold pressing and deformed

by HPT at room temperature under a hydrostatic pressure of 8 GPa (*Fig. 1*) were systematically studied by X-ray diffraction analysis and TEM methods.

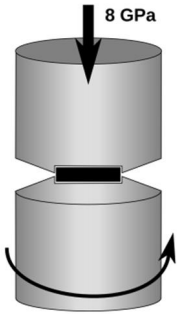


Fig. 1 – Sketch of the HPT deformation technique. The upper and the lower plunger (grey, cylindrical) are pressed against the disk-shaped sample (black). The lower anvil is rotated against the upper one, leading to a torsional deformation in the sample

XRD revealed a value of 24 nm for the as-deposited powder. By the subsequent HPT deformation, the coherently scattering domain size was decreased even further to 13.5 nm.

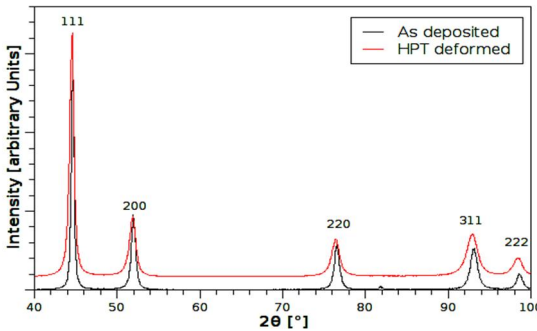


Fig. 2 – X-ray profiles of as-deposited and HPT deformed Ni powder, showing the presence of FCC Ni only.

around 35 nm for the as-deposited and HPT deformed Ni powder.

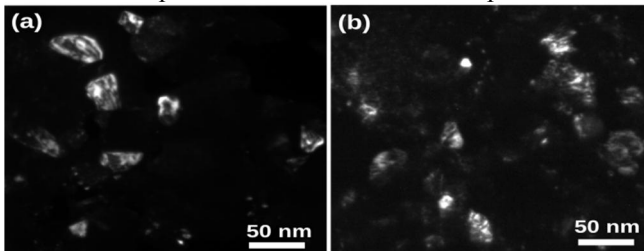


Fig. 3 – Dark field images of (a) as-deposited and (b) HPT deformed Ni powder. The grain size of both samples is comparable (35 nm), but the HPT deformed sample contains a high density of dislocations.

The impurity content was determined by optical emission spectroscopy.

RESULTS AND DISCUSSION

Figure 2 shows X-ray diffraction patterns of the as-deposited and the HPT deformed Ni powder. Coherently scattering domain size measurements by

The low content of impurities and the absence of oxides are crucial for the mechanical properties as impurities would cause embrittlement in the material. Glow discharge optical emission spectroscopy shows a composition of 99.1 at.% of Ni and 0.9 at.% O and C. The TEM study (*Fig. 3*) shows a comparable grain-size of

Due to the small grain size a very high microhardness of 6.6 GPa was achieved in the case of the HPT deformed Ni powder.

CONCLUSIONS

We show that by combining electrodeposition and HPT deformation it is possible to obtain dense bulk specimens with small grain sizes. Preliminary results obtained by XRD and TEM analysis show that the very fine grain size of the as-deposited powder (35 nm) is preserved after HPT deformation. The coherently scattering domain size is reduced during the HPT deformation due to the generation of dislocations in the sample. The small grain size and high dislocation density in the achieved specimen leads to an enhanced microhardness. It can be concluded that the combination of electrodeposition and HPT deformation presents a new route for synthesizing bulk nanostructured metals. A dense specimen with a low content of impurities, a very small grain size and improved mechanical properties was achieved.

Acknowledgements

This research was supported by the research project “Bulk Nanostructured Materials” within the research focus “Material Science” of the University of Vienna and by the Austrian Science Fund (FWF): [S10403, P22440]. The work at CEST was supported within the COMET program by the Austrian Research Promotion Agency (Österreichische Forschungsförderungsgesellschaft, FFG) and the government of Lower Austria.

REFERENCES

- [1] H. Gleiter, *Acta Mater*, 2000, Vol.48, P.1-29.
- [2] R.Z. Valiev, Y. Estrin, Z. Horita, T.G. Langdon, M.J. Zehetbauer, Y.T. Zhu, *JOM* 2006, Vol.58(4), P.33-9.
- [3] C. Mangler, C. Gammer, H. P. Karnthaler, C. Rentenberger, *Acta Mater*, 2010, Vol.58, P.5631-5638.
- [4] L. D. Rafailovic, D. M. Minic, H. P. Karnthaler, J. Wosik, T. Trisovic, G. E. Nauer, *J Electrochem Soc*, 2010, Vol.157, P.295-D301.

DETERMINATION OF EFFECTIVE DIFFUSION COEFFICIENTS FOR INHOMOGENEOUS MEDIA

Yu.O. Lyashenko*, L.I. Gladka

Cherkasy National University, Shevchenko 81, Cherkasy, Ukraine

ABSTRACT

A new model of effective medium is proposed for the transition zone located between two diffusion-interacting phases. In the model the effective diffusivity depends on the kinetic coefficients in each phase, volume fractions of phases and on the additional parameter, which generally characterizes the structure type of the two-phase zone.

Key words: effective diffusivity, two-phase zone, Maxwell's model, percolation effect.

INTRODUCTION

As known, materials can have inhomogeneous structure with essentially different kinetic coefficients in subsystems. As to account of diffusion properties, one can mention two characteristic structure types where effective diffusivities determination becomes a crucial issue in describing solid state reactions. Firstly, it is important to describe effective diffusion permeability of nanocrystal materials [1], when volume fractions of both grains and intergranular amorphous layers between them are considerable. Secondly, effective diffusion permeability in two-phase zones of ternary systems determines the morphology of the diffusion zone as well as the growth rate of phase layers and two-phase zones between them [2]. Traditionally, effective kinetic coefficients are defined on the basis of Maxwell-Garnett model [3] and some other approaches (for details see [4]). Kalnin's model [5] is the most highly developed one from the viewpoint of diffusion processes description by the modified Maxwell-Garnett model. At that, when treating inhomogeneous systems with noticeable volume fractions of both phases, we face the problem of ambiguity, since systems with high-conductive matrix and almost inert inclusions and vice versa will involve different effective diffusivities at equal ratios of phase volume fractions. This means that there always exists a certain branching, like, for example, at choosing between abstract models of parallel and series connection of phases. The aim of the present work is to find a new method of defining effective diffusivities.

* e-mail: urico@ukr.net , tel: (+38)093-9311249

METHODS OF EXPERIMENT AND CALCULATION

We aim at developing a self-consistent method for calculating the effective diffusivities in two-phase regions of ternary systems with the help of Bruggemann’s approach and Kalnin’s basic model for combined transition diffusion zone between two phases (Fig. 1).

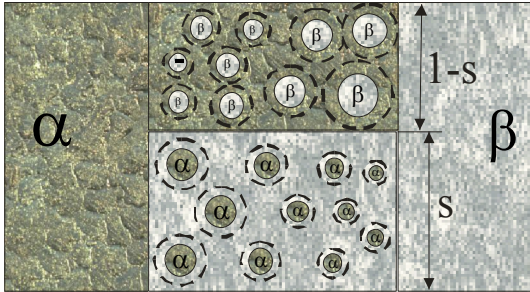


Fig. 1 – Schematic two-phase system. In the transition zone of diffusion contact the particles of α -phase precipitate in the β -phase matrix and the particles of β -phase – in α -phase

The paper provides derivation of the expression for effective kinetic coefficient in the case of transition zone between two phases containing two structure types: both the matrix of β -phase with inclusions of α -phase particles (basic structure K1) and conversely – α -phase matrix with inclusions of β -phase particles (basic

structure K2).

In order to derive the formula of the combined model for defining the effective kinetic coefficients in two-phase cells Kalnin’s basic models are applied:

Kalnin’s model (K1) [5] for the structure, presented in Fig. 1 (left-hand side):

$$L_{eff}^{K1} = \frac{L^\beta}{1 - p^\alpha + \frac{c^\alpha}{c^\beta} \cdot p^\alpha} \left[1 + \frac{\dim \cdot \left(L^\alpha \frac{c^\alpha}{c^\beta} - L^\beta \right) \cdot p^\alpha}{(\dim - 1) \cdot L^\beta + \frac{c^\alpha}{c^\beta} L^\alpha - \left(\frac{c^\alpha}{c^\beta} L^\alpha - L^\beta \right) p^\alpha} \right] \quad (1)$$

Kalnin’s model (K2) [5] for the structure, presented in Fig. 1 (right-hand side):

$$L_{eff}^{K2} = \frac{L^\alpha}{1 - p^\beta + \frac{c^\beta}{c^\alpha} \cdot p^\beta} \left[1 + \frac{\dim \cdot \left(L^\beta \frac{c^\beta}{c^\alpha} - L^\alpha \right) \cdot p^\beta}{(\dim - 1) \cdot L^\alpha + \frac{c^\beta}{c^\alpha} L^\beta - \left(\frac{c^\beta}{c^\alpha} L^\beta - L^\alpha \right) \cdot p^\beta} \right] \quad (2)$$

where c^α, c^β – concentration of component in the α - and β - phases, respectively; L^α, L^β – kinetic coefficients; p^α, p^β – volume fractions of α - and β -

phases, respectively, dim – model’s dimension (in case of $\text{dim}=3$ a three-dimension system is considered), f_{11} – volume fraction of α -phase in the bottom side of the transition zone with respect to the total volume fraction of α -phase; f_{21} – volume fraction of β -phase in at the bottom side of the transition zone with respect to the total volume fraction of β -phase; f_{12} – volume fraction of α -phase in the top side of the transition zone with respect to the total volume fraction of α -phase; f_{22} – volume fraction of β -phase in the top side of the transition zone with respect to the total volume fraction of β -phase.

In our calculations we consider the transition zone to contain basic structures K1 and K2 in arbitrary proportion, given by coefficient s . Using the condition of the parameters unity for the effective medium for two alternative structures of the transition zone $L^1_{\text{eff}} = L^2_{\text{eff}}$, calculate the unknown parameter f_{11} .

The obtained formula for effective kinetic coefficient of the transition zone taking into account the basic structures K1 and K2, as well as their interrelation, given by coefficient s , is as follows:

$$L^{K1+K2}_{\text{eff}}(s) = L^\beta \cdot s \cdot c^\beta \cdot \frac{s[L^\alpha + (\text{dim}-1) \cdot L^\beta] + (L^\alpha - L^\beta)(\text{dim}-1)v^\alpha f_{11}}{[s(L^\alpha + (\text{dim}-1) \cdot L^\beta) - (L^\alpha - L^\beta)v^\alpha f_{11}] \cdot [c^\beta s + v^\alpha f_{11}(c^\alpha - c^\beta)]} \quad (3)$$

RESULTS AND DISCUSSION

In Fig. 2 the dependencies of effective diffusivities, obtained at treating the two-phase media with essentially different kinetic coefficients in each phase, are shown. The comparative analysis confirms branching of the values of effective kinetic coefficients.

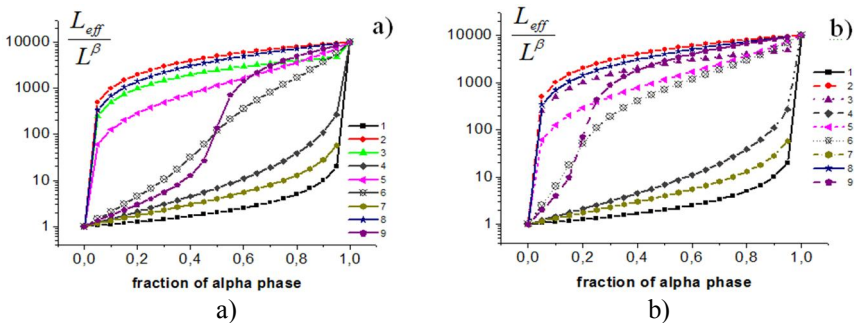


Fig. 2 – The dependencies of effective kinetic coefficients on the volume fraction of α -phase, calculated by the models of: 1 – series phase connection, 2 – parallel phase connection, 3 – combined model of parallel connection of the basic models (those of parallel and series connection) with the weight coefficients $W = 0.5$, 4 – Kalinin’s (K1), 5 – Kalinin’s (K2), 6 – combined model based on Kalinin’s models with the weight coefficients s , 7 – Maxwell-Garnett (MG1), 8 - Maxwell-Garnett (MG2), 9 – combined model based on Maxwell-Garnett models with the weight coefficient s . The calculations were done using the following parameters: $c_1 = 0.1$, $c_2 = 0.6$, $L_1 = 10^{-13}$ arbitrary units, $L_2 = 10^{-17}$ arbitrary units; a) at $s = 0.5$, b) at $s = 0.2$.

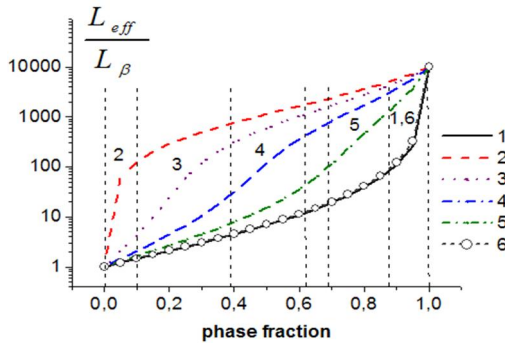


Fig. 1. – Dependencies of effective kinetic coefficients on the volume fraction of α -phase, calculated according to the following models: 1 – Kalnin’s (K1), 2 - Kalnin’s (K2), the model combined of Kalnin’s basic models at weight coefficient 3 - $s = 0.25$, 4 - $s = 0.5$, 5 - $s = 0.75$, 6 - $s = 0.99$ using the parameters, given in Fig. 1

In Fig.3 the dependencies of effective kinetic coefficients on the volume fractions of phases in the developed model of effective two-phase medium, at different values of coefficient s (describing the fraction of base structures K1 and K2 in the combined transition zone), are given.

Using different approaches to the assignment of effective diffusivities we have performed model calculations of diffusion interaction in the planar diffusion couple of a ternary system, the diffusion path crossing the two-phase region on the phase diagram. The detailed calculations are provided in [6].

CONCLUSIONS

The paper provides derivation and further analysis of the expression for effective diffusivity in the general case of transition diffusion zone at the contact of two phases in quasi-steady state conditions, grounding upon Kalnin’s basic models. It is presupposed that effective diffusivity in the transition zone depends on the diffusivities of the phases brought to contact, and an additional parameter s , which allows general considering of the transition zone structure. In the developed model the general expression for effective diffusivity depending upon the additional parameter (correspondingly, depending on the volume fractions of phases and transition zone structure) between two marginal cases of Kalnin’s model, is obtained.

REFERENCES

- [1] I. I.V. Belova, G.E. Murch. Philosophical magazine, 2004, Vol. 84, No1, P. 17-28.
- [2] Ю.А. Ляшенко. // Успехи физики металлов, 2003.Т. 4(2), с. 81-122.
- [3] J.C. Maxwell-Garnett, Phil. Trans. R. Soc, 1904, P. 203– 385.
- [4] Снарский А.А. Процессы переноса в макроскопически неоднородных средах.(А.А. Снарский, И.В. Безсуднов, В.А. Севрюков) М.:УРСС, 2007, с. 303.
- [5] J.R. Kalnin, E.A. Kotomin, J. Maier. J. of physics and chemistry of solids, 2002, Vol 63, P. 449-456.
- [6] Л.І. Гладка, Д.О. Тепаленко, Ю.О. Ляшенко) Вісник Черкаського НУ. Серія Фізико-математичні науки: Вид-во ЧНУ, 2009, No171,С. 54-70.

Advancs in equipment and technologies

SOLID TRANSFORMATIONS AS A VARIANT OF THREEDIMENSION NANOTECHNOLOGY

Vladimir N. Belomestnykh^{1*}, Elena P. Tesleva¹

¹ Yurga Institute of Technology of Tomsk Polytechnic University, Leningradskaya 26, 652050, Yurga, Kemerovskaya obl., Russia

ABSTRACT

The given article discusses a variant of natural nanotechnology in a volume material under solid-phase transformation. The article provides results on acoustic splitting in ammonium oxide NH_4ClO_4 in the low-temperature region. Ammonium oxide NH_4ClO_4 is structurally complex and chemically unstable. It has been stated that splitting of an acoustic wave in ammonium perchlorate under acoustical spectroscopy clearly detects coexistence of centrosymmetrical and noncentrosymmetrical phases. So, by example of ammonium perchlorate we consider possible use of acoustic splitting as a method of onset registration and growth control of a new phase within the parent one.

Key words: solid transformations, nanotechnologies, thermodynamic ambiguity, ammonium perchlorate.

INTRODUCTION

In the recent years words “nanoscience”, “nanotechnology”, “nanomaterials” sound as an overture to innovations. At the same time many previous achievements are being revised from this modern and, in many cases, justified point of view. As an example we can remember soot of the recent past and nanopowder of the present day. The given work can be attributed to the second of the named research areas and its idea is that solid transformations are anomalous properties. Nonequilibrium state of electron, dipole, spin or phonon subsystem of a solid together with the size factor result in lattice lability and practically important, sometimes unique properties which develop in the substance under certain temperature and pressure.

However, we should admit that in solid body technologies there are a lot of “white” spots, for example, we don’t quite understand the mechanisms of onset and consecutive growth of new phases within the parent phase under the phenomenon of “polymorphism”. The most widespread theories about polymorphous transformation going simultaneously in the whole amount of the solid body under elastic deformation have not been confirmed experimentally. The presence of an extended area instead of a line (which is characteristic for usual phase first- and second- order transitions) at the real phase diagram (*fig.1*)

* e-mail: tesleva@mail.ru, tel: (+7)3822750651 tel: (+7)9234915274

supposes existence of a complex heterogeneous structure made up of nanoregions with fluctuating or “frozen” order parameter.

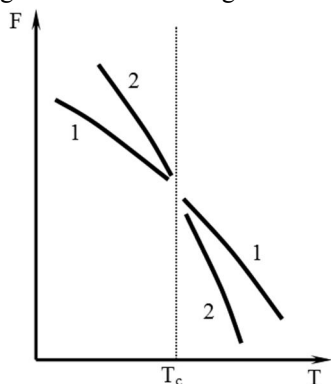


Fig. 1 – “Thermodynamic uncertainty” in the hysteresis area under the phase transition (F – free energy, T – absolute temperature)

electric-antiferroelectric under the polymorphous transformation form non-traditional state of the substance for which the most suitable name will be dipole glass [2]. The characteristic feature of this state is random distribution of nanometer regions with “frozen” local polarization in the crystals.

Obvious interest to the nanocondition of a solid in a natural compact state is limited in diagnostic methods. In work [3] we described the effect of acoustic splitting as an experimental fact of coexistence of two structures of a substance. Potassium nitrate (KNO_3) was used to show that there are two speeds of propagation for a wave of one type under similar ambient conditions. The given report provides results on acoustic splitting in a complex ammonium oxide (ammonium perchlorate, NH_4ClO_4), which structural and chemical instability was described before [4].

METHODS OF SAMPLE MANUFACTURING AND ANALYSIS

Fig. 2 shows the low-temperature spectrum of speed and longitudinal waves damping (internal friction Q^{-1}) in the polycrystal of NH_4ClO_4 received by the method of two-part piezoelectric vibrator at the frequencies ≈ 100 kHz.

When cooling ammonium perchlorate samples from room temperature at about $T = 175$ K the derivative changes its sign du/dT . Under the further decrease of temperature $\nu \rightarrow 0$ when approaching the temperature of liquid nitrogen the “secondary” sound is registered twice – near $T \approx 135$ K and $T \approx 95$ K, i.e. two resonances appear instead of one resonance of the acoustic vibrator. Parallel data on the changes of $Q^{-1}(T)$ at the temperature scale show that absorption of one

Almost 80 years ago academician V.D. Kuznetsov stated an idea in his monograph [1] that under polymorphous transformations “there are moments when transition from one phase into another has not yet been completed and the substance is simultaneously (emphasis added) in its two crystalline modifications”. Such structural crystalline states don’t have a generally accepted name yet and are found in literature under the names of diffuse phase transitions, hybrid crystals, fluctuation of symmetry, structurally-mixed phases, spatially heterogeneous condition, phase mixture, coexisting phases, order-in-disorder (or vice versa) and other. Some crystals of mixed composition, for example, ferroelec-

acoustic wave in the sample of ammonium perchlorate increases and absorption of the second wave decreases. Although both forms of NH_4ClO_4 under low temperatures are orthorhombic, they have different space groups – P_{nma} и $P_{n21/a}$ due to the different environment of ammonium ions in ammonium perchlorate lattice. The corresponding ions are denoted as $\text{NH}_4(1)$ and $\text{NH}_4(2)$.

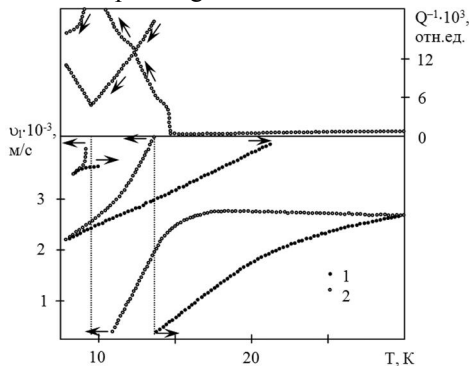


Fig. 2 – Low-temperature changes of ultrasonic speed and internal friction in the polycrystal NH_4ClO_4 . Modes: 1 – heating, 2 – cooling

different speed (one of the cations is less mobile). The sound begins to spread in one as well as in the other group of cations. This is the qualitative interpretation of existence of two sound velocities in one and the same substance under the same conditions. At the reversal of temperature (defrosting) the acoustic diagram is reproduced but it has a significant hysteresis effect – dv/dT sign changes only near the room temperatures (fig. 2 shows the change of $Q^{-1}(T)$ only when cooling).

The observed peculiarities of $v(T)$ and $Q^{-1}(T)$ in NH_4ClO_4 under low temperatures correspond to some results in works [5-13]. Anomalies of some lattice and inner modes of ions ClO_4^- и NH_4^+ near 180 and 40 K in the temperature spectra of Raman scattering in monocrystals of ammonium perchlorate [10]; overlapping of infrared fringes under $T \approx 200$ K [11], appearing of v_1 fringe under 120 K and splitting of forced oscillation fringes v_3 и v_4 of ammonium ion under $T < 50$ K [9]; splitting lines 635 cm^{-1} (oscillation v_4 of ClO_4^- ion) near the temperature of liquid nitrogen [12], abnormal change of quadrupole interaction constant for the atoms of ^{35}Cl in NH_4ClO_4 under the temperatures 200 and 20 K [13] and direct X-ray diffraction study [8] give non-linear temperature dependences of all parameters of ammonium perchlorate lattice.

Fig. 3 shows the parallel results of low temperature X-ray diffraction studies of dimensional changes of elementary ammonium perchlorate lattice in two works [8 and 10].

The first of them has five perchlorate ions and the second has six perchlorate ions (in both phases). Existence of two types of ammonium ions in ammonium perchlorate under low temperatures can be the cause of the observed acoustic splitting. When the ammonium perchlorate crystal is cooled ammonium ions are of the same type until the temperature of 200 K. Below this temperature $\text{NH}_4(1)$ and $\text{NH}_4(2)$ appear. They reorient in the lattice with

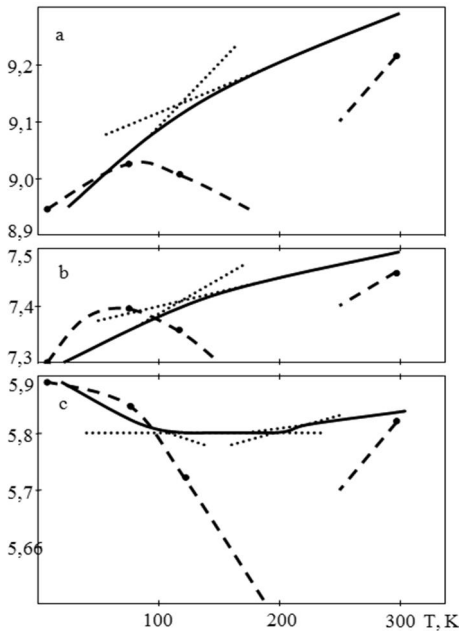


Fig. 3 –Low-temperature changes of lattice parameters a , b and c (in Å) of NH_4ClO_4 monocrystal (full line – the data [8], dashed-dot line – the results [10], averaging and approximation of the data [8] have been done by the authors)

The dynamics of changes in linear dimensions of the ammonium perchlorate lattice appears to be especially impressing as shown by the authors [8] who were completing precise measuring of the lattice parameters in the cooling and heating modes (we provide these data in smoothed form with our own approximation of linear parts of functions $a(T)$, $b(T)$, $c(T)$). Fig. 3 shows that qualitative structural studies of different authors correspond: structural ammonium perchlorate lattice anomalies are grouped near 200 and 100 K. Non-linear change of unit cell parameters near 200 K is caused mainly by parameter c anomaly, and near 100 K all three lattice parameters behave anomalously: at curves $a(T)$ and $b(T)$ we register a knee with a change of quantities da/dT and db/dT (below 120 K the derivatives increase) and derivative dc/dT changes its

sign (below 120 K in direction c (across the layers) the unit cell begins to expand with the decrease of temperature). In the interval $120 \div 298$ K in work [10] the measurements are not completed but the authors note that lattice parameters in similar systems (NH_4IO_4 , NH_4ReO_4) form an arc with an extremum under 200 K and temperature spectra of Raman scattering have pronounced anomalies under 180 K. Comparing our results (fig. 2) and thorough X-ray diffraction and spectroscopic studies of NH_4ClO_4 lattice (fig. 3) we can state coinciding anomalies of acoustic and structural parameters under the temperatures near 100 and 200 K and consider that under the given temperatures we observe transformation corresponding to two isostructural phase transitions.

In ammonium salts structural order or disorder under low temperatures is usually associated with cation reorientation [5]. Orientation ordering (disordering) of some ammonium ions in ammonium perchlorate lattice is represented as follows. In every unit cell with NH_4^+ ion in its middle the connections $\text{N} - \text{H}$ are directed to the neighbouring chlorate ions.

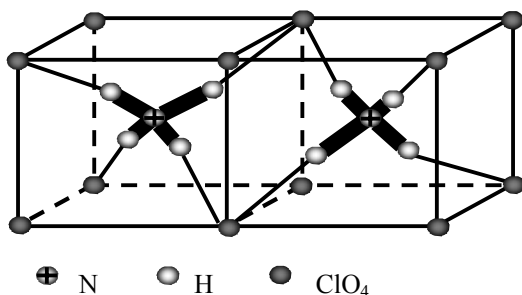


Fig. 4 – Two orientations of ammonium ion NH_4^+ in ammonium perchlorate lattice [14]

In this case every ammonium ion has two possible orientations (fig. 4). In the ordered form under the low temperatures all ions have the same parallel orientation which makes the system an analog of a ferroelectric or a ferromagnetic. With the rise of temperature the ions are disordered along two possible orientations mentioned above which are open for each of them (the collection of unit cells in this phase possesses an effective centre of symmetry) [5].

RESULTS AND DISCUSSION

Splitting of an acoustic wave in ammonium perchlorate under acoustical spectroscopy clearly exposes the coexistence of centrosymmetrical and non-centrosymmetrical phases. Thus, having taken ammonium perchlorate as an example we have considered the possible use of acoustic splitting as a means of onset registration and growth control of a new phase within the parent one. As for the nanoscale we don't exclude that it is the so called secondary structure that is realized under polymorphic transformations ("minimum crystal", "crystal quantum", the minimal size when the crystal keeps its form unchanged: $10^7 \div 10^8$ m). The secondary structure under the usual states of a real crystal is considered to be supplementary to the atom-molecule structure of the substance [15]. In our case it is possible to regulate the dimensions of the secondary structure by changing the time of polymorphic transformation. Another aspect of the problem marked by us is that polymorphic transformation and other solid body reactions where the key role is played by the onset of a new phase can serve as models for studying (yet fragmentary) mechanism of forming bulk materials nanostructures even taking into consideration that the problem of polymorphic transformation itself is far from satisfactory solution. It is appropriate to consider the onset of a new phase on the defects of parent matrix, kinetic and morphological peculiarities, the size factor and other problems of nanosystems physicochemistry in the context of polymorphism.

CONCLUSIONS

Of course, study of the structural forms of a nanometer scale substance in its pre- and posttransition states is not limited by the method of acoustical spec-

trospecty. For example, another classical method of diffuse X-ray scattering in a “classical” object – quartz under the “classical” $\alpha \rightarrow \beta$ -transformation ($T_c \approx 576^\circ\text{C}$) suggests describing the transition from trigonal to hexagonal form in three stages: 1) preparation for the transformation (from 300°C to $540\text{--}560^\circ\text{C}$), 2) transformation itself, so to say, “culmination” ($560\text{--}580^\circ\text{C}$), and 3) completion ($580\text{--}700^\circ\text{C}$) [16]. Meanwhile, it is noted that changes in the Laue maximums ratio are observed in the experiment under the temperature of 100°C , and on the other hand under T_c full symmetry C_6 is not observed yet. Another thing is that acoustical methods allow to register phase transitions of any nature (speed sensitivity is $\Delta v/v \approx 5 \cdot 10^{-7}$).

However, for the natural nanotechnologies in bulk material the first place is probably occupied not by the method but by the object. Mesoscopic materials of a new type with complex molecules ($\text{Sn}(\text{CH}_3)_4$ и $\text{Fe}(\text{CO})_5$) demonstrating nano-effects in bulk are considered with application of Mössbauer effect in work [17].

REFERENCES

- [1] Kuznetsov V.D. Physics of a solid. Tomsk: Kubuch publishers, 1932. 504 p. (in Russian)
- [2] Strukov B.A. Soros Educational Journal 1996. № 4. P. 81-89. (in Russian)
- [3] Belomestnykh V.N. Letters to the Journal of Experimental and Theoretical Physics. 1990. V.51. № 10. P. 526-529.
- [4] Belomestnykh V.N., Tesleva E.P. Acoustical and thermalphysic studies of ion reorientations. Tomsk: Tomsk University press, 2006. 162 p.
- [5] Parsonage N., Staveley L. Disorder in crystals: 2 parts / Transl. from English; edited by G.N. Zhizhin. – Moscow: Mir, 1982. – P. 1. – 434 p.
- [6] Brown R.J.C., Weir R.D., Westrum E.F.Jr. J. Chem. Phys. – 1989. – Vol. 91, № 1. – P. 399-407.
- [7] Stammler M., Bruenner R., Schmidt W., Orcutt D. Advances in X-ray analysis. – New York: Plenum Press, 1966. – Vol. 9. – P. 170-189.
- [8] Hamada A., Yamamoto S., Fujiyoshi O. J. Korean Phys. Soc. – 1998. – Vol. 32. – P. S152-S155.
- [9] Rensburg D.J., Schutte C.J. J. Molec. Struct. – 1972. – Vol. 11, № 2. – P. 229-239.
- [10] Chakraborty T., Khatri S.S., Verma A.L. J. Chem. Phys. – 1986. – Vol. 84, № 12. – P. 7018-7027.
- [11] Schutte C.J.H. St. Com. – 1980. – Vol. 35, № 80. – P. 577-580.
- [12] Corn R.M., Strauss H.L. J. Chem. Phys. – 1983. – Vol. 79, № 6. – P. 2641-2649.
- [13] Segel S.L., Maxwell S., Heydind R.D. Solid State Commun. – 1980. – Vol. 66, № 10. – P. 1039-1041.
- [14] Solymosi F. Structure and stability of salts of halogen oxyacids in the solid phase. – Budapest: Akad. Kiado, 1977. – 467 p.
- [15] Vesnin Y.I. Secondary structure and properties of crystals. –Novosibirsk: Inst. of Neorganic Chemistry of Siberian Branch of Russian Academy of Sciences, 1997. – 102 p.
- [16] Kolontsova E.V., Telegina I.V. Reports of Academy of Sciences of the USSR. 1967. T. 173. № 5. P. 1045 – 1047.
- [17] Shechter H., Akkermans E., Tsidilkovski E. Nanstruct. Mater. 1995. V.6. № 1-4. P.369-372.

NANOSIZE PHASES FORMATION UNDER LOW CARBON STEEL THERMOMECHANICAL STRENGTHENING

Victor E. Gromov^{1*}, Yurii F. Ivanov², Vadim B. Kosterev³,
Sergey V. Konovalov¹

- 1 Siberian State Industrial University, Kirov str., 42, Novokuznetsk, 654007, Russia
- 2 Institute of High Current Electronics, Siberian Branch, Russian Academy of Sciences, av. Akademicheskii, 2/3, Tomsk, 634055, Russia
- 3 West Siberian Iron and Steel Plant, Kosmicheskoe av., 16, 654043, Novokuznetsk, Russia

ABSTRACT

The quantitative regularities of structure phase states formation in different H-beam cross sections under accelerated cooling in different regimes are established. The gradient structure-phase states formation being characterized by the regular change of dislocation substructure parameters, nanosized range α -phase fragments and cementite particles on cross section are revealed by methods of transmission electron diffraction microscopy.

Key words: structure-phase states, dislocation substructure, strengthening, H-beam

INTRODUCTION

Currently, the production of rolled steel uses thermo-mechanical hardening technology, providing enhanced mechanical properties without the use of expensive alloying additives [1-3]. Targeted management of the rolled steel operational properties, and development of optimal modes of its hardening should be based on knowledge of the structure-forming process under various technological operations [1-3].

The aim of this study was to investigate the formation of nanosize structural-phase states of 09G2S steel H-beam subjected to thermomechanical strengthening (accelerated cooling).

MATERIALS AND METHODS

Temperature-speed parameters of rolling and accelerated cooling of two technological options are presented in *Table. 1*. As the research material we used H-beam DP155 made from 09G2S steel (0.095 wt. % C, 1.560 wt. % Mn, 0.660 wt. % Si).

Analysis of structure phase states and dislocation structures were performed by transmission electron microscopy of thin foils on the different distances from cooling surface.

* e-mail: gromov@physics.sibsiu.ru, tel: +7(3843)462277

Table 1. The modes of accelerated cooling

Mode Number	Rolling speed, V, m/s	T, °C			Water pressure at water supply, atm				
		after 3rd roll stand	after 9th roll stand	when entering the cooler	I		II		I
					1b	2t	3b	4t	1m
P1	4.5	1050 - 1150	1040 - 1080	690-730	1.5	1.5	2.5	2.5	3.5
P2	6.0	1050 - 1160	1060 - 1100	800-850	1.5	1.5	2.5	2.5	3.0

The plates with thickness of 0.3 mm were cut out from the segment parallel to the inner surface of the profile of the H-beam at a distances of 4, 7 and 10 mm from the surface cooling, and in addition, the layer structure, directly adjacent to the cooling surface was analyzed.

The diffraction analysis with the dark-field technique and subsequent indexing of microelectron diffraction pictures was used for identification of the phases. The images of material's fine structure (bright-field image) were used to classify the morphological features of the structure; determine the size, the volume fraction and the localization of the particles of the second phases; measure the scalar ρ dislocation density [4, 5].

RESULTS AND DISCUSSION

Thermostrengthening of the 09G2S steel of the H-beam performed on the device of accelerated cooling according to regimes P1 and P2, leads to the formation of a multilayer (surface, transitional and central layers) of the microstructure of the H-beam profile. The structure of the stele in the transition layer and the central zone of the shelve under these cooling conditions resulted from the transformation according to diffusion mechanism, and consists of ferrite, perlite, a "degenerate" pearlite and carbide precipitates along the ferrite grain boundaries. The structure of the surface layer is formed as a result of the intermediate (regime P2) and shear (regime F1) mechanisms of $\gamma \Rightarrow \alpha$ transformation, followed by "self-tempering" process. Quantitative characteristics of the surface (hardened) layer, reflecting the most significant effect of hardening regime on the substructure of steel and identified according to the results of electron microscopic studies are presented in *Table. 2*.

Accelerated cooling of the surface is accompanied by formation of the gradient of the structure phase states. Quantitative relationships that characterize the gradient nature of the organization of the defect substructure of H-beam subjected to forced water cooling are shown in Fig. 1.

Table 2. Quantitative characteristics of the structure of the 09G2S steel hardened layer

Process mode	The parameters of the structure							
	ΔV_1	$d_1, \mu\text{m}$	$\rho_1, 10^{10} \text{cm}^{-2}$	ΔV_2	$d_2, \mu\text{m}$	$\rho_2, 10^{10} \text{cm}^{-2}$	$\langle \rho \rangle, 10^{10} \text{cm}^{-2}$	$\langle d \rangle, \mu\text{m}$
P1	0.9	0.2	5.0	0.1	0.5	2.8	4.78	0.23
P2	0.6	0.3	4.8	0.4	0.5	3.6	3.84	0.38

Note: $\Delta V_1, \Delta V_2$ - the volume fraction of lamellar (martensite or bainite) and subgrain type, respectively; d_1, d_2 - the average transverse sizes of plates and subgrains, respectively; ρ_1, ρ_2 - the scalar density of dislocations arranged in plates and subgrains, respectively; $\langle \rho \rangle$ - the average scalar density of dislocations in the layer (taking into account the types of structures); $\langle d \rangle$ - the average size of the substructure in the layer (taking into account the types of structures).

Analysis of the results presented in this figure confirms the conclusion about the gradient nature of the defected substructure. Namely, the closer to the cooling surface the scalar density of dislocations in the ferrite grains (Fig. 1, curve 2) and ferritic interlayers of pearlite grains (Fig. 1, curve 1), are increasing and the average size of fragments of the ferrite (Fig. 2, curve 1) and particle size of cementite (Fig. 2, curve 2) are reducing.

It can be seen that in the surface layer of H-beam the state is formed, which based on the average size of fragments of α -phase and cementite particles can be regarded as a nanostructure.

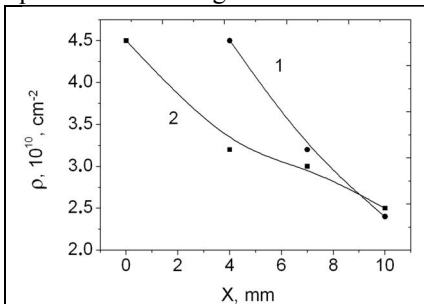


Fig. 1 – Dependence of the scalar density of dislocations located in the ferrite component of the pearlite grains (curve 1) and ferrite grains (curve 2) on the distance to the surface of treatment

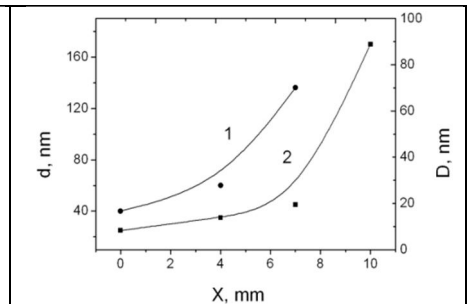


Fig. 2 – Dependence of the cementite fragments average size (curve 2) and ferrite fragments D average size (curve 1) on the distance to the surface of treatment

Formation of nanostructured phases during thermomechanical hardening

Analysis of the results presented above gives us grounds to conclude that the formation of nanoscale phase in the studied steel under thermomechanical processing and subsequent accelerated cooling of rolled products is possible with the implementation of such a processes. First, by dispersing of pearlite cementite plates colonies by cutting them by moving dislocations. Secondly, in

the process of dissolution of pearlite colonies cementite plates and repeated precipitation of cementite particles on the dislocations, the boundaries of blocks, subgrains and grains. Third, during the decay of solid solution of carbon in the α -iron, formed under the conditions of accelerated cooling of the steel ("self-tempering" martensite). Fourth, when during the final transformation of the retained austenite in the structure of carbideless bainite with the formation of α -iron and cementite particles. Fifth, in the implementation of the diffusion mechanism of $\gamma \Rightarrow \alpha$ transformation under the conditions of high degree of deformation and high temperature treatment.

Dispersion of the pearlite colonies cementite plates by cutting them by moving dislocations

Fig. 3 shows electron microscopy images of the pearlite colony, the cementite plates which are divided into separate fragments (the blocks). Sizes of fragments vary from 5 to 30 nm. Simultaneously, cementite particles are found in ferritic interlayers of the pearlite colony, the sizes of whose particles vary from 5 to 10 nm (Fig. 3, the particles are indicated by arrows).

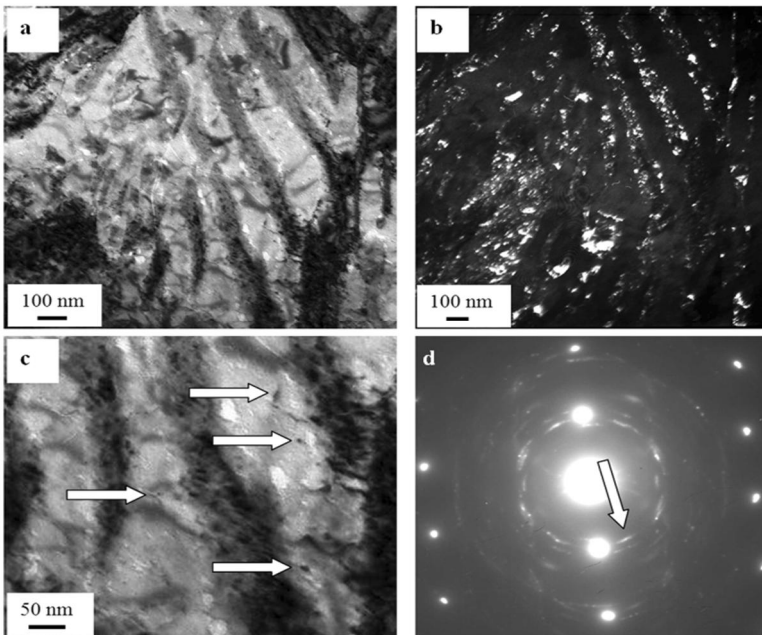


Fig. 3 – The fragmentation of the cementite plates of pearlite grains, a, c – light-field image, b - dark field image obtained in the reflection $[121] \text{Fe}_3\text{C}$; d - electron diffraction pattern image, the arrow indicates the reflection, in which a dark field image was obtained. On c) the arrows indicate cementite particles located in the plates of ferrite

Nanoscale range of the cementite structure of given pearlite colony is confirmed by quasicircular construction of the electron diffraction image derived from this plot foils (Fig. 3, d). Presented micrographs of the steel structure suggest that the thermomechanical processing is accompanied not only by mechanical destruction of the plates of cementite, but also their dissolution of with the departure of the carbon atoms on the dislocation and the subsequent precipitation in the body of ferrite plates.

Dispersion of the cementite plates may be accompanied by the formation of the block (subgrain) structure (Fig. 4). The newly evolved cementite particles in such a structure are located at block boundaries, stabilizing their sizes.

Dissolution of cementite plates of the pearlite colonies and repeated precipitation of the cementite particles on the dislocations, the boundaries of the blocks, subgrains and grains

Removal of carbon atoms from destructed particles of cementite is possible and even at much greater distances. Studies of the block (subgrain) structure of α -iron grains by methods of dark-field analysis revealed the cementite particles in the body of the blocks on the dislocations and block boundaries (Fig. 5). Particles have a rounded shape, particle sizes vary from 5 to 15 nm.

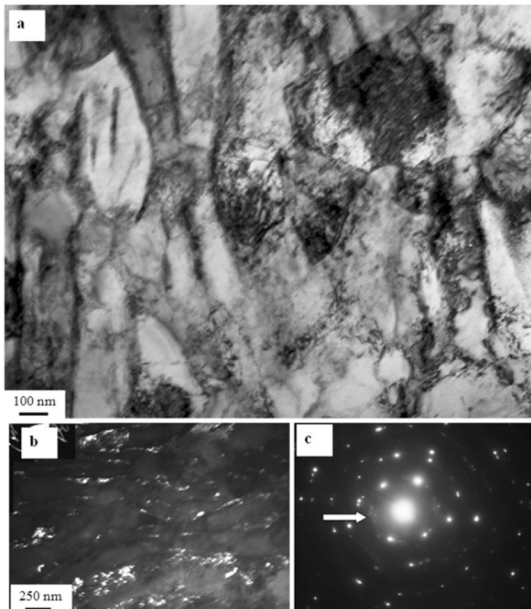


Fig. 4 – The formation of a subgrain structure of the steel and fragmentation of the pearlitic grain cementite plates a - light-field image, b - dark field image obtained in the reflection $[121] \text{Fe}_3\text{C}$; c - electron diffraction pattern image, the arrow indicates the reflection, in which a dark field image was obtained

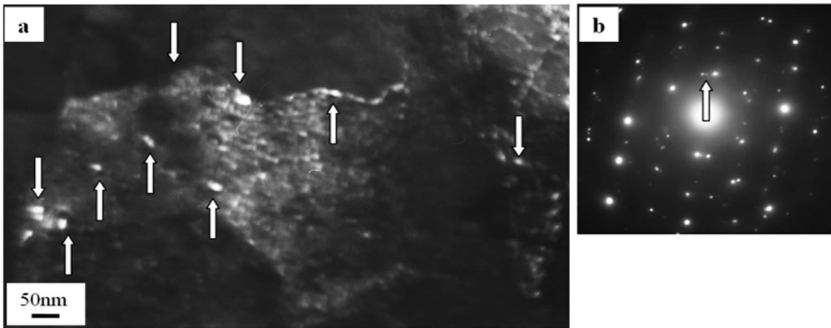


Fig. 5 – Precipitations of second phase particles (cementite) within the body and at the boundaries of α -phase subgrains: a - dark field image, obtained in the reflections $[012] \text{Fe}_3\text{C} + [110] \alpha\text{-Fe}$ (particles indicated by arrows), b - electron diffraction pattern image, the arrow indicates the reflection, in which a dark field image was obtained.

The decay of solid solution of carbon in the α -iron, formed under the conditions of accelerated cooling of steel ("self-tempering" of martensite)

Accelerated cooling of the H-beam leads to the formation of the martensitic structure in the surface layer. Subsequent "self-tempering" of the steel under the influence of the residual heat is accompanied by relaxation of the dislocation substructure, which manifests itself in reducing the scalar density of dislocations, the destruction of low-angle boundaries of martensite crystals, precipitation on dislocations within the body of martensite crystals (*Fig. 6a*) and along the boundaries of cementite particles (*Fig. 6b*). The sizes of particles located on dislocations, vary between 5 ... 10 nm (*Fig. 6a*), located on the borders - in the 10 ... 30 nm range.

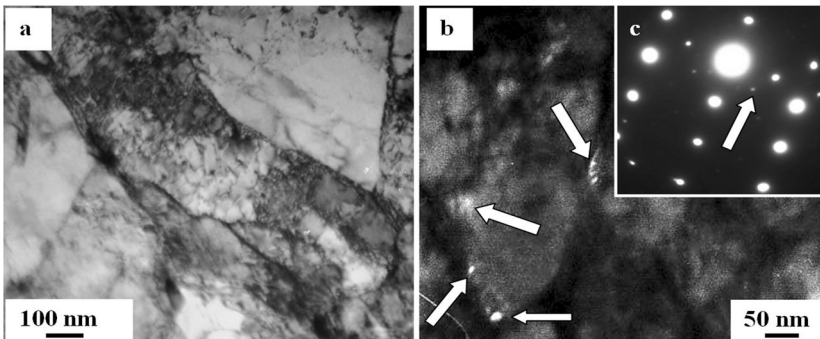


Fig. 6 – The microstructure of the hardened layer of the H-beam, cooled by P1 regime, a - bright-field image, b - dark field image obtained in the reflection $[120] \text{Fe}_3\text{C}$; c - electron diffraction pattern image, the arrow indicates the reflection, in which a dark field image was obtained. On (b) the arrows indicate cementite particles.

Formation of cementite particles during the process of complete transformation of retained austenite presented in the structure of carbideless bainite

In the surface layer of the steel sample cooled according to P2 regime, along with grain-subgrain structure the structure of plate type, the so-called carbideless bainite was observed. As shown above, the plates are arranged parallel to each other and there was an alternation of plates of light and dark contrast. Microdiffraction analysis of these structures revealed the presence of only the reflections of α -phase. Reflections of the retained austenite and carbide phase particles are not detected. At the same time, mottled contrast reminiscent of the contrast from the pre-precipitates of second phase particles (Fig. 7) is revealed within the structure of the darker plates (formed, presumably as a result of the process of complete transformation of residual austenite).

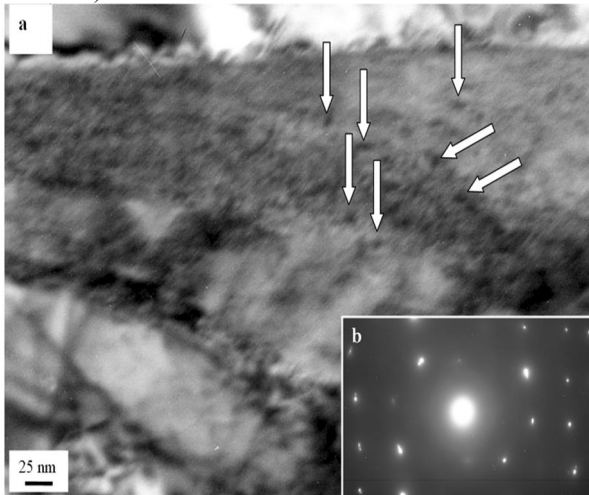


Fig. 7 – Electron microscopic image of the structure formed at the transformation of the residual austenite; a - light field image, b - electron diffraction pattern image of (a). Arrows indicate pre-precipitates of second phase particles

Formation of nanosize phases as a result of polymorphic $\gamma \Rightarrow \alpha$ transformation

The high level of steel plastic deformation, which is realized by thermomechanical processing of rolled products, leads to dispersion of structures formed in the process of diffusion of the $\gamma \Rightarrow \alpha$ transformation. Fig. 8 shows electron microscopy images

of the structure of lamellar pearlite. The measurements show that the thickness of plates of α -phase, separated by the plates of carbide, is about 70 nm; the thickness of the plates of the carbide phase of ~ 25 nm.

Formation of nano-sized particles of the carbide phase, is also observed in the formation of the so-called pseudoperlite, namely ferrite grains, containing particles of cementite of globular morphology (Fig. 9). The sizes of particles of cementite in these grains vary in the range 40 ... 60 nm.

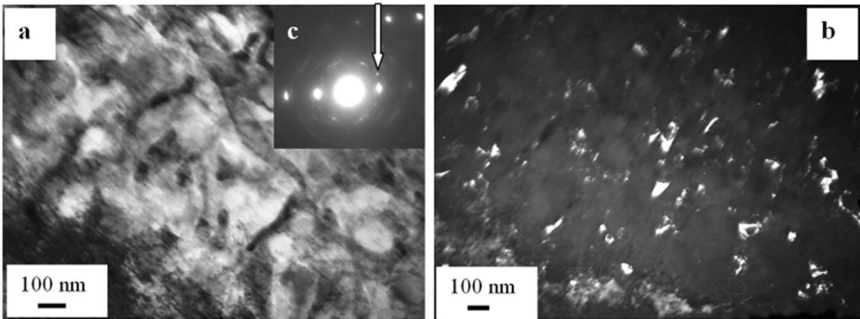


Fig. 8 – Electron microscopic image of the structure of the lamellar (plate) perlite: a – light field image, b - dark field image obtained in $[021] \text{Fe}_3\text{C}$ the reflection; c – electron diffraction pattern image, the arrow indicates the reflection, in which a dark field image was obtained

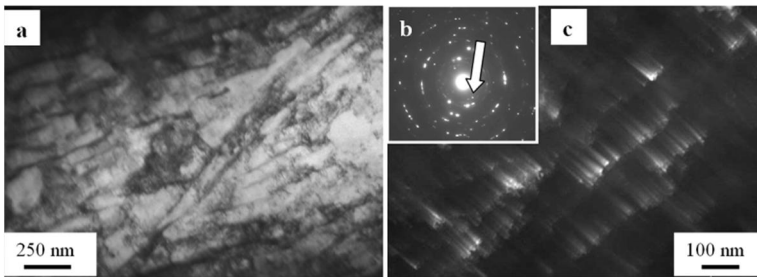


Fig. 9 – Electron microscopic image of the pseudoperlite structure: a – light field image, b - dark field image obtained in the reflection $[012] \text{Fe}_3\text{C}$; c - electron diffraction pattern image, the arrow indicates the reflection, in which a dark field image was obtained.

CONCLUSIONS

A study of the H-beam's structure phase states after thermomechanical strengthening was carried out using the methods of transmission diffraction electron microscopy.

The formation of gradient structure, characterized by regular changes of parameters of the structure-phase states and dislocation substructure as it approaches to the surface of the accelerated cooling was revealed. It was established that nanosize structure-phase states are formed in the surface layer.

The analysis of the processes leading to the formation of the structure within the beam profile of 09G2S steel nanoscale phases was carried out.

It is shown that the formation of nanoscale phases was carried out possibly in the implementation of the following processes. First, during dispersing of the cementite plates of pearlite colonies by cutting them by

moving dislocations. Secondly, during the dissolution of pearlite colonies cementite plates and repeated precipitation of the cementite particles on the dislocations, the boundaries of blocks, subgrains and grains. Third, during the decay of solid solution of carbon in the α -iron, formed under the conditions of accelerated cooling of steel ("self-tempering" of martensite). Fourth, during final transformation of the retained austenite in the structure of carbideless bainite with the formation of α -particles of iron and cementite. Fifth, during the implementation of the diffusion mechanism of $\gamma \Rightarrow \alpha$ transformation under the conditions of high degree of deformation and high temperature processing.

Acknowledgements

This work was supported by the Federal Program "Research and scientific-pedagogical personnel of innovation in Russia 2009-2013" (contract No P332) and Analytical service programme "The development of scientific potential of high school (2009 – 2011)" (project No 2.1.2/13482).

REFERENCES

- [1] V.E. Gromov, O.Yu. Efimov, V.B. Kosterev et al. Structure phase states and properties of the strengthened rolled steel and cast iron rolls. Novokuznetsk. Inter-Kuzbass Publ., 2011.
- [2] E.G. Belov, L.M. Poltoratskii, O.Yu. Efimov, S.V. Konovalov, V.E. Gromov, Steel in Translation, 2010, 40(2), P. 114-118.
- [3] O.Yu. Efimov, A.B. Yur'ev, Yu.F. Ivanov, V.E. Gromov, M.M. Morozov. Steel in Translation, 2008, 38(12), P. 982-986.
- [4] P.B. Hirsch, A. Howie, R.B. Nicholson, D.W. Pashley, M.J. Whelan Electron microscopy of thin crystals, Krieger Publishing Co., Melbourne, 1977.
- [5] N.A. Koneva, E.V. Kozlov, Yu.F. Ivanov, N.A. Popova, A.N. Zhdanov // Material Science and Engineering, 2005, A 410-411, P. 341-344.

PRODUCTION OF SnO₂ NANO-PARTICLES BY HYDROGEL THERMAL DECOMPOSITION METHOD

P. Jajarmi¹, S. Barzegar², G.R. Ebrahimi¹, N. Varahram³

¹ Department of Materials Science and Engineering, SabzevarTarbiatMoallemUniversity, Sabzevar, Iran

² Basic Science Department, JundiShapur University of Technology, Dezful, Iran

³ Department of Materials Science and Engineering, Sharif University of Technology, PO Box 11365-9466, Azadi Ave., Tehran, Iran

ABSTRACT

SnO₂ is an important functional material having a wide range of applications in gas sensors and optoelectronic devices. There is a great interest for finding new cost-effective and straight-forward methods for production of these particles. In this research, hydrogel thermal decomposition method (HTDM) is used for production of high purity SnO₂ nano-particles. Cost effective reactants and green routes of production are the advantages of polysaccharide based hydrogel as starting material for this method. Visual observations indicated that there is very little tendency for agglomeration in the SnO₂ nano-particles produced by this method which can be considered as an advantage for this method over other methods for production of SnO₂ nano-particles. SnO₂ nano-particles are also characterized by X-ray diffraction (XRD) in terms of purity and the sizes. It is found that high purity SnO₂ nano-particles in the size range of 25 – 36 nm can be produced by HTDM.

Key words: nanomaterials, production, SnO₂, X-ray techniques, hydrogel thermal decomposition method

INTRODUCTION

SnO₂ is widely used in gas sensors and optoelectronic devices as a functional material [1, 2]. Depending on the production method, SnO₂ can be produced with various morphologies [3–8]. Recently, SnO₂ with two-dimensional structure has attracted more attention due to its potential applications in gas sensors [9] and photocatalysts [10]. Dai and Pan reported synthesizing SnO₂ diskettes by evaporating SnO₂ powders at elevated temperatures [11]. Two-dimensional (2D) hierarchical SnO₂ were synthesized by Xie et al. [12] using a hydrothermal method based on the reaction between tin foil, NaOH and KBrO₃. Hexagonal SnO₂ nanosheets were synthesized by hydrothermal process using ethanol/ water solution [13]. Flower-like zinc-doped SnO₂ nanocrystals have been prepared by a simple hydrothermal process [14]. In addition, SnO₂ has been synthesized by template-free methods [15]. An in-depth study on the production methods and the morphological characteristics of the produced SnO₂

[2–15] indicates that there is a huge tendency toward finding newcost-effective and straight-forward methods for production of these particles.

In the research presented in this article, hydrogel thermal decomposition method (HTDM) is used for production of SnO₂ nano-particles. The strategy is the application of starch-graft-poly (acrylic acid) acting as an economical and available effective capping agent. Starch-graft-poly (acrylic acid) with hydroxyl and carboxyl functional groups has a certain binding affinity to metal ions, which may control the size and morphology of SnO₂ nano-particles without any agglomeration. The feasibility of synthesizing these nanoparticles by HTDM has been verified using XRD.

METHODS OF SAMPLE MANUFACTURING AND ANALYSIS

0.50 g starch, purchased from Merck Chemical Co., was dissolved in 35 ml distilled degassed water. The three-neck reactor was placed in a water bath at 70 C. 0.05 g of potassium persulfate (KPS, Merck) as an initiator was added to starch solution and was allowed to stir for 10 min at 70 C. 0.3 g acrylic acid (AA, Merck) and methylenebisacrylamide (MBA, Fluka) solution (0.050 g in 5 ml H₂O) were added simultaneously to the starch solution. After addition of monomers, the mixture was continuously stirred (at 200 rpm) for 1 h under argon atmosphere. After 60 min, the reaction product was cooled down to room temperature and neutralized to pH = 8 by addition of 1 N NaOH solution. 500 ml ethanol was added to the gelled product while stirring. After complete dewatering for 24 h, the hardened gel particles were filtered, washed with fresh ethanol and dried at 50°C. A tea bag, i.e., a 100 mesh nylon screen containing 0.1 ± 0.0001 g hydrogel powder was immersed entirely in tin chloride solutions (2000 ppm) and allowed to soak for 48 h at room temperature.

The tea bag was hung up for 15 min in order to remove the excess fluid. A 2000 ppm tin chloride solution was prepared in Erlenmeyer flasks. 0.1 ± 0.0001 g of chelating hydrogel was added to flask. The mixture was shaken for 48 h by a rotary shaker to complete the equilibrium state of reaction. Production line of SnO₂ nano-particles has been schematically shown in *Figure 1*. SnO₂ nano-particles were produced by the following typical synthetic procedure. 0.2 g SnCl₂ and 0.5 g starch-graft-poly(acrylic acid) hydrogel were suspended in 100 ml water.

The suspension was stirred at room temperature for 48 h. The decantation and freeze drying of the white suspension yielded white powder which was heated at 400 C for 8 h. The final product was washed with water and hexane. X-ray diffraction (XRD) was performed with a Siemens D5000 X-ray diffractometer using graphite-mono-chromatized high-intensity Cu-K α radiation ($\lambda = 0.15406$ nm).

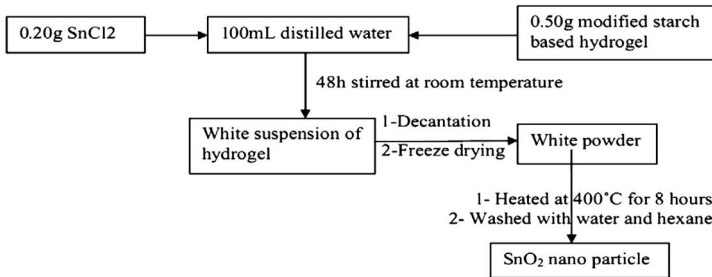


Fig. 1– Schematic presentation of the production procedure of SnO₂ nano-particles.

RESULTS AND DISCUSSION

The produced SnO₂ nano-particles were investigated by visual observations for the possibility of agglomeration and by X-ray diffraction method for checking purity and the size range of the nano-particles. Visual observations of the produced SnO₂ nanoparticles demonstrated that by HTDM there is very little tendency for agglomeration. This can be counted as an advantage of the HTDM method for production of SnO₂ nano-particles.

XRD patterns of the produced SnO₂ nano-particles are shown in *Figure. 2*. It is clear that no obvious reflection peaks from the impurities, i.e., other tin oxides, are detected. This indicates that the HTDM results in a product with high purity which yields an effective procedure for synthesis of pure SnO₂ nano-particles. The Miller indices are indicated on each diffraction peak. The diffraction peaks of the (110), (101), (200), (211), (220), (002), (310), (112), and (301) planes can be readily indexed to the tetragonal structure of SnO₂ with lattice constants of $a = 4.738 \text{ \AA}$ and $c = 3.187 \text{ \AA}$ (JCPDS File No. 41-1445).

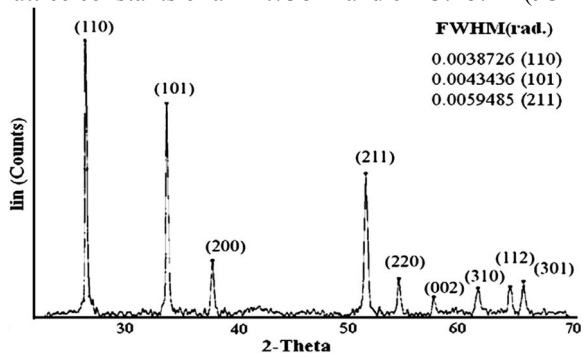


Fig. 2– XRD patterns of the SnO₂ nano-particles

The mean particle size was calculated for the SnO₂ nano-particles using the Scherer's equation, Eq. (1), from the reflections with (110), (101) and (211) indices

$$D = \frac{k\lambda}{\beta \cos \theta} \quad (1)$$

Where D is the mean size of particle (nm), k , a constant (0.89), λ , the X-ray wavelength (0.15405 nm), β , the full-width at half-maximum (FWHM radian) of XRD peaks and θ , the Bragg's angle (deg).

The mean size of nano-particles was calculated in the range of 25 to 36 nm. This value was in good agreement with TEM observation of the SnO₂ nano-particles. This indicates that production of finer SnO₂ nano-particles with high purity is the significant advantage of synthesizing by HTDM. The results demonstrated that the presented hydrogel in this study may serve as a platform for production of tin oxide nano-particles. Low-priced reactants and green routes for synthesis are the advantages of polysaccharide based hydrogel as starting material for this method.

CONCLUSIONS

In this research, the feasibility of synthesizing SnO₂ nano-particles by HTDM was investigated. The sizes and purity of the nano-particles were investigated by X-ray diffraction method. It was found that the presented hydrogel in this study may serve as a platform for production of tin oxide nano-particles. According to the results of the current investigation the following conclusions were made:

1. – Production of high purity SnO₂ nano-particles with a size range of 25–36 nm is possible by application of the HTDM method. Low priced reactants and green routes for synthesis are the advantages of polysaccharide based hydrogel as starting material for this method.

2. – There is very little tendency for agglomeration in the SnO₂ nanoparticles produced by HTDM. This can be considered as an advantage for this method over many other methods for production of these particles.

REFERENCES

- [1] T. Sahn, W. Rong, N. Barsan, et al. *Sens. and Actuat. B*, 2007, 127:63–8.
- [2] N.N. Samotaev, A.A. Vasiliev, B.I. Podlepetsky, A.V. Sokolov, A.V. Pisiakov. *Sens. and Actuat., B*, 2007, 127:242–7.
- [3] H. Wang, J. Liang, H. Fan, et al. *J. Solid State Chem.*, 2008, 181:122–9.
- [4] Z.R. Dai, Z.W. Pan, Z.L. Wang. *Solid State Commun.*, 2001, 118:351–4.
- [5] W.Z. Wang, J.Z. Niu, L. Ao. *J Cryst Growth*, 2008, 310:351–5.
- [6] T. Krishnakumar, N.K. Pinna, P. Kumari et al.. *Mater Lett.*, 2008, 62:3437–40.
- [7] E.R. Leite, I.T. Weber, E. Longo, J.A. Varela. *Adv Mater.*, 2000, 12:965–8.
- [8] C. Nayral, T. Ould-Ely, A. Maisonnat et al. *Adv. Mater.*, 1999, 11:61–3.
- [9] J.P. Ge, J. Wang, H.X. Zhang, X. Wang, Q. Peng, Y.D. Li. *Sens. and Actuat. B*, 2006, 113:937–43.
- [10] W.W. Wang, Y.J. Zhu, L.X. Yang. *Adv. Funct. Mater.*, 2007, 17:59–64.
- [11] Z.R. Dai, Z.W. Pan, Z.L. Wang. *J. Am. Chem. Soc.*, 2002, 124:8673–80.
- [12] Q.R. Zhao, Z.Q. Li, C.Z. Wu, B. Xue, Y.J. Xie. *Nanopart. Res.*, 2006, 8:1065–9.
- [13] X.H. Yang, L.L. Wang. *Mater. Lett.*, 2007, 61:3705–7.
- [14] Z.R. Li, X.L. Li, X.X. Zhang, Y.T. Qian. *J. Cryst. Growth.*, 2006, 291:258–61.
- [15] Y. Li, Y. Guo, R. Tan, P. Cui, Y. Li, W. Song. *Mater. Lett.*, 2009, 63:2085–8.

MICROBIAL SYNTHESIS OF SILVER NANOPARTICLES BY STREPTOMYCES GLAUCUS AND SPIRULINA PLATENSIS

Nelly Ya. Tsibakhashvili^{1,2}, Elena I. Kirkesali¹, Dodo T. Pataraya³,
Manana A. Gurielidze³, Tamaz L. Kalabegishvili^{1,2}, David N. Gvarjaladze²,
Giorgi I. Tsertsvadze⁴, Marina V. Frontasyeva⁵, Inga I. Zinicovscaia^{5*},
Maxim S. Wakstein⁶, Sergey N. Khakhanov⁷, Natalya V. Shvindina⁷,
Vladimir Ya. Shklover⁷

1 Andronikashvili Institute of Physics, 6, Tamarashvili Str., Tbilisi, 0177, Georgia

2 Iliia State University, 3/5, K. Cholokashvili Ave., Tbilisi 0162, Georgia

3 Durmishidze Institute of Biochemistry and Biotechnology, D. Agmashenebeli Kheivani, 10 km, 0159, Tbilisi, Georgia

4 Georgian Technical University, 77, Kostava Str., Tbilisi 0175, Georgia

5 Joint Institute for Nuclear Research, Joliot-Curie Str., 6, 1419890 Dubna, Russia

6 Scientific and Technological Research Center "Nanotech-Dubna", 141980 Dubna, Russia

7 Systems for Microscopy and Analysis, Application Laboratory Department, Leninsky av., 59-2, 119333 Moscow, Russia

ABSTRACT

Microbial synthesis of nanoparticles has a potential to develop simple, cost-effective and eco-friendly methods for production of technologically important materials. In this study, for the first time a novel actinomycete strain *Streptomyces glaucus* 71 MD isolated from a soy rhizosphere in Georgia is for the first time extensively characterized and utilized for the synthesis of silver nanoparticles. Scanning Electron Microscope (SEM) allowed observing extracellular synthesis of nanoparticles, which has many advantages from the point of view of applications. Production of silver nanoparticles proceeded extracellularly with the participation of another microorganism, blue-green microalgae *Spirulina platensis* (*S. platensis*). In this study it is shown that the production rate of the nanoparticles depends not only on the initial concentration of AgNO_3 but also varies with time in a nonmonotonic way. SEM study of silver nanoparticles remaining on the surface of microalgae revealed that after 1 day of exposure to 1 mM AgNO_3 nanoparticles were arranged as long aggregates along *S. platensis* cells strongly damaged by silver ions. However, after 5 days of exposure to silver *S. platensis* cells looked completely recovered and the nanoparticles were distributed more uniformly on the surface of the cells.

Key words: silver, nanoparticles, *Spirulina platensis*, *Streptomyces glaucus* 71 MD, scanning electron microscope

INTRODUCTION

Silver nanoparticles have a great number of applications, e.g. in nonlinear optics, spectrally selective coating for solar energy absorption, biolabelling,

intercalation materials for electrical batteries, high-sensitivity biomolecular detection and diagnostics, antimicrobials and therapeutics, catalysis and micro-electronics.

Various microorganisms (bacteria, yeast, fungi) are known to synthesize silver nanoparticles. The produced nanoparticles have different size and shape. Nanoparticles resulting from some microbial processes are composite materials and consist of inorganic component and special organic matrix (proteins, lipids, or polysaccharides) and they have unique chemical and physical properties different from the properties of conventionally produced nanoparticles and of other microorganisms even when they are incubated in the same medium under the same conditions.

The ability of *Streptomyces glaucus* 71MD, a novel strain of actinomycetes isolated in Georgia, and microalga *S. platensis* to produce silver nanoparticles was studied

METHODS OF SAMPLE MANUFACTURING AND ANALYSIS

Cultivation of Streptomyces glaucus 71MD

Cells were grown aerobically at pH 7–8, 28–30 °C in 500 ml Erlenmeyer flasks. The cells were grown in a liquid medium Gauze-1 [1]: K₂HPO₄ (0.05 %), MgSO₄ (0.05 %), NaCl (0.05 %), KNO₃ (0.1 %), FeSO₄ × 7H₂O (0.001 %), starch (2 %), yeast extract (0.03 %), pH 7.5. The culture was grown with continuous shaking on a shaker (200 rpm) at 30 °C for 9 days. After cultivation, mycelia (cells) were separated from the culture broth by centrifugation (4500 rpm) for 20 min and then the mycelia were washed thrice with sterile distilled water under sterile conditions. The harvested mycelial mass (16 g of wet mycelia) was then resuspended in 100 ml of 10⁻³ M aqueous AgNO₃ solution in 500 ml Erlenmeyer flasks. The whole mixture was put into a shaker at 30 °C (200 rpm).

Cultivation of S. platensis

Cells were cultivated in Zarrouk growth media at constant shaking at 30–31 °C, pH 9 [2]. The bacterial cells were harvested after 5–6 days and then were washed twice in distilled water. Then 1 g of wet biomass was placed in a 250-ml Erlenmeyer flask with 100 ml 10⁻³ M aqueous AgNO₃ and incubated at room temperature for different time intervals (1–5 days). The pH was checked during the course of reaction and it was found to be 5.6.

UV-vis Spectrometry

The UV-vis spectra of the samples were recorded on a “Cintra 10e” spectrophotometer (GBC Scientific Equipment Pty Ltd, Australia, wavelength range 190–1100 nm).

Scanning Electron Microscope

SEM was carried out using the SDB (small dual-beam) FEI Quanta 3D FEG with the EDAX Genesis EDX system with the resolution 1.2 nm. Opera-

tional features of the microscope used in the experiment: magnification 5000 – 150000x; voltage 1–30 kV.

RESULTS AND DISCUSSION

1) Synthesis of silver nanoparticles by a novel actinomycetes strain *Streptomyces glaucus* 71MD

Addition of actinomycetes biomass to a silver nitrate solution led to the appearance of yellowish brown color in the solution after a few days, indicating formation of silver nanoparticles. First, the UV-visible spectroscopy method was used to quantify this process (*Fig. 1*).

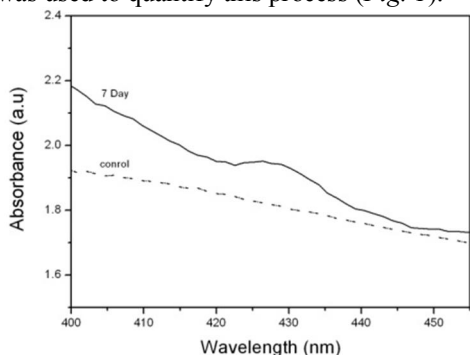


Fig. 1–UV-Vis spectra recorded after one week for the reaction mixture prepared using 1mM silver nitrate and 1 g biomass of *Streptomyces glaucus* 71MD

The cells of *Streptomyces glaucus* 71 MD were imaged by the SEM method after the reaction with the silver nitrate solution for one week. The SEM images (*Fig. 2*) illustrate that most of the particles are spherical-like and do not create big agglomerates.

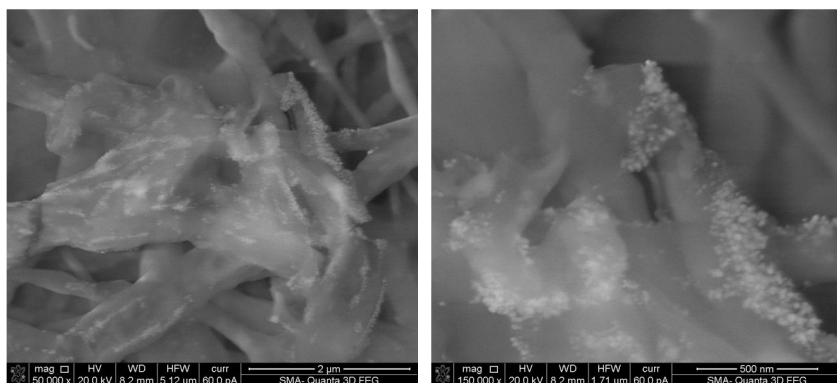


Fig. 2–SEM of *Streptomyces glaucus* 71MD cells with silver nanoparticles

EDAX (Energy dispersive analysis of X-rays) spectra also prove the presence of silver in *Streptomyces glaucus* 71 MD. The particle sizes range from 4 nm to 25 nm with an average of 13 nm.

1) Synthesis of silver nanoparticles by *S. platensis*

Synthesis of silver nanoparticles by *S. platensis* under different experimental conditions was investigated.

The size and the distribution of the silver nanoparticles depend on the time of silver action. After one day of the silver ion action, large agglomerates of nanoparticles could be observed. The mean size of the nanoparticles observed in these agglomerates is about 27 nm (Fig. 3).

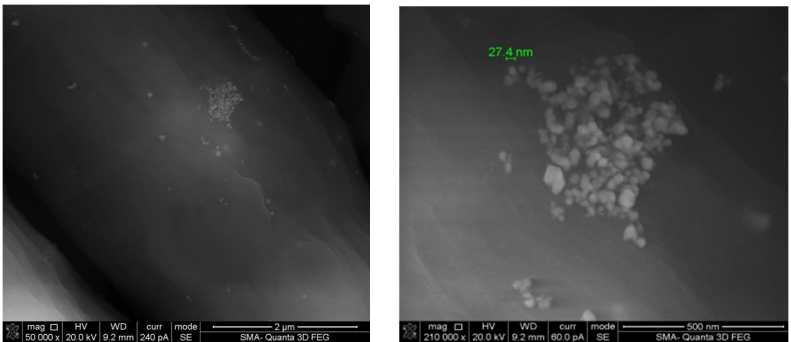


Fig. 3– SEM of *Sp. platensis* cells at different magnifications at 1 mM AgNO_3 for 1 day

After immersion of *S. platensis* cells in the silver nitrate solution for 5 days, the produced silver nanoparticles are relatively uniformly distributed along the surface of the cyanobacterium cells. In this case, the maximum size of the formed agglomerates is about 235 nm and the minimum size is 75 nm (Fig. 4).

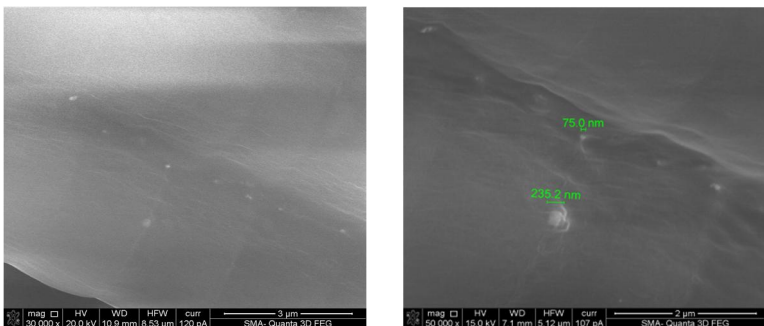


Fig. 4– SEM of *Sp. platensis* cells at different magnifications at 1 mM AgNO_3 for 5 days

CONCLUSIONS

(a) Actinomycetes *Streptomyces glaucus* 71 MD produces silver nanoparticles extracellularly which offers a great advantage over an intracellular process of synthesis from the point of view of applications.

(b) Production of silver nanoparticles proceeded extracellularly by blue-green microalgae *Spirulina platensis*; however, process depends on the experimental conditions

REFERENCES

- [1] D.T. Pataraya, M.A. Gurielidze, T.A. Berishvili et al. *Annals of Agrarian Science*, 2009, 7(2), P. 70-74
- [2] P. Mukherjee, M. Roy, P.B. Mandal, et al., *Nanotechnology*, 2008, 19: 75103, DOI: 10.1088/0957-4484/19/7/075103

NUCLEAR AND RELATED ANALYTICAL TECHNIQUES FOR BIO-NANO-TECHNOLOGY

Frontasyeva Marina.V.*

Frank Laboratory of Neutron Physics, Joint Institute for Nuclear Research,
str. Joliot-Curie, 6, 141980 Dubna, Moscow Region, Russian Federation

ABSTRACT

Some results from applying nuclear and related analytical techniques in medical, environmental and industrial biotechnologies are presented. In the biomedical experiments biomass from the blue-green alga *Spirulina platensis* (*S. platensis*) has been used as a matrix for the development of pharmaceutical substances containing such essential trace elements as selenium, chromium and iodine. The feasibility of target-oriented introduction of these elements into *S. platensis* biocomplexes retaining its protein composition and natural beneficial properties was shown. The negative influence of mercury on growth dynamics of *S. platensis* was observed. Detoxification of Cr and Hg by *Arthrobacter globiformis* 151B was demonstrated. Microbial synthesis of technologically important silver nanoparticles by the novel actinomycete strain *Streptomyces glaucus* 71 MD and *S. platensis* was characterized by a combined use of scanning electron microscopy (SEM) and epithermal neutron activation analysis (ENAA).

Key words: biotechnology, nanotechnology, ENAA, SEM, *Spirulina platensis*, *Arthrobacter globiformis* 151B, *Streptomyces glaucus* 71 MD

INTRODUCTION

Investigation in the field of biotechnology by using various microorganisms is one of actual trends in life sciences and industry. Owing to their small size, relatively simple morphology, and reproduction modes, microorganisms can be easily cultivated under laboratory conditions by microbiological methods in artificial mineral or organic solid or liquid nutrient media.

Neutron activation analysis with epithermal neutrons (ENAA) was used as a well-proven analytical technique for the determination of elemental composition of biological objects. Due to activation with resonance neutrons, the technique makes it possible to minimize matrix effects of biological samples and at the same time to determine concentrations of over 40 major, minor and trace elements. Biochemical investigations for substantiation of the experimental technique were carried out at the Andronikashvili Institute of Physics (Tbilisi, Georgia). Analytical research was conducted at the IBR-2 pulsed fast reactor of the FLNP JINR (Dubna, Russia). Using ENAA, significant results were ob-

* e-mail: marina@nf.jinr.ru, tel: +7(49621)65609, fax: +7(49621)65085

tained in the following three directions – medical biotechnology [1], environmental biotechnology [2–4] and industrial biotechnology [5]. The fourth promising direction of ENAA application in nano-biotechnologies using microorganisms is under development [6]. These studies are reviewed in the given paper.

MEDICAL BIOTECHNOLOGY

The blue-green algae *S. platensis* is a living microorganism and in the process of cell cultivation it is capable to assimilate certain amounts of some essential microelements (Se, Cr, and I) from a nutrient medium and to incorporate them into the composition of its biological macromolecules.

The analytical control of accumulation process makes it possible to establish a unique dependence between the element concentration in the nutrient medium and its content in the obtained *S. platensis* biomass. This dependence determined by means of ENAA serves as a basis for substantiation of biotechnology for the production of substances for pharmaceutical preparations with required doses of a given essential element.

Based on the results of ENAA, the curves of concentrations of elements in question in the obtained *S. platensis* substance *versus* concentrations of these elements in the nutrient medium were built. These curves served as the basis for biotechnology of cultivation of Se, Cr, I- containing biomass of *S. platensis* and they allow a precise choice of doses depending of the purposes these medications (therapeutic or prophylactic) are created for [1].

Methods for obtaining selenium and chromium-containing substances of spirulina are protected by patents of the Russian Federation. Visual microscopic observation of the state of culture, determination of total protein content in the biomass as well as investigation of its electrophoregrams revealed natural properties of the obtained Se-, Cr-, I-containing biomass.

ENVIRONMENTAL BIOTECHNOLOGY

Spirulina platensis as a sorbent of mercury. The possibility to use spirulina in remediation of sewage waters from toxic metal – mercury was studied by means of ENAA at the reactor IBR-2, FLNP JINR. The accumulation of metals in the cells of microorganisms goes at different rates. The binding time of a metal depends on the accumulation mechanism. If a metal is adsorbed on the cell surface, which is caused by ionic interaction, that does not depend on temperature and does not take energy, the process goes fast and takes from several seconds to an hour. The process of active transport of metals inside the cell goes more slowly and takes more than one hour. In the long-term experiments to study the Hg accumulation by the *S. platensis* cells the concentrations of Hg in nutrient medium loading by mercury glycinate constituted 100, 50, 5 $\mu\text{g Hg/L}$. Cultivation of the *S. platensis* cells was conducted for 6 days. Samples in all the series were taken every 24 hours.

The results of ENAA show the exponential character of the dependence of Hg concentrations in *S. platensis* biomass on time. Such character of dependence seems to be clear, as the number of *S. platensis* cells grows exponentially, the number of sites of Hg(II) ion binding surpasses considerably the number of Hg(II) ions in nutrient medium [2]. In the short-term experiments the Hg adsorption by *S. platensis* cells was studied. Concentration of nutrient medium loading of mercury glycinate was 500 $\mu\text{g Hg/L}$. Dynamics of the adsorption process, usually taking place during 1–2 hours, was observed during 1 hour.

Theoretical calculations of the adsorption isotherm on the basis of the obtained experimental data were performed in accordance with the Langmuir-Freundlich model, which takes into account both physical adsorption and chemisorption. Thus, at relatively low Hg concentrations (of the order of 100 $\mu\text{g/L}$) in the medium *S. platensis* can be used in the remediation of industrial and sewage waters from mercury.

Biotechnology of Cr(VI) and Hg(II) transformation. The mechanisms of toxic Cr(VI) transformation into non-toxic Cr(III) by Cr(VI)-reducer bacteria belonging to *Arthrobacter* genera isolated from the polluted basalts from the Republic of Georgia have been studied. In the experiments the dose-dependent formation of Cr(III) complexes and uptake of chromium by *Arthrobacter oxydans* – a gram-positive bacterium from these rocks were studied along with the testing under aerobic conditions of two bacterial strains of *Arthrobacter* genera [3]. ENAA in Dubna was used to track accumulation of chromium in the bacterial cells. To monitor and identify Cr(III) complexes in these bacteria, the electron spin resonance (ESR) spectrometry was employed. It was shown that the tested bacteria of *Arthrobacter genera* could efficiently detoxify high concentrations of Cr(VI). It was revealed that under aerobic conditions accumulation of chromium in bacteria is dose-dependent and its character is changing significantly at higher concentrations of Cr(VI). The chromium accumulation process fits well with the Langmuir-Freundlich model.

Several types of bacteria (*Arthrobacter* genera) can reduce of cationic mercury Hg(II) to the elemental state Hg(0). INAA was applied to study accumulation of Hg(II) in *A. globiformis* 151B and accumulation of Cr(VI) in bacterial cells in the presence of Hg(II) [4]. Experiments were carried out using the facilities of the 2 MW nuclear research reactor “Hoger Onderwijs Reactor” of the Reactor Institute Delft, Delft University of Technology, the Netherlands [4]. In experiments the ability of *A. globiformis* 151B to accumulate Hg(II) was investigated at different (50–5000 $\mu\text{g/L}$) Hg(II) concentrations. The strong accumulation of mercury by bacteria suggests that this undesirable element might be removed from the environment by bacterial trapping and sequestration. Addition of Hg(II) to *A. globiformis* 151B cells enhanced significantly the accumulation and toxicity of other heavy metals, namely Cr(VI) in our case.

INDUSTRIAL BIOTECHNOLOGY

An attempt to study the technological process of bacterial leaching of a wide range of rare and scattered elements contained at low concentrations in lean ores, rocks and industrial wastes in Georgia was undertaken by instrumental epithermal neutron activation analysis at the IBR-2 reactor, FLNP JINR, Dubna. As the source of microorganisms the natural organic mass of vegetal origin – peat – was used. Abundance of peat bogs in West Georgia and thus the opportunity of obtaining a cheap source of microorganisms with their inherent optimal bacterial content predetermined our choice of peat as the natural source of microorganisms.

The study of behaviour of different elements during the bacterial leaching was conducted on the basis of neutron-activation analysis of 30 elements of initial and leached metals also.

The results of NAA showed that bacterial leaching may be used for extraction such elements as Au, Se, Rh, In, Cd, Ir, Ru, Hf, Ta, Zr, as well as the radioactive elements Sr, U, Th [5].

MICROBIAL SYNTHESIS OF NANOPARTICLES

In our study a novel strain of actinomycetes, *Streptomyces glaucus* 71MD, isolated in Georgia, was used to produce silver nanoparticles [6]. In addition, synthesis of silver nanoparticles by *S. platensis* was investigated.

Scanning electron microscopy (SEM), transmission electron microscopy (TEM) and energy-dispersive analysis of X-rays (EDAX) were used as the key techniques. According to our experiments, the tested actinomycete *Streptomyces glaucus* 71 MD produces silver nanoparticles extracellularly when acted upon by the silver nitrate solution (AgNO_3), which offers a great advantage over an intracellular process of synthesis from the point of view of applications. Production of silver nanoparticles proceeded extracellularly by blue-green microalgae *S. platensis*; however, in this study we have shown that this process depends on the experimental conditions. Specifically, it is different under the short-term and long-term silver action.

REFERENCES

- [1] Frontasyeva M.V. et al., Ecological Chemistry and Engineering, 2009, Vol. 16, P. 277-285.
- [2] Frontasyeva M.V. et al., Journal of Neutron Research, 2006, Vol. 14, P. 1-7.
- [3] Tsibakhshvili N. et al., Journal of Radioanalytical and Nuclear Chemistry, 2008, Vol. 278, P. 357-370.
- [4] Tsibakhshvili N. et al., Journal of Radioanalytical and Nuclear Chemistry, 2010, Vol. 286, P. 533–537.
- [5] Tsertsvadze L.A. et al., In: Frontasyeva MV, Perelygin VS, Vater P (eds) Radionuclides and Heavy Metals in Environment. Kluwer, NATO Science Series, Ser. IV. Earth and Environmental Sciences 5, 2001, P. 245-257.
- [6] Tsibakhshvili N et al., Advanced Science Letters, 2011 (in print)

OPTICAL MONITORING OF TECHNOLOGICAL PROCESSES FOR FABRICATION OF THIN-FILM NANOSTRUCTURES

Andrey Yu. Luk'yanov*, Petr V. Volkov, Alexandr V. Goryunov,
Vyacheslav M. Daniltsev, Dmitriy A. Pryakhin, Anatoliy D. Tertyshnik,
Oleg I. Khrykin, Vladimir I. Shashkin

Institute for Physics of Microstructures of the Russian Academy of Sciences,
GSP-105, Nizhny Novgorod, Russia

ABSTRACT

This work illustrates application of the unique fiber-optic instrumentation for in situ monitoring of several technological processes commonly used in fabrication of semiconducting thin-film nanostructures. This instrumentation is based on principles of flow-coherent tandem interferometry, which determines high sensitivity and precision in measuring basic technological parameters, such as thickness of forming layers, temperature and bending of the substrate. The probing wavelength $\lambda = 1.55 \mu\text{m}$ allows carrying out the measurements on majority of substrates for semiconductor technology: Si, SOI, GaAs, InP, GaP, Al_2O_3 , diamond, $\text{ZrO}_2\text{:Y}$. Monitoring of such processes as MOVPE, MBE and plasma etching in various set-ups was realized. The absolute resolution achieved in these experiments was limited only by calibration accuracy and corresponds to 1°C sensitivity of 0.01°C . The accuracy limit in estimating the thickness of layers during their growth is 2 nm.

Key words: in situ characterization, optical monitoring, thin films, plasma etching, MBE, MOVPE

INTRODUCTION

Modern technologies for manufacturing of micro- and nanostructures and devices demand absolute reproducibility at each stage. Besides, efforts are made to improve the production output within a single process. Therefore, presence of reliable instrumentation for in situ control of the technologically important parameters [1] is mandatory. For most processes (including film deposition, annealing or etching of the finished thin film structures), fundamental parameters are the substrate temperature and the rate of growth or etching. Up to now, the substrate temperature is routinely controlled by thermocouples or pyrometers. The accuracy of these methods is fairly low. For the first class, the lack is absence of a good, reproducible thermal contact, especially at reduced pressure. In the second case, uncertainty of irradiation sources and significant variation

* e-mail: luk@ipmras.ru, tel: (+7)8314385535

in optical properties of the objects themselves during experiment are disadvantages. Thus, accurate determination of both temperature and rate of the epitaxial growth of semiconductors in the processes of molecular-beam epitaxy (MBE), metalorganic vapor phase epitaxy (MOVPE) or plasma etching (PE) represents a very important and still challenging problem.

OPERATING PRINCIPLE

The proposed technique is based on the principle of low-coherent tandem interferometry (Fig. 1) [2, 3]. The instrumentation consists of a low-coherent source of light and two interferometers (delay lines) optically coupled via an optical fiber.

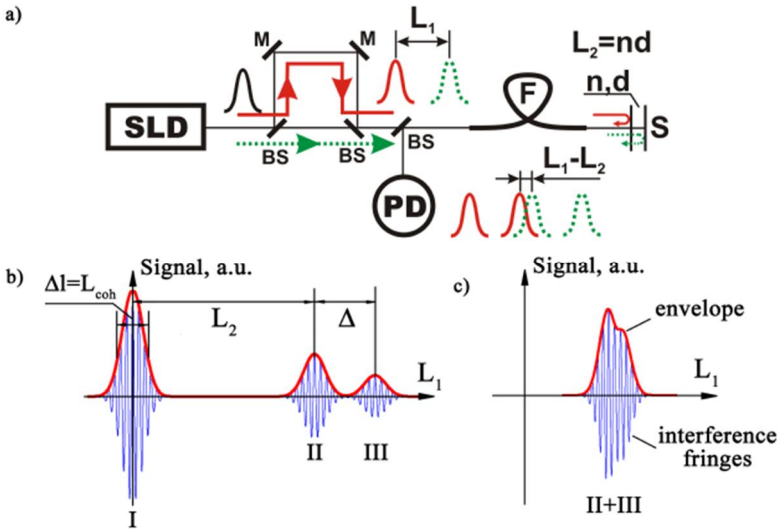


Fig. 1– Optical set up of the apparatus. SLD – a low coherent light source, PD – photodiode, F – optical fiber, BS – beam splitter, M – mirror, S – sample (wafer under test)

First delay line (reference) is placed in the measurement unit. Second delay line is essentially the wafer under testing and operates similarly to a Fabri-Perho interferometer. Two waves reflected from the front and rear surfaces of the wafer have a difference in the optical paths, which is equal to the doubled optical thickness of the wafer $L_2 = 2nD$. Hereinafter, n and D are the refractive index and the geometrical thickness of the wafer, correspondingly. Interference at the device output occurs if I) L_1 or $L_2 < L_{\text{coh}}$ and II) $\Delta L = |L_2 - L_1| < L_{\text{coh}}$. Here, L_1 and L_2 are differences of optical path lengths (delays) of the first and second interferometers, respectively, and L_{coh} is a coherence length of the light source.

Fig. 1b shows the signal at the device output during tuning the length of the first delay line. Peak #I at $L_1 = 0$ corresponds to the first condition. It is determined by the autocorrelation function of the light source. Peak #II at $L_1 = L_2$ corresponds to the second condition. This peak is determined by the cross-correlation function of reference delay line and the wafer. Peak #III appears in presence of an additional reflecting surface located near either surface of wafer (*e.g.*, unruffled surface of the susceptor). If the gap between this additional surface and the surface of wafer Δ meets the conditions $\Delta < L_{\text{coh}}$, then peaks #I and #II merge giving one peak with distorted shape (*Fig. 1c*). Similar distortions arise when additional layer with different refraction index is formed on the wafer surface. By taking this into account, absolute optical thickness of the wafer can be measured as a distance between positions of the envelope maximums of the Peaks #I and #II (measurements “along the envelope”). Similarly, value of the gap between wafer and susceptor is derived from the distance between Peaks #II and #III.

Position (phase) of interference fringes inside the Peak #2 is more sensitive to changes of the optical thickness and less sensitive to the form of the envelope curve. Therefore, recording of the phase shift of the interference fringes (measurements “along the phase”) is preferable for the measurements of minor relative changes in optical thickness.

Thus, we are now able to monitor both growth (etching) process and the temperature of objects using the same experimental set-up. In the latter case, dependence of optical thickness d on the temperature T is used. It may be written as follows: $d = n(T)D(T) = d_0(T_0)(1+f(T))$. Here, $d_0(T_0)$ is optical thickness measured at the known temperature T_0 , and $f(T)$ is a calibration curve.

For the InPsubstrates:

$$f_g(T) = 5 \times 10^{-8} T^2 + 8.1 \times 10^{-5} T - 8.6 \times 10^{-3} \text{ at } T_0 = 100^\circ \text{C} \quad (1)$$

$$f_{ph}(T) = 2.7 \times 10^{-8} T^2 + 5.9 \times 10^{-5} T - 6.2 \times 10^{-3} \text{ at } T_0 = 100^\circ \text{C} \quad (2)$$

Here and after $f_g(T)$ is the calibration curve for the phase velocity of the probe light and $f_{ph}(T)$ is the calibration curve for the group velocity of the probe light.

For the GaPsubstrates:

$$f_g(T) = 3.6 \times 10^{-8} T^2 + 4.9 \times 10^{-5} T - 5.2 \times 10^{-3} \text{ at } T_0 = 100^\circ \text{C} \quad (3)$$

$$f_{ph}(T) = 1.8 \times 10^{-8} T^2 + 4.8 \times 10^{-5} T - 4.9 \times 10^{-3} \text{ at } T_0 = 100^\circ \text{C} \quad (4)$$

For the GaAs substrates:

$$f_g(T) = 4.5 \times 10^{-8} T^2 + 9 \times 10^{-5} T - 9.4 \times 10^{-3} \text{ at } T_0 = 100^\circ \text{C} \quad (5)$$

$$f_{ph}(T) = 3.1 \times 10^{-8} T^2 + 7 \times 10^{-5} T - 7.3 \times 10^{-3} \text{ at } T_0 = 100^\circ \text{C} \quad (6)$$

For the diamond substrates:

$$f_g(T) = 3.9 \times 10^{-8} T^2 + 9.1 \times 10^{-7} T - 3.9 \times 10^{-4} \text{ at } T_0 = 100^\circ \text{C} \quad (7)$$

$$f_{ph}(T) = 2 \times 10^{-8} T^2 + 3.9 \times 10^{-6} T - 5.9 \times 10^{-3} \text{ at } T_0 = 100^\circ \text{C} \quad (8)$$

For the $\text{ZrO}_2\text{:Y}$ substrates:

$$f_g(T) = 1.8 \times 10^{-8} T^2 + 6.4 \times 10^{-6} T - 8.3 \times 10^{-4} \text{ at } T_0 = 100^\circ \text{C} \quad (9)$$

$$f_{ph}(T) = 5 \times 10^{-9} T^2 + 9.8 \times 10^{-6} T - 1 \times 10^{-3} \text{ at } T_0 = 100^\circ \text{C} \quad (10)$$

For the sapphire substrates в диапазоне температур 400 – 1400 K:

$$f_g(T) = 4.327 \times 10^{-9} T^2 + 1.451 \times 10^{-5} T - 1.494 \times 10^{-3} \text{ at } T_0 = 100^\circ \text{C} \quad (11)$$

$$f_{ph}(T) = 3.364 \times 10^{-9} T^2 + 1.543 \times 10^{-5} T - 1.577 \times 10^{-3} \text{ at } T_0 = 100^\circ \text{C} \quad (12)$$

For the Si substrates в диапазоне температур 300 – 800 K:

$$f_g(T) = 3.469 \times 10^{-8} T^2 + 6.6327 \times 10^{-5} T - 6.674 \times 10^{-3} \text{ at } T_0 = 100^\circ \text{C} \quad (13)$$

$$f_{ph}(T) = 2.117 \times 10^{-8} T^2 + 5.445 \times 10^{-5} T - 5.669 \times 10^{-3} \text{ at } T_0 = 100^\circ \text{C} \quad (14)$$

EXPERIMENTS

Experiments were done in several types of reactors. Growth of GaN based structures by MOVPE technique was performed in a home-made apparatus with a vertical-type reactor [4]. Plasma chemical etching of silicon-on-insulator (SOI) structures was carried out in a PlasmaLab 80 Plus reactor (Oxford Instruments). These reactors were equipped with an optical window positioned in front of the measured sample, which provides normal incidence of probing light on the sample. GaAs structures were grown using MOVPE technique in Epiquip VP502-RP with a horizontal-type reactor. Here, the input optical irradiation was implemented through the reactor wall perpendicular to the sample. Finally, growth of Si/Ge structures was carried out by means of MBE using a RIBER station. In this case, the probing light was shed on sample at the angle of 45° . To provide the input and output of the probing light in the same optical fiber, a mirror was installed into the reactor.

RESULTS AND DISCUSSION

Fig. 2 presents “finger print” of growth of a GaN film on sapphire wafer.

In the inset to Fig. 2a, formation of the seeding GaN layer with thickness of 100 nm at 550 °C is monitored for the first time (thickness variations “along the phase” are shown).

In Fig. 3, some results comparing the temperature of GaAs substrate in Epiquip reactor measured by a thermocouple and our instrumentation are given.

Fig. 4 displays therecordofplasmachemicaletchingofthethree-layered SOI structure (a 500 μm thickn-Sisubstrate, a 1 μm thick SiO₂l ayer, and 1.5 μmthickp-Si layer) usingareactiveBCl₃ – Armixture.

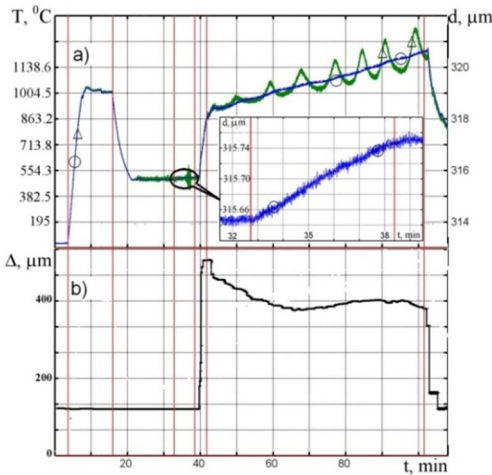


Fig. 2 – Growth of a GaN film on sapphire wafer. a) Changes in optical thickness along envelop (green line) and along phase (blue line). b) Changes in thickness of gap between susceptor plane and rear surface of wafer

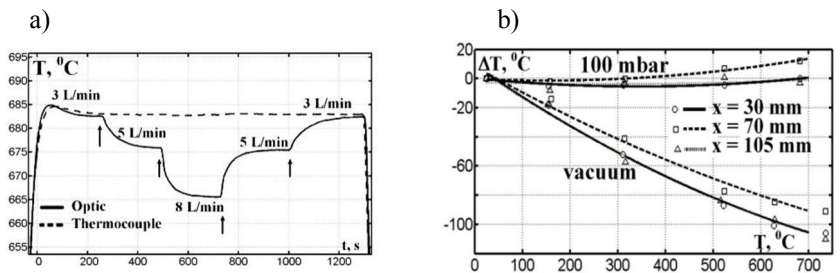


Fig. 3 – Comparison of the GaAs substrate temperature. a) Changes in substrate temperature due to changes flow of a carrier gas (H₂) were recorded by optics and not recorded by thermocouple. b) Difference in temperature measured by a thermocouple and our instrumentation (ΔT) on pressure in the chamber, as well as on the camera point (X = 0 is inlet of the chamber)

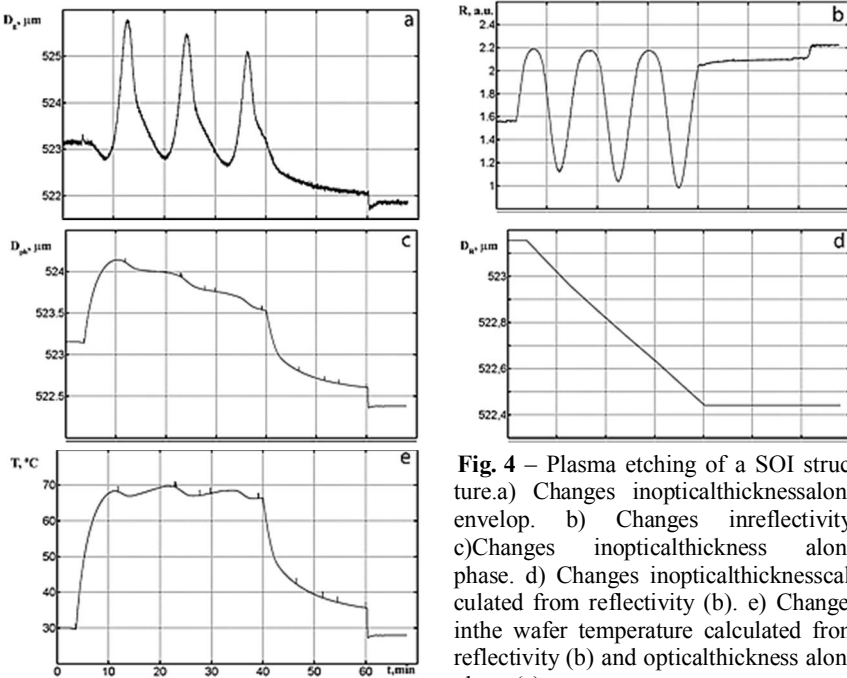


Fig. 4 – Plasma etching of a SOI structure. a) Changes in optical thickness along envelope. b) Changes in reflectivity. c) Changes in optical thickness along phase. d) Changes in optical thickness calculated from reflectivity (b). e) Changes in the wafer temperature calculated from reflectivity (b) and optical thickness along phase (c)

As seen from Figure 4a, estimation of thickness changes along the envelope seems difficult, since the observed oscillations have very complicated shape. However, in general the picture is similar to that observed when reflectivity factor (Fig. 4b) is registered: $I \sim \cos(kh + \varphi)$. Here φ is an additional phase shift that appears due to light interference in underlying layers, k is a wave number, and h is an optical thickness of the film.

In Figure 4a and 4c (changes “along phase”), the temperature induced jump of thickness during around 3600 seconds is seen, which is associated with rapid cooling of sample by incoming cold air from the room. As expected, reflectivity factor (Fig. 4b) is weakly affected by the temperature and depends exclusively on the layer thickness. In Figure 4d the changes in the layer thickness derived from variations of the reflectivity factor are plotted, whereas Figure 5e shows the changes in the substrate temperature that was calculated as difference between 4c and 4d. At that, the calibration data taken from Ref. [5] were used for converting of changes in optical thickness to the temperature.

CONCLUSIONS

By using the novel principles of the optical thickness registration for transparent wafers, we introduced high-accuracy instrumentation for in situ

optical monitoring of the real substrate temperature (the accuracy is equal to $\pm 1^\circ\text{C}$) and bending (the accuracy is limited by the roughness of the susceptor surface, here it is equal to $\pm 3\ \mu\text{m}$), as well as the thickness (the accuracy is equal to $\pm 2\ \text{nm}$) of the growing (etching) layers during MOVPE, MBE and plasma etching processes.

Serious disagreement ($10 - 100^\circ\text{C}$) between the readings of the thermocouple and the temperature measured by the proposed optical method was observed in all cases. This disagreement rises with increasing substrate temperature and gas flow, as well as with decreasing pressure in the MOVPE reactor. In MBE conditions, the discrepancy between the temperature values measured by a pyrometer and by our instrumentation was revealed. Disagreement rises with decreasing substrate temperature and with presence of hot parts inside the reactor. In plasma etching conditions, the temperature may rise up to 200°C depending on the conditions of discharge maintenance and on presence/absence of the stage cooling.

It was shown that changes of overall optical thickness of the structures due to changing temperature can be distinguished from variations in physical thickness of the layer. To do this, the changes of amplitude of zero interference peak caused by an alteration of the interference conditions inside of the layer with increasing (decreasing) thickness should be accounted for. As result, simultaneous determination of both temperature and thickness of the treated layers becomes possible.

Acknowledgements

This work was in part supported by RFBR grant #10-02-01193 and Federal Program "Scientific and pedagogical specialists of innovative Russia" (contracts № 16.740.11.0271 and № 14.740.11.0337).

REFERENCES

- [1] B. Schineller and M. Heuken, *Appl. Phys., A*, 2007, Vol. 87, P. 479.
- [2] Yu. Rao and D.A. Jackson, *Meas. Sci. Technol.*, 1996, Vol. 7, P. 981–999.
- [3] P.V. Volkov, A.V. Goryunov, and A.D. Tertyshnik, Patent RU 2307318.
- [4] P.V. Volkov, et al, *J. of Cryst. Growth*, 2008, Vol.310, P. 4724–4726.
- [5] P.V. Volkov, et al, *J. of Surf. Inv.*, 2008, Vol. 2, No. 4, P. 587–591.

PREPARATION NANO SIZED HMX BY USING ULTRASONIC WAVES

Yadollah Bayat¹, Seyed Hamed Mousavi^{1,2*}, Fatemeh Bayat²,
Gholamhossein Rastegar Nasab², Tahereh Gholamhosseini²

1 Faculty of Chemistry and Engineering Chemistry, Malek Ashtar University of Technology, 16765-3454, Tehran, Iran

2 Zakaria Razi Student Research Center, Rey City, 18735-677, Tehran, Iran

ABSTRACT

The researches done on particle size of explosive materials show that with reducing of particle size of explosive materials, reduced impact, friction and shock waves sensitivity. also by using of ultrafine explosive materials in propellant in comparison to larger particle size improved density, stability, calory and mechanical properties. Meanwhile the reduction of particle size of explosive materials influence on combustion mechanism of propellant and reduced burning rate and exponent pressure of different methods used for reduction of particle size, for example, milling, crystallization and etc. In this article for preparation of ultrafine HMX the method of solvent-anti solvent has been used by assistance of ultrasonic device. In optimum state the average size of particle is 106 nm and size distribution is narrow.

Key words: Sedimentary Crystallization, Ultrasonic, Reduce Particle Size, HMX

INTRODUCTION

By the development of explosive materials with improvement performance and the reduction of sensitivity to mechanical stimuli such as impact and friction is one of the important researches goals in energetic fields. With reducing particle size of explosive materials decrease crystal defects and inclusion. This will reduce the sensitivity of explosive materials. Therefore safety of materials increases during handelling, processing, warehousing, and transportation. There searches done on the role of superfine particles of explosive materials in propellant show that with reducing of particles size increase density, calory, stability, and mechanical properties. Also one of the most important affecting issues on burning rate of propellant is the particles size of explosive materials. By using these ultrafine explosive materials in the propellant, the burning rate and exponent pressure decrease [1]. Various methods used for the reduction of the particles size of materials that the selection methods depend materials and expected properties such as the particles size distribution. Two general methods used for the reduction of the particles size up to down method

* e-mail: mousavi.seyedhamed@gmail.com, tel: (+98)21333625

including mechanical methods (grinding) and down to up method, including crystallization method (sediment crystallization fusion, supercritical fluid, and etc . In the reduction of particles size in mechanical technique reduction of particles size in mechanical technique, solids construction elements have been broken by mechanical forces and increasing the mass distribution happens. To reduce the particles size with mechanical method used various equipment such as pinned disk mill, jet mill, colloid mill, ball mill, etc. . Mentioned methods have disadvantages such as static, electricity, pressure, and trituration that with considering the disadvantages, these methods are powerless and insecure to produce these ultrafine explosive materials [2-6]. Crystallization is the conversion of one or more material from liquid or gas state to crystalline state. This method used for modifying the physical properties of substance. In addition, the crystallization is a process for thickening pure material from solution, melt or gas phase one of the suitable methods for producing these ultrafine crystal of explosive materials is sedimentary crystallization method solvent-anti solvent . Because in method nucleation is high and high degree of saturation is seen. Although crystallization methods for preparing explosive materials have significant and advantages and crystals can grow slowly away from stress and obtain an ideal crystal. These methods have disadvantages such as [6-9]:

A: Sample should be soluble in one or more solvent solution and precipitate with reduction of temperature or increasing of anti-solvent.

B: Contaminate crystals to solvent and other solvate.

C: They spend too much energy.

D: Having lower yield (Because occurs in several stages)

A new method to produce ultrafine explosive is the kinetic spray crystallization that submicron size HMX and RDX are prepared with this method. The obtained particles size distribution with this method is very narrow. This schematic has been shown in *Fig.1* [10] Solvent/anti-solvent for spray solution by air into anti-solvent is used to produce ultrafine HMX The average of the obtained particles size with this method is 245 nm [1]. Also Mr. Lee and et al. by using sedimentary crystallization method have achieved HMX with an average particle size of 300 nm [11].

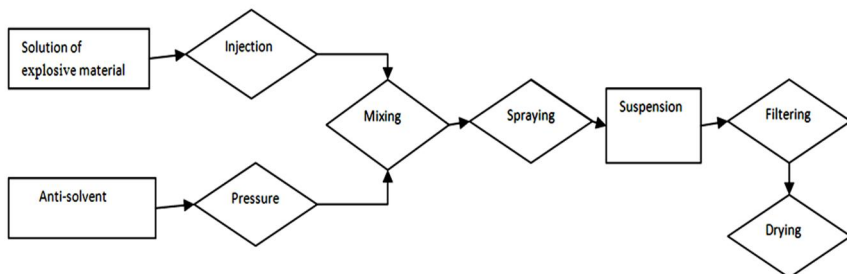


Fig. 1 – Principle of kinetic spray crystallizing method [10].

In this research solvent/anti-solvent method has been used for producing ultrafine HMX by the assistance of ultrasonic device. In this method for controlling the crystallization process, the ultrasonic energy is used. To create ultrasonic waves, piezoelectric converters are used. These converters converted electrical energy into mechanical vibration with the same frequency. Mechanism to reduce the particles size of solid and emulsions by ultrasonic waves is cavitation. Cavitation is used as the center of nucleation of new crystals and growing. Also producing bubbles and bursting them caused trituration and grinding of solid particles [12].

SAFETY

Generally by development of nanotechnology and producing nano particles in different scientific fields due to the specific nature of nano particles produced and creating risk for human health, Considering the work, safety during producing, transportation, warehousing, and applying of nano particles should be considered. Therefore at the same time by growing the technology in producing nano particles, safety problems and diseases have been considered. In Considering the risks of toxicity of nano material in three contact areas in human body with the environment can be mentioned: skin, respiratory system, lungs, digestive system (mouth-esophagus). These three elements are the entries for the nano particles in human body and from the way it can be entered in blood stream and internal systems and nervous. Of course it should be mentioned that the safety hints for producing nano explosive materials are not available. Therefore, the respiratory mask, gloves, and suitable ventilation system can be away to control damages [13].

EXPERIMENT

Equipment

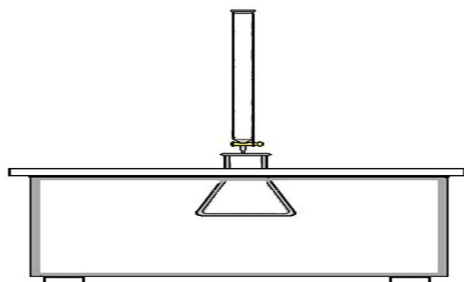


Fig. 2 – Installed Equipment

Procedure

In this method certain concentrations of HMX in acetone solvent prepared at room temperature (*Table 1*) and then by using of a burette of 0.5 cc are injected into an erlenmeyer flask containing anti-solvent (water) that its

Ultrasonic device used H80 model is made in Elma Company of Germany. To determine the morphology and particle size of electronic Microscope XL30 manufactured in Philips Company of Dutch has been used. Installed equipment for doing the experiment is shown in *Fig.2*.

temperature is zero degrees Celsius. Solvent injection rate is about 0.7 ml per minute. Ultrasonic frequency is 80 Hz and its power is 750 Watt.

Table 1 – Characteristic of produced samples

Sample name	Amount of HMX (gr.)	Solvent (acetone) (ml)	Anti-solvent(water)(ml)	Anti-solvent Temperature (centigrade degree)
Sample-1	0.1	5	80	0
Sample-2	0.1	10	80	0
Sample-3	0.1	20	80	0

RESULTS AND DISCUSSION

SEM image and the particles size distribution graph of sample respectively have been shown in *Fig. 3* and *Fig. 4*. Also SEM image and the particles size distribution graph of sample-2 in *Fig. 5*, *Fig. 6* and sample-3 in *Fig. 7*, *Fig. 8* have been shown respectively.

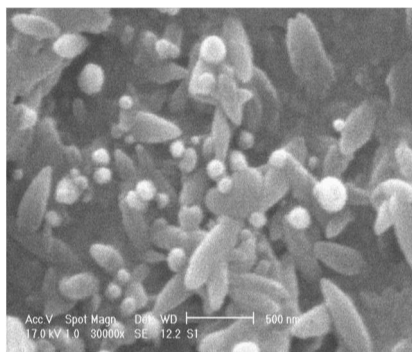


Fig. 3 – SEM image of sample -1

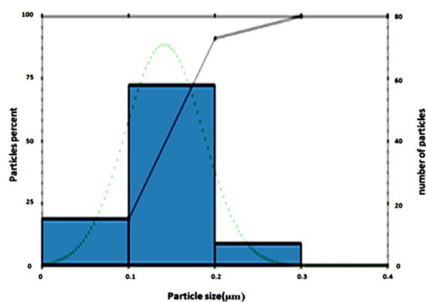


Fig. 4 – The particles size distribution by analysis of sample -1

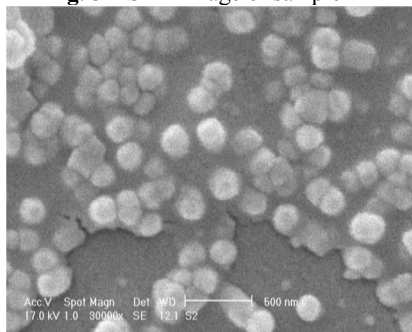


Fig. 5 – SEM image of sample -2

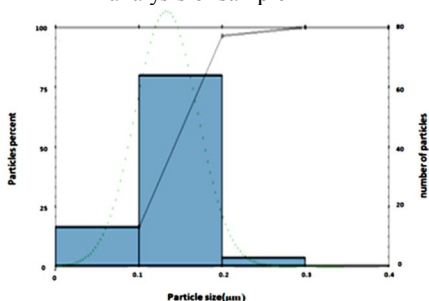


Fig. 6 – The particles size distribution by analysis of sample -2

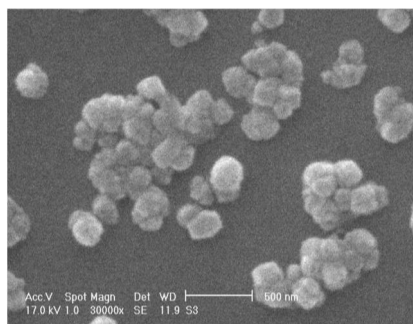


Fig. 7 – SEM image of sample -3

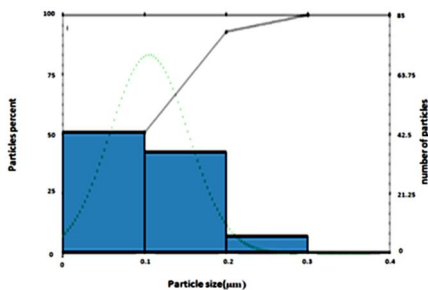


Fig. 8 – The particles size distribution by analysis of sample -3

According to the images and the particles size distribution graph, it is observed with reduction of concentration samples can be achieved to smaller particle size. The best particle size is related to sample -3 that have the lowest concentration among the prepared solutions. The obtained average particles size is 106 nm. The reason for the reduction of the particles size with reduction of concentration is expressed with the degree of relative supersaturated theories. In other words, with reduction of samples concentration increases the degree of relative super saturation. Consequently, nucleation rate is more than nuclei growth and obtained smaller particle size. The results about the obtained particles size have been shown in *Table 2*.

Table 2 – The analysis of particles size distribution

Sample name	Number of particles	Average of particles	Minimum of particles size	Maximum of particles size
Sample-1	80	0.0141	0.061	0.261
Sample-2	85	0.133	0.043	0.0210
Sample-3	85	0.106	0.037	0.0261

CONCLUSION

By the development of science in various fields application of nano materials has been expanded considerably. Among its applications can be mentioned to pharmaceuticals, explosive materials, and etc. Various methods such as grinding, crystallization and sol-gel are used for producing materials in nano scale. One of the most common methods for producing nano-size explosive is sedimentary crystallization or solvent/anti-solvent method. Ultrasonic method combining this method and it can be a good idea for producing materials in nano scale. In this method different factors can influence on the particles size and the particles size distribution production. One of these factors is the concentration of produced solution. Investigation results showed that by reduction of solution concentration can achieve to smaller particle. In

optimum state, the average of particle size was 106 nm. One of the most important factors for producing of the nano particles that should be considered is agglomeration of them that it has been a little reduced by using of ultrasonic. But research should be done to prevent agglomeration of nano-sized particles.

REFERENCES

- [1] S.H. Mousavi, M.sc. thesis, Malek Ashtar University of Technology, 2010, P. 82-86,
- [2] M.H. Prior, M. Rhodes, "Size reduction", Principles of Powder Technology, Wiley, Chichester, 1980, P. 227-297.
- [3] D. Eskin, H. Kalman, Chemical Engineering Technology, Vol. 25, No. 1, 2002, P. 57-64,
- [4] U. Teipel, Journal of Propellants, Explosives, Pyrotechnics, Vol. 24, 1999, P. 134-149.
- [5] S. Miranda, S. Yaegeer, Chemical Engineering, Vol. 11, No. 12, , 1998 P. 102-110.
- [6] R. Brooks, A.T. Horton, J.L Torgesen, Journal of Crystal Growth, 1968, P. 279-283.
- [7] W.H.M. Welland, Van Der Heijden, A.E.D.M., Cianfanelli, S., Batenburg, L.F., 43rd AIAA/ASME/SAE/ASEE Joint Propulsion Conference & Exhibit, 2007, P. 1-7.
- [8] W.H.M. Veltmans, A.E.D.M. Van Der Heijden, J.M. Bellerby, M.I. Rodgers, , "Nitroformate Product Characteristics", Proceedings 30th International Annual Conference of Fraunhofer-Institut fur Chemische Technologie(ICT), Karlsruhe, "The Effect of Different Crystalization Techniques on Morphology and Stability of HNF", Proceedings 31st International Annual Conference of Fraunhofer-Institut fur Chemische Technologie(ICT), Karlsruhe, 2000, P. 22.
- [9] A.E.D.M. Van Der Heijden, G.M. Van Rosmalen, D.T.J. Hurler, , Handbook of Crystal Growth, Elsevier, Amsterdam, 1994, Vol. 2, part A, P. 315.
- [10] Z. Shuhai, Z. Jinglin, W. Jingyu, Fraunhofer-Institut fur Chemische Technologie(ICT), 2004, P. 100-1 – 100-4.
- [11] K.Y. Lee, D.S. Moore, B.W. Asay, A. Llobet, Journal of Energetic Materials, Vol. 25, 2007, P. 161-171.
- [12] U. Teipel, I. Mikonsaari, Propellants, explosives, pyrotechnics, Vol. 27, 2002, P. 168-174.
- [13] Y. Bayat, H. Dehgani, N. Zekri, F. Abrishami, "Investigation and producing nano-size HMX in lab scale" Project report, Malek Ashtar University of Technology, 2005, P. 215-225.

SPECTROGRAPHS FOR ANALYZING NANOMATERIALS

Nadezhda K. Pavlycheva*, Mazen A. Hassan

A.N. Tupolev Kazan State Technical University, 10 K. Marks Str., Kazan, Russia

ABSTRACT

The optical schemes of high numerical aperture spectrographs based on concave holographic diffraction gratings are described. A calculations of an optical schemes using flat field spectrograph method for analyzing the fluorescence of all kinds of Quantum dots in a wide range of wavelengths with spectral resolution of 6,3 nm are submitted. A special calculation of spectrographs for investigating CdSe/ZnS, InP Quantum dots with high resolution of 1 nm are given because of their wide uses.

An experimental mounting for analyzing Raman scattering in carbon nanotubes is described. Experimental results are given. On the basis of these results the requirements for optical characteristics of a compact specialized spectrograph for analyzing Raman scattering in carbon nanotubes are developed. The calculation of an optical scheme using flat field spectrograph method with spectral resolution of 3.5 cm^{-1} is submitted.

Keywords: Quantum Dots, carbon nanotubes, fluorescence, Raman scattering, spectrograph, holographic diffraction gratings, an optical scheme, aberration.

INTRODUCTION

We calculated the various options for optical schemes spectrographs to study the two types of nanomaterials -quantum dots and carbon nanotubes.

Highly and long luminescent lifetime quantum dots (QDs) potentially can overcome the functional limitations encountered with chemical and organic dyes. They are highly stable against photobleaching and have narrow, symmetric emission spectra. In particular, the emission wavelength of QDs can be continuously tuned by changing the particle size or composition, and a single light source can be used for simultaneous excitation of all different coloured dots. In practice, by variation of size and composition of QDs, the luminescence photon energy can be tuned in steps of 30 nm from the IR to the UV. These novel remarkable spectral properties can render QDs ideal fluorophores for sensitive, multicolour, and multiplexing applications in molecular bioengineering, medicine, photonic studies, micro-electronics and optoelectrical devices [1, 2].

The most commonly used to study the carbon nanotubes (CNT) Raman scattering, because this method requires minimal sample preparation and is

* e-mail: pavlych@oes.kstu-kai.ru , tel. +7 843 238 41 10

quite informative[3]. To study the possibility of investigating CNT Raman scattering in the spectrograph low resolution, we also developed an experimental mounting to analyze the Raman scattering.

For analysis of the fluorescence spectra and Raman scattering, a high numerical aperture spectral instruments with low level detection and enough high resolution are required. To these conditions satisfy the optical schemes based on concave holographic diffraction gratings with aberration correction.

In this paper we represent calculations of different optical schemes intended for analyzing nanomaterials.

THE OPTICAL SCHEMES SPECTROGRAPHS FOR ANALYZING OF QUANTUM DOTS

The wavelength range of QDs fluorescence emission are given in *Table 1* [4].

Table 1. Emission wavelength range of some QDs

Material of QDs	Emission wavelength range, nm
ZnS	300-380
CdS	380-460
ZnSe	360-500
CdSe (CdSe/ZnS)	480-660
CdTe	600-1000
CdHgTe/ZnS	630-860
InP	650-750
InAs	830-1350
PbS	700-1600

Taking into account, that as the receiver of radiation in modern devices, mainly, multichannel photo-electric receivers (array) are used, as optical system we have chosen the flat-field spectrograph (*Fig. 1*).

1. An optical scheme with one grating

To built one spectrograph to investigate all kind of QDs fluorescence, we need to calculate the parameters of the optical scheme that can detect the fluorescence in a wide range of wavelengths from 300-1600 nm.

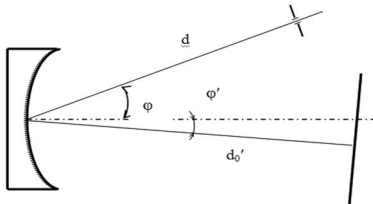


Fig. 1 - Optical scheme for a flat-field spectrograph

The parameters of the scheme are determined from relationships for “flat-field spectrograph” [5], which provide an aberration correction of coma, defocus and astigmatism. The spectrograph has the following parameters: the spectral range 300-1600 nm, grating curvature radius of 200 mm, ruled surface diameter of 50 mm, the groove

density of the grating 110 1/mm, the length of the spectra of 29 mm
 $d = 197.9$ mm, $d_0' = 197.842$ mm, $\varphi = 09^\circ 05' 23''$, $\varphi_{950} = - 03^\circ 03' 56''$.
 The recording parameters of the grating are:
 $d_1=200.075$ mm, $d_2= 202.007$ mm, $i_1=09^\circ 32' 28''$, $i_2= 06^\circ 43' 46''$.
 The aberrations are given in the *table 2*.

Table 2. Aberrations of the spectrograph with one grating

y	z	$\lambda = 300$ nm, $y' = -14,23$		$\lambda = 950$ nm, $y' = 0$		$\lambda = 1600$ nm, $y' = 14,18$	
		$\delta y'$	$\delta z'$	$\delta y'$	$\delta z'$	$\delta y'$	$\delta z'$
25	0	-0,077	0	0,040	0	-0,077	0
12,5	0	-0,04	0	0,020	0	-0,039	0
-12,5	0	0,039	0	-0,020	0	0,042	0
-25	0	0,074	0	-0,040	0	0,090	0
0	12,5	0,002	0,32	-0,001	0	-0,002	-0,32
0	25	0,008	0,64	-0,003	0	-0,007	-0,64

The instrumental function when we use entrance slit width of 0,1 mm do not exceed 0,14 mm. As the reciprocal linear dispersion is 45 nm/mm, we obtain a resolution of 6,3 nm. Taking into account that the bandwidth at half maximum of the fluorescence line is 20-25 nm at room temperature, we have a good resolution. Instrumental function for the three wavelengths (the center and the edges of the spectral range) is represented in *figure 2*.

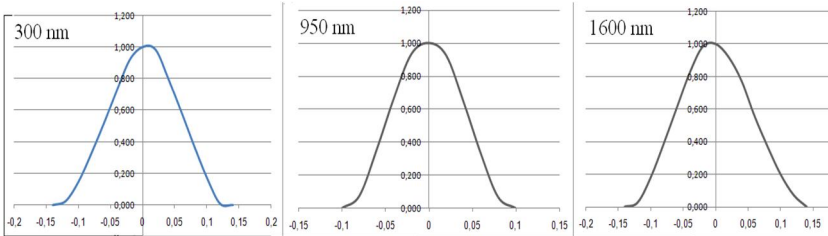


Fig. 2 - The instrumental function for three wavelengths

2. An optical scheme with two changeable gratings

To get a better resolution the spectral range is separated into two sub-ranges with two different gratings, but one optical scheme. First sub-range is 300-700 nm, it is for the ZnS, CdS, ZnSe, CdSe and CdSe/ZnS quantum dots. the second one is 600-1600 nm, it is for the CdTe, CdHgTe/ZnS, InP, InAs and PbS.

The parameters of the scheme are:

$d = 197.9$ mm, $d_0' = 197.977$ mm, $\varphi = 10^\circ 10' 05''$, $\varphi_{500,1100} = - 01^\circ 17' 29''$.

The first grating has a groove density of 308 1/mm, and the following recording parameters:

$$d_1=198,569 \text{ mm}, d_2= 202,14 \text{ mm}, i_1=10^\circ 05' 30'', i_2= 02^\circ 14' 50''.$$

The aberrations are given in the *table 3*.

Table 3. Aberrations of the spectrograph with changeable gratings – first grating

y	z	$\lambda = 300 \text{ nm},$ $y'=-12,23$		$\lambda = 500 \text{ nm},$ $y'= 0$		$\lambda = 700 \text{ nm},$ $y'= 12,12$	
		$\delta y'$	$\delta z'$	$\delta y'$	$\delta z'$	$\delta y'$	$\delta z'$
25	0	-0,0578	0	0,032	0	-0,072	0
12,5	0	-0,0309	0	0,016	0	-0,033	0
-12,5	0	0,0324	0	-0,016	0	0,031	0
-25	0	0,064	0	-0,032	0	0,061	0
0	12,5	-0,0013	0,2	0	0	0	-0,2
0	25	-0,0054	0,4	0,001	0	0,001	-0,4

The instrumental function when use entrance slit width of 0,1 mm do not exceed 0,1 mm, as the reciprocal linear dispersion is 14 nm/mm, we obtain a resolution of 1,4 nm.

The second grating has a groove density of 140 1/mm, and the following recording parameters:

$$d_1=199,91 \text{ mm}, d_2= 201,535 \text{ mm}, i_1=07^\circ 57' 59'', i_2= 04^\circ 24' 10''.$$

The aberrations are given in the *table 4*.

Table 4. Aberrations of the spectrograph with changeable gratings – second grating

$\square y$	z	$\lambda = 600 \text{ nm},$ $y'=-13,9\text{mm}$		$\lambda = 1100 \text{ nm},$ $y'= 0$		$\lambda = 1600 \text{ nm},$ $y'= 13,88\text{mm}$	
		$\delta y'$	$\delta z'$	$\delta y'$	$\delta z'$	$\delta y'$	$\delta z'$
25	0	-0,085	0	0,032	0	-0,096	0
12,5	0	-0,045	0	0,016	0	-0,048	0
-12,5	0	0,046	0	-0,016	0	0,044	0
-25	0	0,092	0	-0,032	0	0,088	0
0	12,5	-0,002	0,227	0	0	0	-0,228
0	25	-0,007	0,456	0	0	-0,001	-0,458

The instrumental function when use entrance slit width of 0,1mm do not exceed 0,1mm, as the reciprocal linear dispersion is 35 nm/mm, we obtain a resolution of 3,5 nm.

3. Special optical scheme with high resolution

For more resolution we carried out in special the calculation of the optical schemes for two types of QDs - CdSe/ZnS and InP, the most wide spread QDs.

The parameters of the scheme are determined from empirical relationships for "spectrograph with the extended spectral range" [5], providing a flat spectrum with astigmatism and meridional coma correction for two wavelengths located symmetrically relative to the spectrogram center and edges:

$$d = r(1,01056 - 0,0393k\lambda_m N),$$

$$d'_0 = r[1,0037 - 0,014k\lambda_m N + 0,058(k\lambda_m N)^2],$$

$$\varphi = -0,016 + 0,748k\lambda_m N.$$

k - order of diffraction, λ_m - middle wavelength of the spectral range.

The spectrograph for CdSe/ZnS has the following parameters: the spectral range 480-660 nm, grating curvature radius $r = 100$ mm, ruled surface diameter of 33 mm, the groove density of the grating 500 1/mm, the length of the specter of 9 mm, $d = 99,94$ mm, $d' = 100,44$ mm, $\varphi = 11^\circ 18'$, reciprocal linear dispersion of 20 nm/mm.

The spectrograph for InP has the following parameters: the spectral range 600-780 nm, grating curvature radius of 100 mm, ruled surface diameter of 33 mm, the groove density of the grating 500 1/mm, the length of the spectra of 9 mm, $d = 99,7$ mm, $d' = 100,58$ mm, $\varphi = 13^\circ 52'$, reverse linear dispersion of 20 nm/mm.

The recording parameters of the concave holographic diffraction gratings provide the aberration correction: bandwidth at half maximum of instrumental functions of the spectrographs for an input slit of 0,05 mm on all field does not exceed 0,05 mm and the astigmatic extension do not exceed 0,03 mm.

The calculations were performed for center entrance slit ($l = 0$). When $l = 1$ mm for an input slit of 0,05 mm on all field does not exceed 0,08 mm and the astigmatic extension do not exceed 0,08 mm for CdSe/ZnS and 0,03 mm for InP. Aberrations of the meridional and sagittal cross sections are practically identical, that allows to relate this schema to the imaging diffraction grating.

A similar method was used to calculate a spectrograph for investigating CdSe QDs. A ultra high resolution of 0.25 nm was obtained using a cylindrical lens to correct the residual aberration in front of the photo-detector [6].

THE OPTICAL SCHEME OF SPECTROGRAPH FOR ANALYZING RAMAN SCATTERING IN CARBON NANOTUBES

1. The experimental mounting

To determine the feasibility of developing a compact device on modern element base - compact diode lasers, holographic concave diffraction gratings, and diode arrays as detectors, established the experimental mounting based on the spectrograph Sirius [7]. The unit includes: a source of laser radiation, a collimator, short-throw lens aperture, the substrate to be coated test substance, a spherical mirror that collects the scattered radiation, and sends it to the entrance slit, Notch-filter aperture spectrograph. Spectrographs to study the Raman spec-

tra should be of great luminosity, low levels of ambient light and a large variance. The spectrograph Sirius meets these requirements: it has a relative aperture 1:3, its optical scheme is based on holographic diffraction gratings with correction of aberrations and has a minimal number of optical components. The studies were conducted with a diffraction grating 1153gr./mm, which provides a working spectral range 486-680 nm. The spectrograph is equipped with a multichannel recording system based on the spectrum of the diode line with the number of pixels 2048 and a pixel size of 1914 * 150 microns. To suppress the laser beam in front of the entrance slit set Notch-filter [8]. In the experiments, spectra were obtained by surface-enhanced Raman scattering (SERS) on silver substrate. *Figure 2* shows spectrum of carbon nanotubes obtained under the following conditions: laser power 200 mW at 532 nm with a Notch-filter, the relative aperture of 1:4, the width of the entrance slit of 50 microns.

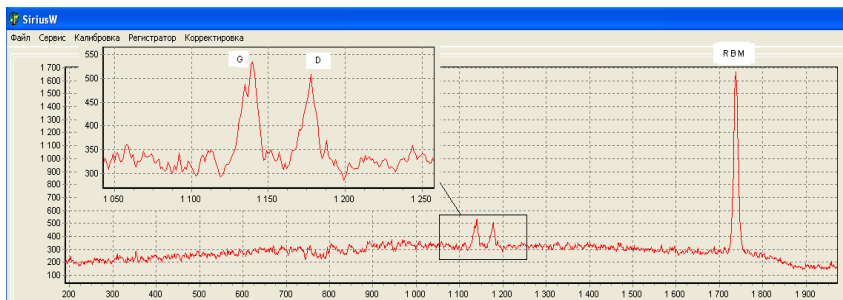


Fig. 2 – The spectrum of carbon nanotubes

Raman shift $\Delta \nu$ lines for RBM, D and G was 475 cm^{-1} , 1436 cm^{-1} and 1511 cm^{-1} , respectively.

2. The optical scheme of the spectrograph

Our experiments allowed to form the following requirements for the optical system of the spectrograph: the relative aperture of 1:4, the width of the entrance slit of 50 mm, the working spectral range of 536-622 nm, reciprocal linear dispersion of 3 nm / mm and a length range of 29 mm. In accordance with these requirements was designed optical layout according to the method of calculation of the spectrograph with a flat field.

To obtain a higher resolution before the receiver is a cylindrical concave-plane lens with a radius of curvature of 50 mm. The design parameters of the scheme with the lens have the following meanings: $d = 205 \text{ mm}$, $d_0' = 205,47 \text{ mm}$, $\varphi = 310 \text{ } 37' \text{ } 45''$, $\varphi'579 = -160 \text{ } 37' \text{ } 45''$, $N = 1400 \text{ gr./mm}$, and recording parameters of the grating: $d_1=488,048 \text{ mm}$, $d_2=211,145 \text{ mm}$, $i_1=720 \text{ } 39' \text{ } 34''$, $i_2 = 190 \text{ } 39' \text{ } 08''$. Instrumental function of the spectrograph across the field does

not exceed 0,035 mm, which corresponds to the spectral resolution of 0,1 nm or 3,5 cm⁻¹.

CONCLUSIONS

Thus, using the concave holographic diffraction gratings with aberration correction we can be created compact spectrographs with the high enough optical characteristics to investigate Quantum dots fluorescence and the Carbon nanotubes Raman scattering.

REFERENCES

- [1] Maureen A. Walling, Jennifer A. Novak and Jason R. E. Shepard. International journal of Molecular sciences, 2009, 10, 441-491.
- [2] Medintez I.L., Mattoussi H., Clapp R.A. International journal of nanomedicine, 2008, 3(2), 151-167.
- [3] Dresselhaus M.S. et al. Annu. Rev. Mater. Res. 2004. V.34. P.247-278.
- [4] Oleynikov V.A., et al. Rossisskaya nanoteghnologiya, 2007, 2, № 1-2.
- [5] Nazmeev M., Pavlycheva N. Optical Engineering, 1994, 33, 2777-2782.
- [6] Pavlycheva N., Hassan M. J. of optical technology, 2010, 77, 12, 3-5.
- [7] Pavlycheva N., Peplov A., Demin A. J. of optical technology, 2007, 74, 3, 29-32.
- [8] Pavlycheva N., Venderevskya I. G., Hassan M. International Conference on Applied Optics-2010 – S-Peterburg, 2010, P.191-194.

Synthesis, Characterization And Performance Study Of Phosphosilicate Gel-Sulfonated Poly (Ether Ether Ketone) Nanocomposite Membrane For Fuel Cell Application

Chandan Dhole¹, Aniket Nando¹, Kajari Kargupta¹, Saibal Ganguly²

1 Jadavpur University, 700032, Kolkata, West Bengal, India

2 University Teknologi Petronas, Perak Darul Ridzuan, 31750, Tronoh, Malaysia

ABSTRACT

Phosphosilicate gel – SPEEK (Sulfonated Poly Ether Ether Ketone) hybrid nanocomposite membranes are proposed for performance enhancement of polymer electrolyte fuel cell. The nanocomposite membranes are synthesized and characterized at 60 weight percent of inorganic loading. Phosphosilicate gel particles of varying size (sub micro to nanometer) are synthesized using sol gel approach followed by grinding using planetary ball mill for different time. Transmission Electron Microscopy (TEM) reveals less than 10 nm particle size for 20 hr grinding. Nanocomposite membrane having inorganic particles of size less than 10 nm exhibits higher values of proton conductivity, ion exchange capacity and water uptake compared to composite membrane comprising of larger (400 nm and above) inorganic particles. The membrane is assembled with the electrode in the unit cell and the polarization characteristics are measured at different operating temperatures. Performance study reveals that between 65 to 75 °C the membrane offers best performance in terms of peek power generation and of allowable load current. For the same conditions 40% nano-enhancement of peek power generation is achieved by reducing the average gel particle size from sub micro to less than 10 nm. At medium temperature (between 65 to 75°C) the nanocomposite membrane offers more than 75% enhancement of peek power generation compared to that generated by SPEEK membrane.

Key words: Organic-inorganic nanocomposite, Fuel cell, Phosphosilicate gel, SPEEK, Performance enhancement

INTRODUCTION

In the wake of the emerging market potential for fuel cell based energy generation using hydrogen as raw material, it becomes imperative to research upon the development of nanomaterials to improve its real-life performance.

The proton exchange membrane fuel cells (PEMFC) are today in the focus of interest as one of the most promising power generator for a wide range of applications in transportation and in portable electronics [1, 2]. These fuel cells convert the chemical energy of the fuel and oxidant into electrical energy releasing the balance as heat. The major material components are the proton conductive electrolyte membrane and the electrodes. The performance of PEMFC

is crucially dependent on the proton conductivity, ion exchange capacity and water uptake of the electrolyte membrane.

Inorganic–organic hybrid nanocomposite membranes generated substantial research interest due to their potential of having a wide range of physical, chemical, thermal and mechanical properties. The nanocomposite membranes comprising of nanosize inorganic phase/building block often demonstrate interesting properties due to nano scale of constituent phases, high interfacial area and synergetic properties [3]. The structural and physicochemical properties and hence the performance of such composite membranes depends on their composition, size of the inorganic particle, interfacial interactions etc. [4].

It has been reported in literature that sol-gel derived phosphosilicate gel has served as a very promising proton conductor with high proton conductivity in the low and medium temperature range, which is attributed to phosphoric acid and thermally stable inorganic silica networks [5]. Presence of phosphosilicate gel provides phosphoric acid functionalised, inorganic silica network electrolytes having solid pores for water to be absorbed. Pores having smaller diameters become filled with water even at lower humidity and act to form the pathways for proton transfer. The organic component, Poly (ether ether ketone) is a thermally stable and mechanically tough polymer. On sulfonation, the polymer becomes hydrophilic and ionically conductive. Due to these properties, SPEEK membranes find application as polymer electrolyte membrane in proton exchange membrane fuel cell (PEMFC).

The synthesis, characterization and performance of hybrid nanocomposite (phosphosilicate gel-SPEEK) membrane for the application in fuel cells has hardly been explored in literature. The present paper describes the experimental synthesis, characterization and performance studies for the novel hybrid nanocomposite membranes. The enhancement of performance of proton exchange membrane fuel cells, as demonstrated in this publication, highlights the promising potential for their commercial exploitation.

METHODS OF SAMPLE MANUFACTURING AND ANALYSIS

Synthesis of phosphosilicate gel nano particle:

The phosphosilicate gel was prepared by sol-gel process [6] using tetraethoxysilane and ortho phosphoric acid at a molar ratio of P/Si = 1.5. Tetraethoxysilane (TEOS) was diluted with ethanol (EtOH) and hydrolyzed with water (H₂O) containing HCl with stirring at room temperature for 10-15 min. An appropriate amount of ortho-phosphoric acid was added drop by drop under constant stirring. After stirring for another 50-60 min, a homogeneous gel was formed. The mole ratio of TEOS:EtOH:H₂O:HCl:H₃PO₄ was fixed as 1:4:4:0.01:1.5. The gel formed was further dried at 80⁰C for 24 h. The dried gels, which were pulverized into powders with an agate mortar and a pestle, were heat treated in muffle furnace at high temperatures of 150-600⁰C for 6-7

h. The dried gel powders were further ground into fine powders using a planetary ball mill. Grinding time is varied from 8 hrs to 20 hrs to obtain sub-micro to nanometer sized particles, respectively.

Synthesis of phosphosilicate gel –SPEEK nano composite membrane by precursor method:

Poly(ether ether ketone) was first sulfonated. 15 wt% SPEEK (Sulfonated Poly ether ether ketone) was dissolved in DMAc (N,N Dimethyl Acetamide) using magnetic stirrer, and subsequently it was mixed with finely ground phosphosilicate gel powder. After dissolving the polymer in solution, appropriate amount of gel powder was mixed. It was stirred periodically using a magnetic stirrer and an ultra-sonicator until the gel powder became completely miscible. The obtained slurry was then cast on transparent sheet and was dried under ambient condition until it became fully dried. Subsequently, it was then peeled off from the sheet. Membranes were casted for 80 % inorganic weight loading for different average particle size varying from sub-micrometer to nanometer scale.

Characterization

Structural characterization of the phosphosilicate gel particles were done by TEM analysis. The surface morphology of the membrane was obtained using SEM analysis of the composite membrane.

Proton Conductivities of the composite membranes were determined by impedance data taken at different constant temperatures. Potentiostat (AUTOLAB PGSTAT 302 n manufactured by Ecochemie, BV, Netherland) was used to obtain the impedance data in a frequency range of 100 KHZ to 1MHZ. Ion exchange capacity and water uptake of the membrane were recorded at room temperature.

Performance Study of fuel cell

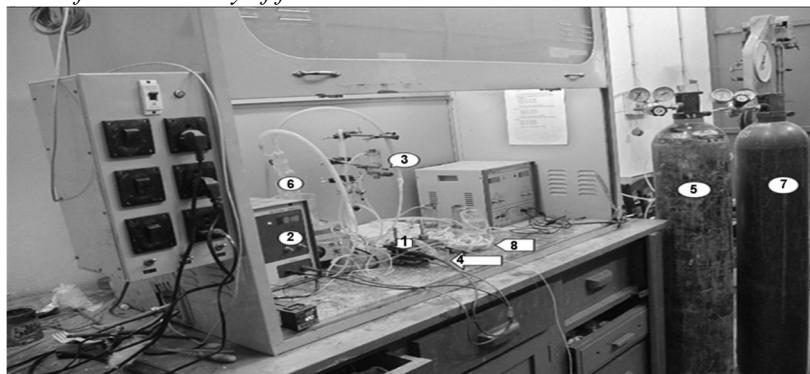


Fig. 1 – Experimental setup for performance study of PEMFC unit cell [Specifications: 1) PEMFC unit cell 2) Constant current source 3) Flow meters 4) Probes connected to cell 5) H₂ cylinder 6) Humidifier 7) O₂ cylinder 8) Adsorbers]



Fig. 2 – Electrochemical Workbench

The single fuel cell tests were carried out for the membrane/electrode assemblies (MEAs) which consisted of the composite sheets as an electrolyte and commercially available Pt-loaded carbon paper sheets as electrodes. The current vs. voltage characteristic (DC polarization) of the fuel cell was measured at different temperatures. From the polarization data power versus current data were evaluated. The enhancement of peak power generation with respect to the particle size was investigated and reported. The relevant TEM and SEM results are also appended in the present work. *Figures 1* and *Figures 2* represent the experimental setup and the electrochemical workbench setup for the present study.

RESULTS AND DISCUSSION

TEM analysis reveals that grinding of material for 20 hrs produces less than 10 nm size of particles; while grinding for less than 8 hr produces average particle size more than 500 nm.

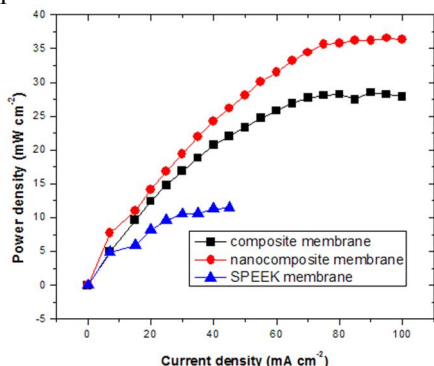


Fig. 3 – Power density versus Current density for the fuel cell at 70°C

(Fig. 3). Reduction in particle size from submicro to nanometer range causes enhancement of water uptake, ion exchange capacity and the proton conductivity; thus enhances the performance. The performance study also reveals that at medium cell temperature (65 to 75°C) Phosphosilicate gel-SPEEK hybrid nanocomposite membrane offers more than 75% enhancement of peak power generation compared to that offered by SPEEK membrane.

The single fuel cell tests were carried out for the membrane/electrode assemblies (MEAs) which consisted of the composite sheets as an electrolyte and commercially available Pt-loaded carbon paper sheets as electrodes. The current vs. voltage characteristic (DC polarization) of the fuel cell was measured at different temperatures. From the polarization data power versus current data were evaluated. The enhancement of peak power generation with respect to the particle size was investigated and reported. The relevant TEM and SEM results are also appended in the present work. *Figures 1* and *Figures 2* represent the experimental setup and the electrochemical workbench setup for the present study.

Figure 3 depicts the performance enhancement achieved in a fuel cell using nanocomposite phosphosilicate gel-SPEEK membrane comprising of less than 10 nm particle size at 70°C. Data analysis reveals that the composite membrane offers best performance at 70°C. For 60 weight percent inorganic loading of the membrane almost 40% nano enhancement of peak power generation is obtained by varying the gel particle size from sub micrometer to nanometer

CONCLUSION

Phosphosilicate gel – SPEEK (Sulfonated Poly Ether Ether Ketone) hybrid nano composite membranes are proposed for performance enhancement of polymer electrolyte fuel cell at low to medium cell temperature. Almost 40% enhancement in power generation is achieved by replacing the composite hybrid membrane with coarse submicro or micrometer size phosphosilicate particles by a nanocomposite membrane comprising of less than 10 nm particles. The present paper standardizes the procedure for experimental synthesis, characterization and performance studies for the novel hybrid nanocomposite membranes. The study highlighted the promising potential for using hybrid nanocomposite membrane for the enhancement of performance of proton exchange membrane fuel cells.

Acknowledgements

This work was funded by Naval Material Research Laboratory, DRDO, India.

REFERENCES

- [1] A. Biyikoglu, International Journal of Hydrogen Energy, 2005, 30, P. 1185–1212.
- [2] J. H. Hirschenhofer, J.H., Stauffer, D.B., Englemen, R.R., 1994. Fuel Cells Handbook. U.S. Department of Fossils Energy, Morgantown Energy Technology Center, WV, USA, 2004.
- [3] B. McCaughey, J.E. Hampsey, D.H. Wang, Y.F. Lu, Self assembled organic/inorganic nanocomposites, H.S. Nalwa Editor, Encyclopedia of nanoscience and nanotechnology, Vol 9 Stevenson Ranch, CA; American Scientific publishers, 2004 p 529-559.
- [4] Y. Gao, N.R. Choudhury, Organic-inorganic hybrid ionomer, H.S. Nalwa, Editor, Handbook of organic-inorganic hybrid materials and nanocomposites, vol 2. Stevenson Ranch, CA, American Scientific Publishers, 2003, p 278-293.
- [5] N. Nakamoto, A. Matsuda, K. Tadanaga, T. Minami, M. Tatsumisago, Solid State Ionics, 2001, 145.
- [6] Y. Jin, J.C. Diniz da Costa, G.Q. Lu, Solid State Ionics, 2007, 178.

SPARK PLASMA SINTERING THE SPARK-EROSION POWDERS OF FUNCTIONAL ALLOYS

Gennady E. Monastyrsky^{1*}, Patrick Ochin², Andrij V. Gilchuk¹,
Victor I. Kolomytsev³, Yuri N. Koval^{3,1,*}

1 NTUU "KPI", 37 Peremogy av., UA-03506 Kyiv, Ukraine

2 ICMPE-CNRS, 2-8, rue Henri Dunant-94320 Thiais, France

3 IMP of NASU, 36 Vernadsky av., UA-03142, Kyiv, Ukraine

ABSTRACT

Various shape memory alloys (Ti-Ni-Hf, Ni-Al and Cu-Al-Ni) were elaborated by spark plasma sintering method from the micron, submicron and nano- sized particles prepared by spark-erosion method in cryogenic liquid from preliminary melted master alloys. These alloys are being developed as one of the alternatives for the intermediate temperature applications (100-900°C). Spark plasma sintering method is express method, which provides lower temperature and shorter holding time of sintering. It makes possible to sinter materials from the pre-alloyed powders and eliminate the intensive grains growth and precipitating processes influencing the mechanical and functional properties of functional materials. The effects of processing parameters on the martensitic transformation and microstructure of the sintered compacts were investigated using XRD and SEM study. Temperatures of sintering were chosen according to the assessed data of the decomposition, oxidation and others processes carrying out in material. Although the precipitating processes were usually not completely depressed, the intensive grain growth was also not found in most cases. Most of the microstructure peculiarities of as processed powder were inherited by the sintered material.

Key words: shape memory alloys, spark-erosion powders, spark plasma sintering, Ti-Ni, Ni-Al, Cu-Al-Ni

INTRODUCTION

Attractive perspectives for the practical application of modern functional materials such as materials with conventional and magnetic shape memory, high-temperature shape memory materials and bulk amorphous materials stimulate continuous searching of new production and processing methods, like powder metallurgy (PM). Search direction is caused by their typical characteristics and requirements that are imposed to them. In most cases shape memory materials (Ti-Ni-X, Ni-Al-X, Ni-Mn-Ga, Cu-Al-Ni-X) have precision composition. High temperature shape memory materials, moreover, contain or highly reactive components (Zr-Cu-X, Hf-Pd, Zr-Pd, Ti-Ni-Hf, Ti-Ni-Zr), or high-cost

* e-mail: monastyrsky@yahoo.com, tel: (+38)0444068512

(Hf-Pd, Zr-Pd, Ru-Nb, Ru-Ta, Ti-Pt, Ti-Pd, Ti-Au). Bulk amorphous materials that act as precursors for the manufacture of shape memory materials (Ti-Zr-Hf-Ni-Cu) are a multicomponent. Most of the above mentioned materials tend to the decomposition during the heat treatment. In addition, they, with few exceptions, have poor ductility and machinability.

In this communication we will focus on three materials, which are representative most of above mentioned peculiarities of functional materials: Ti-Ni-Hf, Ni-Al and Cu-Al-Ni-Ti-Cr shape memory alloys (SMA). These kinds of SMA are being developed as ones of the alternatives for the intermediate and high temperature applications depending on the alloying content.

Enriched with Ni intermetallic Ni-Al is a promising shape memory alloy (SMA) for high-temperature applications. The start temperature of martensitic transformation varies from 200 to 1200K in the range of 60-70 at.% Ni. Currently, its wide application is limited by low plasticity, in particular due to the formation of intermetallic compounds Ni_3Al and Ni_5Al_3 during the preparation or heat treatment. By means of the traditional methods of the production (induction or arc melting) or by the sintering of elemental powders the obtaining of homogeneous alloys, free of these phases, is not achievable.

Cu-Al-Ni is considered as good candidate for the intermediate temperature applications (100-300°C). In Cu-Al-Ni, during the quenching the metastable β phase undergoes several types of martensitic transformation (MT) depending on Al content. The characteristics of the martensitic transformation MT are very sensitive to the order degree of the β phase and the precipitation processes. Primary γ_1 precipitation limits the high temperature applications of these alloys modifying the MT. The eutectic decomposition takes place above 440°C and finally the $\beta \rightarrow \alpha + \gamma_1$ eutectoid decomposition appears at 500°C. Increasing Al content promotes the formation γ_1 phase that embrittles the alloy. In addition Cu-Al-Ni alloys are brittle due to their very high elastic anisotropy ($A \sim 13$) and large grain size and in general show poor mechanical properties. Powder metallurgy is to be a good method in order to obtain fine grain size in Cu-Al-Ni SMA.

Ti-Ni-Hf(Zr) alloys could perform reversible martensitic transformation at 100-150°C higher than the room temperature depending on Hf content. Although the decomposition processes modifying their properties were not found in the working interval temperature, the limited ductility, poor machinability and formability restrict their wide practical applications. As well as for Cu-Al-Ni, the powder metallurgy (PM) is thought to be good alternative method for their production and allowing skip over the stages of the shaping parts. Usually PM processes using for the production Ni-Ti-based alloys from elemental components impacts with unresolved synthesis problems: extra phases such as Ti_2Ni , Ni_4Ti_3 , Ni_3Ti [1], contaminations like $Ti_4Ni_2O_x$ [2]. Therefore the using of pre-alloyed powders looks as preferable way for PM processing.

In current work the spark erosion (SE) powders of Ti-Ni-Hf, Ni-Al and Cu-Al-Ni-Ti-Cr obtained in liquid argon were used [1,3,4,5]. Spark erosion is probably the most versatile technique available for producing the particles of metals, alloys, compounds with the diameters of particles from a few nm to >100 μm . In case of liquid argon used as working liquid, SE method allows obtaining the powders from pre-alloyed material with a given composition, which is vitally important for functional material like SMA, free from large quantities of oxides.

In turn, the operation with pre-alloyed powders has unambiguous feedback caused by the peculiarities of the mechanism of powder sintering. The combustion sintering passing through the eutectic reactions or consumption the heat of formation of intermetallic compounds, promoting the sintering of elemental powders, is not available anymore. The mechanism of solid state diffusion sintering between the different powders particles of the same composition presumes the long term ageing. The precipitation processes are superimposed on the sintering processes during the annealing causing a decomposition of alloys with the formation of supplementary phases. Therefore the spark plasma sintering (SPS) method looks as a promising alternative of the conventional sintering method of pre-alloyed powders.

SPS method is express method allowing the sintering powders within 10 minutes in vacuum or inert gas atmosphere. It employs simultaneously the relatively high pressure, high temperature of sintering and heavy current passing through the samples that destroys the oxidation film on the powder surface providing good sintering. The method is very informative. It gives "on line" the information about the progress of the compacting, temperature interval of degassing and softening of the materials, which could be exceptionally useful for the optimization of the sintering regimes.

The goal of this work was to preliminary study the applicability of SPS method for the rapid sintering of pre-alloyed SE powders of Ti-Ni-Hf, Ni-Al and Cu-Al-Ni-Ti-Cr shape memory alloys.

EXPERIMENTAL PROCEDURE AND ANALYSIS

Commercially pure Ti, Ni, Cu and Hf and Zr (99.9%) were used for the alloys production by the induction melting. The rods of Ni_{49.87}-Ti_{40.25}-Hf_{9.44}-Zr_{0.30}-Cu_{0.14}at.% and Cu-13.01Al-3.91Ni-0.37Ti-0.24Crwt.% with a diameter of 6 mm was produced by AMT (Belgium). Alloy with a nominal composition Ni₆₃Al₃₇ arc melted and molded into bars with a diameter of 4 mm and the length of 12 cm. Part of the rods were used as electrodes for SE apparatus and the remaining were broken at 3-4 mm pieces and were used to obtain powder by spark erosion method.

The general principle of the spark-erosion processing was described in details in [3,6] and involves the application of a heavy current between two elec-

trodes and a lot of pieces (chunks) that prepared from the pre-alloyed material both being immersed in a dielectric refrigerant inside a container. The key idea of the method is the melting (evaporation) of the material by the electric discharge with a duration of 5-100 μsec with subsequent quenching of molten droplets in liquid argon *in situ*. After spark erosion treatment of 100 g of granules of master alloys in liquid argon about between 40 to 70 g of powder was received depending on the material composition. In order to prevent eventual explosion of finest particles of powders it was kept in a vessel with liquid argon during the day until all argon was evaporated. Then the powders were sieved and divided into three fractions: the size of less than 128 and more than 65 μm , less than 65 and more than 32 μm and less than 32 μm .

Fig. 1 shows the main components of the SPS apparatus (DR.SINTER® LAB Series, Metal Processing Systems, Inc. Japan). A 50 kN uniaxial press together with an AC power supply simultaneously provide a mechanical load through the die plungers for densification and an alternating current through the sample placed in the graphite die. About 1 g of powder was preliminary slightly compacted in the die. A graphite paper was put between the sample and the graphite plungers. The die was then placed inside the working chamber of the apparatus and the system was evacuated. To avoid overheating of the sample the heating rate was no more 350 $^{\circ}\text{C}/\text{min}$.

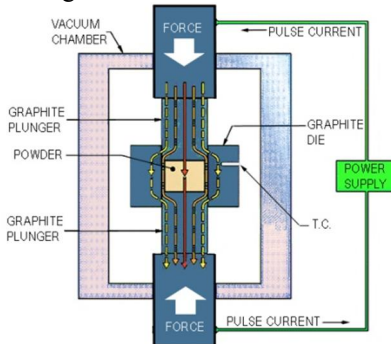


Fig. 1 A general scheme of spark plasma sintering apparatus

Maximum applied uniaxial pressure was 99.5 MPa. Temperatures of the samples during the sintering were measured by a sheathed thermocouple, which was inserted into a small hole in one side of the graphite mold, as illustrated on Fig. 1. The temperature, vacuum in the chamber, current applied force, shrinkage displacements of the powder compacts, voltage and current were recorded during the processing.

The electric current provides a rapid Joule heating in the compact die-sample system. The experiment is initiated with the heating by the application of continuously increasing electric current together with the continuously increasing pressure. When the temperature get to preliminary setting temperature of sintering (T_{SINT}) a set constant value of the electric current was applied for a given time, hereafter indicated as sintering time (t_s). After that, the sample was unloaded, cooled and removed from the die. Temperatures of sintering were chosen according to the assessed data of the decomposition, oxidation and others processes carrying out in material. A typical program of the sintering is shown

on Fig. 2a. The performed programs of sintering are listed in Table 1. As a result of sintering a sintered compacts with a diameter of 8 mm and height of 4-6 mm were obtained.

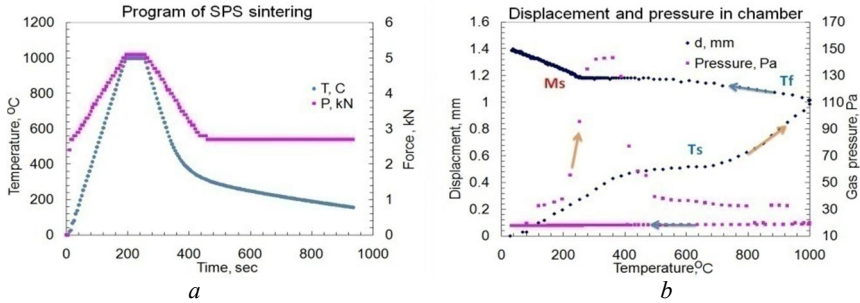


Fig. 2 a) – typical program of sintering ($T_S=1000^{\circ}\text{C}$; $t_S=1$ min); b) – shrinkage displacement of the sample and gas pressure in the chamber vs. temperature

Table 1 – The regimes of SPS treatment; F – applied force, HR – heating rate, D – displacement (shrinking)

Regime	T_{SINT} , $^{\circ}\text{C}$	t_S , min	F, kN	HR, $^{\circ}\text{C}/\text{min}$	D, mm	Remark
Cu-Al-Ni						
CAN-1000-1	1000	1		330	1.60	Melt, 32/65
CAN-700-1	700	1		280	1.97	MT, 32/65
CAN-650-1	650	1		160	1.72	MT, 32/65
CAN-600-1	600	1	5	150	1.72	MT, 32/65
CAN-480-1	480	1		96	1.52	32/65
CAN-440-1	440	1		88	1.07	32/65
CAN-390-1	390	1		65	1.05	MT?, 32/65
Ni-Al						
NA-400-10	400	10		200	0.22	32/65
NA-500-10	500	10		250	0.24	32/65
NA-850-10	850	10		212	0.87	MT, 32/65
NA-850-4s	850	4.5	5	212	0.86	MT, 32/65
NA-900-2	900	2		225	0.92	MT, 32/65
NA-850-4b	850	4.5		212	1.40	MT, 65/128
NA-1000-1	1000	1		250	1.53	MT, 65/128
Ti-Ni-Hf						
TNH-500-0	530	0		100	0.29	<32
TNH-1000-2	980	2	2.5	100	1.20	<32
TNH-860-1H	860	1	5	250	1.19	MT, 32/65
TNH-1000-1H	1000	1	5	200	1.42	MT, 32/65

XRD study of the compacts were carried out at room temperature by the Debye-Sherrer method with a $\text{CoK}\alpha_{1,2}$ radiation. Instrument Philips PW1830 with Multi-Purpose XRD Diffraction System from PANalytical were used.

The morphology and microstructure of the sintered samples were analyzed by LEO 1530 instrument equipped by PGT PRISM 2000 (Ge) spectrometer without the references standards. Detail composition study were carried out with JSM-6490LV (Jeol) and JAMP-9500F (Jeol) both equipped with EDX spectrometer INCA PentaFETx3 (Oxford Instruments).

RESULTS AND DISCUSSION

Fig. 2b illustrates the behavior of the shrinkage displacement of the powder compacts and gas pressure in the chamber during processing. This behavior corresponds to the program of sintering NA-1000-1. The first stage of the sample shrinking is accompanied by the vacuum fall and connected with the mechanical compressing of powder and partial welding while the second one starts at about 700°C (T_S on figure) – with the sintering of the particles. Such a kind of behavior is typical for all powders. The temperature of the first (T_1) and second (T_S) shrinkage displacement upon the heating depends on the kind of powder. In case of Ti-Ni-Hf powder there was third interval too. Temperature intervals of sintering are listed in Table 2. First sintering interval contributes about 15%, 30-40% and 8-15% of the total displacement for Cu-Al-Ni, Ni-Al and Ti-Ni-Hf powders respectively. The value of contribution depends on the sizes of powders particles. The more the diameters of particle sizes, the more this contribution. Because the effect of preliminary compacting (before the processing) is the less, the more the particles size, this first interval can associate mainly with the initial mechanical shrinkage of the powders particles. It accompanied by the emission of gas (air), which is kept between the particles. The other process such as reverse martensitic transformation and precipitation of extra phases (Ni_5Al_3 in case of Ni-Al powders) can also contribute the shrinkage effect. It is seen also from Table 1 that the more the diameters of particle sizes (denoted in field “Remark” of Table 2 like 32/65 – min and max sizes of particles in powder fraction), the more total shrinkage of the compact. Thus the succeeding sintering interval doesn’t practically depends on the particles size and defined only by the high temperature plasticity of the material as well as the decomposition processes, which take place at this temperatures.

Table 2 – Temperature intervals of sintering

Powder	$T_{1 \text{ start}}, ^\circ\text{C}$	$T_{1 \text{ finish}}, ^\circ\text{C}$	$T_{S \text{ start}}, ^\circ\text{C}$	$T_{S \text{ finish}}, ^\circ\text{C}$	$T_{3 \text{ start}}, ^\circ\text{C}$	$T_{3 \text{ finish}}, ^\circ\text{C}$
Cu-Al-Ni	120	250	300	>700	-	-
Ni-Al	50	400	600-650	>1000	-	-
Ti-Ni-Hf	300	425	475	850	910	>1000

It is interesting also that upon the cooling the extra shrinkage appeared which was displaying as sharp incline on the reduction displacement curve (M_s on Fig. 2a, MT in Table 1). Because the position of sharp incline correlate with the martensitic start point of the respective powder one can assume that this extra compacting relates with the martensitic transformation stimulated by the external uniaxial pressure of the plungers.

The powders, which were sintered at relatively low temperature ($<400^\circ\text{C}$), were mechanically stable (although special mechanical test were not carried out). However the best quality of samples was found for the compacts sintered at higher temperature within the interval $850\text{-}1000^\circ\text{C}$ depending on the composition of powder.

SEM investigation confirmed that after the first stage of sintering only initial welding and partial compacting appeared. The particles remained mainly non-deformed with the typical round shape of SE powders (Fig. 3). Contrary, the particles after the second stage of sintering were gathered tight and have been deformed. EDS microanalysis has shown it is not possible avoid the decomposition processes during SPS processing even if the very short time of sintering was used. Typical for each of powders under investigation extra phases were found. The type of precipitates depends on the temperature of sintering mainly. γ_1 or α -phase or both of them were found in the compacts of Cu-Al-Ni after different sintering programs (Fig. 4). Enriched with Ni phase (perhaps Ni_3Al) was found in Ni-Al powder after NA-850-4s program (Fig. 5a). It seems to be inherited from the initial microstructure on Ni-Al SE powders described elsewhere [5]. It is interesting that after NA-1000-1 program the traces of Ni_3Al phase were not found and some of the particles were recrystallized (Fig. 5b). Taking into account that this phase disappears after the heating above about 1150°C , also the fact that Cu-Al-Ni powder after heating to 900°C was melted, one can conclude that real temperature of the compact inside the die was high than the recorder one on about $150\text{-}200^\circ\text{C}$.

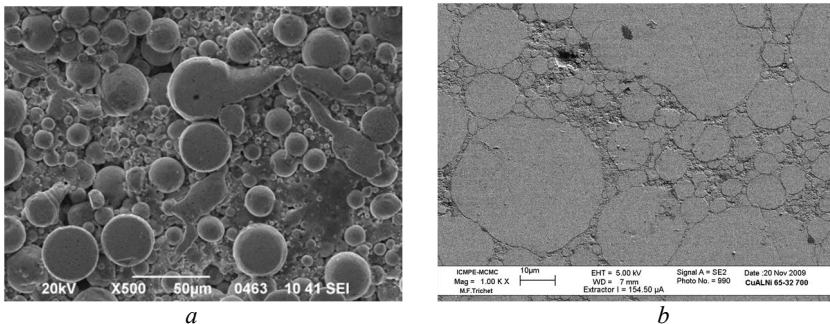


Fig. 3 – SE images of Cu-Al-Ni powder after the compacting programs a) – CAN-390-1, b) – CAN-700-1

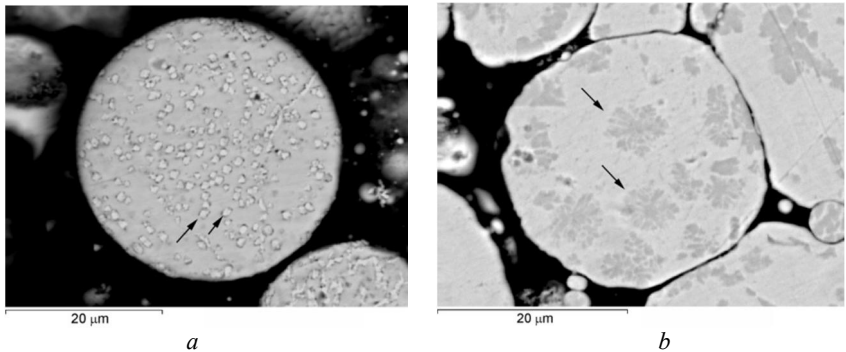


Fig. 4 – BSE images of Cu-Al-Ni powder after the compacting programs: *a*) – CAN-390-1, arrows show α -phase precipitates; *b*) – CAN-650-1 arrows show γ_1 -phase precipitates

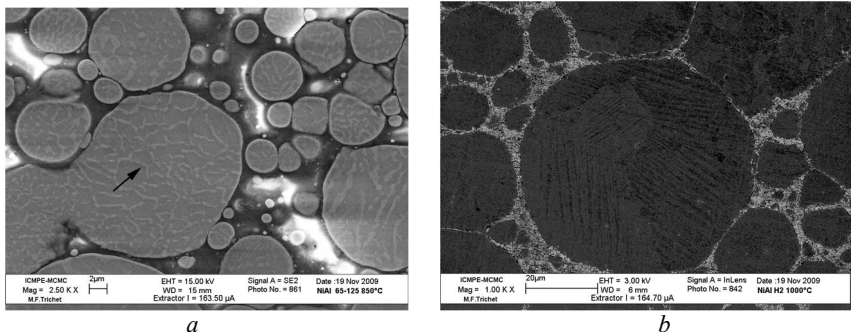


Fig. 5 – Ni-Al powder after the compacting programs: *a*) – NA-850-4s, arrows show the enriched with Ni precipitates; *b*) – NA-1000-1

Banded structure resembling the martensite was also found. In addition to the enriched with Ni phase (seems to be Ti_2Ni), a lot of enriched with Hf and oxygen precipitates (with the composition close to HfO_2) were found into Ti-Ni-Hf powders particles as well as on their boundaries (*Fig. 6*).

XRD study confirmed the results of SEM investigation. B2, 2H, 18R, γ_1 and α -phase or both of them are the main phases in the Cu-Al-Ni blends. In addition some noticeable quantity of Cu_2O was found.

Although the sintering time was rather short (1-4 min) it does not prevent the formation of the Ni_5Al_3 phase below $900^\circ C$; Ni_3Al phase has formed in the samples sintered at higher temperatures while the lowest amount of this phase was found for Ni-Al powders treated according to the program NA-1000-1. Some minute peaks could be considered as belonging to Al_2O_3 phase.

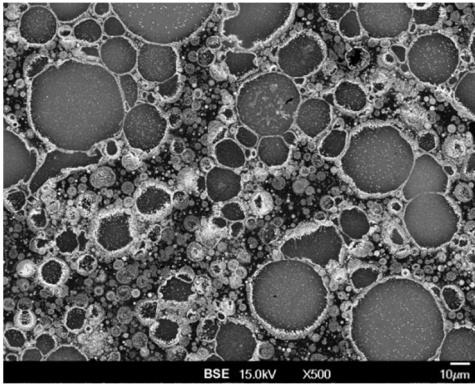


Fig. 6 – Ti-Ni-Hf powder after the compacting programs TNH-1000-1H. Bright spots are the enriched with Hf and oxygen phase

In addition to B2, Ti_2Ni and B19' (martensite) phases a lot of HfO_2 were found in Ti-Ni-Hf blends. The formation of the oxides in the sintered samples is due to pure vacuum and remains of the air, which is kept along with the preliminary compacted particles. The nano-fraction of powders, filling the interspaces between the micron sized particles, promotes also the oxidation; thus the oxides appear mainly between micron sized particles. One exception is Ti-Ni-

Hf powder where chemically active Hf is oxidized in the middle of particles.

CONCLUSIONS

The powders of shape memory alloys with the compositions Ni_{49.87}-Ti_{40.25}-Hf_{9.44}-Zr_{0.30}-Cu_{0.14}at.%, Cu-13.01Al-3.91Ni-0.37Ti-0.24Crwt.% and Ni₆₃Al₃₇ were elaborated by the spark plasma sintering method from the micron, submicron and nano- sized particles prepared by spark-erosion method in liquid argon from preliminary melted master alloys.

Although the powders were sintered already at relatively low temperature (<400°C), the best quality of samples was found for the compacts sintered at higher temperature within the interval 850-1000°C depending on the composition of powder.

Even the sintering time was rather short (1-10 min) it does not prevent the formation of extra phases. Most of the microstructure peculiarities of as-processed powder were inherited by the sintered material. The intensive grain growth was not found in most cases.

The remains of the air, which is kept in the interspaces between the preliminary compacted particles as well as nano-fraction of powders promotes the oxidation processes during the SPS processing.

The martensitic transformation in most of the sintered compacts has been clearly indicated during the cooling in spark-plasma apparatus; martensitic structure was confirmed by SEM and XRD study.

Acknowledgements

The authors are grateful to CNRS PICS-3717, STCU (#3520, #3144) and ECONET projects for the supporting of this work.

REFERENCES

- [1] G.E. Monastyrsky, V. Odnosum, J. Van Humbeeck, V.I. Kolomytsev, Y.N. Koval, *Intermetallics* 10 (2002) 95.
- [2] M. Nishida, C.M. Wayman, T. Honma, *Metall. Trans.* 17A (1986) 1505.
- [3] G.E. Monastyrsky, P.A. Yakovenko, V.I. Kolomytsev, Yu.N. Koval, A.A. Shcherba, R. Portier, *Mater. Sci. & Eng. A* 481-482 (2008) 643-646.
- [4] G.E. Monastyrsky, P. Ochin, G.Y. Wang, A.V. Gilchuk, V.I. Kolomytsev, Yu.N. Koval, V.O. Tinkov, A.A. Shcherba, S.M. Zaharchenko, Effect of particles size on chemical composition of Ti-Ni-base spark erosion powder obtained in liquid argon, to be published in *Chemistry of Metals and Alloys*
- [5] G.E. Monastyrsky, V.V. Odnosum, V.I. Kolomitsev, Yu.N. Koval, P. Ochin, R. Portier, A.A. Shcherba, S.N. Zaharchenko, *Metallofizika i novejschie tehnologii*, 30 (2008) 761-772.
- [6] A.E. Berkowitz, M.F. Hansen, F.T. Parker, K.S. Vecchio, F.E. Spada, E.J. Lavernia, R. Rodriguez, *J. Magn. Magn. Mater.* 254-255 (2003) 1.

APPLICATION OF SIMULATION TECHNOLOGIES TO THE INVESTIGATION OF THE BEAM GENERATING SYSTEMS

Ivan V. Barsuk, Alexandr V. Bondar, Gennadiy S. Vorobjov,
Aleksy A. Drozdenko*

Sumy State University, R-Korsakov 2, 40007, Sumy, Ukraine

ABSTRACT

A series of numerical calculations of electron beam generation in the three-electrode electron-optical system has been performed with the help of the electromagnetic modeling FIT method both with the PBA technology. Effects of the initial blocking and ray laminarity failure have been modeled. Optimum electrode potentials have been obtained for generation of the low-energy intensive axial-symmetric electron beam with beam-crossover behind the last anode of electron gun.

Key words: beam crossover, electron-optical system, electron beams, FIT method, perveance.

INTRODUCTION

Electron beams (EB) of different intensity levels are widely used nowadays in the microwave devices and different technological units. Optimization of their electron-optical system (EOS) parameters is generally based on the EB characteristics. Due to the numerical methods progress nowadays programs of electromagnetic simulation are actively used to collect such information. Usually these programs allow to avoid providing effortful and very expensive experiments. High requirements are applied to modern EOS with a high current density (up to tens or hundreds A/m^2) and creation of the focusing EOS with a high EB compression level helps us to achieve such density level. This paper leads with the detecting of the optimal electrode potentials for the electronic gun of the task geometry to achieve the high levels of EB compression.

SYSTEM DESCRIPTION AND SIMULATION RESULTS

The investigation object is the electron beam, generated by the three-electrode axial-symmetric electron gun, which is widely used in devices of the type TWT [1]. EOS configuration and disposition layout view is shown in the *figure 1*.

Such type guns allows us to form EB with the crossover diameter about 0,05 – 0,5 mm, beam current 5 – 30 mA, acceleration potential nearly 6000 V.

* e-mail: aleksy.drozdenko@gmail.com, tel: +38(095)9193335

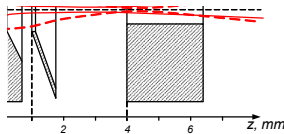


Fig. 1 – Scheme of EOS of axially symmetric electron gun: 1 – hot cathode (U_k), 2 – focusing electrode (U_f), 3 – first anode (U_{a1}), 4 – second anode (U_{a2}).

realized it in the program CST Particle Studio.

This method is more multipurpose than the finite difference method, and it has some preferences in comparison with other methods: there are no restrictions on the element grid type (supports nonorthogonal cell shape) and this method can be realized both in time and frequency domain. Moreover, simultaneously with the Perfect Boundary Approximation (PBA) technology, this method allows us to avoid the staircase approximation of complex boundaries – the main disadvantage of the finite difference method. FIT method approval showed high level of correlation with experimental results [3], so this method is suitable for EOS optimization in the case of unconditioned geometry. Initial parameters of the electron gun is a combination of electrode potentials [4]: beam perveance $P = 0,045 \text{ mA/V}^{1,5}$, initial energy of electrons $E = 20 \text{ eV}$.

After the numerical simulation of the electron gun operating conditions we have established, that the beam crossover is located in the area between first and second anodes, but not at the gun outlet, in the case of overestimate potentials of the focused electrode ($U_f \approx -40 \text{ V}$).

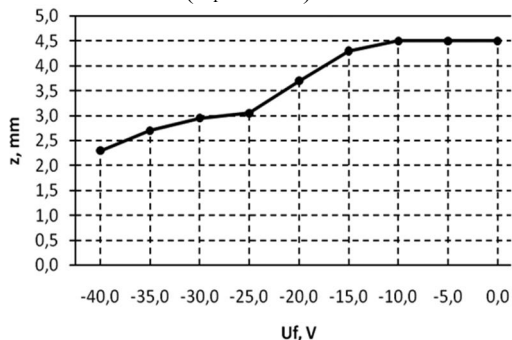


Fig. 2 – Influence of the focusing electrode potential U_f on EB crossover position

For the decision of the assigned task the complex simulation of the EOS has been made, electrostatic fields have been evaluated with the further tracking analysis. There are a lot of popular and widely used numerical algorithms of three-dimensional electromagnetic simulation (FDTD, FEM, MoM, integral equations method etc). We choose the method of finite integrals (well known as FIT – The Finite Integration Technique [2]), and

Decreasing of the U_f value reduces the beam crossover to the range of the drift channel of the second anode, as it is shown in the *figure 2*. Crossover beam diameter decreases and current propagation increases, when U_f changes from $U_f = -10 \div 0 \text{ V}$ to 100%. However, it is impossible to move the beam crossover beyond the second anode only with

the help of focusing electrode potential variation.

In addition, the focusing electrode placing in the neighborhood of the cathode causes the effect of the partial blocking appears. In this case the kinetic energy of outgoing electrons is too low to overcome the potential barrier and it decreases the degree of the current propagation and breaks the EB laminarity. For example, results of simulation of the electrons emission and starting moment of the beam creation are shown in the *figure 3*. It should be noted, that we have used only 50 particles for the best performance of the results. It is obvious, that particles majority is able to come back to the cathode, but the rest of the particles highly disturb the laminarity, especially the extreme ones.

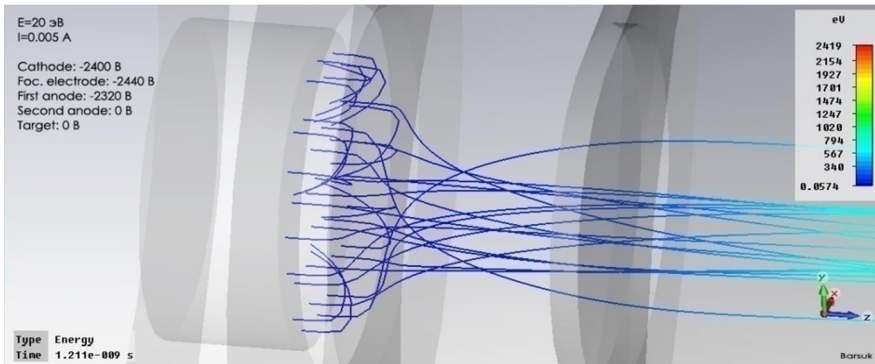


Fig. 3 – Blocking effect and beam laminarity disturbance

Then the particles lifetime has been explored in the observable system. The particles amount per time dependence is shown in the *figure 4*. From the plot on the figure 4 we can say, that about 28% of particles moved back to the cathode (first falloff 1000-720 particles), the rest particles have reached the collector (720-0 particles).

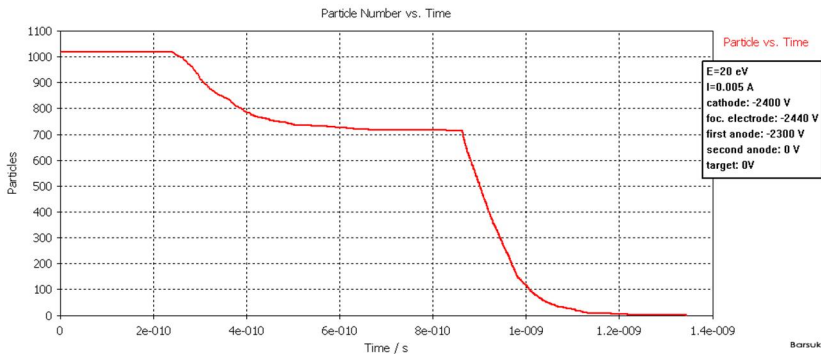


Fig. 4 – Amount of particles/time

Flat second falloff indicates that particles have reached the cathode not at the same time. It is obvious from detailed investigations that particles of the central part of the beam secure the collector much faster than the particles of the outer part of the beam. We consider the laminarity disturbance at the starting moment leads to this energy dispersion in the EB.

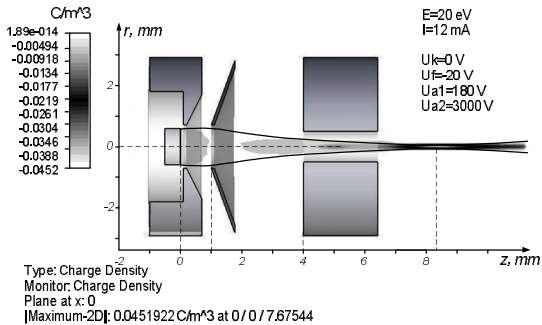


Fig. 5 – EB configuration, which was obtained after the electron gun mode optimization

The beam crossover is located behind the second anode of the electron gun at the distance 8,4 mm, the beam diameter is 0,1 mm, it corresponds to the compression coefficient 150 (on area) and beam energy 3 keV.

CONCLUSIONS

Series of numerical experiments of creating the axially symmetric EB have been described in the paper. Basic method of numerical investigation is FIT method, which has been realized in the program CST Particle Studio. Optimal operation modes of the three-electrode electron gun has been determined in the case of low-energy electron beam creating.

REFERENCES

- [1] E.V. Belousov, G.S. Vorobjov, G.S. Korzh, K.A. Pushkarev, A.I. Ruban, Visnyk SumDU, Ser.: Phys., Math., Mech., 1997, 1(7), P 73—76.
- [2] M Clemens., T Weiland, Progress In Electromagnetics Research, PIER 32, 2001, P. 65—87.
- [3] 7-ja Mezhdunarodnaja Molodezhnaja Nauchno-Technicheskaja Konferencija RT-2011 (I.V. Barsuk, A.A. Drozdenko), Sevastopol: SevNTU, 2011, P. 324—325.
- [4] G.S. Vorobjov, A.A. Drozdenko, A.G. Ponomarjov, Izvestja Vuzov, Radioelektronika, 2006, 6(49), P. 11—16.

Then a system of numerical experiments have been carried out to find the optimal operation modes of the electron gun (fig. 1), with the help of varying of electrodes potential values U_f , U_{a1} , U_{a2} , which helped to create the EB of the optimal geometry, as it is shown in the figure 5.

Radiation effects in solids

CRITICAL EXPONENTS IN PERCOLATION MODEL OF TRACK REGIONS WITH DIFFERENT DEPTH DISTRIBUTION

Demchyshyn Andriy, Selyshchev Pavlo

Taras Shevchenko National University of Kyiv, Faculty of Physics, 03187, Ukraine, Kyiv

ABSTRACT

As a result of irradiation with Xe with $E = 250$ MeV in InP at room temperature [1] defects, similar to the "chain of pearls", which are placed along the trajectory of the ions at depths ranging from 35 to 100 nm and from 7 to 10 microns have been identified. Such defects called tracks, and they can occur at different depths and have different shapes. Tracks were examined like a chain of deal spherical regions; it was assumed that each incident ion creates one such chain. In this model, we assume that the track is formed randomly, but in that place of the ion path, where the energy value, which loses each ion to the unity of the way, is above some threshold value.

As a result of irradiation the number of tracks will continue to grow, areas of the single tracks modified substance continue to overlap, form of modified matter becomes more complicated, creating branched structure.

Percolation threshold, fraction of spanning cluster modified material for different doses and different distributions of track areas in depth were evaluated. Based on the scaling hypothesis large-scale curve were constructed, critical exponents for this percolation model were established.

Calculated values of critical exponents were compared with the known values for the model of continuous percolation. Parameters of the percolation and critical exponents depend on the distribution of track areas in depth, which indicates the difference in the order parameters of the track structure obtained for different distributions in depth.

Key words: track, branched structures, swift heavy ions, the Monte Carlo method, critical exponents, percolation threshold, percolation.

INTRODUCTION

Under swift heavy ions (SHI) irradiation track of various shapes and lengths, filled with a modified (with respect to the material of the sample) material, are formed in a solid. They are generated as a result of the strong relaxation of electronic excitations and formed along the trajectory of the ion. Tracks are beginning both from the irradiated surface and at some distance from it. Continuous and discontinuous cylindrical and spherical track field were found.

Elongated defects, similar to the "chain of pearls" that are placed along the trajectory of the ions at depths ranging from 35 to 100 nm and from 7 to 10 microns, were found after irradiation by xenon ions with $E = 250$ MeV in InP at room temperature [1]. Also in the iron garnet irradiated by ions with energies

around 12 MeV in a mode of high speed [2] with the energy loss in the range of $4.5 - 7 \text{ KeV}\cdot\text{nm}^{-1}$ the appearance of spherical domains of the modified material were observed. Discrete tracks point-shaped and oblong dark spots with a diameter equal to an average of about 3 - 10 nm along the trajectories of incoming ions in the form of a "chain of pearls" with a number of "pearls" in the track of two to five pieces were observed on the bright-field pictures in the paper [3].

Physical mechanisms of track formation, probability distribution of their formation along the trajectory and in the chain have not been yet fully clarified. The distribution of the tracks in the depth of the sample did not correlate with either the distribution of implanted ions, or the distribution of point defects formed by the ions. The experimental results do not uniquely determine the distribution of tracks.

However, it is widely recognized that the track is formed as a result of redistribution of the energy transmitted by one ion in the electron subsystem. Also it is known that the track is formed randomly in that place of the ion path, where the value of missing energy per unit of ion path is above a certain threshold, in a place where the rush of energy release is presented. It was noted that the simulation results of energy spectra using the SRIM 2008, shows that the maximum energy during the passage of high-energy ions are also located in an average of 25-40 nm. From the experimental data it is known that the tracks in the form of a chain of spheres are created at different depths (between 0 and 50 nm, between 0 and 500 nm) for different materials and conditions of exposure. For example, for InP irradiated by xenon ions, the average distance between tracks spherical averages of 25-40 nm, length of the chain is in the range from 50 nm to 150 nm.

Study of changes in material properties as a result of electronic excitation upon irradiation by fast heavy ions and the creation of latent tracks in these materials is an exciting and promising field for new research and development. However, despite the relevance of the topic and practical significance of the expected results, the formation of branched structures of the individual tracks has been insufficiently studied.

FORMULATION OF THE PROBLEM

We simulated a sample in the form of plane-parallel plate with a thickness of 50 to 300 nm. For the calculations was chosen fragment of the plate in the shape of the box size from 50 to 300 nm. The case where the ion energy is sufficient to create a chain of spheres modified substances, energy is 20-40 MeV / amu around was modeled. Each incident ion creates a track in a sequence of a certain number of spherical regions. The trajectories of all ions are parallel to each other. In this model, we simulate different distribution areas in depth, such as: a) a sphere in the chain b) a sphere in a chain or two areas in the chain) is a sphere or two areas or three areas. And so on up to six spheres in the chain.

The first spherical region is equally likely to appear anywhere in the segment of the trajectory of an ion from its point of penetration into the sample to the point of 2ρ , where ρ - the average distance between the spheres. In the calculations ρ is equal to 40 nm. The distance from the first sphere to the second is chosen randomly from range of values between 0 and 2ρ , the form of distribution doesn't depend on the «history» (it is the same as for the preliminary scope, only shifted along the ion path in the appearance point of the previous sphere). Some specific distribution of tracking areas in depth was obtained as a result, distribution for the case when there are maximum three spheres in the chain is shown in Fig.1.

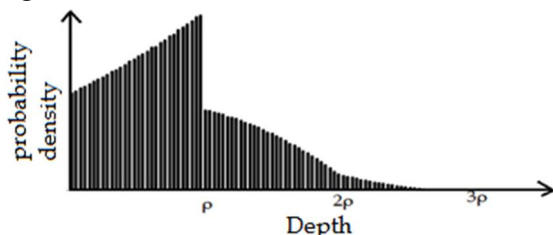


Fig.1. - Distribution for a chain with one, two or three spheres.

Consecutively two surfaces were exposed to radiation. With the irradiation modified substance areas of individual tracks start to overlap, as a result modified form of matter becomes more complicated, forming a branched structure. Some part of this branched structure is bordered on one surface of the sample, while others lie on the boundary with the opposite surface. When these parts connect one to another, they will create so-called "spanning cluster," which percolates from one surface to another.

RESULTS AND DISCUSSION

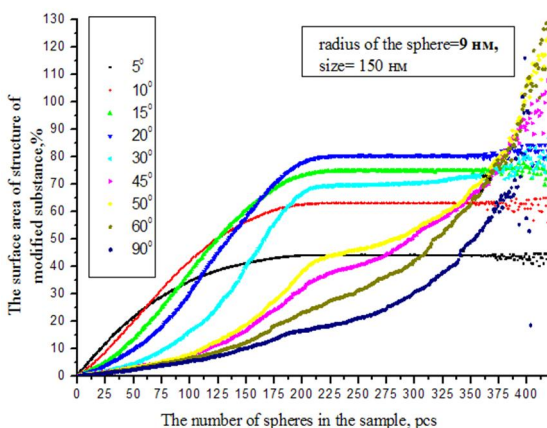


Fig.2. - Dependence of the branched structure surface area on the dose and from different angles

Computed dependence of the branched structure surface area on the dose and from different angles has previously been reported (Fig.2).

This nontrivial dependence is related with the distribution of track regions in depth, namely, the correlation between the modified regions of different tracks as a "chain of spheres." Scaling hy-

pothesis has been used to separate influence of this distribution on the angular and dose dependence of structural parameters.

Percolation threshold, fraction of spanning cluster modified material for different doses and different distributions of track areas in depth for different scales of the sample were evaluated. Based on the scaling hypothesis large-scale curve were constructed, critical exponents for this percolation model was established.

Scale was changed in the following way: the sample size was increased in two times, irradiation dose – in four times, the number of spheres in the chain in two times (to make modified structure density and percolation effects didn't change).

For each scale dependence of the appearance frequency of first spanning cluster (percolation) on the number of spheres was obtained, in each case deal number of areas, where percolation is most frequent, was defined. This value corresponds to a value of modified material share, which is the percolation threshold for corresponding finite size of sample and will approach the percolation threshold of the infinite cluster. Using the percolation threshold dependence on the number of track regions in the sample the percolation threshold of the infinite cluster was determine.

Differences between the critical exponents of this model and the well-known model of uniform distributed spherical domains in volume (continuous percolation model) were received.

CONCLUSIONS

As a result, it was found that the difference critical exponents of this model and the continuous percolation model indicates that the dependence of the modified structure area on the dose and the angle related with the distribution of track regions in the depth of the sample. Also, correlation of individual track regions result in higher ratio of the critical exponents than in a continuous percolation model, that talks about the higher connectivity of track regions structure in this model. Also it causes fact that percolation threshold in this case is below the percolation threshold of continuous percolation. Created model based on experiments and has vivid scaling properties, that allows us to predict different parameters of the modified structure at different scales of the sample.

REFERENCES

- [1] Herre O., Wesch W., Wendler E. Phys. Rev. B —1998.—vol. 58 —p.4832.
- [2] Meftah A., Brisard F., Costantini J. M. et al. Physical Review B.- 1993. — Vol. 48. — P. 920 – 925.
- [3] Gaiduk P.I., Nylandsted Larsen A. et al. Phys. Rev. B., — 2002. — Vol. 66.— P. 045316-2 - 045316-3.

POROUS MATRIXES BASED ON ION-IRRADIATED POLYMER AS TEMPLATES FOR SYNTHESIS OF NANOWIRES

D.Zagorskiy^{1*}, S.Bedin¹, V.Korotkov^{1,2}, V.Kudravtsev², V.Oleinikov³,
P.Ershov¹, A.Vilenski¹

1 Institute of Crystallography of RAS, Moscow, Russia, *

2 Mendeleev University of Chemical Technology of Russia, Moscow

3 Institute of Bioorganic Chemistry of RAS, Moscow

ABSTRACT

Irradiation with swift heavy ions is usually used for production of track membranes (nuclear filters). These membranes traditionally used as filters for fine filtration in medicine and biology.

Another application is matrixes for so called matrix synthesis. The idea of this technique is to fill pores by any desired material- metal, polymer, semiconductor and so on.

This work is devoted to formation of membrane for template synthesis, to investigation of filling process and to study some properties of obtained structures.

It was found that filtration track membranes are not the best material for template synthesis –another type of matrixes are needed- with different pores profiles and parallel pores orientation. These parameters could be obtained during irradiation. Different types of etching gave possibility to vary by will the shape of the pores and to obtain pores with conical shape. The process of etching in the alkali solution in mixture of water and alcohol was investigated.

The main part of the work devoted to fabrication of micro- and nanowires via electrodeposition. Different types of metals-copper, silver, cobalt and nickel were used for galvanic deposition of the pores. Two types of the processes- galvanostatic and potentiostatic were investigated.

It was also demonstrated that obtained metallic nanowires could be used as the substrates for deposition of the probe (biological molecules) in mass-spectrometer.

The application of such structures in non-linear optic was also described.

Keywords: heavy ion irradiation, porous polymer matrix, template synthesis, conical pores, metallic nanowires

RESULTS AND DISCUSSION

Nanosized materials are of great interest now. One of the most promising technique for production of these materials is template (or matrix) synthesis: filling of the pores in the special matrix by the desired material. The last one

* e-mail: dzagorskiy@gmail.com

can be metal, semiconductor or polymer. We used polymer track membranes or porous polymer material as such matrixes for the filling process. In our work the matrixes with cylindrical and conical pores were utilized and obtained structures (ensembles of metal micro- and nanowires) were used as the emitters for mass-spectrometry analysis.

Obtaining of the matrixes

Usually commercial TM are used for formation of replicas- nanowires. We used not only commercial TM, but specially prepared polymer matrixes. In this case the polymer films (Polyethyleneterephthalate, PET, thickness 15-20 mcm) were irradiated with swift heavy ions –usually Xe or Ar (for conical pores) with the energy 1-2 MeV/nucleon and surface density $10^6 - 10^8$ ions per cm^2 , and perpendicular orientation. All irradiations were done in Joint Institute for Nuclear Research (JINR, Dubna).

For the formation of cylindrical through pores standard etchant (water solution of 5 M NaOH, and treatment (room temperature, a few minutes etching) were used.

We used 3 M NaOH solution in the water-ethanol mixture (with different proportion) for obtaining pores of conical shape (usually: tapered, dead-end pores). It is important that by varying of the etching conditions (composition, temperature and time) we could vary the shape and the size of the pores. It was found that the top angle of pores (and, therefore, the replica cones angle) increases with decrease of temperature of the track etching and with the increase of alcohol concentration. We also demonstrated the possibility of conical pores formation by using the addition of salt (BaCl_2) to etchant (0,25 M KOH+0,1 M BaCl_2).

Investigation of the process of etching of conical pores

The process of chemical etching of cylindrical pores was investigated in many papers and gave information about structure of latent track area. On the contrary the process of etching of conical pores –in the alkali solution in the mixture of water and alcohol-was not investigated. In our mind this process is different from the first one. So, we investigated the process of etching of conical pores in the mixed etchant (i.e. with the alcohol) by using IR-spectroscopy.

Polymer films (PET with thickness 10 mcm) were irradiated with Ar ions (fluence 10^9 ions per sq.cm) at cyclotron in JINR, Dubna. The irradiated films were then etched in 9N solution of NaOH in the mixture of water and alcohol (50:50). The etching temperature was 25°C. The etching times were taken as 10 min, 20 min, 30 min, 40 min and 50 min. After each etching process the etching solution (with the reaction products) was taken for analysis. IR-analysis of etching solution were carried out using IR-spectrometer Specord M80 with computer data development. All obtained spectra demonstrate the changing in

the composition of etchant during the etching. The calculation of these data gave possibility to estimate the quantity of the etching product in solution. It is known that destructed polymer from track areas pass into the solution at the beginning of the etching and this process depends on time. The dependence of two bands (1444 cm^{-1} (aromatic) and 1696 cm^{-1} (carbonil)) intensity on etching time confirms the changing of etchant composition during the first 30 min of etching, than saturation took place. So we have etching of destructed polymer (from track area) during first 30 min, than only non-destructed polymer slowly passed into the etchant. The size of the area of destructed polymer (at the surface) could be estimated as 200 nanometers.

Fabrication of micro- and nanowires via electrodeposition

The standard electrodeposition process was used for filling the pores and obtaining of replicas. Different types of metals – Cu, Ag, Ni and Co were used for filling of the pores. Specific features of galvanic processes in these cases were investigated. Different types of cells were utilized and the influence of ultrasound treatment was tested. All the samples obtained had the following parameters (SEM-testing): the diameter - $0.1\text{--}2.0\text{ }\mu\text{m}$, the height - up to $10\text{ }\mu\text{m}$ (for cylindrical wires); the base - $0.1\text{--}1.5\text{ }\mu\text{m}$, the height - up to $5\text{--}10\text{ }\mu\text{m}$ and the cone angle- $5^\circ\text{--}25^\circ$ (for conical wires).

All processes of electrodeposition were done in potentiostatic regimes (at constant potential) with recording the dependence of current on time.

For copper the standard electrodeposition process (electrolyte: $\text{CuSO}_4 - 135\text{ g/l}$ and $\text{H}_2\text{SO}_4 - 15\text{ g/l}$, room temperature) was used for filling the pores and obtaining of replicas. Specific features of electrodeposition into the dead-end pores of conical shape is that in this case we have to carry out all the procedures (vacuum deposition of conductive layer and electrodeposition of metal) at one side of the membrane. A short ultrasound treatment (before the electrodeposition) improved the homogeneity of obtained ensembles- probably because of removing of air bubbles out of the pores. The dependences of current on time for deposition of copper into the matrixes with cylindrical and conical pores were measured.

Other results are for deposition of cobalt into the cylindrical pores of template matrix. In contrast to copper, cobalt is deposited with high cathodic overpotential. Electrodeposition of cobalt can hardly be obtained under low overpotential because of low rate of cobalt ions discharge. However, too high overpotential will cause abundant hidrogen discharge because of low concentration of cobalt ions in the cathodic layer. The higher is the concentration of cobalt, the higher rate of reaction (and overpotential) is allowed, that is why an electrolyte with high concentration of cobalt was used : $\text{CoSO}_4 \cdot 7\text{H}_2\text{O} - 320\text{ g/l}$, boric acid- 40 g/l , temperature $40\text{--}45\text{ }^\circ\text{C}$. Since the electrolyte has no electro-conductive additives, the ions of cobalt are delivered to the cathode by both

processes: migration and diffusion, so the higher current densities can be reached.

Dependence on potential. It was shown that more negative potentials correspond to higher cathode currents, higher growth rate of metal rods and less time required to complete filling the pores with the metal. This dependence is monotonic. Overgrowing time depends slightly on the pore diameter in the examined range of diameters.

Dependence on the pores diameter. The growth rate remains approximately constant in the process of metallization of pores with diameter of 0.5 microns at potentials -555, -530, -505 mV, and at more negative potentials (-580, -630, -680 mV) it increases slightly with time. The independence of current on time at this phase indicates that the diffusion of metal ions from the depths of electrolyte being balanced with consumption of discharging ions by the cathodic process. When filling pores of a small diameter the current dependence on time passes through a minimum, especially pronounced for smaller diameter pores, where the relative slowdown is most significant. Thus, in the pores of small diameter (0.1 and 0.2 microns) the effect of deceleration of the wires growth rate is observed in the process of electrofilling the pores. At the same time, the curve "current – time" is linear. It can be supposed that the difficulties, appearing while filling micro- and nanosized pores, are related to the peculiarities of diffusion in narrow channels.

It should be noted also the high current densities, which occur when metal is being deposited into micro- and nano-sized pores – up to 100 A/dm^2 . At the same time the current density establishes at 15 A/dm^2 (for growing metal fills the whole surface of the sample). The additional investigation are needed to explain this effect.

The investigation of Co deposition into the conical pores is now in progress.

Mass-spectra, optical properties and stability

In our previous works the possibility of ion-beam formation (for the molecules of the probe, deposited on such surface with microwires) in the Mass-spectrometer was demonstrated. In this work the peculiarities of this ion emission were investigated. The surfaces with copper wires were used as the substrates for deposition of the probe in mass-spectrometer. We found that using of such a surface leads to increasing of the signal of mass-spectra (to compare with the flat copper surface). Conical wires with rather low surface density and aspect ratio 2-5 demonstrated the highest emission efficiency. It was found that intensity of mass-spectra signal non-linearly increases with increase of probe concentration and the intensity of laser pulse. At the same time this intensity decreases with the increasing of surface density of wires-possible, because of superposition, overlapping of the fields of neighboring wires.

Raman spectra of some probes deposited on such surfaces were also investigated – and increasing of the signal was detected. These effects could be connected with increasing of electrical field tension near the ends of NWs – due to so-called “lighting rod effect”. The effect of the samples destruction, degradation was also found and tested: after 100 pulses we observed melting and bending of wires. This process could be the reason of rather low efficiency and instability of ion emission.

Composite material –AFM investigations

Just after the deposition we obtain metal wires embedded in polymer matrix – this “composite material” is rather perspective. In our opinion it could be used in some practical application. Moreover it gave an additional possibility to investigate metal wires by AFM: it was done by using tapping and contact modes. For samples with wire diameters 100 nm and 50 nm conductivity was investigated. The I-V dependences (for single wire) were measured and demonstrated the linear character. Using these data two specific resistances were estimated – $1.8 \cdot 10^{-3}$ ohm · m and $2.5 \cdot 10^{-3}$ ohm · m (correspondingly).

Acknowledgements

To Prof. P.Apel (JINR, Dubna). This work was supported by Grants: RFBR 10-08-01009a and OFN RAS “New Materials and Structures” B65.

INFLUENCE OF γ -IRRADIATION ON OPTICAL PROPERTIES OF GaSe CRYSTALS

Yurij I. Zhirko^{1*}, Nikolaj A. Skubenko¹, Vladimir I. Dubinko²,
Zakhar D. Kovalyuk³, Oleg M. Sydor³

1 Institute of Physics NAS of Ukraine, 46 Prospekt Nauki, 03028, Kiev, Ukraine

2 NSC Kharkov Institute of Physics and Technology, 1 Akademicheskaya Str., 61108, Kharkov, Ukraine

3 Chernivtsy Department of Institute for Material Science Problems, 5 Iriny Vilde Str., 58001, Chernivtsy, Ukraine

ABSTRACT

Performed in this work are low-temperature ($T = 4.5\text{K}$) investigations of exciton photoluminescence spectra in layered GaSe crystals both non-doped and doped with Zn and Sn in concentrations < 0.01 wt. %. The crystals were irradiated with γ -quanta of the energy within the range 0 to 34 MeV with the doses up to 10^{14} γ/cm^2 . It has been shown that irradiation with the above doses results in improvement of quality in non-doped GaSe crystals: there disappears the “thin structure” of the emission line inherent to free excitons related with stacking fault defects of crystalline layers, observed is ordering the sets of bound exciton lines related with deep acceptors. As a consequence, there observed is an essential increase in the parameter S_0 – integrated intensity of radiative recombination of free and bound excitons.

Analogous changes related with healing of defects in GaSe crystalline lattice are observed after doping with Zn impurity. Irradiation of these crystals with γ -quanta causes increasing S_0 , too. By contrast, doping with Sn impurity results in a sharp drop of S_0 that begins to grow after irradiation with γ -quanta.

Key words: GaSe, layered crystals, γ -quanta, semiconductor sensors

INTRODUCTION

GaSe layered crystals are related to A^3B^6 binary compounds. Due to sharp anisotropy of their chemical bonds – strong ion-covalent ones inside layers and weak van-der-Waals between layers – GaSe crystals can be easily intercalated both with atoms and molecules, which makes them to be promising materials for hydrogen energetics [1, 2], accumulators of electric energy [3], and heterostructures with high photosensitivity based on them can be applied in solar cells [4-6].

At the same time, it seems interesting to investigate influence of γ -irradiation on optical properties of these crystals with the aim to use them as components of sensors for ionizing radiation.

* e-mail: zhirko@nas.gov.ua, tel: (+38)0442396637

EXPERIMENTAL METHODS AND SAMPLE MANUFACTURING

GaSe single crystals, both pure and intentionally doped with impurities, were grown using the Bridgmann method. The concentration of Zn and Sn impurities in charge did not exceed 0.01 wt. %.

To study the irradiation influence on optical properties, we chipped the plates with the thickness 3 to 5 mm from GaSe ingots and then cut the samples with dimensions $5 \times 5 \text{ mm}^2$ from these plates.

Prepared by this way semiconductor samples was irradiated with γ -quanta in the electron accelerator providing the electron energy 35 MeV and average beam current close to 250 mA. The electron beam was converted into bremsstrahlung on tantalum target. The samples were placed at the angle 90° relative to the incident electron beam. Irradiation was carried out with γ -quanta possessing energies within the range 0 to 34 MeV. The spectrum of γ -quanta from a thick tantalum converter was calculated using the program "GEANT". Duration of exposure was chosen in such a manner that could provide the necessary fluence of γ -quanta within the interval 10^{11} to $10^{15} \gamma/\text{cm}^2$.

Quality of reference and irradiated crystals, the amount of impurities in them as well as their distribution in crystals were checked using the optical transmission microscope Carl Zeiss Primo Star 5 providing the 1000-fold magnification and electron scanning microscope Zeiss EVO 50 XVP with INCA ENERGY 450 detector.

Measurements of photoluminescence (PL) spectra were made using 0.6-m monochromator MDP-23 with the grating 1200 lines/mm. The spectral width of the slit did not exceed 0.25 meV during experiments. Investigations of PL spectra at $T = 4.5\text{K}$ were made using the helium cryostat A-255 designed in the Institute of Physics, NAS of Ukraine. It is equipped with the system UTRECS K-43 allowing to control the sample temperature within the range 4.2 to 350K with the accuracy 0.1K. Excitation of PL spectra was made using a current-wave semiconductor laser with the wavelength 532 nm and stable power 80 mW. Photomultiplier tube $\Phi\text{EY-79}$ served as a radiation detector.

RESULTS AND DISCUSSION

Fig. 1a shows electron-microscopic image of GaSe crystal surface, when the crystal does not contain any intentionally introduced impurity. These crystals are characterized by the presence of spherical formations with the size 100 to 500 nm. As shown in [2], these formations are inclusions of the amorphous phase inherent to red monoclinic β -Se precipitating in the course of growth into interlayer space of GaSe. These inclusions can be easily eliminated in the following annealing of crystals placed into an evacuated ampoule for 2 to 3 hours at $T = 400^\circ\text{C}$. There, residual selenium escapes from the crystal and is deposited on ampoule walls, and the inclusions observed in the electron microscope disappear.

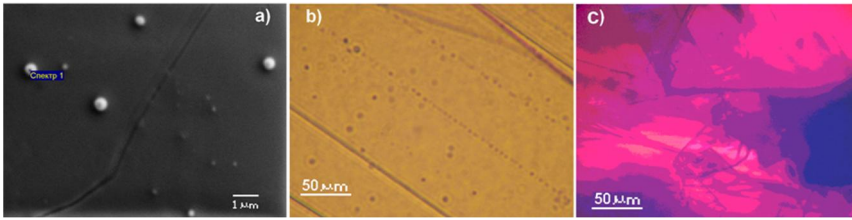


Fig. 1 – a) SEM image of undoped GaSe crystal sample obtained at 10000-fold magnification on Zeiss EVO 50 XVP scanned electron microscope, b) and c) image of GaSe crystal doped with 0.01 wt.% Zn and 0.2 wt.% Zn obtained on transmission optical microscope Carl Zeiss Primo Star 5 at 1000-fold magnification.

The investigations performed in this work using the INCA ENERGY 450 detector with energy dispersion showed that Zn and Sn impurities are inhomogeneously distributed in GaSe crystals even at low concentrations (0.01 wt. %).

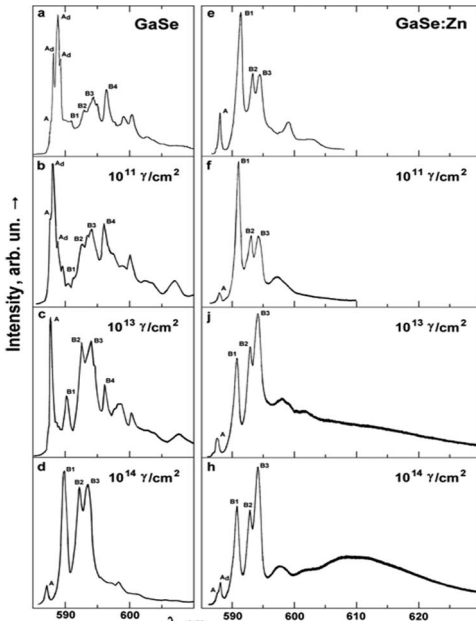


Fig.2. PL spectra of the non-irradiated (a) and irradiated with γ -quanta of the doses 10^{11} , 10^{13} and 10^{14} γ/cm^2 (b – d) GaSe crystals at $T = 4.5\text{K}$. (e – h) – PL spectra of the GaSe crystal doped Zn (0.01 wt. %) obtained in the same experimental conditions

doped with Zn (0.01 wt. %) GaSe crystals obtained at $T = 4.5\text{K}$ for the cases of crystals non-irradiated and radiated up to the doses 10^{14} γ/cm^2 . Low-

They are mainly accumulated in the vicinity of dislocations (*Fig. 1b*) generated by the very impurities in the growing process. When their concentration exceeds 0.1 wt. % (see *Fig. 1c*), the inhomogeneous distribution can be observed even in the optical microscope Primo Star 5.

Scanning the sample surface with an electron beam using the step 1 – 20 μm showed that the actual local concentration even at low its values 0.01wt. % can differ by 5 to 10 times in various parts of the crystal, while irradiation of the crystals with γ -quanta up to the doses 10^{14} γ/cm^2 does not result in any redistribution of impurities and does not influence on quality of studied crystal surfaces.

Depicted in *Fig. 2* are the PL spectra of non-doped and doped with Zn (0.01 wt. %) GaSe crystals obtained at $T = 4.5\text{K}$ for the cases of crystals non-irradiated and radiated up to the doses 10^{14} γ/cm^2 . Low-

temperature emission spectra of non-doped GaSe crystals are well studied [7]. They are characterized (see *Fig. 2a* and *Table 1*) by the presence of the “thin structure” inherent to A-line of free exciton emission as well as a wide set of B1 to B4 emission lines related to bound excitons. Besides, there is a band at 610 nm attributed to point defects.

The presence of the “thin structure” inherent to free excitons in GaSe is, as a rule [8, 9], related with stacking fault defects of crystal layers, and availability of bound excitons – with various point defects inside these layers.

As it is seen from *Fig. 2*, γ -irradiation of non-doped crystals up to the doses $10^{11} \gamma/\text{cm}^2$ does not result in essential changes of the spectrum. The following increase in the irradiation dose up to $10^{13} \gamma/\text{cm}^2$ results in the fact that there vanishing are: the “thin structure” of the line for free exciton (Ad-lines) as well as the group of lines for bound excitons. For the doses $10^{14} \gamma/\text{cm}^2$, the emission spectrum consists of A- and B1- to B4-lines of free and bound excitons.

Besides, *Table 1* and the insert in *Fig. 3c* show that with increasing the irradiation dose in non-doped GaSe crystals one can observe the three-fold increase in the parameter S_0 , where S_0 is the integrated intensity of radiative recombination (PL) of free and bound excitons reduced to the initial (non-irradiated and non-doped) GaSe crystal.

Table 1

Crystal; irradiation doses, γ/cm^2	Wave length of emission line maximum, nm					S_0
	A, Ad	B1	B2	B3	B4	
GaSe	587.8, 588.1, 588.6, 589.3	590.9	592.6	594.1	596.5	1
10^{11}	587.8, 588.1, 588.9, 589.3	590.9	592.6	594.1	596.6	1.3
10^{13}	587.8	590.2	592.6	594.0	596.3	2
10^{14}	587.4	590.0	592.4	593.5	597.4	3.1
GaSe:0.01Zn	587.8	591.2	593.0	594.2	598.6	1.5
10^{11}	588.0	591.0	593.0	594.2	597.1	1.2
10^{13}	587.7	590.8	593.0	594.2	598.1	1.6
10^{14}	587.7, 588.2	591.0	592.9	594.4	597.8	2.8
GaSe:0.01Sn	587.2	591.7	-	594.2	596.7	0.05
10^{11}	587.2	591.7	-	594.2	596.7	0.04
10^{13}	587.6	591.4	593.3	595.7		0.06
10^{14}	587.6	591.2	593.0	595.5		0.12

This transformation of the spectrum for the non-doped GaSe crystal as well as increase of S_0 indicate improved quality of the crystalline structure in the process of γ -quantum “annealing”, as a consequence of reduced amount both of point defects and the layer packing ones. In its turn, it leads to reduced decay (scattering) of free excitons by lattice defects and increased their lifetime, which causes growth of the integrated intensity of exciton radiative recombination.

Analogous changes related with a lowered amount of emission lines for excitons related with lattice defects were observed earlier after isothermal annealing of GaSe crystals [10], however, as shown in [11], multiple irradiation of these crystals with power laser pulses at the wavelengths lower than the forbidden gap width results in essential extinction of the PL spectrum.

As a rule, GaSe crystals possess p -type conduction. Due to various growth technologies, there present are deep acceptor levels located 80 to 150 meV above the valence band [12, 13]. Therefore, in accord with [14], doping the Ga^{++} vacancies [8] with low concentrations of iron group impurities being in the $2+$ charge state results in healing of point defects in the crystalline structure of GaSe.

Indeed, as seen from *Fig. 2e*, doping with the Zn impurity possessing the concentration 0.01 wt. % also results in healing of point and packing defects in crystalline layers – there remain only lines for free exciton and those bound with deep acceptors. In this case, the spectrum of non-irradiated GaSe:0.01Zn crystals (*Fig. 2e*) becomes practically identical with that of non-doped GaSe crystal irradiated with high doses of γ -quanta (*Fig. 2d*), and the integrated radiation intensity S_0 becomes even a little higher than that in non-doped non-irradiated GaSe. Like to the case of non-doped crystals, increasing the γ -irradiation dose for the crystals GaSe:0.01Zn results in growth of the parameter S_0 . Thereof, one can conclude that doping the GaSe crystals with Zn impurity in low concentrations and γ -irradiation of non-doped GaSe crystals lead to healing of point defects in the crystalline lattice and ordering the crystal layers.

Indeed, Zn impurity (possessing two valence electrons), when substituting Ga^{++} vacancies in crystalline layers, could recover covalent bonds between Ga and Se atoms, which essentially improve crystal quality. However, contrary to two-valence Zn, the Ga atom belonging to the third group in Periodic Table possesses three valence electrons that form in GaSe hybrid s - p bond with Se. Here, two electrons form covalent bonds with three Se atoms, which complete $4p$ -shells of Se atoms, and the residual electron being bound with the electron of the neighbor Ga atom completes their s -shells.

As a consequence, Zn impurity cannot heal the acceptor caused by absence of Ga atom in the layer. It only partially heals the crystal layer by binding some part of residual Se present in the interlayer space, and retains the Ga^+ vacancy (acceptor). When the irradiation dose increase, there arises a point

defect center, which causes appearance of the intense PL band around 610 nm. At the doses close to $10^{14} \gamma/\text{cm}^2$, the integrated intensity of this band becomes comparable with the radiation intensity of free and bound excitons (Fig. 2h).

In relation with the mentioned above, it seems also interesting to study the influence of doping the GaSe crystals with fourth-group impurities on PL spectra and their stability in the course of γ -irradiation. As this impurity, we chose Sn atoms that have four valence electrons and possess ability of the hybrid chemical *s-p* bonding. When substituting Ga vacancies, this impurity is able to recover covalent bonds both with Ga atoms inside the layer and with Se atoms precipitating into the interlayer space.

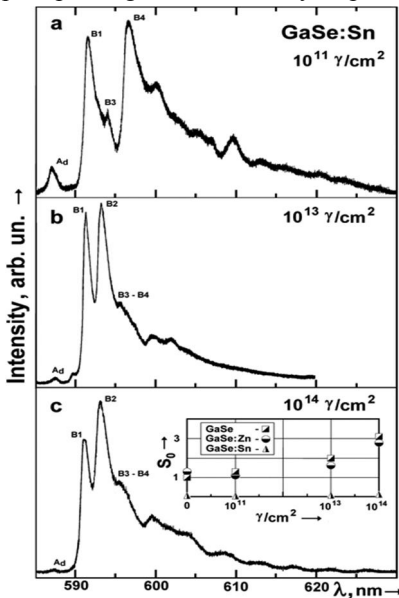


Fig. 3. PL spectra of GaSe:0.01Sn crystals (γ -irradiated with the doses 10^{11} , 10^{13} and $10^{14} \gamma/\text{cm}^2$) measured at $T = 4.5\text{K}$ (a - c). In the insert: dependence of the parameter S_0 on the irradiation dose for the crystals GaSe, GaSe:0.01Zn and GaSe:0.01Sn under the same temperature conditions

This sharp decrease of the parameter S_0 when doping GaSe crystals with Sn needs special further investigation. Perhaps, this impurity creates centers (defects) that are able to efficiently quench secondary radiation due to radiationless recombination of excitons on them. To confirm this assumption our

In this case, Sn impurity has one excess electron that may create a deep donor level in the forbidden gap. Perhaps, just these levels located 350 – 400 meV below the conduction band bottom were observed in [8, 15].

It should be noted that the grown GaSe:0.01Sn crystals as well as studied by us GaSe crystals both Zn-doped and non-doped possess mirror chipped surfaces. However, contrary to Zn-doped and non-doped crystals, their integrated radiation intensity S_0 at $T = 4.5\text{K}$ (see Table 1) was about 5% of a pure GaSe crystal. PL spectra of these crystal are not changed with increasing γ -irradiation doses up to $10^{11} \gamma/\text{cm}^2$; one can clearly observe PL emission within the range typical for free and bound excitons (see Fig. 3a). But as it can be seen in the insert to Fig. 3c and in Table 1, S_0 parameter begins to grow with next increasing the γ -irradiation dose, while the structure of emission spectrum tends to be closer to that of Zn-doped and non-doped GaSe crystals.

preliminary investigations of conductivity have shown that GaSe:0.001Sn are low-resistant instead to high-resistant pure GaSe.

CONCLUSIONS

It has been shown that γ -irradiation with the doses up to 10^{14} γ/cm^2 results in improvement of quality in non-doped GaSe crystals: there disappears the “thin structure” of the emission line inherent to free excitons related with stacking fault defects in crystalline layers, observed is ordering the sets of bound exciton lines related with deep acceptors. As a consequence, there observed is an essential increase in the parameter S_0 – integrated intensity of radiative recombination of free and bound excitons.

Analogous changes related with healing of defects in GaSe crystalline lattice are observed after doping with Zn impurity. Irradiation of these crystals with γ -quanta causes increasing S_0 , too. By contrast, doping with Sn impurity results in a sharp drop of S_0 that begins to grow after irradiation with γ -quanta.

Acknowledgements

This work was funded by joint STCU and NAS of Ukraine project #22-5228/10.

REFERENCES

- [1] Yu. I. Zhirko, Z. D. Kovalyuk, M. M. Pyrlja, V. B. Boledzyuk T.N., in book Hydrogen Materials Science and Chemistry of Carbon Nano-materials (Eds. N.T.Vezirogly et al.) © Springer, 2007, P. 325-340.
- [2] Yu.I. Zhirko, Z.D. Kovalyuk, V.V. Trachevsky, A. K. Mel'nik, Seventh International Conference on Inorganic Materials, Biarritz, France, Sept., 12-14, 2010, P.2.72.
- [3] I.I. Grigorchak, A.V. Zaslonskin, Z.D. Kovalyuk at all., Patent of Ukraine 2002, Bulletin No5, No46137.
- [4] A. A. Lebedev, V.Yu. Rud', Yu.V. Rud', Fiz.Tekch.Polupr, 1998, V.32, P. 353-355.
- [5] J. Martinez-Pastor, A.Segura, J.L.Valdes, J. Appl. Phys., 1987, V. 62, P. 1477-1483.
- [6] S. Shigetomi, T. Ikari, J. Appl. Phys., 2000, Vol. 88, P. 1520-1524.
- [7] Yu.P. Gnatenko, Z.D. Kovalyuk, P.A. Skubenko, Yu.I. Zhirko, Phys. st. sol.(b), 1983, Vol.117, No 1, P.283-287.
- [8] J.J.Forney, K.Maschke, E.Moozer, Nuovo Cimento, 1977, V.38B, No 2, P. 418-422.
- [9] N. Kuroda, Y. Nishina, Nuovo Cimento, 1976, Vol. 32B, No 1, P.109-115.
- [10] Yu.P. Gnatenko, P.A. Skubenko, Z.D. Kovalyuk, V.M. Kaminskii, Fiz. Tekhn. Polupr. (in Rus.), 1984, Vol. 18, No.7, P. 1300-1303.
- [11] P.E. Mozol', E.A. Salkov, N.A. Skubenko, P.A. Skubenko, Z.D. Kovalyuk, Fiz. Tverd. Tela (in Rus.), 1985, Vol. 27, No 12, P. 3696- 3699.
- [12] Ph. Schmid, J.P. Voitchovsky, A. Mercier, Phys. st. sol.(a), 1974, Vol. 21, No 2, P. 443-449.
- [13] Yu.I. Zhirko, Phys. st. sol.(b), 2000, Vol. 219, P. 47-62
- [14] Yu.P. Gnatenko, Z.D. Kovalyuk, P.A. Skubenko, Ukr. Fiz. Zhurn. (in Rus.), 1982, Vol.27, No 6, P.838-842.
- [15] S. Shigetomi, T. Ikari, H. Nishimura, Jap. J. App. Phys., 1991, Vol. 69, P. 7996 – 8001.

TEMPERATURE DEPENDENCE OF A PERIOD OF THE MODULATED STRUCTURE IN ATOM–VACANCY SOLID SOLUTION

Olena V. Oliinyk*, Valentyn A. Tatarenko

G.V. Kurdyumov Institute for Metal Physics, N.A.S.U.,
36 Academician Vernadsky Boulevard, UA-03680, Kyiv-142, Ukraine

ABSTRACT

The effective vacancy–vacancy interaction is considered. Based on the continuum approximation for the Fourier components of strain-induced vacancy–vacancy interaction energies, approximating expressions for their expansion coefficients are obtained depending on the elasticity moduli, longitudinal and transverse phonon frequencies, and vacancy-concentration-dependent lattice parameter. The behaviour of \mathbf{k} -dependent Fourier components of the strain-induced vacancy–vacancy interaction energies near the Brillouin zone centre, $A(\mathbf{n})+B(\mathbf{n})k^2$, is analysed. As shown, $A(\mathbf{n}) < 0$ and $B(\mathbf{n}) > 0$ along all the high-symmetry [100], [110], [111], $[\frac{1}{2}10]$ directions in reciprocal space for f.c.c. crystals with negative anisotropy factor. The criterion of modulated-structure formation for interacting vacancies in f.c.c. crystals is considered. Dependence of the modulated-structure period on temperature is plotted.

Key words: vacancies, strain-induced interaction, modulated structures

INTRODUCTION

Within the crystals under irradiation, modulated structures can be formed [1]. We consider the case when, due to irradiation, the vacancies were generated in f.c.c. crystal; then the irradiation was stopped. Another way to produce the atom–vacancy solid solution is a high-temperature quenching, which fixes a raised amount of pre-melting vacancies. At the initial stage of an annealing, the average concentration of vacancies is constant until vacancies have time to approach the surface or to disappear in sinks. The vacancy interactions are governing mechanism of formation of the modulated structures in vacancy-containing crystals.

RESULTS AND DISCUSSION

With decreasing temperature, T , or increasing concentration of vacancies (v), c , their interaction-caused drift begins dominating in their random motion, and the damping decrement becomes negative for every values of wave vector,

* e-mail: neutrino@ukr.net, tatar@imp.kiev.ua tel: +380 44 4241221

\mathbf{k} , which belongs to the sphere of a radius $k_0(T, c)$ about $\mathbf{k} = \mathbf{0}$, and the modulated structures appear. For $|\mathbf{k}| > k_0(T, c)$, the damping decrement is positive, and the modulated structures disappear [2].

A given paper is based on overrunning continuous approximation for the Fourier components, $\tilde{V}^{vv}(\mathbf{k})$, of the strain-induced vacancy–vacancy interaction energies. Within the finite region near $\mathbf{k} = \mathbf{0}$ [2, 3], the $\tilde{V}^{vv}(\mathbf{k})$ may be represented as follows: $\tilde{V}^{vv}(\mathbf{k}) \cong A(\mathbf{n}) + B(\mathbf{n})|\mathbf{k}|^2 + Q(\mathbf{n} = \mathbf{k}/|\mathbf{k}|)$. Here, the well-known first term is based on long-wave-limit approximation [2]; the second term is a correction to this approximation, and the third term is a gauge, which eliminates strain-induced self-action of vacancies. The transition to the direct-lattice space is defined according to the formula:

$$V^{vv}(\mathbf{r} - \mathbf{r}') = \frac{1}{N} \sum_{\mathbf{k} \in 1^{\text{st}} BZ} \tilde{V}^{vv}(\mathbf{k}) e^{i\mathbf{k} \cdot (\mathbf{r} - \mathbf{r}')} ,$$

where summation is carried out over all N \mathbf{k} -points of quasi-continuum within the 1st Brillouin zone (BZ) of f.c.c. lattice.

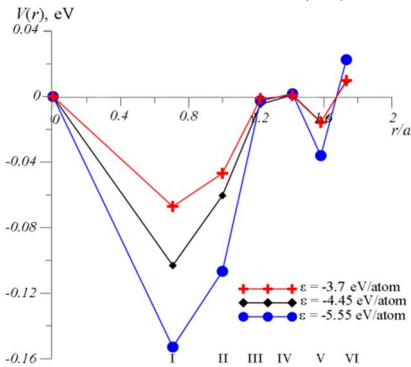


Fig. 1 – The dependence of the strain-induced vacancy–vacancy-interaction energies on the normalized radius of coordination sphere in a crystal with various cohesion energy, ε [3–5], which is used to estimate the concentration-dependent dilatation coefficient, L^v

In the direct-lattice space, the dependence of the strain-induced vacancy–vacancy interaction energy on the normalized radius of coordination sphere is shown in Fig. 1. One should pay attention to the quasi-oscillating and long-range character of the strain-induced vacancy–vacancy interaction energies. Thus, its contribution on distant coordination spheres can be dominant.

The modulated structure can be formed along those crystallographic direction, which is parallel to $\mathbf{n}_c = \mathbf{k}_c/|\mathbf{k}_c|$ corresponding to the highest growth rate and has the wave vector with a magnitude of

$$|\mathbf{k}_c| \cong \{-A(\mathbf{n}_c) + Q + \tilde{\varphi}_{\text{el.chem}}(\mathbf{0}) + k_B T / [c(1-c)] / [2(B(\mathbf{n}_c) + \gamma)]\}^{1/2} ;$$

$\tilde{\varphi}_{\text{el.chem}}(\mathbf{k})$ is the Fourier component of ‘mixing’ energies for direct ‘electrochemical’ interactions in atom–vacancy solid solution, k_B is the Boltzmann constant. Within the wave-length approximation, $\tilde{\varphi}_{\text{el.chem}}(\mathbf{k}) \cong \tilde{\varphi}_{\text{el.chem}}(\mathbf{0}) + \gamma|\mathbf{k}|^2$.

The ‘mixing’ energies, $\varphi_{\text{el.chem}}(r)$, for a solid solution are calculated with use of the Machlin potential [6] or the Morse potential [7] (Fig. 2).

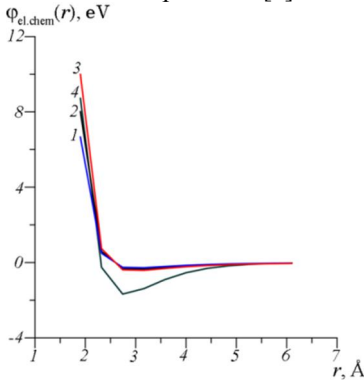


Fig. 2 – The ‘mixing’ energies, $\varphi_{\text{el.chem}}(r)$, for direct ‘electrochemical’ interactions in atom–vacancy solid solution based on a crystal with various cohesion energies, ε : (1) $\varepsilon = -3.7$ eV/atom [4], (2) $\varepsilon = -4.45$ eV/atom [3], and (3) $\varepsilon = -5.55$ eV/atom [5] in Machlin potential [6]; (4) Morse potential [7]

The approximated expansion coefficients for Fourier components of the strain-induced v – v -interaction energies are dependent on the elasticity moduli of f.c.c. crystals, C_{11} , C_{12} , C_{44} ; e.g.,

$$A[100] = -9K^2(L^v)^2 a_0^3 / (4C_{11}) \quad [2, 8],$$

$$B[100] \cong 9K^2 a_0^4 (L^v)^2 M \omega_L^2 / (256C_{11}^2),$$

where $K = (C_{11} + 2C_{12})/3$ —compressibility modulus, a_0 —an f.c.c.-lattice parameter, L^v —concentration coefficient of f.c.c.-lattice dilatation, M —the Ni atom mass, ω_L —the longitudinal-polarized phonon frequency at the high-symmetry X -point of the BZ surface. $B(\mathbf{n})$ is positive along all the high-symmetry $[100]$, $[110]$, $[111]$, $[\frac{1}{2}10]$ directions in reciprocal space for f.c.c. crystals with anisotropy factor $\xi \equiv (C_{11} - C_{12} - 2C_{44})/C_{44} < 0$. $B(\mathbf{n})$ increases with temperature along the $[100]$, $[110]$, $[111]$ directions (see Fig.3, where $L^v = -0.149$, $L^v = -0.124$, $L^v = -0.187$ were calculated using the Machlin potential, and $L^v = -0.0153$ corresponds to the Morse potential).

If $\xi < 0$, $\tilde{V}^{vv}(\mathbf{k})$ has a one-sided minimum along the $[100]$ direction, but it is greater than $\tilde{V}^{vv}(\mathbf{0})$ as a result of the long-range nature of strain-induced interaction. Besides, there are inequalities as follow:

$$\tilde{V}^{vv}(\mathbf{k}_{\parallel X\Gamma} \rightarrow \mathbf{0}) < \tilde{V}^{vv}(\mathbf{k}_{\parallel Y\Gamma} \rightarrow \mathbf{0}) < \tilde{V}^{vv}(\mathbf{k}_{\parallel K\Gamma} \rightarrow \mathbf{0}) < \tilde{V}^{vv}(\mathbf{k}_{\parallel L\Gamma} \rightarrow \mathbf{0}).$$

If $(A[100] + Q + \tilde{\varphi}_{\text{el.chem}}(\mathbf{0}) + k_B T / [c(1-c)]) / [2(B[100] + \gamma)] < 0$, where, e.g., within the scope of the Debye approximation,

$$Q \cong 9K^2(L^v)^2 (a_0^3/4) \langle (1 + 2\xi X + 3\xi^2 Y) / D(\mathbf{n}) \rangle_{\mathbf{n}},$$

$$D(\mathbf{n}) = C_{11} + \xi(C_{11} + C_{12})X + \xi^2(C_{11} + 2C_{12} + C_{44})Y,$$

$X = n_x^2 n_y^2 + n_x^2 n_z^2 + n_z^2 n_y^2$, $Y = n_x^2 n_y^2 n_z^2$, the modulated structure can appear along the [100] direction.

Dependence of the modulated-structure period on T is plotted in Fig. 4. With increasing temperature, the period of modulated structures increases.

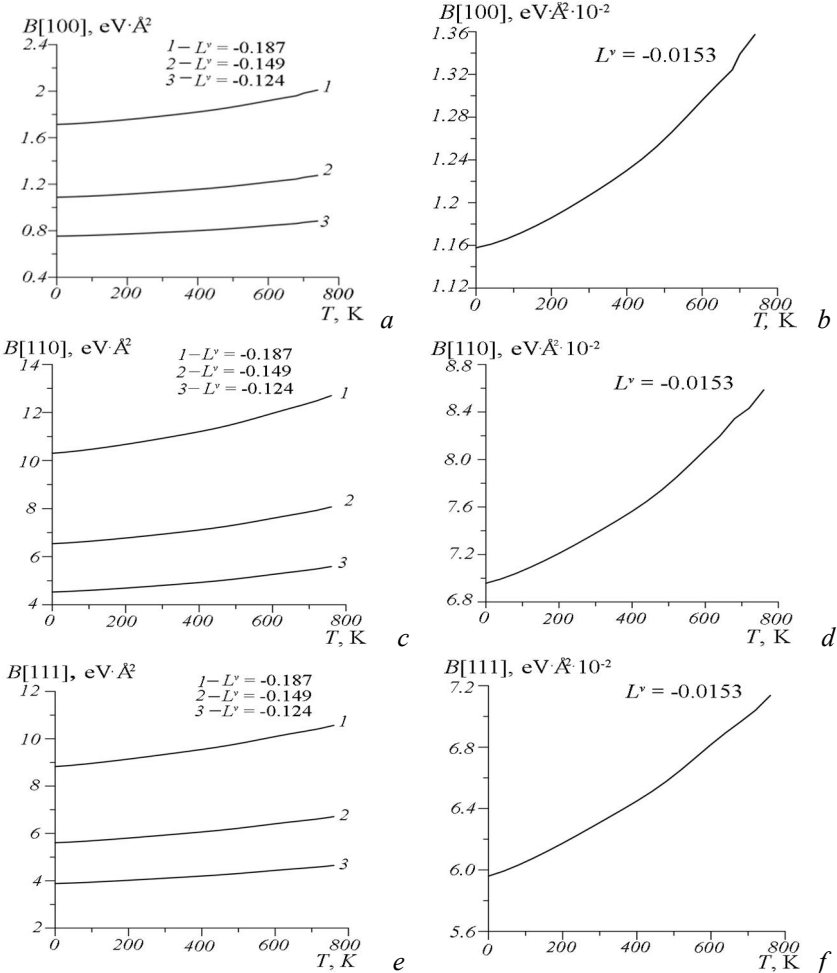


Fig. 3 – The temperature dependence of $B(\mathbf{n})$: a, b— $B[100]$, c, d— $B[110]$, e, f— $B[111]$

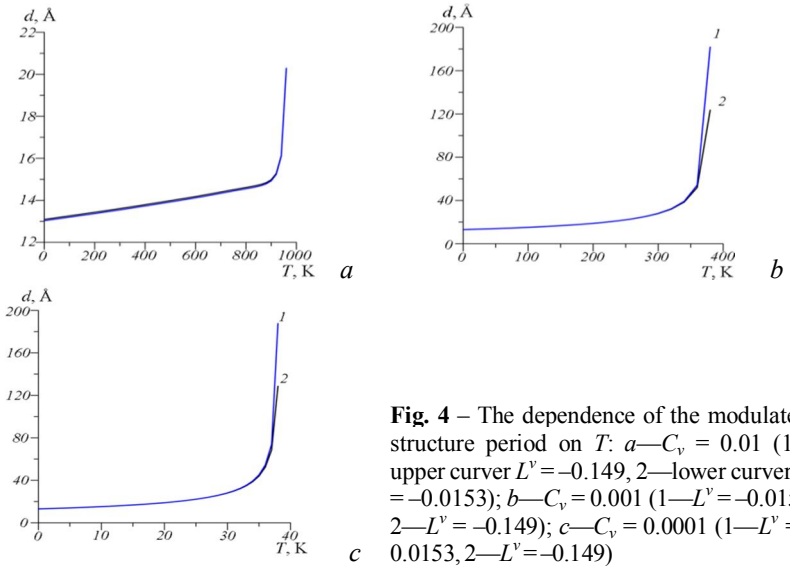


Fig. 4 – The dependence of the modulated-structure period on T : a — $C_v = 0.01$ (1—upper curve $L^v = -0.149$, 2—lower curve $L^v = -0.0153$); b — $C_v = 0.001$ (1— $L^v = -0.0153$, 2— $L^v = -0.149$); c — $C_v = 0.0001$ (1— $L^v = -0.0153$, 2— $L^v = -0.149$)

CONCLUSIONS

The strain-induced vacancy–vacancy interaction energy has the long-range and quasi-oscillating nature. As shown, $B(\mathbf{n})$ is positive along all the high-symmetry $[100]$, $[110]$, $[111]$, $[\frac{1}{2}10]$ directions in reciprocal space for f.c.c. crystals with negative anisotropy factor ($\xi \equiv (C_{11} - C_{12} - 2C_{44})/C_{44} < 0$) and increases with temperature. As revealed, the two vacancies are attracted at the distance of less than 7 \AA . At distances over 7 \AA , vacancies do not significantly interact with each other. An elevation of the temperature leads to increase of the period of modulated structure.

REFERENCES

- [1] C. Abromeit, *Int. J. Mod. Phys. B*, 1989, 3, P. 1303-1314.
- [2] A. G. Khachaturyan, *Theory of Structural Transformations in Solids*, New York, John Wiley&Sons, 1983.
- [3] L. Brewer in *High-Strength Materials*, Wiley, Zackay, V.F., Ed.; Wiley New York, 1965, p.12; L. Brewer, *The Cohesive Energies of the Elements LBL-3720*, Berkeley, California, May 4, 1977.
- [4] H. Brooks, *Transactions of the Metallurg. Soc. Aime*, 1963, 227, P. 546-555.
- [5] D. N. Movchan, V. N. Shyvyanyuk, B. D. Shanina, and V. G. Gavriljuk, *Phys. Status Solidi*, 2010, A 207 (8) P. 1796-1806.
- [6] E. S. Machlin, *Acta Metallurgica*, 1974, 20, P. 95-100.
- [7] L. A. Girifalco and V. G. Weizer, *Phys. Rev.*, 1959 114 (3), P. 687-693.
- [8] A. A. Katsnelson, A. I. Olemskoi, *Microscopic Theory of Inhomogeneous Structures*, Moscow, MGU Publ., 1987 (in Russian).

X-RAY and RAMAN INVESTIGATIONS OF LAYERED In- Se AND GaSe SINGLE CRYSTALS IRRADIATED WITH HIGH-ENERGY GAMMA-QUANTA

Zakhar D. Kovalyuk^{1*}, Volodymyr G. Tkachenko², Igor M. Maksymchuk²,
Oleg M. Sydor¹, Oksana A. Sydor¹, Volodymyr I. Dubinko³

1 Chernovtsy Department of Institute of Materials Science Problems, 5 I. Vilde Str., 58001, Chernovtsy, Ukraine

2 Institute of Materials Science Problems, 3 Krzhyzhanivskogo Str, 03142, Kyiv, Ukraine

3 NSC Kharkov Institute of Physics and Technology, 1 Akademicheskaya Str., 61108, Kharkov, Ukraine

ABSTRACT

In the present paper regularities of the effect of high-energy γ -quanta on the defects system of layered InSe and GaSe semiconductors is investigated by means of X-ray diffraction analysis and Raman scattering. It is established that the absorbed dose of γ -radiations in 140 kGy does not lead to changes of the crystal structure and a considerable modification of the lattices parameters of III-VI crystals that testifies to preservation of their structural perfection. This fact makes layered compounds attractive from the point of view of radiation resistance. The radiation influence comes to the appearance of point vacancy defects.

Key words: layered crystals, InSe, GaSe, high-energy irradiation, radiation hardness, Raman spectra, X-Ray diffraction

INTRODUCTION

Wide application of high-energy radiations in science, many technological processes, medicine, the safety in atomic power engineering demand a search of radiation-resistant materials and working out of electronic equipments capable to operate at high radiation levels.

A use of the semiconductors of modern electronics (silicon, gallium arsenide, and germanium) and dielectric layers of their intrinsic oxides shows insufficient radiation stability of based on them devices [1]. As the alternative to them one can consider anisotropic III-VI crystals with a layered crystalline structure, in particular InSe and GaSe [2]. The presence of weak Van-der-Waals bonds between the layers enables easily to gain substrates with atomically smooth surfaces that in a combination with simple production techniques (oxidation, Van-der-Waals contact) gives a possibility to create high-efficiency

* e-mail: chimsp@ukrpost.ua, tel: (+30)372525155 tel: (+30)372520050

photoconverters [3-5]. A considerable quantity of intrinsic defects in layered crystals allows to apply them under conditions of large radiation doses.

At present there is a great number of papers devoted to radiation physics of the classical semiconductors but researches of the influence of high-energy radiation on III-VI crystals is not less important.

METHODS OF SAMPLE MANUFACTURING AND IRRADIATION

InSe and GaSe single crystals were grown by the vertical Bridgman method. Intentionally undoped InSe had *n*-type conductivity with a concentration of uncompensated donors of $10^{14} - 10^{15} \text{ cm}^{-3}$ and a Hall mobility along the layers $\mu_n \sim 10^3 \text{ cm}^2 \text{ V}^{-1} \text{ s}^{-1}$ at 300 K. For obtaining *p*-type conductivity InSe was doped with 0.2 wt.% Cd what leads to the following parameters: $p = 10^{13} \text{ cm}^{-3}$ and $\mu_p \sim 10^2 \text{ cm}^2/\text{V}\cdot\text{s}$. In order to increase the electrical conductivity of GaSe, we doped this semiconductor with dysprosium in an amount of 0.1 wt %. At room temperature, the concentration and mobility of charge carriers were $\sim 5 \cdot 10^{14} \text{ cm}^{-3}$ and $35-50 \text{ cm}^2/\text{V}\cdot\text{s}$, respectively.

Investigated samples have a form of plane-parallel plates with average sizes $8 \times 8 \text{ mm}$ and about of 2 mm thick.

The samples have been irradiated bremsstrahlung γ -photon in the energy range of $0.5-11.5 \text{ MeV}$ with a maximum at 3 MeV at a linear electron accelerator KUT-10. The flux of γ -photon was about $2 \times 10^{11} \text{ cm}^{-2} \text{ s}^{-1}$, and the irradiation time was chosen so that to give the total γ -fluence $2 \times 10^{16} \text{ cm}^{-2}$ that corresponds to the absorbed dose 140 kGy .

X-ray diffraction (XRD) investigations of the samples were made in monochromatic $\text{CuK}\alpha$ -radiation with a DRON-UM1 diffractometer. Raman spectra of the crystals were excited by an argon laser with a wavelength of 514.5 nm and registered by a spectrometer DFS-24. All measurements were carried out at room temperature.

RESULTS AND DISCUSSION

The carried out analysis of the X-ray diffraction patterns of the initial InSe and InSe:Cd crystals before (*Fig. 1a* and *Fig. 2a*) and after (*Fig. 1b* and *Fig. 2b*) irradiation with fluence $10^{16} \text{ } \gamma \text{ cm}^{-2}$ enables to conclude that in all the states these crystals are single phase InSe of the 3R structure. The measurements of the unit cell parameters by using the Bond method at 110 and 0027 reflections indicate on the γ -polytype of InSe (the space group $R\bar{3}m$). A typical feature of the X-ray diffraction patterns for the samples under investigation is the presence of diffusion maxima nearby the 009, 00.12, and 00.18 peaks of the 3R structure. These peaks are situated from the side of smaller angles and can be interpreted as caused by the stacking faults in the 3R structure, which lead to stacking of the layers typical for the 2H structure of InSe ($P6_3/mc$). Similar results are received for *p*-GaSe crystals (*Fig. 3a* and *Fig. 3b*) with the 4H struc-

ture (the space group $P6_3/mc$). As one can see from Figs. 1-3, there are no essential changes in the crystals after irradiation with γ -quanta except for a small decrease (in the case of InSe) or increase (for GaSe) of the lattice parameters.

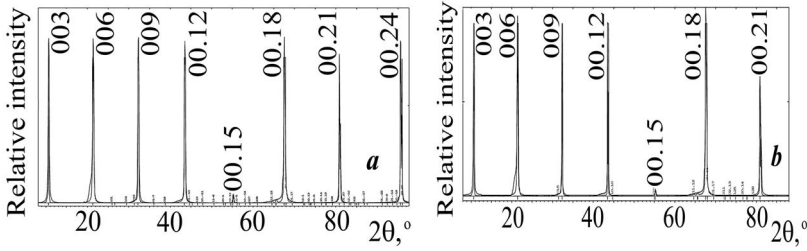


Fig. 1. - XRD spectra of the initial *n*-InSe crystal (a) and irradiated (b).

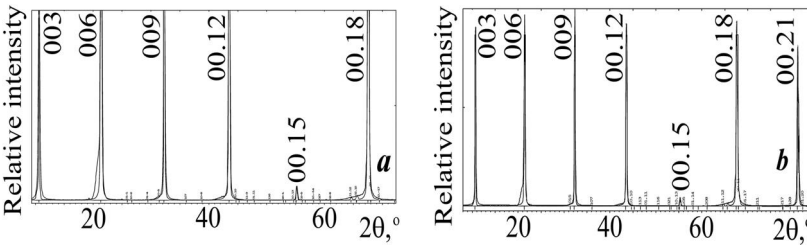


Fig. 2. - XRD spectra of the initial *p*-InSe crystal (a) and irradiated (b).

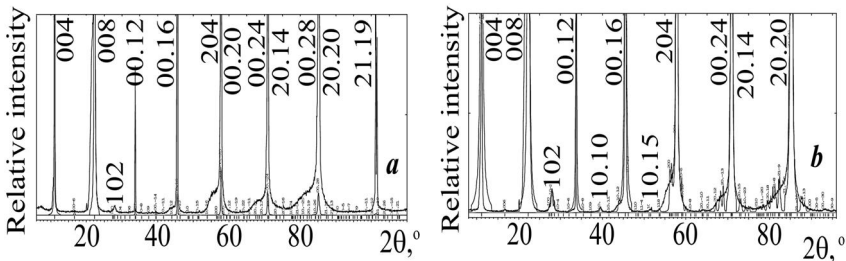


Fig. 3. - XRD spectra of the initial *p*-GaSe crystal (a) and irradiated (b).

The Raman spectra of *n*-InSe and *p*-InSe crystals in the initial state (Fig. 4a, curves 1 and 2, respectively) are very similar each other, except for a small transferring intensity between the two bands in the range of 215 and 230 cm^{-1} . Note that in the *p*-InSe sample the band at 215 cm^{-1} , which is caused by the presence of Cd atoms, is more well expressed. The Raman spectra of the irradiated *n*-InSe and *p*-InSe crystals contain the bands at frequencies 120.8,

184.8, 205.7, 218.0, 231.8, 409.3, and 430.3 cm^{-1} (Fig. 4a, curves 3 and 4, respectively). These bands correspond to those known from the literature Raman spectra of InSe [6]. Only insignificant transferring relative intensities between the bands in the spectra of different samples was observed. It is caused by different defect concentrations in these samples after their irradiation. Other peculiarities related to a change of atoms coordination were not found.

The Raman spectrum of the *p*-GaSe sample (Fig. 4b, curves 1) sharply differs from that of InSe. It does not contain the doublet band at 410-420 cm^{-1} but has intensive bands at frequencies 260 and 215 cm^{-1} and as well as the intensive band at 175 cm^{-1} what is typical for GaSe crystals [7]. The Raman spectra of irradiated GaSe crystals (Fig. 4b, curves 2) contain narrow lines at frequencies 138.7, 216.6 and 313.5 cm^{-1} . One can also see some redistribution between the relative intensities of the lines above. Other features related to changes of the atom coordination have not been observed.

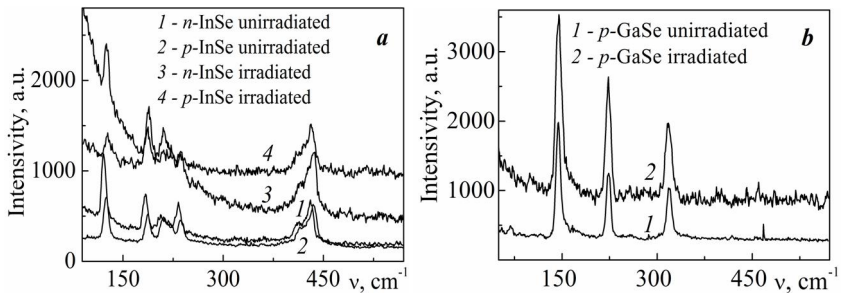


Fig. 4. - Raman spectra of InSe (a) and GaSe (b) crystals.

Thus, one can conclude that irradiation of the layered crystals has not led to qualitative changes in the investigated Raman spectra which are extremely sensitive to variation of the coordination of Raman scattering centres. The conclusion about insignificant influence of irradiation with γ -quanta at fluences up to $5 \cdot 10^{15} \text{ cm}^{-2}$ on a change of the vacancy and impurity subsystems in layered crystals is indirectly confirmed by the authors of [8].

CONCLUSIONS

Thus, irradiation of layered crystals does not result in qualitative changes of the investigated spectra, including Raman one, which is extremely sensitive to changes in the coordination of Raman scattering centres. It is possible to say about saving structural perfection of these semiconductors against the background of radiation-induced defects.

The obtained results prove the resistibility of III-VI crystals lattice for γ -radiation that is especially important for the case of the mixed bonding in them:

strong ionic-covalent bonding within the layers and weak Van-der-Waals between neighboring layers.

It is possible to put forward a preliminary hypothesis that Cd atoms in In-Se and Dy atoms in GaSe act as centres of the localization of radiation vacancies, whereas in the intentionally undoped compounds the vacancies are localized in the sublattices In or Ga.

REFERENCES

- [1] Radiation Effects in Semiconductors (Eds. V.S. Vavilov, N.P. Kekelidze, L.S. Smirnov) Nauka, Moscow, 1988.
- [2] J.S.J.M. Terhell, Prog. Cryst. Growth and Charact., 1983, Vol. 7, P. 55-110.
- [3] J. Martinez-Pastor, A. Segura, J.L. Valdes, A. Chevy, J. Appl. Phys., 1987, Vol. 62, No4, P. 1477-1483.
- [4] Z.D. Kovalyuk, V.M. Katerynychuk, A.I. Savchuk, O.M. Sydor, Mater. Sci. Eng. B, 2004, Vol. 109, P. 252-255.
- [5] S. Shigetomi, T. Ikari, J. Appl. Phys., 2000, Vol. 88, No3, P. 1520-1524.
- [6] N. Kuroda, Y. Nishina, Sol. State Commun., 1979, Vol. 30, No2, P. 95-98.
- [7] N.M. Gasanly, A. Aydinli, H. Özkan, C. Kocaba, Materials Research Bulletin, 2002, Vol. 37, No1, P. 169-176.
- [8] T.D. Ibragimov, E.A. Dzhafarova, Z.B. Safarov, Semiconductors, 2002, Vol. 36, P. 805-810.

INVESTIGATION ON THE EFFECTS OF TITANIUM DIBORIDE PARTICLE SIZE ON RADIATION SHIELDING PROPERTIES OF TITANIUM DIBORIDE REINFORCED BORON CARBIDE-SILICON CARBIDE COMPOSITES

Bulent Buyuk^{1*}, A. Beril Tugrul¹, A. Cem Akarsu², A. Okan Addemir²

1 ITU Energy Institute, Nuclear Science Division, Ayazaga Campus, 34669, Istanbul, Turkey

2 ITU Metalurgical and Materials Engineering Faculty, Ayazaga Campus, 34669, Istanbul, Turkey

ABSTRACT

Composite materials have wide application areas in industry. Boron Carbide is an important material for nuclear technology. Silicon carbide is a candidate material in the first wall and blankets of fusion power plants. Titanium diboride reinforced boron carbide-silicon carbide composites which were produced from different titanium diboride particle sizes and ratios were studied for searching of the behaviour against the gamma ray. Cs-137 gamma radioisotope was used as gamma source in the experiments which has a single gamma-peak at 0.662 MeV. Gamma transmission technique was used for the measurements. The effects of titanium diboride particle size on radiation attenuation of titanium diboride reinforced boron carbide-silicon carbide composites were evaluated in related with gamma transmission and the results of the experiments were interpreted and compared with each other.

Key words: Nanocomposite, Boron Carbide, Titanium Diboride, Silicon Carbide, Cs-137 Gamma Source, Gamma Transmission Technique

INTRODUCTION

Boron carbide has wide application areas in industry. Some of these areas are nuclear technology, military industry, ceramic industry and air-space industry [1, 2]. Boron carbide has some important properties such as low-density, high hardness and corrosion resistance, chemical stability and high neutron capture feature [2]. Some boron carbide application fields are lightweight ceramic armor, sand blasting nozzles, nuclear reactors, reactor control rods and the radiation shielding materials [2, 3]. However, boron carbide is brittle, has low strength and high temperature sintering properties [3, 4]. Sintering of pure boron carbide to high densities is difficult. So, specific additives such as SiC, TiB₂, AlF₃, elemental boron and carbon have been used as sintering aids to increase the density of composite [2-5]. Silicon carbide has been considered as a candidate material in the first wall and blankets of future fusion power plants because of its safety, environmental and economic benefits [6].

* e-mail: buyukbu@itu.edu.tr , tel: (+90)2122853894

In this study, titanium diboride reinforced boron carbide- silicon carbide composites which were produced from different titanium diboride particle sizes and ratios were studied for searching of the behaviour against the gamma ray. For the investigation of the gamma radiation behaviour of these materials, Cs-137 radioisotope was used as gamma source in the experiments. Cs-137 gamma radioisotope source has a single gamma-peak at 0.662 MeV and its half life is 30.1y [7, 8]. Gamma transmission technique was used for the measurements.

Different titanium diboride particle sizes and ratios in titanium diboride reinforced boron carbide-silicon carbide composites were evaluated in related with gamma transmission and the results of the experiments were interpreted and compared with each other. Therefore, the effects of boron carbide particle size in titanium diboride reinforced boron carbide-silicon carbide composites on gamma radiation attenuation were investigated against Cs-137 gamma radioisotope source by using gamma transmission technique.

EXPERIMENTS AND MATERIALS

Gamma transmission technique is based on passing gamma rays through the materials. Detector and gamma source put both sides of the material. Detector material and gamma source are in the same axis. The gamma radiation counts are measured reaching to detector from the source. The counts with material and without material are compared and evaluate [7-9]. Fig.1 shows schematic view of gamma transmission technique.

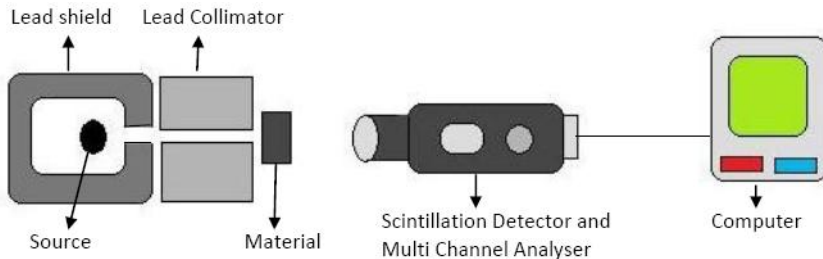


Fig. 1. Schematic View of Gamma Transmission Technique

The radiation passing through the material is calculated by the following equation: where I and I_0 are the transmitted and initial gamma ray intensities, respectively, μ is linear attenuation coefficient of material at specific γ - ray and x is the thickness of the material.

$$I = I_0 e^{-\mu x}$$

The materials which were used in the experiments have different boron carbide particle size ratios in the composites. Thus they are coded according to their boron carbide and titanium diboride ratios by volume in composites and

particle size ratios. *Table 1* shows the materials that used in the experiments and their ratios by volume in the composite materials.

Table 2 shows the hardness, strength and density properties of the materials which were used in the experiments [5].

For production of nano scale titanium diboride, titanium diboride materials were milled in Spex 8000 mill for one hour with WC balls.

All composite materials were sintered at 2250 °C for 2 hours under 130 MPa pressure. Cs-137 Gamma Radiation source which has 8.9 μCi was used in the experiments. Lead blocks were used for radiation shielding and collimation. The collimator diameter is 7 mm. The distance between the detector and source is 10 cm.

Firstly background radiation measured. Then Cs-137 Gamma source was set. Initial intensity count (I_0) was measured. Then materials were set and intensity counts (I) were measured for different thickness values. All counts were measured three times for 600 seconds. Net counts calculated by reducing background value. Average values and standard deviations were calculated. For rational evaluating, relative intensity (I/I_0) values were calculated. Results were given with tables. Relative intensity-Material Thickness Graph was drawn for each Titanium diboride ratio and particle size. Exponential distribution was shown on graphs and exponential equations were calculated. Then results were evaluated and discussed.

RESULTS AND DISCUSSION

Results for 8202_b, 8202_k, 8204_b, 8204_k, titanium diboride reinforced boron carbide-silicon carbide composites at different thicknesses with Cs-137 Gamma source are given on table 3, table 4, table 5 and table 6.

Using the values on the tables Relative Intensity-Material Thickness Graphs were drawn for all titanium diboride reinforced boron carbide-silicon carbide composites. Exponential fitted equations were calculated. Figure 3 shows Relative Intensity-Material Thickness Graphs of all boron carbide-Titanium diboride composites.

Using the graphs on fig 3 the linear attenuations of the composite materials and correlation coefficients were calculated. The linear attenuation values and correlation coefficients of the composites are given on table 6.

The mass attenuation coefficients (μ/ρ) of the composite materials were calculated. The linear attenuation coefficients of milled titanium diboride reinforced boron carbide-silicon carbide composites are higher than unmilled reinforced ones.

CONCLUSIONS

It could be understood that for 8202_k the linear attenuation coefficient is higher than 8202_b. For 8204_k the linear attenuation coefficient is higher than

8204_b. The experimental values and theoretical values from XCOM are closed to each other.

In conclusion, 8202_k and 8204_k composite materials are more convenient than 8202_b and 8204_b for gamma radiation shielding in nuclear technology.

Acknowledgements

The authors are thankful to BMBT Co. for production of materials.

REFERENCES

- [1] Büyük B., Tuğrul A.B., Akarsu A.C., Addemir A.O., 2011. Investigation of Behaviour of Titanium Diboride Reinforced Boron carbide-Silicon carbide composites Against Cs-137 Gamma Radioisotope Source by Using Gamma Transmission Technique. Advances in Applied Physics&Materials Science Congress Book of Abstracts Vol.1,pp 486
- [2] Thevenot F., 1990. Boron Carbide – A Comprehensive Review, Journal of European Ceramic Society, 6, pp205-22
- [3] Cho N., 2006. Processing of Boron Carbide, Ph. D.Thesis, pp5-6-7-9, Georgia Institute of Technology.
- [4] Aktop S., 2010. An investigation on the effects of sub micron boron carbide addition and reaction sintering to the boron carbide-titanium diboride composites. M.Sc. Thesis. ITU Institute of Science and Technology. Istanbul.
- [5] Akarsu A.C. 2009. An investigation on the properties of titanium diboride hot pressed boron carbide-silicon carbide composites. M.Sc. Thesis.ITU Institute of Science and Technology. Istanbul.
- [6] Taylor N.P., Cook I., Forrest R.A., et al. Fusion Engineering and Design, 2001. - 58-59,991-995
- [7] Halmshaw, R., 1991. Non-Destructive Testing. E. Arnold, London
- [8] Büyük B., Tuğrul A.B., 2009. Thickness measurement for the different metals by using Cs-137 gamma source with gamma transmission technique. X. National Nuclear Science and Technologies Congress full text edition, pp 49-58.Mugla
- [9] Földiák, G., 1986. Industrial Application of Radioisotopes, Elsevier, Amsterdam
- [10] Berger M.J., Hubbell J.H., Seltzer S.M., et al. XCOM: photon crosssection database. <http://www.nist.gov/pml/data/xcom/index.cfm>, U.S.

INFLUENCE OF HIGH REACTOR IRRADIATION ON SOME PARAMETERS OF Al_2O_3 CRYSTALS AND PROCESS GENERATION OF A SEVERAL POINTS NANODEFFECTS

Izida Kh. Abdukadyrova *

Institute of Nuclear Physics Usbek Academy of Sciences. Taskent. Uzbekistan

ABSTRACT

In this connection the peculiarities of radiation effect on lattice parameters, form and position of several reflections, reflection coefficient and frequency of valence and deformation oscillations of Al-O bonds, optical characteristics of the oxide aluminium Al_2O_3 were studied with techniques of X-diffraction, absorption-luminescence and IR-reflection spectroscopy. The characteristic features of the process of radiation-defect formation and generation of some points nanodefects, change in the structural, optical properties of Al_2O_3 crystals exposed to gamma and reactor radiation have been investigated by spectroscopic methods. The dose dependence's of the generation in crystals the color and luminescence centers, nanodefects - type F- and F-aggregate, change of the structural parameters was determined. For example, in work presented of temperature-dose dependence on the intensity of the 330, 420 nm bands in FL and GL spectrum of crystals. As the $T= 600\text{-}700^\circ\text{C}$ and fluence $1.10^{16} \text{ cm}^{-2} - 1.10^{19} \text{ cm}^{-2}$ of intensity this bands increasing (nanodefects - F^+ centers) was can see. In this paper was given dose dependence of generation on the oxide in the absorption spectra a bands 257 and 358 nm (nanodefects of a type F- and F-aggregate defects). The possible mechanism of damage structure of a samples irradiated in a reactor is discussed.

Key words: nanodefects, F^+ centers, FL and GL spectrum, oxide aluminium, absorption-luminescence spectroscopy, reactor radiation, dose dependence's.

INTRODUCTION

Al_2O_3 oxide is one of the prospective high-k electro-insulators und construction oxides materials, in partocular, for the ceramical fuel material and for a first wall thermonuclear arrangement. Besides, this oxide used widely as an active element or substrate at creation of laser and MOS systems, as a film coating and receiver of IR-radiation [1-7]. From here this work aim at investigation of radiation stability of the physical properties and a structure of Al_2O_3 crystalline oxide after irradiated in the reactor of a high fluence and course Co^{60} .

* e-mail izida@inp.uz, tel.+ 998 90 2892673

RESULTS AND DISCUSSION

In this connection the peculiarities of radiation effect on lattice parameters (a , c), form and position of several reflections, reflection coefficient and frequency of valence and deformation oscillations of Al-O bonds, electric characteristics of the oxide were studied with techniques of X-diffraction, dielectric, optic and IR-reflection spectroscopy.

The fracture our maximum on the dose curves $Y(F)$ of intensity photoluminescence (FL) at 330, 390 and 510 nm, colour centers 205-460 nm and 570 nm in the range of identical doses was determined at the analysis of the obtained results. Fig. 1 presents the temperature-dose dependence of the intensity of the 330 nm band in FL spectrum of crystals. As the $T= 600-700^{\circ}\text{C}$ of intensity this band increasing, this can be used in creating tunable lasers [4].

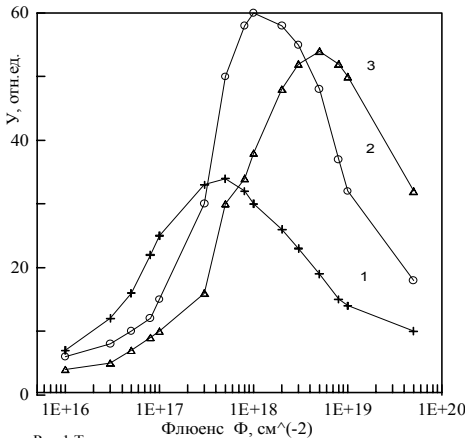


Рис. 1 Температурно-дозовая зависимость интенсивности полос ФЛ 330 нм: кривая 1, $T= 300^{\circ}\text{C}$; кривая 2, $T= 600^{\circ}\text{C}$; кривая 3, $T= 700^{\circ}\text{C}$.

A similar kinetics of a process of decolouration of 510 nm FL band was established when temperature was varied. On the basis results obtained that the temperature dependence of photodecoloration of this band has an extremum character, because the maximum rate up to $T>900^{\circ}\text{C}$ on a change in the time UV illumination of plates from 0 to 600 sec. The $I/I_0(\Phi, T, t)$ graphs obtained can be approximated

by exponential dependence's of the formula

$$I = \sum I_i^0 \exp(-\alpha_i t), \quad (1)$$

where α_i - constant of decay ($i = 1-3$), which is a function of temperature and dose.

For example, in present communication it is submitted the results of X-ray structure investigation of after irradiation by high neutron doses (F). X-diffraction patterns were obtained using a roentgen diffractometer. Particular attention was given to dynamics of form and positions some representative reflexes with $hkl = 014, 110, 03.12$ and ets. The diffraction patterns were found essential changes of peak intensity and position depending upon F , the Bragg angle 2Θ decreases with an increase in dose, the regularity is shown if $K\alpha_1$ and $K\alpha_2$ doublet is splintered. For example, on figure 2 was given to radia-

tion dynamics of the function $2\Theta(F)$ for this doublet ($K\alpha_1$ and $K\alpha_2$) in the reflexes 03.12.

From fig. 2 is shown that the displacement of this peak $\Delta(2\Theta) = 40-50^\circ$ at dose $F=10^{20}-10^{21} \text{ cm}^{-2}$. At high doses the reflexes at $2\Theta > 70^\circ$ are eroded and weakened and doublets are not splitting, the lattice parameters of crystals (a, c, d/n - tab.1) was undergoes anisotropy expansion, at very high dose of change this parameters is composed not so many as $\Delta c = 0,0038 \text{ nm}$ and $\Delta a = 0,0014 \text{ nm}$.

Table 1. Influence of neutrons on some parameters of crystals.

F, cm^{-2}	5.10^{16}	1.10^{17}	5.10^{17}	1.10^{18}	5.10^{18}	8.10^{18}
D_1 , a.u.	0,18	0,27	0,34	0,62	1,29	1,29
D_2 , a.u.	0,10	0,12	0,15	0,35	0,51	0,64
F, cm^{-2}	8.10^{18}	1.10^{19}	5.10^{19}	8.10^{19}	1.10^{20}	5.10^{20}
D_1 , a.u.	1,29	1,27	1,28	1,70	1,95	2,15
D_2 , a.u.	0,64	0,93	1,05	1,00	1,21	1,99
c, nm	1,298	1,298	1,298	1,299	1,300	1,301
d/n, nm	0,2379	0,2379	0,2380	0,2381	0,2383	0,2386
$(2\Theta)^\circ$	89,04	89,03	88,99	88,98	88,95	88,86

In table 1 was given dose dependence of generation in the absorption spectra a bands 257 and 358 nm (D_1 , D_2 , F- and F-aggregate defects). The mechanism of atom displacement out of lattice knots plays the main role in radiation damage of irradiated of high doses crystals.

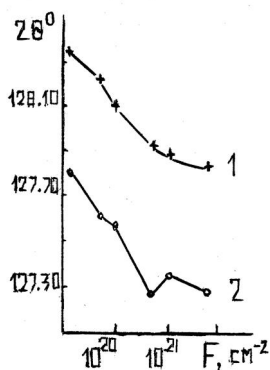


Fig. 2 – Dose dependence of $2\Theta(F)$ for doublet $K\alpha_1$ (1) and $K\alpha_2$ (2) of reflexes 03.12

reflexes, of peak intensity and the Bragg angle), a density and a linear size of irradiated samples were found near a neutron fluence 10^{20} cm^{-2} and 10^{21} cm^{-2} ,

The optical characteristics - a reflection coefficient and frequency of valence ($736, 614 \text{ cm}^{-1}$) and deformation (464 cm^{-1}) oscillations of Al-O bonds of the oxide were studied with techniques of IR-reflection spectroscopy in region $400-1200 \text{ cm}^{-1}$. The partly decrease of intensity (R) and frequency (ν) of this modes at fluence $8.10^{19} \text{ cm}^{-2}$ was observed. The change of these parameters were found near a neutron fluence $(6-8).10^{19} \text{ cm}^{-2}$. Some change of these optical (valence and deformation oscillations of Al-O bonds) and structural parameters (the lattice parameters of crystals (a, c, d/n) and positions some representative

but the structure state remained stable at the following increase of the irradiation dose (at $F= 1.10^{21} \text{ cm}^{-2}$ and $7.10^{21} \text{ cm}^{-2}$ and higher).

CONCLUSIONS

Thus, such thermal-radiation treatment may serve as a method leading to the permittivity growth at elevated irradiation doses and temperatures, decrease and improvement of several physical and optical characteristics of the oxide Al_2O_3 . A conclusion about the radiation-induced modification of the optical and structural parameters of crystals, nonlinear generation of point nanodefects, a possible their at solution for a problems of the management optical properties oxides. The removal about the action of large fluences neutron on the order of a structure, a parameters of lattice and the formation of region of disordering at the places of accumulation of the radiation defects as a result of implementation of the mechanism of displacement of atoms in the crystal lattice of a dielectric has been made.

REFERENCES

- [1] И.Г.Романов, И.Н.Царева, Письма в ЖТФ, 2001, Vol. 27, P. 65-70.
- [2] В.В. Соболев, С.В. Смирнов, В.Вал. Соболев, ФТТ, 2001, Т. 43, С.1966-1968.
- [3] В.В. Вольхин, И.Л. Казакова, Неорган. Материалы, 2000, Т. 36, С. 464-469.
- [4] Я.А. Валбис, М.Е. Спрингис, Электронные и ионные процессы в ионных кристаллах, Рига, 1980, P. 16-19.
- [5] В. Evans, M. Stapelbrok, Sol. St. Com., 1980, Vol. 33, P. 765-770.
- [6] П.А. Кулис, М.Е. Спрингис, Я.А. Валбис, 1V Int. Conf. of PCIC, Riga, 1978, P. 127-128.
- [7] I.Kh. Abdukadyrova, N.N. Mukhtarova, The third Int. Conf. of Modern problems of nuclear physics, Bukhara, 1999, P. 320-321.

INVESTIGATION OF THE NANOSTRUCTURES FORMATION IN THE IRRADIATED BY γ – QUANTA SINGLE-CRYSTAL SILICON WITH ULTRASONIC METHOD

T. Khaydarov, I.Kh. Abdukadirova, Yu. Karimov*

Institute of Nuclear Physics Academy of Sciences, Tashkent, 100214, Uzbekistan

ABSTRACT

It's determined that a phasic dynamics of deformation strengthening of single-crystal silicon irradiated by γ – quanta (with energy $\sim 1,27$ MeV) in the wide region of doses (from 10^2 up to 10^9 rad) by the internal friction measurement with widely known ultrasonic resonance method. We have detected appearance maximum on the dependence of internal friction (Q^{-1}) from dose at 10^5 rad in the samples p-Si with density of dislocations more than 10^3 cm $^{-2}$. Besides it the instability of nanodimensional dislocation structures has been established in the doses interval from 10^6 up to 10^9 rad, due to the formation and accumulation in the crystal lattice of the point like and continuous radiation defects (evolution of the dislocation densities in metals with rise of deformation were considered in [1-4]). On the temporal dependence $Q^{-1}(t)$ throughout 1,5 - 2 hours after irradiation the maximum has been established which position depends from ionizing dose. At the increasing of the observation time after stopping of the sample irradiation it is observed a monotonic decrease of $Q^{-1}(t)$ dependence, which is obviously connected with decreasing of the radiation defects densities in the result of their annihilation.

Key words: internal friction, density of dislocations, Si, radiation defects.

INTRODUCTION

A lot physical properties of materials are connected with their dislocated structure. It can be create a dislocated structure by plastic deformation or under influence of gamma irradiation [1]. Radiations damages are closely connected with dislocation strengthening. A mechanism of deformation strengthening and of formation fragmentary dislocation structures in the metals has been theoretically discussed in investigations [2, 3].

Although the processes of multiplication and of diffusion and of annihilation of dislocation in the metals and semiconductors has been considered in [2, 3, 5, 6, 7, 8], but main goal of majority investigations consist in possibility of analysis that effects from kinetics positions.

However dynamic processes of dislocation and other radiations defects after interruption of irradiation of the materials still not clear. Such information

* e-mail: yuri@inp.uz tel: +(998)712893136

allows us to predetermine about resource of the semiconducting material, and about character and staging of curves of deformation strengthening, and of specific structures at mechanical fatigue of crystals. The investigation of this process importantly not only from practical standpoint but also importantly from standpoint of the description of theory of this process. In this connection it's interesting the investigation of dynamic of radiations defects in the semiconductor after stopping of influence of the radiation.

METHODS AND OBJECTS OF INVESTIGATION

Measurements of internal friction (Q^{-1}) of the single-crystal silicon have been made with ultrasonic resonance method [9] before and after irradiation.

The prismatic rods of dimensions 1x3x35mm, 1,2x4,1x28,7mm и 1x1x20mm has used in the measurements.

Ranges of value of intrinsic of the bending vibrations were varied from 20 kHz to 200 kHz. The power of vibration for stimulation of the specimen was approximately 10mW. As initial specimens we used types KEF-100 and KDB-10 of single crystal of silicon.

The samples of silicon with density of dislocations more than 10^3 cm^{-2} were selected for quantitative description of origin of defects in the silicon and their further evolution after irradiate of gamma-rays these samples.

Method of fixing of sample is shown on insertion b (Fig. 1). After irradiation during 10 minutes the sample was set up between acoustic lines 1 and 3. From that time the measurement of the internal friction Q^{-1} was started.

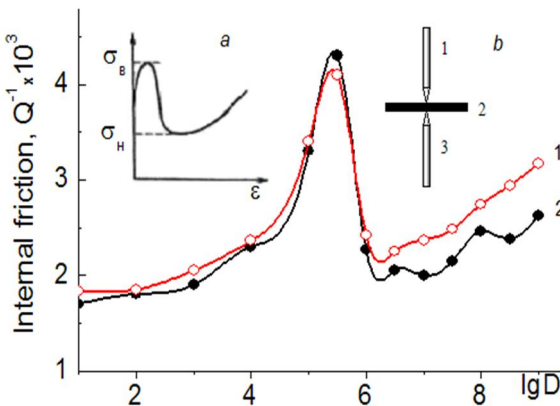


Fig. 1 – Dependence the internal friction of single-crystal of the silicon from the irradiation dose. Curve #1 is measured on frequency 149 kHz, curve #2 - 90 kHz. On insertions are shown: a- typical dependence of the tension from of the deformation which demonstrate down up tension as result of the moving dislocation formation [12]. b - method of fixing of sample where 1 is transfer acoustic line and 3 – receive acoustic line, 2-sample

RESULTS AND DISCUSSION

Dependence Q^{-1} from the irradiation dose is shown on *Fig. 1*. It's can be divided on three regions: I-background where Q^{-1} essentially not changed with increase of the irradiation dose (D) from 10 to 103 rad ; II-intermediate region where Q^{-1} was reached maximum with increase of D to 105 rad ; III-region where Q^{-1} was dropped down with increase of D from 106 до 109 rad but after that again rise.

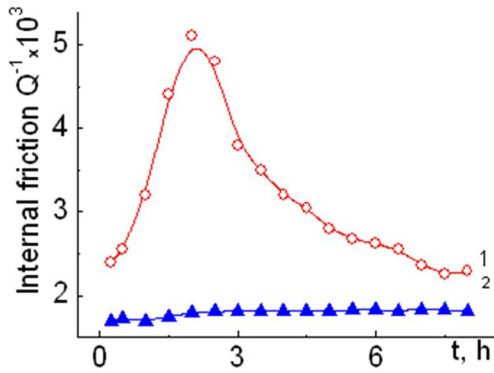


Fig. 2 – Time dependence of the single-crystal silicon internal friction after stop of the irradiation action.(1) - 10^8 rad, (2) – initial sample

it's growing in 2,5 times starting from the initial up to the maximum value. At the increasing of the observation time after stopping of the sample irradiation it is observed a monotonic decrease of $Q^{-1}(t)$ dependence, which is obviously connected with decreasing of the radiation defects densities in the result of their annihilation.

CONCLUSIONS

It has been demonstrated in the present work that received dependences of internal friction (Q^{-1}) from the irradiation doses have characterized the staging step of the deformation strengthening.

We have detected appearance maximum on the dependence of internal friction (Q^{-1}) from dose at 10^5 rad in the samples p-Si with density of dislocations more than 10^3 cm^{-2} .

Acknowledgements

The authors are thankful to Prof. M. Karimovu for important remark and R. Khamraevoy and Sh. Makhmudovu for concession of samples. This work was funded by project A14- Φ 070.

On the temporal dependence $Q^{-1}(t)$ (*Fig. 2*) throughout 1,5 - 2 hours after irradiation the maximum has been established which position depends from ionizing dose.

We suppose that such behavior of the $Q^{-1}(t)$ function is connected with manifestation of migration activity which coherent with annihilation of the dislocation loops in the first 1,5-2 hours when

REFERENCES

- [1] Physical Acoustics, Principles and Methods (Ed. W. Mason), Vol. III, Part A. The Effect of Imperfections, New-York, 1966, P. 578.
- [2] Г.А. Мальгин, УФН, 1999, Vol. 169, P. 979-1010.
- [3] Г.А. Мальгин, ФТТ, 2006, Vol. 48, P. 651-657.
- [4] Г.А. Мальгин, ФТТ, 2009, Vol. 51, P. 1709-1715.
- [5] M.W. Tompson Defects and Radiation Damage in Metals, Cambridge, 1969.
- [6] L.J. Teutonico, A.V. Granato, K. Lucke, J. Appl. Phys., 1964, Vol. 35, P. 220-237.
- [7] Б.И. Смирнов, Дислокационная структура и упрочнение кристаллов. Л.: Наука, 1981.
- [8] А.Р. Велиханов, ФТП, 2010, Vol. 44, P. 145-148.
- [9] В.М. Баранов, Акустические измерения в ядерной энергетике, М.: Энергоатомиздат, 1990.
- [10] J.V. Sharp, Philos. Mag., 1967, Vol. 16, P. 77-96.
- [11] K.V. Ravi, Imperfections and Impurities in Semiconductor Silicon, New-York – Toronto, 1981.
- [12] М.А. Лебедкин, Л.Р. Дунин-Барковский, ЖЭТФ, 1998, Vol. 113, P. 1816-1820.
- [13] L.J. Teutonico, A.V. Granato, K. Lucke, J. Appl. Phys., 1964, Vol. 35, P. 220-237.
- [14] И. Хидиров, Д.И. Сотиболдиев, С.З. Зайнобиддинов, К.О. Бактибаев, ДАН АН РУз, 2008, № 6, P. 67-71.

“ETCHABILITY” OF ION TRACKS IN SiO₂/SI AND Si₃N₄/SI THIN LAYERS

Liudmila A. Vlasukova^{1*}, Fadei F. Komarov¹, Vera N. Yuvchenko¹,
Vladimir A. Skuratov²

1 Belarusian State University, Nezaleznosti Ave. 4, 220030, Minsk, Belarus

2 Laboratory of Nuclear Reactions, Joint Institute for Nuclear Research, 141980, Dubna, Russia

ABSTRACT

We have calculated radii and lifetime of the molten regions or the regions heated to the melting point that are formed under irradiation of amorphous SiO₂ and Si₃N₄ with swift ions. A computer simulation was carried out on the base of thermal spike model. A comparison of calculated track parameters with ion track etching data have been made for these materials.

It is shown that an existence of molten region along swift ion trajectory may be a criterion for a track “etchability” in the case of SiO₂. In the same conditions of chemical etching diameter of etched tracks in SiO₂ is proportional to the radius and lifetime of the molten region. This information is important for a correct choice of irradiation regime aimed at preparation of nanoporous layers with high pore density ($\geq 10^{10}$ cm⁻²).

Key words: SiO₂ и Si₃N₄, swift ions, ion tracks, chemical etching, nanoporous layers.

INTRODUCTION

The discovery of ion tracks dates back to 1959 when Silk and Barnes published transmission electron micrographs of mica with long, straight damage trails created by single fragments from the fission of ²³⁵U [1]. Soon after that, it has been realized that ion tracks are narrow (<5 nm), stable, chemically reactive centers of strain that are composed mainly of displaced atoms rather than of electronic defects [2]. It also became clear that these displaced atoms are not due to direct collisions between ions and the target nuclei, but are the result of the interaction of the projectile ions with the target electrons. Later it was found that tracks were formed in insulators and badly conducting semiconductors, if the electronic stopping power S_e exceeded a material-dependent threshold value S_{e0} . At that time no tracks could be detected in metals [3]. Nanochannels can be created in track regions by means of proper chemical etching. Thin dielectric layers (SiO₂ and Si₃N₄) with the etched tracks integrated into silicon wafers are of special interest for nanotechnologies and microelectronics [4 – 8]. A material-dependent threshold value S_{e0} is often treated as a criterion for ion

* e-mail: vlasukova@bsu.by, tel: (+375)0172095929

track “etchability”. S_{e0} varies from 4 to 1.5 keV/nm for SiO₂ according different Refs [2, 9 - 11]. There is practically no information about S_{e0} for silicon nitride in literature. We know three papers only that devoted to track investigation in this material [12 - 14]. Though, in addition to S_{e0} it is necessary to know track parameters in order to obtain dielectric layers with the definite nanopore density by means of swift ion irradiation followed by chemical etching.

In this paper, we evaluate a possibility to use track formation parameters calculated on the base of thermal spike as criterions for ion track “etchability” in amorphous SiO₂ and Si₃N₄ layers.

METHODS OF SAMPLE MANUFACTURING AND ANALYSIS

SiO₂/Si samples were cut from the thermally oxidized Si wafer. The thickness of SiO₂ layer was evaluated from RBS measurements and equal to 600 nm. Si₃N₄/Si samples were cut from the Si wafer with the amorphous silicon nitride layer deposited by gas phase low pressure deposition from ammonia and dichlorosilane at 300° C. The Si₃N₄ layer thickness measured by the Rutherford backscattering method was 600 nm, too. SiO₂/Si and Si₃N₄/Si structures were irradiated normally to the surface with Ar (290 MeV), Fe (56 MeV), Kr (84 MeV), and W (180 MeV) ions in the Flerov Laboratory of Nuclear Reactions of the Joint Institute for Nuclear Research (Dubna). The ion fluence in all cases did not exceed $5 \times 10^8 \text{ cm}^{-2}$. The ion flux was kept constant and equal to $2 \times 10^8 \text{ cm}^{-2} \text{ s}^{-1}$. To provide reliable thermal contacts the samples were fixed on a massive metallic holder with a heat conducting paste. The irradiated samples were treated in hydrofluoric acid (HF) dilute aqueous solutions at room temperature. Then the samples were investigated using the scanning electron microscope Hitachi S-4800.

THE COMPUTER SIMULATION OF THE TRACK FORMATION IN SILICON DIOXIDE AND NITRIDE IN TERMS OF THERMAL SPIKE

The track formation processes in amorphous SiO₂ (α -SiO₂) and Si₃N₄ were simulated in terms of the thermal spike model [15] with the application of a software system we designed. The model was successfully used earlier to describe swift ion travel in silicon dioxide and other dielectrics. The track radii in α -SiO₂ we computed by this model were in good agreement with the experimental results in [16, 17]. The model involves the thermalization of the electronic subsystem of a solid within a time not exceeding 10^{-14} s. A few picoseconds later, the electron–phonon interaction leads to fast heating of the region along the fast ion trajectory. The process of energy transfer from the electronic to atomic subsystem of a solid is described by a system of two differential equations. The macroscopic parameters of the target material are used to calculate thermal fields. The model involves one free parameter: the electron mean free path under electron–phonon interaction λ . If the density of the energy released in electronic excitations is sufficiently high, we observe the melting of

the material and the formation of a cylindrical domain with a diameter of a few nanometers - the future track. A few tens of picoseconds later, the melt cools to the temperature of the surrounding matrix.

The thermophysical parameters for SiO₂ were taken from [15], the parameter λ was 4 nm. For Si₃N₄ the parameter λ was 4.8 nm [15]. Thermophysical properties of amorphous SiO₂ - one of the basic materials of microelectronic processing - are thoroughly studied and described in the literature. The situation is different for amorphous Si₃N₄. We failed to find reference data on latent heat of melting of this material. In addition, distillation or thermal decomposition of the material can take place upon the heating of Si₃N₄, along with solid phase melting. Therefore, as a track region in Si₃N₄ we took the region heated to the melting point instead of the melted region. The latent heat of melting of Si₃N₄ was taken to be 10⁸ J kg⁻¹, which is higher by two orders of magnitude than average values of semiconductors.

RESULTS AND DISCUSSION

Table 1 presents the results of computer simulation of ion track formation, namely, the radius and lifetime of molten region for SiO₂ and Si₃N₄.

Table 1 – The results of computer simulation for SiO₂ and Si₃N₄

Material	Ion type and energy, MeV	The electronic stopping power S_e , keV/nm	The radius of the molten region r^{**} , nm	The lifetime of the molten region t^{**} , ps
SiO ₂	Ar (290)	2.8	-	-
	Kr (253)	9.8	3.4	7.0
	Kr (84)	9.4	3.8	8.9
	W (180)	15.8	6.3	24.4
	Fe (56)	6.9	2.7	3.9
Si ₃ N ₄ ***	W (180)	20.4	5.3	4.7
	Kr (84)	11.9	3.0	1.3
	Fe (56)	9.0	1.7	0.5

* S_e were calculated by SRIM' 2003 code

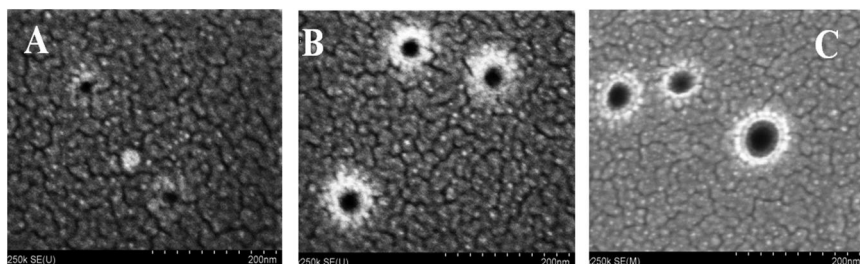
** for Si₃N₄ the parameters r and t are the radius of the region heated to the melting point and the lifetime of this region, accordingly

*** the density of Si₃N₄ was taken to be 2.85 g cm⁻³ [18] for S_e calculation

In the case of Ar (290 MeV) S_e is equal to 2.8 keV/nm. It is higher than the threshold value for the preferential track etching reported in [10, 11]. One can see that in the case of SiO₂ irradiation with Ar ions (290 MeV) there is no formation of molten region along the ion trajectory. Accordingly, we did not found the etched tracks in the SiO₂/Si samples irradiated with Ar even after the treatment in 6% HF for 20 minutes. Evidently, in order to forecast the “etchability” of ion tracks it is not enough to know S_e only. We have to take into account “velocity effect” [19]. In our calculation this effect is demonstrated for

SiO₂ irradiated with Kr ions with the energies of 253 and 84 MeV. For Kr (253 MeV) the electronic stopping power is 9.8 keV/nm. This is higher than a value 9.4 keV/nm for Kr (84 MeV). However, the radius and the lifetime of the molten region are larger in the case of slower ion. In the conditions of similar S_e the most part of released energy is localized in narrow regions along ion trajectories during slow ions passing. During swift ion passing a substantial part of energy goes away from the ion trajectory for significant distances with high-energy δ -electrons. Thus, a substance temperature in the region of future track ought to be higher in the case of slow ion passing. Evidently, the molten region formation along ion trajectory is more reliable criterion for track “etchability” in comparison with S_e . Figure 1 shows images of etched tracks in SiO₂/Si samples irradiated with Fe, Kr and W ions and chemically treated in the same conditions.

One can see from *Fig. 1* that tracks were etched in all samples. It should be noted a correlation between etched pore diameters and calculated radii and lifetimes of the molten regions. Pore diameter in SiO₂ irradiated with Fe ions was \approx 15 nm after the etching in 1.5% HF solution during 9 min. For the samples irradiated with Kr and W ions pore diameters were 30 and 45 nm, accordingly. Thus, the smallest pore diameter was observed for silicon dioxide irradiated with ions that formed molten regions with small radii and lifetime. The biggest one was observed in the case of W irradiation. According to our calculation W ions created the biggest molten regions with the longest lifetime from three ion species used in our experiment. Earlier for α -SiO₂ irradiated with Bi (710 MeV) it was shown a good correlation between minimum etched tracks diameters and molten region radii calculated by thermal spike [17]. In this way, one can forecast minimum etched tracks diameters on the base of the molten region radius knowledge. It is important for a choice of proper irradiation regime aimed at preparation of nanoporous layers with high pore density ($\geq 10^{10}$ cm⁻²).



Irradiated samples were treated in 1.5% HF for 9 min.

Fig. 1 – Etched tracks in SiO₂. A – irradiation with Fe (56 MeV, 2.4×10^8 cm⁻²), B – Kr (84 MeV, 2.4×10^8 cm⁻²), C – W (180 MeV, 3×10^8 cm⁻²)

As analysis of calculated track parameters shows, a region heated to the melting point exists during the irradiation with all three ion species in the case of Si_3N_4 .

Though, track formation process needs more energy spend in comparison with SiO_2 . At more high level of the electronic stopping power in Si_3N_4 for Fe, Kr and W ions the calculated lifetime of the region heated to the melting point were substantially shorter in comparison with the lifetime of the molten region for SiO_2 .

In the $\text{Si}_3\text{N}_4/\text{Si}$ samples irradiated with Fe and Kr, no tracks were revealed even after 60 min treatment in an HF solution. Tracks were etched only upon exposure to W ions. *Figure 2* depicts the scanning electron microscope image of the W irradiated sample after etching. Ten pores were recorded on a scan area of $7.8 \times 5.5 \mu\text{m}^2$. The track etching efficiency, defined as $\xi = N_p/\Phi$, where N_p is the number of pores per unit area and Φ is the fluence, did not exceed 12%. The low track etching efficiency and the considerable difference in the diameters of the etched pores allow us to assume that discontinuous tracks are formed in silicon nitride upon irradiation with tungsten (180 MeV). This means that the electronic stopping power of W ions are sufficient for order–disorder transformation; however, they are lower than the threshold electron losses necessary for the formation of extended etched tracks in this material. This conclusion on the formation of discontinuous tracks in amorphous Si_3N_4 irradiated with lead ions with $S_e = 19.3 \text{ keV/nm}$ was also drawn by Canut et al. [13]. They reported about track etching efficiency $\xi = 60\%$ with an appreciable size spread of pores.

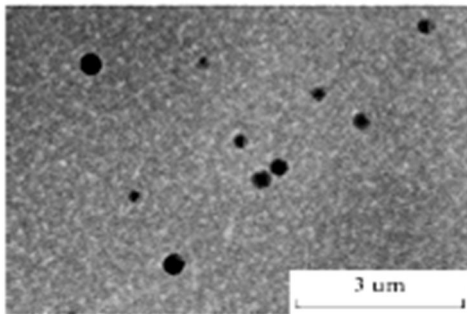


Fig. 2 - Scanning electron microscope image of Si_3N_4 surface irradiated with W ions (180 MeV, $2 \times 10^8 \text{ cm}^{-2}$) and etched in 4% HF for 50 min

To obtain nanoporous Si_3N_4 with the pore density controlled by ion fluence, the formation of extended continuous tracks is required. This condition can be fulfilled with the use of ions with $S_e > 20 \text{ keV/nm}$.

According to computer simulation data the regions heated to the melting point exist in Si_3N_4 during the irradiation with all three ion species (Fe, Kr and W). Though, chemical treatment results show the preferential etching of discontinuous tracks only for the samples irradiated with tungsten. This ion type is characterized with the maximal energy losses in electron subsystem for our experiment. Probably, we have done incorrect assumptions in computer simulation of track

formation in Si_3N_4 because the absence of reliable data on thermophysical properties of this material. A fitting of thermal spike model in application to amorphous Si_3N_4 is a subject of further investigation.

CONCLUSIONS

The radii and lifetime of the molten regions or the regions heated to the melting point formed in amorphous SiO_2 and Si_3N_4 irradiated with swift ions have been calculated on the base of thermal spike model. A comparison of calculated track parameters and etching of ion track data have been made for these materials.

It is shown that an existence of molten region along swift ion trajectory may be used as a criterion for track “etchability” in the case of SiO_2 . In the same conditions of chemical etching diameter of etched tracks in SiO_2 is proportional to the radius and lifetime of the molten region. This information is important for a correct choice of irradiation regime aimed at preparation of nanoporous layers with high pore density ($\geq 10^{10} \text{ cm}^{-2}$).

As a computer simulation shows, in the case of irradiation with Fe (56 MeV), Kr (84 MeV), and W (180 MeV) at more high level of the electronic stopping power in Si_3N_4 the calculated lifetime of the region heated to the melting point were substantially shorter in comparison with the calculated lifetime of the molten region for SiO_2 .

In silicon nitride irradiated with swift ions, tracks were etched only after exposure to W ions (180 MeV) with $S_e = 20 \text{ keV/nm}$ being maximal for our experiment. The low track etching efficiency and the considerable size spread of pores allow assuming the formation of discontinuous tracks.

An existence of the regions heated to the melting point along swift ion trajectory can not be used as a criterion for track “etchability” in the case of Si_3N_4 . It needs an additional investigation for a fitting of thermal spike model in application to amorphous Si_3N_4 .

Acknowledgements

This work was supported by the Belarusian Foundation for Basic Research, grant T10R–142.

REFERENCES

- [1] E.C.H. Silk, R.S. Barns, *Philos. Mag.*, 1959, Vol.4, P.970.
- [2] *Nuclear Tracks in Solids* (Eds. R.L. Fleischer, P.B. Price, R.M. Walker) University of California Press, Berkeley, 1975.
- [3] S. Klaumünzer, *Nucl. Instr. and Meth.*, 2004, Vol. B225, P. 136 - 153.
- [4] M. Toulemonde, C. Trautman, E. Balanzat *et al*, *Radiat. Measurements*, 2005, Vol. 40, P. 191.
- [5] K. Hoppe, W.R. Fahrner, D. Fink *et al*, *Nucl. Instr. and Meth.*, 2008, Vol. B266, P. 1642 - 1646.

-
- [6] F. Bergamini, M. Bianconi, S. Cristiani *et al*, Nucl. Instr. and Meth., 2008, Vol. B266, P. 2475.
- [7] M. Fujimaki, C. Rockstuhl, X. Wang *et al*, Optics Express, 2008, Vol.16, P. 6408.
- [8] N. Fertig, R. H. Blick, J. C. Berhends, Biophysical J. 2002, Vol. 18, P. 3056 - 3062.
- [9] A. Sigrist, R. Balzer, Helv. Phys. Acta, 1977, Vol. 50, P.75.
- [10] J. Jensen, M. Skupinski, A. Razpet, G. Possnert, Nucl. Instr. and Meth., 2006, Vol. B245, P. 269 - 273.
- [11] A. Dallanora, T. L. Marcondes, G. G. Bermudez *et al*, J. Appl. Phys., 2008, Vol. 104, P. 024307(8).
- [12] S. J. Zinkle, V. A. Skuratov, D. T. Hoelzer, Nucl. Instr. and Meth., 2002, Vol. B191, P. 758.
- [13] B. Canut, A. Ayari, K. Kaja *et al*, Nucl. Instr. and Meth., 2008, Vol. B266, P. 2819 - 2823.
- [14] L.A. Vlasukova, F.F. Komarov, V.N. Yuvchenko, Bulletin of the Russian Academy of Sciences: Physics, 2010, Vol. 74, P. 206 – 208.
- [15] M. Toulemonde, C. Dufour, A. Meftah, E. Paumier, Nucl. Instr. and Meth. 2000, Vol. B166–167. P. 903–912.
- [16] F.F. Komarov, L.A. Vlasukova, V.N.Yuvchenko *et al*, Izv. Akad. Nauk, Ser. Fiz., 2006, Vol. 70, P. 798 - 801.
- [17] F.F. Komarov, L.A. Vlasukova, P.V. Kuchinskyi *et al*, Lithuanian J. Phys., 2009, Vol. 49, P. 111 - 115.
- [18] Gmelin Handbook on Inorganic and Organometallic Chemistry, Springer–Verlag, 1994, vol. B5e, p. 264.
- [19] A. Meftah, F. Brisard, J. M. Costantini *et al*, Phys. Rev. B., 1994, Vol. 49, P. 12457 - 12463.

SURFACE MODIFICATION OF ZnO AND TiO₂ NANOPARTICLES UNDER MILD HYDROTHERMAL CONDITIONS

Behzad Shahmoradi^{1,*}, Afshin Maleki²

1 Environmental Health Research Center, Faculty of Health, Kurdistan

2 University of Medical Sciences, Sanandaj, Kurdistan-Iran

ABSTRACT

There are various techniques for synthesizing different Nanoparticles depending upon the desired properties, application, etc. One of these widely applied techniques is Hydrothermal. However, this technique is known for bulky materials and fabrication of nano-scale materials requires adopting some strategies to alter the properties of materials synthesized. We developed surface modification for this drawback. Application of surface modifier, or surfactant, or capping agent, or organic ligands in proper concentration could not only change morphology, reduce particle size, but also change the surface chemistry of the nanoparticles fabricated. The ZnO and TiO₂ nanoparticles were modified using *n*-butylamine and caprylic acid as surface modifier under mild hydrothermal conditions (*p*= autogenous, *T*= 150-250°C, and *t*= 18 h). The nanoparticles modified were systematically characterized using Powder XRD, FTIR, SEM, zeta potential, and BET surface area. The characterization results revealed that nanoparticles have small size range, low agglomeration and highly stable.

Key words: surface modification, *n*-butylamine, caprylic acid, ZnO/TiO₂ nanoparticles, hydrothermal conditions

INTRODUCTION

Surface modification and characterization of nanomaterials is a field of immense research potential for researchers worldwide for nearly half a century. Zinc oxide is a promising group II-VI oxide semiconductor showing quantum confinement effects at room temperature [1-3]. ZnO and TiO₂ nanoparticles have broad applications such as UV absorption [4], deactivation of bacteria [5], photocatalysis of industrial effluents [6-7], etc. Furthermore, they are an environmentally friendly material, which are desirable especially for bio-applications, such as bioimaging, cancer detection, and chemical sensors [8].

The photoactivity of zincite and titanium dioxide is generally detrimental for their application as photocatalyst or filler that oxidatively degrades, leading to embrittlement and chalking when exposed to sunlight or UV irradiation, especially in presence of moisture. Hence, some form of modification is im-

* e-mail: bshahmorady@gmail.com Tel: (+98)9187705355

plemented in order to reduce the surface photoactivity, to alter their hydrophobic/hydrophilic character and improve their dispersibility in various media, to introduce new functional groups, which can react with organic molecules and enhance their compatibility with organics. Therefore, caprylic acid and *n*-butylamine were selected as surface modifiers to resolve the abovementioned problems. The present authors have modified ZnO and TiO₂ nanoparticles with these surfactants because they have low toxicity, eco-friendly, low density and low melting temperature.

Most of the ZnO/TiO₂ crystals have been synthesized by traditional high temperature solid-state method, which is energy consuming and difficult to control the particle properties. ZnO/TiO₂ nanoparticles can be prepared on a large scale at low cost by simple solution-based methods, such as chemical precipitation [9], sol-gel synthesis [10], and solvothermal/hydrothermal reaction [11, 12]. Hydrothermal technique is a promising alternative synthetic method because of the low process temperature and very easy to control the particle size. The hydrothermal process has several advantages over other growth processes such as use of simple equipment, catalyst-free growth, low cost, large area uniform production, environmental friendliness and less hazardous [13].

EXPERIMENTAL PREPARATION OF SURFACE MODIFIED ZNO/TIO₂ NANOPARTICLES

ZnO and TiO₂ nanoparticles were modified under mild hydrothermal conditions ($T=150 - 250^{\circ}\text{C}$, $P = \text{autogeneous}$). 1M of reagent grade ZnO/TiO₂ (Loba Chemie, India) were taken as starting material. A certain amount of 1 N NaOH and HCl was added as mineralizer to the precursors respectively. Caprylic acid and *n*-butylamine (Sisco Research Lab PVT, Ltd., Mumbai, India) with different concentration (0.8, 1.0, 1.2, 1.4 and 1.6 ml) was added into the above-mentioned mixtures separately and it was stirred vigorously for a few minutes. The final mixture was then transferred to the Teflon liner ($V_{\text{fill}}=15 \text{ ml}$), which was later placed inside a General-Purpose autoclaves. The autoclaves were provided with Teflon liners of 30 ml capacity. Then the assembled autoclave was kept in an oven with a temperature programmer-controller. The temperature was programmed and kept at $150-250^{\circ}\text{C}$ for 18 hr. After the experimental run, the autoclaves were cooled to the room temperature. The resultant product in the Teflon liner was then transferred in to a clean beaker and the product was washed with double distilled water. The surplus solution was removed using a syringe and the remnants were centrifuged for 20 minutes at 3000 rpm. The product was recovered and dried in a hot air oven at 50°C for a few hours. The dried particles were subjected to a systematic characterization using powder XRD, FTIR, SEM, Zeta potential and BET surface area measurement.

CHARACTERIZATION OF THE SURFACE MODIFIED ZnO/TiO₂ NANOPARTICLES

The Powder X-ray diffraction patterns were recorded using Bruker, D8 Advance, Germany, with Cu K α , λ 1.542 Å radiation, Voltage = 30 kV, Current 15 mA, Scan speed ~5° min⁻¹. The data were collected in the 2 θ range 10–80°. The Fourier transform infrared (FTIR) spectra were recorded using FTIR, JASCO-460 PLUS, Japan, at resolution of 4 cm⁻¹. SEM images of surface modified ZnO hybrid nanoparticles were recorded using Hitachi, S-4200, Japan. Zeta potential and BET surface area was measured using Zetasizer 2000 instrument (Malvern instruments), UK

RESULTS AND DISCUSSION

The powder XRD data reveals a highly crystallized wurtzite and anatase structures and there is a small new peak, which may be corresponded to caprylic acid (Fig. 1). There is a slight change in the lattice parameters of surface modified ZnO/TiO₂ nanoparticles at a-axis and c-axis when compared to pure one (Table 1); this confirms the existence of surface modifier in ZnO/TiO₂ hybrid nanoparticles.

Table 1 – Cell parameters of modified ZnO and TiO₂ nanoparticles

Nanoparticles	Surface modifier	<i>a</i> (Å)	<i>c</i> (Å)	<i>a c</i> ratio	<i>V</i> (Å ³)	Ref
Pure ZnO	NIL	3.249	5.207	0.6239	47.60	[17]
Used ZnO	NIL	3.2556	5.2166	0.6241	47.88	pw ^a
ZnO	Caprylic acid	3.2567	5.2021	0.6260	47.78	pw
ZnO	<i>n</i> -butylamine	3.2435	5.1996	0.6238	47.37	pw
Pure TiO ₂	NIL	3.7845	9.5143	0.3977	136.30	pw
Used TiO ₂	NIL	3.7918	9.5296	0.3979	137.02	pw
TiO ₂	Caprylic acid	3.7881	9.5230	0.3978	136.65	pw
TiO ₂	<i>n</i> -butylamine	3.7837	9.4983	0.3983	135.98	pw

^apw = Present work

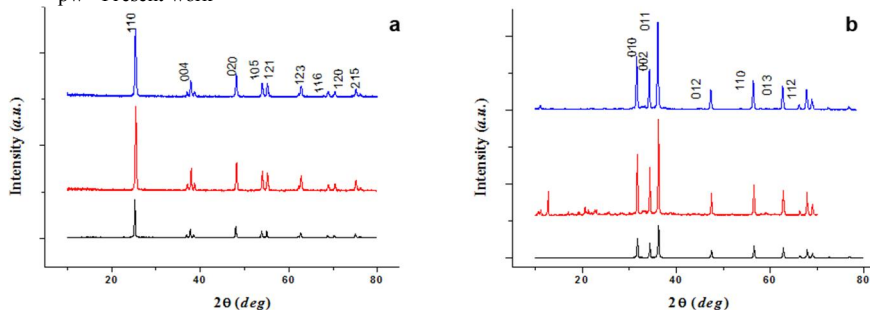


Fig. 1 – Powder XRD patterns of — pure nanoparticles without surfactant, surface modified using — *n*-butylamine and — caprylic acid as surface modifier: a) TiO₂, b) ZnO

As Fig. 1 indicates, the presence of new peaks is more in the case of using HCl as solvent for surface modification of ZnO nanoparticles; these new peaks can be contributed to the presence of mixed phases of ZnO and ZnCl_2 . The modification with caprylic acid resulted in changing the crystal structure (Fig. 1). The functional groups present in the modified nanoparticles can be studied using FTIR spectroscopy. Fig. 2 shows the FTIR spectra of the reagent grade ZnO/TiO_2 , surface modified ZnO/TiO_2 nanoparticles modified with *n*-butylamine and caprylic acid as surface modifier respectively. The intensity of the peaks was more when concentration of surface modifier was increased. The FTIR spectra of the modified nanoparticles show the presence of new peaks imply that the reagents were chemically immobilized on the surface of nanoparticles. Thus, it can be concluded that the ZnO/TiO_2 nanoparticles modified with the above said modifiers, have organic coverage on their surfaces, which has changed surface property of the nanoparticles. The absorption peaks corresponding to the presence of CH₃, N-H, O-H, C=O, etc. have been identified and illustrated in Fig. 2 [15].

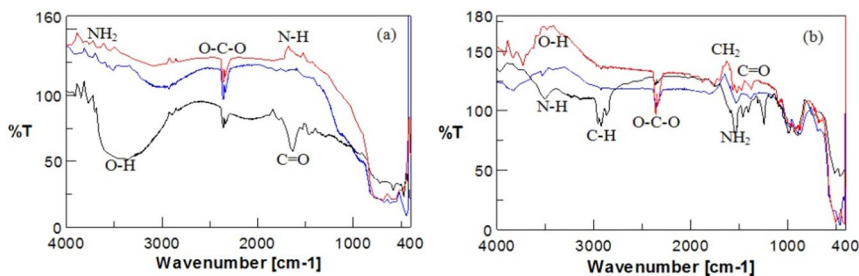


Fig. 2 – FTIR spectra of — reagent grade surface modified undoped hybrid nanoparticles using — caprylic acid, and — *n*-butylamine: a) TiO_2 , b) ZnO .

Fig. 3 and Fig. 4 show characteristic SEM and HRSEM images of ZnO/TiO_2 nanoparticles modified with (0.8 and 1.4 ml) *n*-butylamine and caprylic acid using 0.1 N NaOH and HCl as solvent.

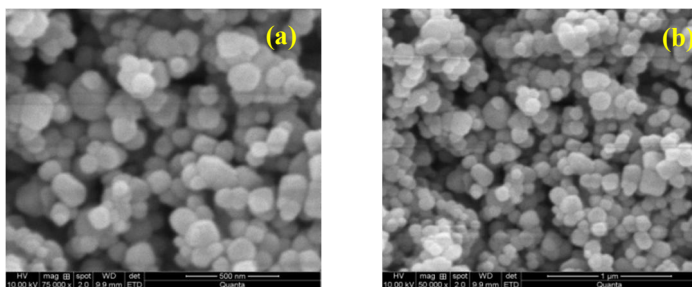


Fig. 3 – Characteristic SEM images of surface modified TiO_2 nanoparticles using NaOH as solvent: a) *n*-butylamine, and b) caprylic acid as surface modifier

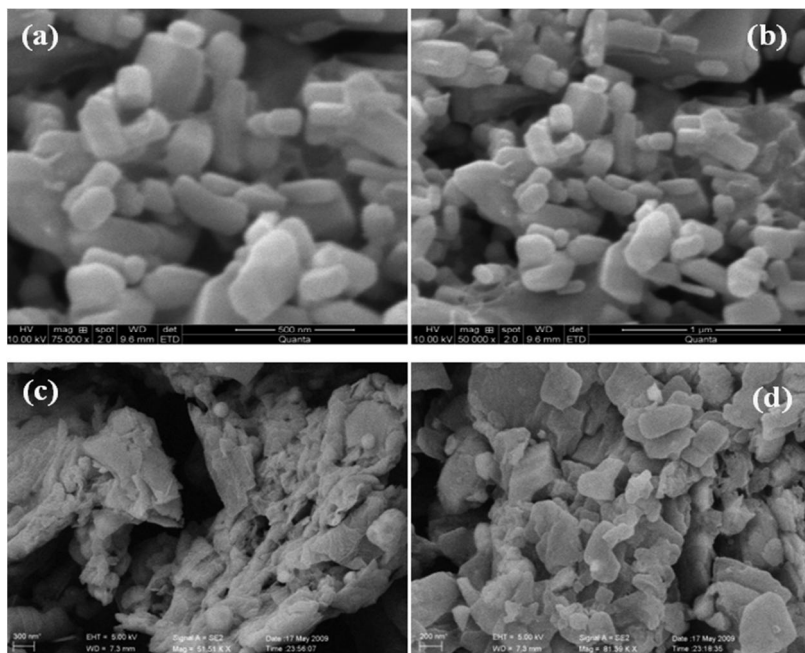


Fig. 4 – Characteristic SEM and HRSEM images of surface modified ZnO hybrid nanoparticles using: a) NaOH and n-butylamine as solvent and surface modifier respectively, b) NaOH and caprylic acid as solvent and surface modifier respectively, c) HCl and n-butylamine as solvent and surface modifier respectively, and d) HCl and caprylic acid as solvent and surface modifier respectively.

These figures show effect of the surface modifiers on the nanoparticles morphology. The agglomeration was less when a higher concentration of the surface modifier was used. The surface modification has led to the controlling of growth direction, also particle size and preventing agglomeration. It was found that the surface modifier could not only affect the dispersibility of the modified ZnO nanoparticles, but also change their morphology and size of the particles. The achieved morphology is quite suitable for the photodegradation purposes, since the ZnO/TiO₂ nanoparticles are rounded, they can be more active in photodegradation of the organic pollutants presenting in the municipal and industrial effluents

ZETA POTENTIAL OF SURFACE MODIFIED ZnO/TiO₂ NANOPARTICLES

Zeta (ζ) potential measurement was performed for ZnO/TiO₂ nanoparticles in order to characterize the surface charge of nanoparticles and Fig. 5 shows the result as a function of pH. The obtained ζ potential of the nanoparti-

cles was found to decrease with increase of pH as is expected for a surface with acid-base group. The iso-electric point or point of zero charge (PZC) for ZnO nanoparticles was found to be 4.0 and 4.2 for modification by caprylic acid and *n*-butylamine respectively. For small enough nanoparticles, a high ζ potential will confer stability, i.e. the solution or dispersion will resist aggregation. When the potential is low attraction exceeds repulsion and the dispersion will break and flocculate [16,17]. Therefore, colloids with high ζ potential (negative or positive) are electrically stabilized while colloids with low zeta potentials tend to coagulate or flocculate. Our results indicate that the both surface modified nanoparticles are stable and highly negatively charged (at pH > 4.0 -4.2) and this negative charge intensity is proportional to the increasing pH. On the other hand, the particles modified are positively charged at pH < 4.0. The modified nanoparticles synthesized had low agglomeration, which prevents their flocculation or coagulation tendency.

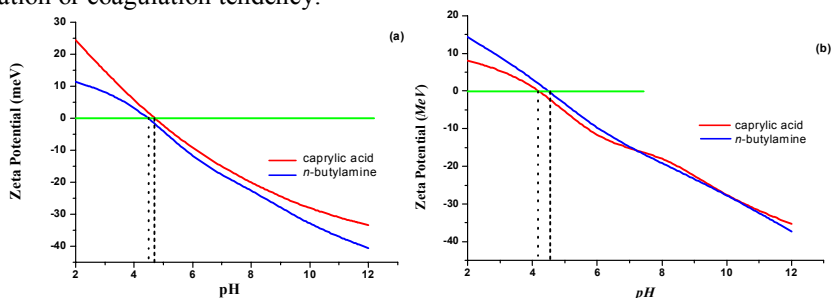


Fig. 5 – Zeta potential of surface modified a) TiO₂ and b) ZnO nanoparticles

BET SURFACE AREA OF SURFACE MODIFIED ZnO/TiO₂ NANOPARTICLES

BET surface area was measured for the surface modified hybrid ZnO nanoparticles using Malvern 2000. It was found that the BET surface area is 5.630 and 4.513 m²/g for surface modified ZnO hybrid nanoparticles using and *n*-butylamine and caprylic acid as surface modifier respectively. The BET surface area was found to be 15.928, 14.140 m²/g for surface modified TiO₂ hybrid nanoparticles using *n*-butylamine and caprylic acid respectively. In both cases, NaOH was used as solvent. The results reveal that *n*-butylamine makes the surface area more; the reason for having such low surface area can be contributed to the complex formation of ZnO nanoparticles with caprylic acid. It is known that surface modifiers are used to reduce agglomeration and hence reducing the particle size by controlling its growth direction. However, it was found that the affinity of ZnO nanoparticles to give bigger particles is proportional to the increasing concentration of the surfactant. Such phenomenon was not observed in the case of TiO₂.

EFFECT OF SOLVENT ON HYDROPHILICITY AND HYDROPHOBICITY

One of the most important effects of surfactant on nanomaterials is changing their hydrophilicity property. Density of ZnO is high (about 7.0 g/m^3) so that they are getting settle down quickly. We observed that *n*-butylamine could make the nanoparticles highly hydrophilic, which is very favorable for photo-degradation purposes. The reason is controlling the crystal growth, reducing agglomeration, and reducing density of the nanomaterials modified. The surface modification of the nanoparticles gives them an organic-inorganic hybrid so that the nanoparticles with desired properties can be fabricated. It was also observed that when HCl was used as solvent in modification of ZnO in presence of caprylic acid, it made the nanoparticles highly hydrophobic while using NaOH as solvent in presence of caprylic acid made the ZnO hybrid nanoparticles hydrophilic and reduced density of the nanoparticles modified. However, both surfactants gave hydrophilic property to TiO_2 nanoparticles. Reduction of density was directly proportional to the concentration of the surface modifier (i.e. caprylic acid) added. Such interesting hydrophobic and hydrophilic properties of the ZnO nanoparticles have been shown in Figs. 6-8.

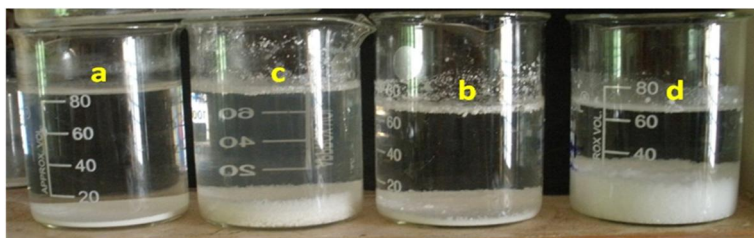


Fig. 6 – Effect of caprylic acid concentration on density and in turn hydrophilicity of the ZnO nanoparticles using NaOH as solvent a) 0.6 mL, b) 0.8 mL, c) 1.0 mL, and d) 1.2 mL caprylic acid



Fig. 7 – Effect of caprylic acid concentration on density and in turn hydrophobicity of the ZnO nanoparticles using HCl as solvent and caprylic acid as surface modifier

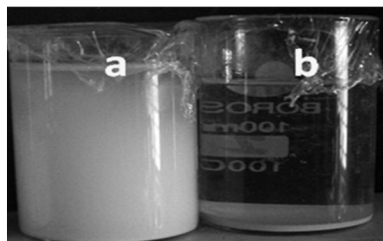


Fig. 8 – Effect of surfactant on hydrophilicity property of TiO_2 nanoparticles: a) using *n*-butylamine as surface modifier and b) without surface modifier

It seems HCl reacts with ZnO and give highly low dense mixed phases of ZnCl_2 and ZnO, which their density is less than water, which made them float at the surface of the water as a separate supernatant powder.

CONCLUSIONS

Surface modified ZnO/TiO₂ nanoparticles were successfully carried out under mild hydrothermal conditions. Caprylic acid and n-butylamine were used as surface modifier separately. Surface modification changed morphology and size of the ZnO/TiO₂ hybrid nanoparticles modified. In addition, it changed the surface charges and increased stability of the nanoparticles, which is necessary to achieve higher photodegradation efficiency. Using suitable solvent with respect to the precursors is an important factor in obtaining desired properties. Surface modifier along with solvent could give hydrophilic or hydrophobic property to the in situ surface modified ZnO hybrid nanoparticles. The results revealed that both caprylic acid and n-butylamine could be used for surface modification of ZnO particles. The strategy applied for surface modification could not only reduce agglomeration but also enhance the ZnO nanoparticles dispersibility.

REFERENCES

- [1] M. Zamfirescu, A. Kavokin, B. Gil et al. *Phys. Rev. B.*, 65 (2002) 161205.
- [2] S.W. Jung, W.I. Park, H.D. Cheong, G.C. Yi. *Appl. Phys. Lett.* 80 (2002) 1924.
- [3] K.J. Klabunde, Ed., *Nanoscale Materials in Chemistry*. Wiley-Interscience, New York, 2001.
- [4] L. Sanchez, J. Peral, X. Domenech. *Electrochim. Acta.* 41 (1996) 1981-1985.
- [5] Z. Huang, X. Zheng, D. Yan. Et al. *Langmuir*, 24 (2008) 4140-4144.
- [6] L. Wang, H. Wei, Y. Fan et al. *Nanoscale Res. Lett.* 4 (2009) 558-564.
- [7] J. Lahiri, M. Batzill. *J. Phys. Chem. C* 112 (2008) 4304-4307.
- [8] R. Hong, T. Pan, J. Qian, H. Li. *Chem. Eng. J.* 119 (2006) 71-81.
- [9] U. Narkiewicz, D. Sibera, I. Kuryliszyn-Kudelska et al. *ActaPhysicaPolonica A*. 113(2008) 1695-1700.
- [10] A.R. Bari, M.D. Shinde, V. Deo, L.A. Patil. *Indian J. Pure & Appl. Phys.* 47 (2009) 24-27.
- [11] B. Shahmoradi, K. Soga, S. Ananda et al. *Nanoscale*, 2 (2010) 1160-1164.
- [12] B. Shahmoradi, I.A. Ibrahim, K. Namratha et al. *IJCER*, 2 (2010) 107-117.
- [13] K. Byrappa, M. Yoshimura, *Handbook of Hydrothermal Technology*, Noyes Publications/William Andrew Publishing LLC, U.S.A. 2001.
- [14] L.N. Dem'yanets, D.V. Kostomarov, I.P. Kuz'mina. *Inorganic Materials*, 38 (2002) 124-131.
- [15] L.P. Donald, M.L. Gary, S.K. George, *Infrared spectroscopy*. In *Introduction to Spectroscopy*, Thomson Learning: 3rd Ed. USA, 2001. pp. 13-101.
- [16] *Zeta Potential of Colloids in Water and Waste Water*, ASTM Standard D 4187-82, American Society for Testing and Materials, 1985.
- [17] J. Lyklema, *Fundamentals of Interface and Colloid Science*. Elsevier, Wageningen, 1995.

RADIATION EFFECTS IN NANOSIZED CLUSTERS

Valiantsin M. Astashynski¹, Irina L. Doroshevich², Nicolai T. Kvasov^{2,*},
Andrey V. Punko², Yury A. Petukhou², Vladimir V. Uglov³

1 B.I. Stepanov Institute of Physics, NAS B, Nezalezhnasti 68, 220070, Minsk, Belarus

2 Belarusian State University of Informatics and Radioelectronics, Brouka 6, 220030, Minsk, Belarus

3 Belarusian State University, Nezalezhnasti 4, 220030, Minsk, Belarus

ABSTRACT

In this communication we present results of computer simulation of radiation-enhanced processes in nanosized ferromagnetic clusters under the irradiation by elementary particles and ions. Dynamic defects and possibility of their experimental monitoring are considered. Radiation resistance of nanostructured materials is characterized by the size of instability region for knocked-out atom. Heating and thermoelastic effects on defect structure and materials functionality are discussed.

Key words: magnetic nanocluster, irradiation, defects.

INTRODUCTION

Application of magnetic nanomaterials for data storage and recording devices makes it possible to increase writing density in 10⁴ times. Data record is made in separate nanosized single-domain particle with two energy states corresponding to magnetic moment orientation and separated by potential barrier. Significant advantages and perspective applications of these data carriers determine intensive development of this scientific and technological direction [1-4].

Magnetic nanoclusters are formed by different physical- and chemical-based techniques. For example, injection of metallic powder (Fe, Ni, Co) to dense compression plasma with temperature 2-3 eV [5-6] results in the formation of metallic vapor that condenses under certain thermodynamic conditions (*Fig. 1*). Deposition of metallic vapor on the substrate lets to the formation of metal layer consisting of spherical clusters with multi-level structure: submicron clusters (0,1-0,2 μm radius) are formed from a number of nanosized ones (10-25 nm radius).

Magnetic nanostructured cluster arrays have great prospects in the development of new generation of devices for operation in open space conditions. Nevertheless, the problem of their radiation stability is still insufficiently studied.

* e-mail: kvasov@bsuir.by, tel: (+375)172938613

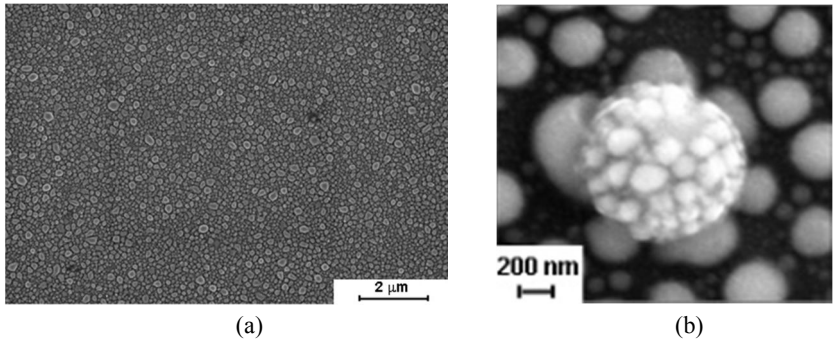


Fig. 1 – Scanning electron microscopy images (20k and 150k magnification) of iron clusters deposited from dense compression plasma on silicon surface

DYNAMIC RADIATION EFFECTS

Let us consider atom dynamics in the substance irradiated by changed and neutral particles (protons, ions, electrons, neutrons). Assume that atom with mass M is knocked-on by incident particle (or other displaced atom) and has kinetic energy W (W is less than defect formation energy E_d). It's motion is described by the following expression:

$$\frac{d^2\rho}{dt^2} + \xi \frac{d\rho}{dt} + f(\rho) = 0 \quad (1)$$

where ρ – distance from atom to lattice point; $\xi = n \cdot \mathfrak{S}$; n – number of force interactions between moving atom and lattice atoms; \mathfrak{S} – number of electrons in a cylinder with base Σ and height $\nu_a = d\rho/dt$ ($\Sigma \sim \pi r_0^2$, r_0 – covalent atomic radius);

$$f(\rho) = -\frac{1}{M} \frac{dU(\rho)}{d\rho} \quad (2)$$

$$U(\rho) = \sum_{i,j} \frac{e^2 i \cdot j}{\varepsilon_0 \varepsilon \rho} \varphi_{ij} \quad (3)$$

φ_{ij} – probability of “vacancy-interstitial atom” system to have configuration with charge states i and j , respectively, ε_0 – electric constant, ε – material permittivity, e – elementary charge.

Fig. 2 shows results of computer simulation of the process described by eq. (1) for iron atom with initial kinetic energy $W=50$ eV.

Dynamic state of vacancy and interstitial atom results in generation of electromagnetic radiation pulse. Its power I is proportional to the acceleration of interstitial atom w

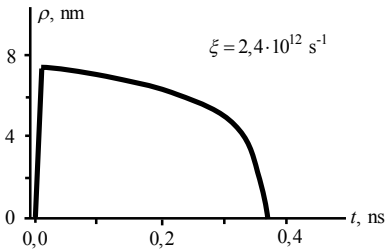


Fig. 2 – Time dependence of the distance between iron atom and lattice point

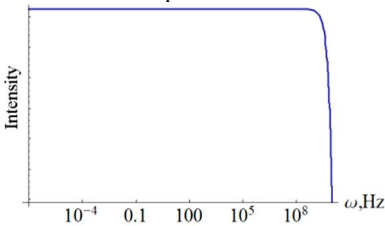


Fig. 3 – Electromagnetic radiation spectrum of dynamic defect generated by knocked-out iron atom with initial energy 50 eV

$$I \sim w^2(t) \tag{4}$$

Fourier transformation of (4) subject to atom’s motion law (1) gives electromagnetic radiation spectrum shown on *Fig. 3*. Thus, dynamic defects under the irradiation of materials by elemental particles and ions can be registered by the analysis of electromagnetic spectral composition.

Life time of the dynamic defect is about 10^{-10} с that is three orders greater than Debye period of lattice atoms oscillations. Therefore, acoustic lattice relaxation in this region results in the formation of shock pressure P propagating radially in cluster volume. Consider displacement cascade to be a sphere with radius R. At the moment $t=0$ rectangular “velocity pulse” v_0 is generated by m dynamic defects

$$v_0 = \left(\frac{2MW}{\gamma \cdot B} \right)^{1/2} \frac{m\xi}{4\pi R^2} \tag{5}$$

where γ – material density, B – bulk modulus. Velocity of deformation propagation v is obtained from nonlinear equation for mass velocity.

In the interaction of medium disturbance and dynamic defect (with deformation volume ω_0) the latter is affected by force $\vec{F} = -\gamma u \omega_0 \vec{\nabla} v$ (where u – speed of velocity in the matter). On the other hand, $\vec{F} = \vec{P} \cdot \delta$, where $\vec{P} = \gamma \cdot u \vec{v}$, δ – scattering cross-section

$$\delta = \left[\frac{2(1+\nu)\omega_0 G}{3(1-\nu)\pi^2 B} \ln \frac{R_d}{r_d} \right]^2 \sum_i K_i^4 \tag{6}$$

where ν – Poisson’s ratio, G – shear modulus, R_d – radius of the region deformed by the defect, r_d – defect radius, K_i – wave vector magnitude of the i -th spectral component of the deformation pulse, ω_0 – dilation volume. For body-centered iron lattice $F \sim 10^{-11} \div 10^{-10}$ N. Energy Q , obtained by the defect is estimated by the expression

$$Q = \frac{(F \cdot \tau)^2}{2M_d} \tag{7}$$

where τ – time of interaction between deformation pulse and defect with mass M_d ($\tau \sim 10^{-12}$ s).

When $F > F_0$ and $Q > E_m$ (where F_0 is critical force equal to U_a/a ; U_a – activation energy; a – lattice parameter; E_m – migration energy) one obtains diffusionless motion of the defect to nanoparticle surface (for iron $F_0 \sim 7 \cdot 10^{-12}$ N). One should take into account that thermal heating of the cluster results in activation of diffusion processes. Diffusion length $\sqrt{D\tau_p}$ (D – diffusion coefficient, τ_p – heating time) may exceed cluster size. For $D \sim 4 \cdot 10^{-4}$ m²/s ($T \sim 1200 \div 1500$ K) and “temperature life time” $\tau_p \sim 10^{-12}$ s one obtains $\sqrt{D\tau_p} \sim 2 \cdot 10^{-8}$ m, $Q \sim 1,5 \div 6,0$ eV.

Since kinetic energy of incident particle transforms to atoms displacement and heating of the deceleration region, we consider displacement cascade to be an instant heat source with temperature field $T(r, t)$ (Fig. 4). Radial thermoelastic stresses $\sigma_{rr}(r, t)$ and their gradient were calculated as

$$\sigma_{rr}(r, t) = 4\mu\alpha \frac{3\lambda + 2\mu}{\lambda + 2\mu} \left\{ \frac{1}{R_k^3} \int_0^{R_k} T(r, t) \cdot r^2 dr - \frac{1}{r^3} \int_0^r T(r, t) \cdot r^2 dr \right\}, \quad (8)$$

where μ and λ are Lamé coefficients, α – linear expansion coefficient, R_k – cluster radius.

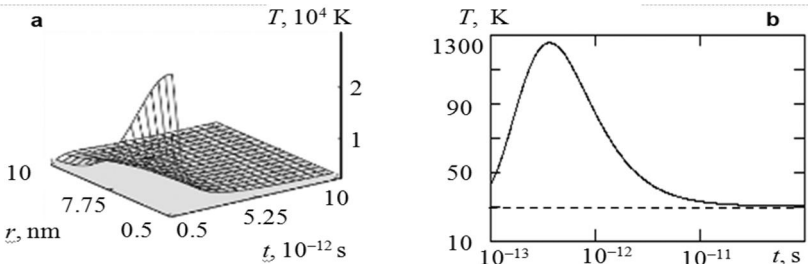


Fig. 4 – Space-time temperature distribution (a) and temperature evolution at $r = 7$ nm (b) for point heat source in iron nanocluster ($R_k = 15$ nm)

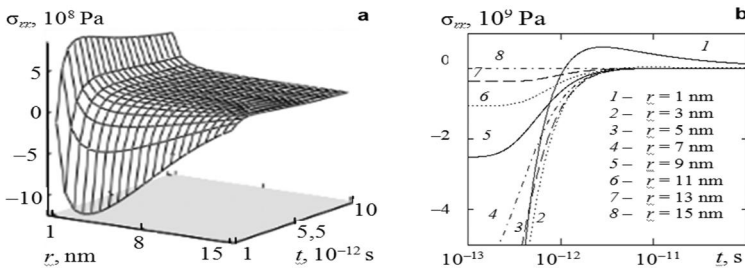


Fig. 5 – Space-time distribution of radial thermoelastic stresses (a) and stress evolution (b) in spherical iron nanoparticle ($R_k = 15$ nm)

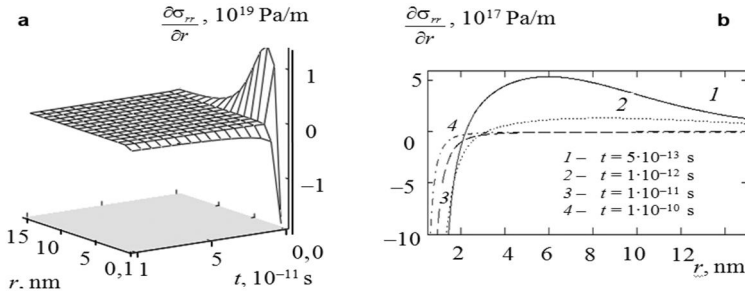


Fig. 6 – Space-time distribution of radial thermoelastic stresses gradient (a) and their evolution (b) in spherical iron nanoparticle ($R_k=15$ nm)

Fig. 5-6 show that elastic, thermal and thermoelastic response of cluster on radiation-induced structural changes results in defects elimination in nanoparticle (in this case Le Chatelier-Broun principle works in a special way).

Radiation-induced heating affects magnetic properties of nanocluster. Let us consider barrier height V between stable and metastable magnetic states of the ferromagnetic nanocluster (the value of V , obviously, determines stability of the recorded information). According to [7] it is estimated from the following expression:

$$V = \frac{4\pi R_k^3 K_{eff}}{3} \left[1 - \frac{H}{H_c} \right]^2 \tag{9}$$

where H – external magnetizing force; H_c – coercive force; K_{eff} – effective magnetic anisotropy constant. Temperature dependence of K_{eff} is expressed in the following manner [2]:

$$K_{eff} = \frac{4\pi\mu_0 (H_c)_{max} J_s(0)}{2} (1 - B_J T^b) \tag{10}$$

where $(H_c)_{max}$ – theoretical limit of coercive force; $J_s(0)$ – saturation magnetization for $T = 0$; B_J and b are values determined by cluster material and size.

In the absence of external magnetic field $V = V_0$:

$$V_0(T) = \frac{8\pi^2 \mu_0 R_k^3 (H_c)_{max} \cdot J_s(0)}{3} [1 - B_J T^b] \tag{11}$$

Calculations performed for experimental data [2] on iron clusters with $R_k \geq 7$ nm with extrapolation to high temperature regions give following values: $B_J = 4,76 \cdot 10^{-5} \text{ K}^{-3/2}$; $b = 1,5$; $J_s(0) = 6,58 \cdot 10^4 \text{ A/m}$; $(H_c)_{max} = 4,78 \cdot 10^4 \text{ A/m}$. Fig. 7 shows temperature dependence of potential barrier height V_0 .

Thus, V_0 turns to zero at temperature $T \approx 760$ K that is less than Curie temperature of bulk iron ($T_C = 1044$ K [8]).

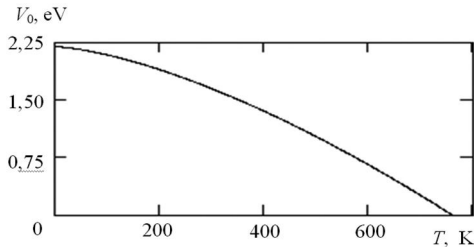


Fig. 7 – Temperature dependence of potential barrier height V_0 between magnetic states of iron nanocluster ($R_k=7$ nm)

Calculation results show that temperature of the nanocluster under irradiation is higher than temperature of magnetic transition (when $V_0=0$). Therefore, it results in failure of information record in the nanosized memory elements. This effect becomes more considerable for small-sized clusters.

CONCLUSIONS

1. Dynamic radiation defects that affect defect-impurity system of the cluster can be examined by electromagnetic radiation spectrum.
2. Irradiation of nanosized particles under the irradiation by charged and neutral particles results in radiation-enhanced self-organization tending to minimize bulk imperfection.
3. Temperature rise in nanoparticles under irradiation is one of the most significant factors that determine radiation stability of nanosized memory elements.

REFERENCES

- [1] J. Bansmann, S.H. Baker, C. Binns, et al. Surface Science Reports, 2005, Vol. 56, No. 6-7, P. 189-275
- [2] S.P. Gubin, Yu.A. Koksharov, G.B. Khomutov, G. Yu. Yurkov, Russian Chemical Reviews, 2005, Vol. 74, No. 6, P. 489-520.
- [3] R. A. Andrievskii. The Phys. of Metals and Metallography, 2010, Vol. 110, No. 3, P. 229-240
- [4] V. V. Podol'ski, V. P. Lesnikov, E. S. Demidov, et al., J. of Surf. Investigations: X-ray, Synchrotron and Neutron Techniques., 2010, Vol. 4, No. 3, P. 366-373.
- [5] V.M. Astashynski, S.I. Ananin, E.A. Kostyukevich, et al. High Temperature Material Processes, 2007, Vol. 11, №4, P. 537-548.
- [6] V.M. Astashynski, V.V. Uglou, N.T. Kvasovet al. VIth International Conference "Plasma Physics and Plasma Technology", 2009, Minsk, Contributed Papers: Vol. I, P.406-409
- [7] K.A. Zvezdin, Phys. Solid State, 2000, Vol. 42, No. 1, P. 120-125.
- [8] Smithells Metals Reference Book (Eds. E.A. Brandes, G.B. Brook), Butterworth-Heinemann, Oxford, 1992.

PECULIARITIES OF GENERATION AND TRANSPORT OF STRUCTURAL DEFECTS INDUCED BY THE LASER IRRADIATION

Alexander E. Pogorelov

G.V. Kurdyumov Institute for Metal Physics, NAS, Vernadsky 36, 03142, Kiev, Ukraine

ABSTRACT

In this work we discuss the peculiarities of generation and transport of the structural defects caused by external pulsed action on a crystal and, in particular, by a laser irradiation. The conditions for such processes to take place are defined and a novel approach is proposed for studying the kinetics of transport under the pulsed laser irradiation. Taking into account electronic character of a thermal conduction in metals a general model for the transport in pulse deformable crystals is presented.

Key words: crystal, structural defects, dislocations, mass-transport, thermal conduction, laser irradiation

INTRODUCTION

High-speed deformation of metals in the solid phase leads to the generation and migration of lattice defects at large distances. As shown in [1,2], dislocations are the most likely carriers, in particular of the mass. Their formation during pulsed laser irradiation has been confirmed experimentally in [3]. Direct study of concentration changes with the use of radioactive isotopes have shown that a region with a high content of dislocations (30 ÷ 40 micron) is several times larger than the area of mass transfer [4]. At the same time the mass-transfer occurs to the depths several times exceeding the area of thermal influence of a laser pulse.

CRITERIONS AND ANALYSIS

Processes of transport occurring in a crystal have a threshold nature and are determined by the criterion setting the boundary between the stationary state of the matter and its existence in highly nonstationary state [5]. This boundary can be set by comparing the time t_i the energy is supplied into the substance and time t_r of its relaxation. In a case if $t_i \geq t_r$, the relaxation processes occur in a stationary or quasi-stationary state. If $t_i <$ or $\ll t_r$, the state changes from the quasi-stationary to highly nonstationary.

Besides, for the dislocations to be generated in the crystal it is required that the portion of the energy supplied into it was sufficient to create stresses σ larger than the Young's modulus E . For the motion of dislocations it is sufficient that stresses developed by an energy pulse $\sigma > 10^{-4} \div 10^{-2} E \approx \sigma_p$ (Peierls

stress). When selecting the mode it is important to remember that high portions of energy may result in crystal fracture.

When the region d is irradiated by axisymmetric laser beam the required criterion is in first approximation determined as

$$t_c = \pi d^2 / 4a, \quad (1)$$

Where a - a material thermal diffusivity. As follows from (1) the critical time t_c of the energy supply strongly depends on the size of irradiated area. When irradiating metals by laser impulses in a free generation mode ($\tau_i \approx 10^{-3}$ s) or by continuous irradiation the relaxation is limited only by the thermal conduction mechanism. The value of thermal gradient during such irradiation does not cause significant deformations, which could lead to the formation of excessive number of structural defects such as dislocations and interstitial atoms.

The irradiation of metals by huge laser pulses with $\tau_i \approx 10^{-8}$ s cannot restrict the energy drain only to the thermal conduction mechanism. This process causes a significant temperature gradient accompanied by the rapid thermal expansion of the irradiated area and occurrence of thermal stresses σ .

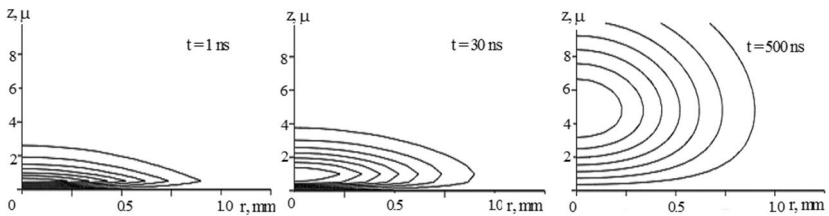


Fig. 1 – Maximum of the thermal stresses gradient is moving from laser irradiated surface deep into the crystal.

The relaxation of the energy by unrelaxed thermal conduction occurs through the appearance of a shock wave in a metal and generation of the excess number of structural defects of all types. The density of dislocations ρ arising as a result of these processes is determined from [1]

$$\rho_j(z, t) = \rho_{j-i} - \frac{2\alpha}{(1-\nu)b} \int_1^n \nabla T(0, z, \lambda\tau) d\lambda \quad (2)$$

where α – thermal expansion coefficient of the metal, b – Burgers vector, ν – Poisson's ratio, n – number of laser actions.

RESULTS AND DISCUSSION

Figure 2 shows the dislocation density as a function of the depth z of the pulsing laser influenced *Armco-Fe*, calculated using the formula (2) and compared with the experimental data obtained in [3].

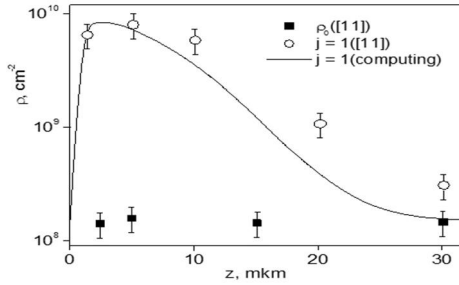


Fig. 2 – Dislocation density vs. depth z of pulsing laser influenced Armco-Fe.

Figure 3 presents schematics of generation and transport of the structural defects caused by a laser irradiation.

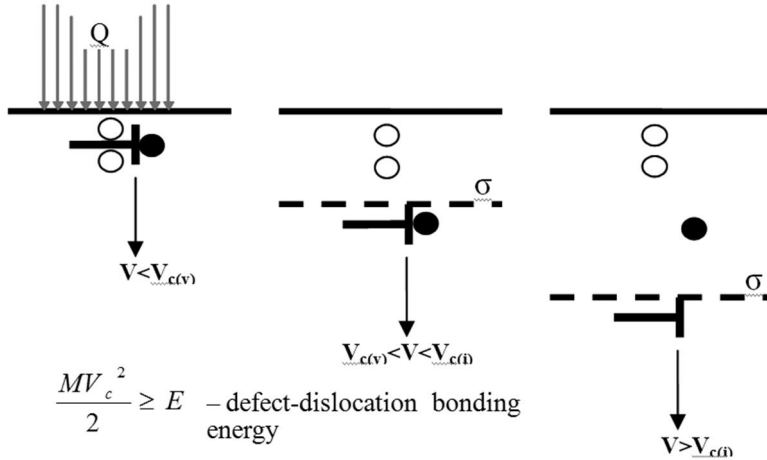


Fig. 3 – Generation and transport of structural defects caused by a laser irradiation

The particular interest in studying of the structural defects generated and migrating under the influence of a laser irradiation is their detection in real time. It has been noted that when measuring a thermal diffusivity by the laser flash method [6], the increase of temperature T on the opposite side of the flat sample of the given thickness reaches values $T/2$ for different time $t_{1/2}$ for a different pulse length. Moreover, the value of $\Delta t_{1/2}$, which is the determining parameter in the calculation of a , does not exceed the time required for the acoustic wave to pass through the sample. Considering the electronic nature of a thermal conduction in metals and above discussions, a general model for the transport in pulse deformable crystals is proposed. Also proposed is the technique to study a kinetics of transport under specified conditions.

CONCLUSIONS

Under conditions of pulsed deformation of crystals a directed transfer of point defects (PD) is carried out. These defects are produced due to displacement and interaction of dislocations, which are trapping and transporting PD during directional movement in the field of dynamically varying stresses σ . Movement of such a complex «dislocation + PD» is happening until its kinetic energy V_c becomes higher than the defect-dislocation bonding energy E . When moving with the speed higher critical value the dislocation is dropping an atmosphere containing vacancies while its core is continuing the movement together with trapped interstitial atoms. As a result the near-surface layers are being saturated with vacancies. At the same time the deeper layers are saturated with interstitial atoms, entrained by dislocations to larger depth from the near-surface layer.

REFERENCES

- [1] A. Pogorelov, A. Zhuravlev. Defect and Diffusion Forum. Switzerland, Scitec Public., V.194-199, 2001, P. 1247-1252.
- [2] A.E. Pogorelov, K. P. Ryaboshapka, A. F. Zhuravlev. JAP, 92(2002), p. 5766-5771.
- [3] P.Yu. Volosevich, A.E. Pogorelov. Poverhnost. Fizika, himia, mehanika, 9(1986), c. 126-130.
- [4] A.E. Pogorelov. PhD Theses, Kiev, 1985.
- [5] A. Pogorelov. International Conference NANO-2010, Ukraine, Kiev, October 19-22, 2010, P. 162.
- [6] M.E.Gurevich, A.E. Pogorelov. – In: «Fizicheskie metody issledovania metallov». Kiev, Naukova dumka, 1981, P. 3-23.

INFLUENCE OF MIGRATION THE RADIATION-INDUCED EXCITATIONS IN HETERO-FULLERENES C₅₈Si₂ AND C₆₈Si₂ OF THEIR PROBABILITY OF DAMAGE

M.V. Kobets*, P.A. Selyshchev

Taras Shevchenko national university of Kyiv, Ukraine

ABSTRACT

Theoretically investigated the role of migration of radiation-induced excitation in the damaged hetero-fullerenes C₅₈Si₂ and C₆₈Si₂. Defined expressions for the probability collapse of fullerenes different structures. Investigate the changing probability on irradiated conditions.

Key words: irradiation, energy migration, probability of collapse, hetero-fullerenes.

INTRODUCTION

Physical properties of materials under irradiation significantly changed, due to changes in the microstructure of this material. One result of the impact of exposure to the material is radiation-induced excitation of the electron subsystem of molecules matter [1-4].

In a molecule such transfer occurs repeatedly, and energy can shift from place of absorb on relatively large distance [5]. On moving, excitation energy dissipated in each between the atomic transition.

In the presence in a molecule atoms of several varieties can be expected that the energy bind of different sorts of atoms will be different, while some will be more strongly linked that other less. In some cases the difference of energy strong coupling and weak will be significant. We can expect that the vagus excitation, which arose due on the strong bind, reaching the weak, break it, resulting in damage or collapse of the molecule.

Thus, of interest to investigate the lifetime and the likelihood of damage to the molecules, in which are formed vagus excitation, and to identify the basic patterns are caused by this process.

Thus, if there is a walk of excitation, the probability of damage (collapse) of the molecule depends on the mechanisms of migration of energy to a large extent depends on its structure, the number of weak binds, and the configuration of the placement of weak binds in the molecule. Another important factor that affects the probability of collapse of the molecule is the

* e-mail: max.kobets@gmail.com, tel: (+093)7877523

energy of initial excitation, which determines the maximum length path of migration of excitation to the moment of its complete decay.

In this work the probability of damage of the Herero-fullerenes $C_{58}Si_2$ and $C_{68}Si_2$ [6-7] depending on the structure of molecules, initial excitation energy, the number and configuration of weak binds.

RESULTS AND DISCUSSION

Results of numerical calculations of the probability of collapse of the herero-fullerenes $C_{58}Si_2$ and $C_{68}Si_2$, depending on the excitation path, and placement configurations of impurity atoms are represented in the graphs in Fig. 1-2, respectively. The calculations were carried out at values of energy bonds: Si-C - 290 kJ/mol, C-C - 344 kJ/mol and independent placement of atoms Si. Length of run, on condition of exponential decay of the excitation path length was defined expressions:

$$n = \frac{x_0}{h} \ln \left(\frac{E_0}{E_{\min}} \right),$$

where, n is number of excitation jumps, x_0 is distance at which the excitation energy decreases in e times, h is distance between neighboring atoms, E_0 is initial value of excitation energy, E_{\min} – minimum energy at which the gap weak connection is still possible.

Magnitude L – distance between atoms Si (in units of interatomic distance). Ortho and meta configuration [7] correspond to the case when Si atoms are in the neighborhood.

Based on the results can be noted that with increasing length of run initial perturbation probability of damage of hetero-fullerene as $C_{58}Si_2$ and $C_{68}Si_2$ increases, approaching to the one.

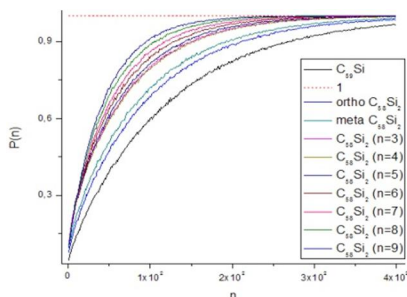


Fig. 1 – The probability of damage hetero-fullerene $C_{58}Si_2$ depending on the initial excitation energy and configuration placement of weak ties

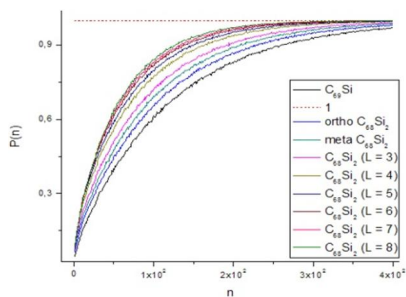


Fig. 2 – The probability of damage hetero-fullerene depending on the initial excitation energy and configuration placement of weak ties

Change of configuration the placement of weak ties also lead to a change in the probability of collapse of the molecules. In particular, with increasing distance (L) between the atoms replacing possibility damage Herero-fullerenes also increases.

CONCLUSIONS

Based on the assumption that the radiation excitation of electron subsystem of atoms can wander through the molecule and outrage break weak binding, using numerical methods, built graphics of damage herero-fullerenes $C_{58}Si_2$ and $C_{68}Si_2$ depending on the energy of the initial disturbance.

Investigated the influence of configuration placing weak bonds on the probability of damage of hetero-fullerenes $C_{58}Si_2$ and $C_{68}Si_2$.

Determine the average time of impact to radiation, after it is off.

REFERENCES

- [1] В.М. Агранович, М.Д. Галанин, Перенос энергии электронного возбуждения в конденсированных средах // М., 1978.
- [2] Г. Дермингер, Х. Юнг, Молекулярная радиофизика // М., 1973, с. 248
- [3] С. Рид, Возбуждение электронные состояния в химии и биологии // М., 1960.
- [4] К. Смит, Ф. Хэнеуолт, Молекулярная фотобиология // М., 1972.
- [5] Н.Н. Шафрановская, Э.Н. Трифонов, Ю.С. Лазуркин, М.Д. Франк-Каменецкий. Письма в ЖЭТФ, Том 15, No 7, с. 404-408.
- [6] Jan C. Topics in Current Chemistry, 1999, Vol. 199, P. 94-123.
- [7] C. Ray, M. Pellarin. Physical review letters, Vol. 80, No24, P. 5365.

INVESTIGATION ON THE EFFECTS OF TITANIUM DIBORIDE PARTICLE SIZE ON RADIATION SHIELDING PROPERTIES OF TITANIUM DIBORIDE REINFORCED BORON CARBIDE-SILICON CARBIDE COMPOSITES

Bulent Buyuk^{1*}, A. Beril Tugrul¹, A. Cem Akarsu², A. Okan Addemir²

1 ITU Energy Institute, Nuclear Science Division, Ayazaga Campus, 34669, Istanbul, Turkey

2 ITU Metalurgical and Materials Engineering Faculty, Ayazaga Campus, 34669, Istanbul, Turkey

ABSTRACT

Composite materials have wide application areas in industry. Boron Carbide is an important material for nuclear technology. Silicon carbide is a candidate material in the first wall and blankets of fusion power plants. Titanium diboride reinforced boron carbide-silicon carbide composites which were produced from different titanium diboride particle sizes and ratios were studied for searching of the behaviour against the gamma ray. Cs-137 gamma radioisotope was used as gamma source in the experiments which has a single gamma-peak at 0.662 MeV. Gamma transmission technique was used for the measurements. The effects of titanium diboride particle size on radiation attenuation of titanium diboride reinforced boron carbide-silicon carbide composites were evaluated in related with gamma transmission and the results of the experiments were interpreted and compared with each other.

Key words: Nanocomposite, Boron Carbide, Titanium Diboride, Silicon Carbide, Cs-137 Gamma Source, Gamma Transmission Technique

INTRODUCTION

Boron carbide has wide application areas in industry. Some of these areas are nuclear technology, military industry, ceramic industry and air-space industry [1, 2]. Boron carbide has some important properties such as low-density, high hardness and corrosion resistance, chemical stability and high neutron capture feature [2]. Some boron carbide application fields are lightweight ceramic armor, sand blasting nozzles, nuclear reactors, reactor control rods and the radiation shielding materials [2, 3]. However, boron carbide is brittle, has low strength and high temperature sintering properties [3, 4]. Sintering of pure boron carbide to high densities is difficult. So, specific additives such as SiC, TiB₂, AlF₃, elemental boron and carbon have been used as sintering aids to increase the density of composite [2-5].

Silicon carbide has been considered as a candidate material in the first wall and blankets of future fusion power plants because of its safety, environmental and economic benefits [6].

In this study, titanium diboride reinforced boron carbide- silicon carbide composites which were produced from different titanium diboride particle sizes and ratios were studied for searching of the behaviour against the gamma ray. For the investigation of

* buyukbu@itu.edu.tr, tel: (+90)2122853894

the gamma radiation behaviour of these materials, Cs-137 radioisotope was used as gamma source in the experiments. Cs-137 gamma radioisotop source has a single gamma-peak at 0.662 MeV and its half life is 30.1y [7, 8]. Gamma transmission technique was used for the measurements.

Different titanium diboride particle sizes and ratios in titanium diboride reinforced boron carbide-silicon carbide composites were evaluated in related with gamma transmission and the results of the experiments were interpreted and compared with each other. Therefore, the effects of boron carbide particle size in titanium diboride reinforced boron carbide-silicon carbide composites on gamma radiation attenuation were investigated against Cs-137 gamma radioisotope source by using gamma transmission technique.

EXPERIMENTS AND MATERIALS

Gamma transmission technique is based on passing gamma rays through the materials. Detector and gamma source put both sides of the material. Detector material and gamma source are in the same axis. The gamma radiation counts are measured reaching to detector from the source. The counts with material and without material are compared and evaluate [7-9]. *Fig.1* shows schematic view of gamma transmission technique.

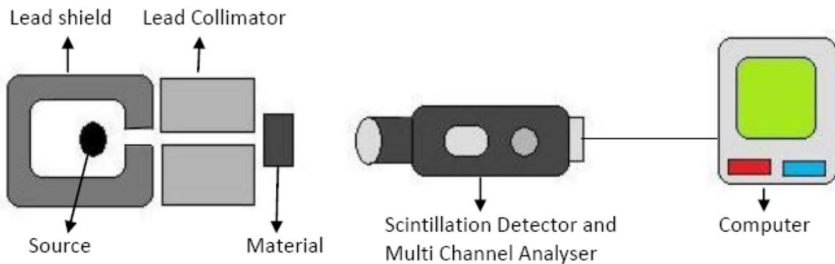


Fig. 1. Schematic View of Gamma Transmission Technique

The radiation passing through the material is calculated by the following equation: where I and I_0 are the transmitted and initial gamma ray intensities, respectively, μ is linear attenuation coefficient of material at specific γ - ray and x is the thickness of the material.

(1)

The materials which were used in the experiments have different boron carbide particle size ratios in the composites. Thus they are coded according to their boron carbide and titanium diboride ratios by volume in composites and particle size ratios. *Table 1* shows the materials that used in the experiments and their ratios by volume in the composite materials.

Table (1). The contents of the composite materials which were used in the experiments

Material (Code)	Boron Carbide (% Volume)	Silicon Carbide (% Volume)	Titanium Diboride (% Volume)	Nano Titanium Diboride (% Volume)
8202_b	78,4	19,6	2	-
8202_k	78,4	19,6	-	2
8204_b	76,8	19,2	4	-
8204_k	76,8	19,2	-	4

Table 2 shows the hardness, strength and density properties of the materials which were used in the experiments [5].

Table (2). The hardness, strength and density properties of the composite materials which were used in the experiments

Material (Code)	Strength (MPa)	Hardness (Vickers)	Density (g/cm³)
8202_b	261,425±25,60	1902,57±131,8	2,361
8202_k	233,25±36,45	1868,29±96,74	2,394
8204_b	276,125±78,79	1983,67±56,78	2,429
8204_k	279,5±45,51	2211,80±168,17	2,476

For production of nano scale titanium diboride, titanium diboride materials were milled in Spex 8000 mill for one hour with WC balls. Average particle sizes were decreased to about 170 nm. Figure 2 shows particle size distribution graph of milled titanium diboride particles.

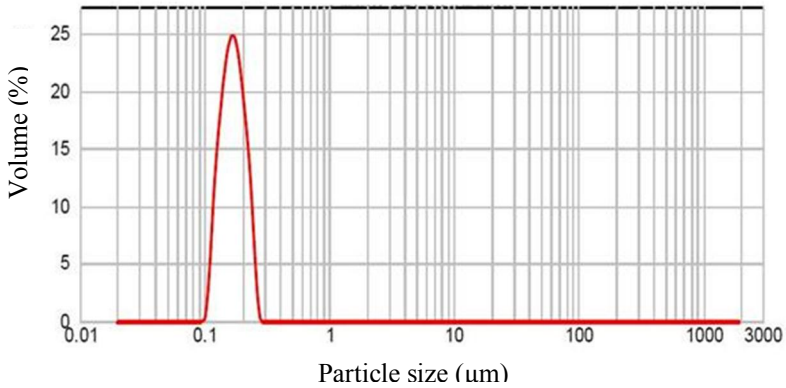


Fig 2. Particle Size Distribution of 60 minutes milled Boron Carbide

All composite materials were sintered hot pressed method at 2250 °C for 2 hours under 130 MPa pressure. Cs-137 Gamma Radiation source which has 8.9 μ Ci was used in the experiments. Lead blocks were used for radiation shielding and collimation. The collimator diameter is 7 mm. The distance between the detector and source is 10 cm.

Firstly background radiation measured. Then Cs-137 Gamma source was set. Initial intensity count (I_0) was measured. Then materials were set and intensity counts (I) were measured for different thickness values. All counts were measured three times for 600 seconds. Net counts calculated by reducing background value. Average values and standard deviations were calculated. For rational evaluating, relative intensity (I/I_0) values were calculated. Results were given with tables. Relative intensity-Material Thickness Graph was drawn for each Titanium diboride ratio and particle size. Exponential distribution was shown on graphs and exponential equations were calculated. Then results were evaluated and discussed.

RESULTS AND DISCUSSION

Results for 2% titanium diboride reinforced boron carbide-silicon carbide composites (8202_b) at different thicknesses with Cs-137 Gamma source are given on Table 3.

Table (3). Results for 8202_b titanium diboride reinforced boron carbide-silicon carbide composites with Cs-137 Gamma source

Thickness (cm)	8202_b			Average Count	Standart Deviation	Relative Count
	Net Count 1	Net Count 2	Net Count 3			
0,000	8135	8128	8211	8158	46	1,000

0,590	7372	7393	7320	7362	38	0,902
1,165	6654	6652	6780	6695	73	0,821
1,725	6147	6121	6073	6114	37	0,749
2,287	5736	5689	5621	5682	58	0,696

Results for 2% nano titanium diboride reinforced boron carbide-silicon carbide composites (8202_b) at different thicknesses with Cs-137 Gamma source are given on *Table 4*.

Table (4). Results for 8202_k titanium diboride reinforced boron carbide-silicon carbide composites with Cs-137 Gamma source

Background = 89						
8202_k						
Thickness (cm)	Net Count 1	Net Count 2	Net Count 3	Average Count	Standart Deviation	Relative Count
0	8081	8134	8096	8103	27	1,000
0,5879	7287	7280	7306	7291	13	0,900
1,1837	6630	6644	6640	6638	7	0,819
1,766	6090	6050	6071	6070	20	0,749
2,3512	5512	5538	5532	5527	13	0,682

Results for 4% titanium diboride reinforced boron carbide-silicon carbide composites (8204_b) at different thicknesses with Cs-137 Gamma source are given on *Table 3*.

Table (5). Results for 8204_b titanium diboride reinforced boron carbide-silicon carbide composites with Cs-137 Gamma source

Background = 89						
8202_b						
Thickness (cm)	Net Count 1	Net Count 2	Net Count 3	Average Count	Standart Deviation	Relative Count
0,000	8135	8128	8116	8127	10	1,000
0,571	7346	7297	7367	7337	36	0,903
1,119	6718	6696	6725	6713	15	0,826
1,664	6163	6121	6171	6152	27	0,757
2,229	5610	5656	5590	5619	34	0,691

Results for 4% nano titanium diboride reinforced boron carbide-silicon carbide composites (8202_b) at different thicknesses with Cs-137 Gamma source are given on Table 4.

Table (6). Results for 8204_k titanium diboride reinforced boron carbide-silicon carbide composites with Cs-137 Gamma source

Background = 89		8202_k				
Thickness (cm)	Net Count 1	Net Count 2	Net Count 3	Average Count	Standart Deviation	Relative Count
0	8178	8093	8085	8118	52	1,000
0,5661	7266	7332	7382	7327	58	0,902
1,1332	6662	6658	6728	6683	40	0,823
1,7	5996	6184	6052	6077	96	0,749
2,27	5502	5572	5588	5554	46	0,684

Using the values on the tables Relative Intensity-Material Thickness Graphs were drawn for all titanium diboride reinforced boron carbide-silicon carbide composites. Exponential fitted equations were calculated. Figure 3 shows Relative Intensity-Material Thickness Graphs of 2% titanium diboride reinforced boron carbide-silicon carbide composites.

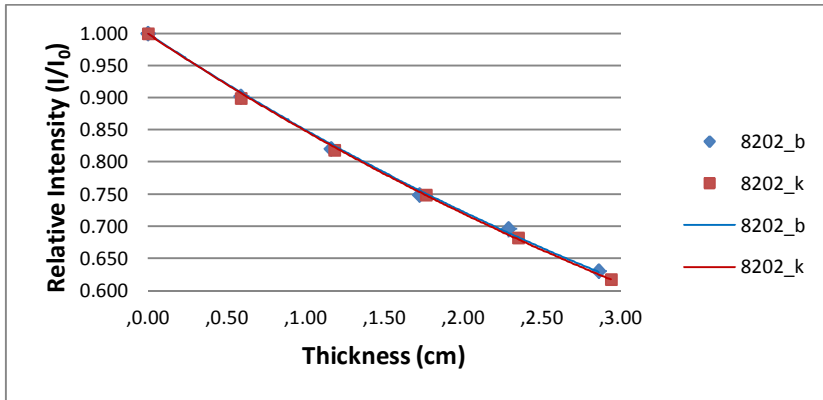


Fig. 3. Relative Intensity-Material Thickness Graphs of 2% titanium diboride reinforced boron carbide-silicon carbide composites.

Figure 4 shows Relative Intensity-Material Thickness Graphs of 4% titanium diboride reinforced boron carbide-silicon carbide composites

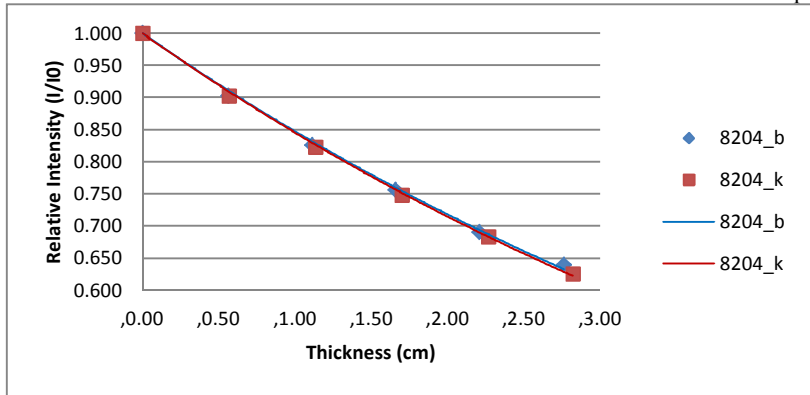


Fig. 4. Relative Intensity-Material Thickness Graphs of 4% titanium diboride reinforced boron carbide-silicon carbide composites.

Using the graphs on *Fig 3* and *Fig 4* the linear attenuations of the composite materials and correlation coefficients were calculated. The mass attenuation coefficients (μ/ρ) of the composite materials were also calculated. Then mass attenuation coefficient values were compared with the theoretical values which were taken from XCOM computer code.

The linear and mass attenuation values and XCOM values of the composites are given on *Table 6*.

Table (7). The Linear and Mass attenuation coefficient of the composite materials.

Material (Code)	Linear attenuation coefficient (cm^{-1})	Mass Attenuation Coefficient (cm^2/g)		
		Experimental (10^{-2})	Theoretical (XCOM)	Difference (%)
8202_b	0,162	6,862	7,355	6,710
8202_k	0,164	6,850	7,355	6,867
8204_b	0,165	6,793	7,352	7,605
8204_k	0,168	6,785	7,352	7,712

All correlation coefficient values of the linear attenuation coefficients are over 0.99. The linear attenuation coefficients of milled titanium diboride reinforced boron carbide-silicon carbide composites are higher than unmilled reinforced ones. The mass

attenuation values are closed to theoretical values which were taken from XCOM. The differences of theoretical and experimental values are between 6-8%.

CONCLUSIONS

It could be understood that for 2% milled titanium diboride reinforced boron carbide-silicon carbide, the linear attenuation coefficient is higher than unmilled one. In addition for 4% milled titanium diboride reinforced boron carbide-silicon carbide, the linear attenuation coefficient is higher than unmilled one the linear attenuation coefficient is higher than unmilled one. The experimental values and theoretical values from XCOM are closed to each other. Therefore it can be said that decreasing the titanium diboride particle size in the composites causes higher linear attenuation values.

In conclusion, milled composite materials are more convenient than unmilled composite materials for gamma radiation shielding in nuclear technology.

ACKNOWLEDGEMENTS

The authors are thankful to BMBT Co. for production of materials.

REFERENCES

- [1] Büyük B., Tuğrul A.B., Akarsu A.C., Addemir A.O., 2011. Investigation of Behaviour of Titanium Diboride Reinforced Boron carbide-Silicon carbide composites Against Cs-137 Gamma Radioisotope Source by Using Gamma Transmission Technique. *Advances in Applied Physics&Materials Science Congress Book of Abstracts Vol.1*,pp 486
- [2] Thevenot F., 1990. Boron Carbide – A Comprehensive Review, *Journal of European Ceramic Society*, 6, pp205-22
- [3] Cho N., 2006. Processing of Boron Carbide, *Ph. D.Thesis*, pp5-6-7-9, Georgia Institute of Technology.
- [4] Aktop S., 2010. An investigation on the effects of sub micron boron carbide addition and reaction sintering to the boron carbide-titanium diboride composites. *M.Sc. Thesis*. ITU Institute of Science and Technology. Istanbul.
- [5] Akarsu A.C. 2009. An investigation on the properties of titanium diboride hot pressed boron carbide-silicon carbide composites. *M.Sc. Thesis*. ITU Institute of Science and Technology. Istanbul.
- [6] Taylor N.P., Cook I, Forrest R.A., Forty C.B.A., Han W.E., Ward D.J., 2001. The safety, environmental and economic implications of the use of silicon carbide in fusion power plant blankets. *Fusion Engineering and Design*,58-59,991-995
- [7] Halmshaw, R., 1991. Non-Destructive Testing. *E. Arnold*, London
- [8] Büyük B., Tuğrul A.B., 2009. Thickness measurement for the different metals by using Cs-137 gamma source with gamma transmission technique. *X. National Nuclear Science and Technologies Congress full text edition*, pp 49-58. Mugla
- [9] Földiák, G., 1986. Industrial Application of Radioisotopes, *Elsevier*, Amsterdam
- [10] Berger M.J., Hubbell J.H., Seltzer S.M., Chang J., Coursey J.S., Sukumar R., Zucker D.S., Olsen K. , XCOM: photon crosssection database. <http://www.nist.gov/pml/data/xcom/index.cfm>, U.S.

- Structural changes in friction-stir welded Al-Li-Cu-Sc-Zr (1460) alloy** 247
A. L. Berezina, N. N. Budarina, A. V. Kotko, O. A. Molebny, A. A. Chayka, A. Ya. Ischenko
- Improving thermo-mechanical properties of tabular alumina castables via using nano structured colloidal silica** 254
A. Soury, F. K. Nia, H. Sarpoolaky
- Ultrafine grain refinement of iron induced by severe plastic deformation in assistance of multi-directional deformation mode** 260
A. I. Yurkova, A. V. Byakova, M. Gricenko
- Cold-spray technique as efficient alternative process for consolidation of powdered Al-Fe-Cr alloys reinforced by nanoquasicrystalline particles** 270
A. V. Byakova, A. I. Yurkova, V. V. Cherednichenko, A. I. Sirko
- High pressure torsion of nickel powders obtained by electrodeposition** 279
L.D. Rafailović, C. Rentenberger, A. Gavrilović, C. Kleber, H. P. Karnthaler, C. Gammer
- Determination of effective diffusion coefficients for inhomogeneous media** 282
Yu.O. Lyashenko, L.I. Gladka
- Solid transformations as a variant of three-dimension nanotechnology** 287
V. N. Belomestnykh, E.P. Tesleva
- Nanosize phases formation under low carbon steel thermomechanical strengthening** 293
V. E. Gromov, Yu. F. Ivanov, V.B. Kosterev, S. V. Konovalov
- Production of SnO₂ nano-particles by hydrogel thermal decomposition method** 302
P. Jajarmi, S. Barzegar, G.R. Ebrahimi, N. Varahram
- Microbial synthesis of silver nanoparticles by streptomyces glaucus and spirulina platensis** 306
N. Ya. Tsibakhashvili, E.I. Kirkesali, D.T. Pataraya, M. A. Gurielidze, T.L. Kalabegishvili, D. N. Gvarjaladze, Giorgi I. Tsertsvadze, M.V. Frontasyeva, I. I. Zinicovscaia, M.S. Waksstein, S. N. Khakhanov, N. V. Shvindina, V. Ya. Shklover
- Nuclear and related analytical techniques for bio-nanotechnology** 311
Frontasyeva M.V.
- Optical monitoring of technological processes for fabrication of thin-film nanostructures** 315
A. Yu. Luk'yanov, P.V. Volkov, A.V. Goryunov, V. M. Daniltsev, D.A. Pryakhin, A. D. Tertyshnik, O.I. Khrykin, V.I. Shashkin
- Preparation nano sized HMX by using ultrasonic waves** 322
Ya. Bayat, S.H.Mousavi, F. Bayat, Gh. Rastegar Nasab, T.Gholamhosseini

Spectrographs for analyzing nanomaterials	328
<i>N. K. Pavlycheva, M.A. Hassan</i>	
Synthesis, characterization and performance study of phosphosilicate gel-sulfonated poly (ether ether ketone) nanocomposite membrane for fuel cell application	335
<i>Ch. Dhole, A. Nando, K. Kargupta, S. Ganguly</i>	
Spark plasma sintering the spark-erosion powders of functional alloys	340
<i>G. E. Monastyrsky, P. Ochin, A. V. Gilchuk, V. I. Kolomytsev, Yu.N. Koval</i>	
Application of simulation technologies to the investigation of the beam generating systems	350
<i>I.V. Barsuk, A.V. Bondar, G.S. Vorobjov, A.A. Drozdenko</i>	
Critical exponents in percolation model of track regions with different depth distribution	355
<i>Demchyshyn A., Selyshchev P.</i>	
Porous matrixes based on ion-irradiated polymer as templates for synthesis of nanowires	359
<i>D.Zagorskiy, S.Bedin, V.Korotkov, V.Kudravtsev, V.Oleinikov, P.Ershov, A.Vilenski</i>	
Influence of γ-irradiation on optical properties of GaSe crystals	364
<i>Yu.I. Zhirko, N.A. Skubenko, V.I. Dubinko, Z. D. Kovalyuk, O. M. Sydor</i>	
Temperature dependence of a period of the modulated structure in atom–vacancy solid solution	371
<i>O.V. Oliinyk, V.A. Tatarenko</i>	
X-ray and raman investigations of layered InSe and GaSe single crystals irradiated with high-energy gamma-quanta	376
<i>Z. D. Kovalyuk, V. G. Tkachenko, I. M. Maksymchuk, O. M. Sydor, O. A. Sydor, V. I. Dubinko</i>	
Investigation on the effects of titanium diboride particle size on radiation shielding properties of titanium diboride reinforced boron carbide-silicon carbide composites	381
<i>B. Buyuk, A. B. Tugrul, A. C. Akarsu, A. O. Addemir</i>	
Influence of high reactor irradiation on some parameters of Al₂O₃ crystals and process generation of a several points nanodefects	385
<i>I. Kh. Abdukadyrova</i>	
Investigation of the nanostructures formation in the irradiated by γ – quanta single-crystal silicon with ultrasonic method	389
<i>T. Khaydarov, I.Kh. Abdukadirova, Yu. Karimov</i>	
“Etchability” of ion tracks in SiO₂/Si and Si₃N₄/Si thin layers	393
<i>L. A. Vlasukova, F. F. Komarov, V. N. Yuvchenko, V. A. Skuratov</i>	

-
- Surface modification of ZnO and TiO₂ nanoparticles under mild hydrothermal conditions** 400
B. Shahmoradi, A. Maleki
- Radiation effects in nanosized clusters** 408
V.M. Astashynski, I.L. Doroshevich, N. T. Kvasov, A. V. Punko, Yu.A. Petukhou, V.V. Uglov
- Peculiarities of generation and transport of structural defects induced by the laser irradiation** 414
A. E. Pogorelov
- Influence of migration the radiation-induced excitations in hetero-fullerenes C₅₈Si₂ and C₆₈Si₂ of their probability of damage** 418
M.V. Kobets, P.A. Selyshchev
- Investigation on the effects of titanium diboride particle size on radiation shielding properties of titanium diboride reinforced boron carbide-silicon carbide composites** 421
B. Buyuk, A. B. Tugrul, A. C. Akarsu, A. O. Addemir

Наукове видання

1-st INTERNATIONAL CONFERENCE

**NANOMATERIALS: APPLICATIONS &
PROPERTIES**

NAP-2011

**PROCEEDINGS
Vol. 2, Part II**

(Alushta, Crimea, Ukraine Sept. 27-30, 2011)

Відповідальний за випуск декан ф-ту ЕЛІТ	доцент	С.І. Проценко
Комп'ютерне верстання	доцента доцента	С.М. Братушко Т.В. Лютого
Дизайн обкладинки	доцента	С.М. Братушко
Відповідальний редактор	доцент	Т.В. Лютий

Формат 60 × 84/16. Ум. друк. арк. Обл.-вид. арк. Тираж 100 пр.

Зам. №

Видавець та виготовлювач
Сумський державний університет,
вул. Р.-Корсакова, 2, м. Суми, 40007,
Свідоцтво про внесення суб'єкта видавничої справи ДК №3062 від 17.12.2007 р.

